A CABLE FORCE ESTIMATION METHOD FOR CABLE-TRUSS STRUCTURES BASED ON STATIC DISPLACEMENT MEASUREMENT

* G. Y. Tian，Y. L. Guo，X. A. Wang，K. Wang and B. H. Zhang

Department of Civil Engineering，Tsinghua University，Beijing，100084，China
* Email：tgy07@mails. thu. edu. cn

KEYWORDS

Cable force estimation，static displacement，pre-stress，cable-truss，displacement measurement error.

ABSTRACT

With respect to the topological property of cable-truss structures，this paper presents a cable force estimation method based on static displacement measurement：using difference between measured and theoretically calculated nodal displacement to achieve real cable force. Only displacement at loaded degrees of freedom is needed. This method can be operated with general finite element program ANSYS，and the result of cable force estimation is accurate. Influence of displacement measurement error on force estimation result is studied，and relation between them is obtained through numerical and theoretic analysis. By comparing several load-measurement schemes，it is shown that the more effect the geometric stiffness of cable pre-stress in the cable truss structures takes，the faster the iteration converges；the larger displacement is caused by loads，the less error in force estimation result there is due to displacement measurement error.

INTRODUCTION

Obtaining exact cable forces is precondition for estimating and checking whether mechanical properties of tensile structures satisfy design and construction requirement. For tensile structures，there are several methods to measure cable force，such as reading of jack's oil pump，elasto-magnetic（EM）sensor and tension-compression force sensor installed before tension process. However，once the jacks are removed after tension，or sensors are not installed before tension，they do not work out. In this situation，dynamic method（frequency method）was developed. Although it has been widely used in cable-stayed bridges，its application in tensile structural roof is limited because mechanical relation between dynamic properties and internal forces is not as simple as that in cable-stayed bridges due to complicated cable's boundary condition. Besides，vibration frequencies of large span structures are so intensive that it is difficult to measure them precisely. Static response has been studied to do parameter estimation in rigid structures. Sheena[1] proposed a method to correct stiffness matrix by using static test results，but all DOFs（degree

of freedoms） should be measured. Sanayei and Scampoli[2]，Sanayei and Saletnik[3][4]，Banan and Hjelmstad[5][6] studied iteration method for parameter identification based on sub-structures' strain or displacement，discussed relation of input and output errors to improve identification result. Hjelmstad[7] developed mutual residual energy method to achieve real parameter by iteration，and studied how to choose load and measurement schemes. Reference[2]~[7] depended on Monte Carlo Method to study influence of measurement error. In tensile structures，Wei[8] brought forward a method to identify a single cable's force with its profile. But there are few researches reported on complex tensile structures.

Different from rigid structures，tensile structures' geometric configuration，pre-stresses' values and their distribution interact and they influence each other. In cable truss structures，especially in spoke structures where cable trusses are arranged in circle（Figure 1），every joint is connected with 3 bars or cables in a plane，or 4 in a space. According to equilibrium matrix theory[9][10]，there is only one self-stress mode in the structure if self-stress mode exists，otherwise the structure is not stable. Structures with same configuration and different pre-stress will perform differently when bearing same loads.
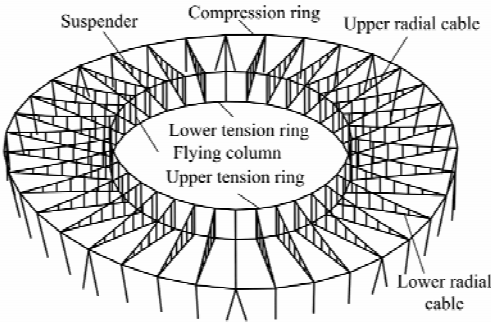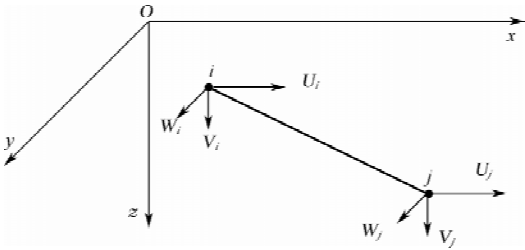

Figure 1   Spoke structure

Figure 2   Cable element

The method to estimate cable force in this paper has precondition as following：（1） structural configuration，loads，members' cross section and elastic module are known exactly.（2） When bearing loads for force estimation，the structure's performance satisfies linear elasticity and small deformation assumption.

CABLE FORCE ESTIMATION METHOD

Cable is simulated in general FE software ANSYS as a two-node linear bar shown in Figure 2. Element stiffness matrices are Eqn. 1 and Eqn. 2，representing elastic stiffness and pre-stress geometric stiffness respectively. l，m and n are cosine of angles between local coordinates and global coordinates $l = (X_j - X_i)/L_{ij}^0$，$m = (Y_j - Y_i)/L_{ij}^0$，$n = (Z_j - Z_i)/L_{ij}^0$. p_e^0 and L_{ij}^0 are element's pre-stress and length at initial state. When bearing loads，structural FE equation is Eqn. 3，where K_E and K_G are global elastic and geometric stiffness matrix assembled from Eqn. 1 and Eqn. 2[11]. U is nodal displacement vector. P is equivalent nodal force vector and R is non-linear residual term which is not considered in this paper.

$$k_E = \frac{EA}{L_{ij}^0} \begin{bmatrix} l^2 & & & & & \\ lm & m^2 & & & sym. & \\ ln & mn & n^2 & & & \\ -l^2 & -lm & -ln & l^2 & & \\ -lm & -m^2 & -mn & lm & m^2 & \\ -ln & -mn & -n^2 & ln & mn & n^2 \end{bmatrix} \tag{1}$$

$$k_G = \frac{p_e^0}{L_{ij}^0} \begin{bmatrix} 1-l^2 & & & & & \\ -lm & 1-m^2 & & & sym. & \\ -ln & -mn & 1-n^2 & & & \\ l^2-1 & lm & ln & 1-l^2 & & \\ lm & m^2-1 & mn & -lm & 1-m^2 & \\ ln & mn & n^2-1 & -ln & -mn & 1-n^2 \end{bmatrix} \tag{2}$$

$$(K_E + K_G)U = P + R \tag{3}$$

$$A_{3j \times b} t_{b \times 1} = F_{3j \times 1} \tag{4}$$

$$t = t' + \sum_{i=1}^{s} \alpha_i \bar{t}_i \tag{5}$$

$$t = t' + \alpha \bar{t} \tag{6}$$

On the other hand, a tensile structure with j free nodes, b elements should follow Eqn. 4, where A is equilibrium matrix determined by structural configuration, t is internal axial force vector, F is equivalent nodal force vector caused by load[9]. The rank of A is r, which is no more than b, and structure has $s = b - r$ self-stress modes. When $s > 0$, any self-stress mode $\bar{t}_i$ ($i = 1, 2 \cdots, s$) and their linear combination satisfy $A\bar{t}_i = 0$. So general solution of Eqn. 4 is Eqn. 5, where t' is a special solution of Eqn. 4. For cable-truss structures, especially spoke structures, $s = 0$ or $s = 1$. If $s = 0$, the structure is not stable. If $s = 1$, Eqn. 5 can be written as Eqn. 6.

Case 1: No Loads Applied before Cable Force Estimation
Assuming there is no loads before cable force estimation, so $t' = 0$ in Eqn. 6. Structure's equilibrium matrix equation is $A \cdot \alpha \bar{t} = 0$, where α is arbitrary scalar. It means that all the pre-stresses that satisfy ratio of self-stress and make all cables be tensioned will make structure obtain its configuration.

Denote structural real cable force as t_t, corresponding pre-stress geometric stiffness as K_G and elastic stiffness as K_E. When bearing load F, the real nodal displacement is U_t. So the finite element equilibrium equation is Eqn. 7. When estimating cable force, structural pre-stress is assumed to be t_a which satisfy equilibrium matrix equation $At_a = 0$ so that $t_a = \alpha_a t_t$. Structural finite element equilibrium equation is Eqn. 8 where α_a is an unknown scalar and U_a is calculated nodal displacement. Solving Eqn. 7 and Eqn. 8 will get Eqn. 9 where α_a seems to be achieved. However, it is usually difficult to get K_G because it is assembled in software's background. It is needed to find another way to get α_a.

$$(K_E + K_G)U_t = F \tag{7}$$

$$(K_E + \alpha_a K_G)U_a = F \tag{8}$$

$$\alpha_a = 1 - \frac{(U_a - U_t)F}{U_a^T K_G U_t^T} \tag{9}$$

$$\alpha' = 1 - \frac{(U_a^T - U_t^T)F}{U_a^T F} = \frac{U_t^T F}{U_a^T F} \tag{10}$$

On the other hand, in Eqn. 9, if $U_a = U_t$, $\alpha_a = 1$. So if a series of t_{ai} are substituted in Eqn. 8, the t_{ai}, whose corresponding calculated nodal displacement U_{ai} is equal to real nodal displacement U_t, is equal to real cable force t_t. An iteration method can be used to find t_t from an initial value of t_{ai}. Using F instead of $K_G U_t$ in Eqn. 9, an iteration coefficient α' is gotten in Eqn. 10. The right hand of Eqn. 10 is a fraction, whose numerator and denominator are both products of forces and displacements. In other

words, α' represents proportion of two works: load F's works on real structure and analytic model. If t_{ai} is less than t_t, $U_a > U_t$, then $\alpha' < 1$. If t_{ai} is larger than t_t, $U_a < U_t$, then $\alpha' > 1$. So t_{ai} multiplying $1/\alpha'$ will converge to t_t.

Case 2: Loads Applied before Cable Force Estimation

If there are loads before cable force estimation, for example dead load, initial analytic cable force is $t_{a0} = t' + \alpha_a \bar{t}$, where t' is special solution of Eqn. 4 and $\bar{t}$ is general solution of $At = 0$. Denoting K_{Ga} as pre-stress geometric stiffness corresponding to t' and K_{Gs} corresponding to $\bar{t}$, Eqn. 7 and Eqn. 8 become Eqn. 11 and Eqn. 12. ΔF is the load applied for cable force estimation. Correspondingly, ΔU_t and ΔU_a are real and analytic nodal displacements' increment when ΔF is applied. Since real cable force is unknown, K_{Ga} might not be equal to K_G, but their difference is equal to K_{Gs} multiplying β, as shown in Eqn. 13 where β is a scalar. This is because difference of two special solution of Eqn. 4 is general solution of $At = 0$. Solving Eqn. 11 to Eqn. 13 will get Eqn. 14.

$$(K_E + K_G)\Delta U_t = \Delta F \tag{11}$$

$$(K_E + K_{Ga} + \alpha_a K_{Gs})\Delta U_a = \Delta F \tag{12}$$

$$K_{Ga} - K_G = \beta K_{Gs} \tag{13}$$

$$\alpha_a + \beta = -\frac{(\Delta U_a^T - \Delta U_t^T)\Delta F}{\Delta U_a^T K_{Gs} \Delta U_t} \tag{14}$$

$$\alpha'' = -\frac{(\Delta U_a^T - \Delta U_t^T)\Delta F}{\Delta U_t^T \Delta F} = 1 - \frac{\Delta U_a^T \Delta F}{\Delta U_t^T \Delta F} \tag{15}$$

However, since β is unknown and K_{Gs} is in background of software, $\alpha_a + \beta$ can not be used directly to get t_t. Instead, an iteration coefficient α'' is used, as shown in Eqn. 15. α'' represents relative difference between F's works on analytic model and real structure. If analytic cable force t_{ai} is less than real cable force t_t, $U_a > U_t$, then $\alpha'' < 0$. If t_{ai} is larger than t_t, $U_a < U_t$, then $\alpha'' > 0$. So subtracting $\alpha'' \bar{t}$ from t_{ai} will converge to t_t.

For the two cases above, real cable force can be achieved by iteration. Notice that both α' and α'' presents relation between load's works on real structure and analytic model. The nodal displacements of DOFs where load is zero do not need to be measured because it contributes none to load's works. The iteration process is following:

Step 1: Measure the real structural configuration and build an FE model. Apply F or ΔF on structure, measure nodal displacements of DOFs where F or ΔF is applied. The real displacement is U_t. U_t's elements are denoted zero at unloaded DOFs.

Step 2: Get structural self-stress mode $\bar{P}$ for Case 1 and both self-stress mode $\bar{P}$ and special solution P' for Case 2. Set the pre-stress in analytic model $P_0 = a\bar{P}$ for Case 1 and $P_0 = P' + a\bar{P}$ for Case 2.

Step 3: Solve finite element equation Eqn. 8 and Eqn. 12 in ANSYS and get calculated nodal displacement U_{a0} or ΔU_{a0}. Calculate iteration coefficient α'_i for Case 1 or α''_i for Case 2, using Eqn. 10 and Eqn. 15.

Step 4: For Case 1, if $\| U_{ai} - U_t \| \leqslant \varepsilon_1$ or $|\alpha'_i - 1| < \varepsilon_2$, stop iteration and P_i is equal to structure's real cable force. Otherwise, go to step 6. For Case 2, condition to stop iteration is $\| \Delta U_{ai} - \Delta U_t \| \leqslant \varepsilon_1$ or $|\alpha''_i| < \varepsilon_2$, where ε_1 and ε_2 are convergence tolerance according to accuracy of calculation.

Step 5: Adjust pre-stress of analytic model. For Case 1, it is $P_i = P_{i-1}/\alpha'_{i-1}$. For Case 2, it is $P_i = P_{i-1} - \alpha''_{i-1}\bar{t}$. Then go back to Step 3.

ERROR ESTIMATION AND COMPARE OF LOAD-MEASUREMENT SCHEMES

If there is displacement measurement error δu_{mi} ($i = 1, 2, \cdots N_m$), denote measured displacement as U_m or ΔU_m which is equal to δu_{mi} plus U_t or ΔU_t. Calculated nodal displacement U_a or ΔU_a converge to U_m or ΔU_m, not U_t or ΔU_t, causing relative force estimation errors shown in Eqn. 16 and Eqn. 17 for Case 1 and 2 respectively, where N_d is the number of DOFs, N_m is number of measured DOFs, u_a and u_t are U_a's and U_t's elements, and k_G is K_G's element. In this case, condition to stop iteration should be $|\alpha'_i - 1| < \varepsilon_2$ or $|\alpha''_i| < \varepsilon_2$, because δu_m may not follow the deformation compatibility condition and $\| U_{ai} - U_t \| \leqslant \varepsilon_1$ or $\| \Delta U_{ai} - \Delta U_t \| \leqslant \varepsilon_1$ may never be satisfied.

Since U_a and ΔU_a contain δu_{mi}, Eqn. 16 and Eqn. 17 are nonlinear equations. Partial derivative of output error δ' with respect to measured displacement u_{ak} is Eqn. 18, whose right hand's sign (positive or negative) is independent of u_{ak}. This means that δ' is monotone to every u_{ak}. However, whether δ' is u_{ak}'s monotonic increasing function or decreasing function depends on structural stiffness and loads. Eqn. 17 is similar with Eqn. 16.

$$\delta' = (\alpha_a - 1)/1 = -\frac{\sum\limits_{i=1}^{N_m} \delta u_{mi} f_i}{\sum\limits_{j=1}^{N_d} \sum\limits_{i=1}^{N_d} u_{ai} k_{G\,ij} u_{tj}} \tag{16}$$

$$\delta'' = \frac{(\alpha_a + \beta)\bar{t}}{t_t} = -\frac{t_t}{\sum\limits_{j=1}^{N_d} \sum\limits_{i=1}^{N_d} \Delta u_{ai} k_{Gs\,ij} \Delta u_{tj}} \cdot \sum\limits_{i=1}^{N_m} \delta u_{mi} f_i \tag{17}$$

$$\frac{\partial \delta'}{\partial u_{ak}} = \frac{f_k \left(\sum\limits_{j=1}^{N_d} \sum\limits_{i=1}^{N_d} u_{ai} k_{G\,ij} u_{tj} \right) - \left(\sum\limits_{i=1}^{N_m} (u_{ai} - u_{ti}) f_i \right) \left(\sum\limits_{j=1}^{N_d} k_{G\,kj} u_{tj} \right)}{\left(\sum\limits_{j=1}^{N_d} \sum\limits_{i=1}^{N_d} u_{ai} k_{G\,ij} u_{tj} \right)^2} =$$

$$\frac{\sum\limits_{j=1}^{N_d} \sum\limits_{i=1,i \neq k}^{N_d} u_{ai} k_{G\,ij} u_{tj} f_i - \sum\limits_{j=1}^{N_d} \sum\limits_{i=1}^{N_d} u_{ti} k_{G\,ij} u_{tj} f_i}{\left(\sum\limits_{j=1}^{N_d} \sum\limits_{i=1}^{N_d} u_{ai} k_{G\,ij} u_{tj} \right)^2} \tag{18}$$

Example 1. Figure 3 is a cable-truss without loads. Arrows with numbers are DOFs' directions and numbers. Element 1~6 are cables while Element 7~8 are bars. Elements' young's module is 2.1×10^5 MPa, cross-section areas are shown in Table 1 and pre-stresses in Table 2. Take 5 times of pre-stresses in Table 2. as initial cable force for iteration. 8 load-measurement schemes and their number of iteration before convergence to real cable force are shown in Table 3. The influence of displacement measurement

errors on cable force estimation results is shown in Table 4，Figure 5 and Figure 6.

From Table 3，it can be seen that iteration numbers of Scheme 4 and 6 are the largest in all schemes. Scheme 5，which has a pair of forces in opposite directions vertically，has the smallest iteration number. This is because pre-stress geometric stiffness takes different effect in different schemes due to their loads：the least effect in Scheme 4 and 6 while the most in Scheme 5. Scheme 5's displacement mode is quite the same with cable-truss's mechanism mode（Figure 4），both of which are anti-symmetric. Iteration numbers of Scheme 1 to 3 and Scheme 7 to 8 are close to Scheme 5.

In Table 4，it is shown that Scheme 4 and 5，whose loads are the same with Scheme 4 in Table 2，have enormous output errors（force estimation errors）even their input errors（displacement measurement errors）are smaller than other schemes（if the input errors had become larger，the numerical divergence would appear）. Scheme 2 and 3，whose loads are the same but errors are of different signs，have quite different level of output errors. In Figure 5，－2kN load is applied at DOF 2 and 2kN at DOF 8. Eqn. 16's solution is denoted as lines. Relative output errors due to uniformly distributed random measurement errors between －10 mm to 10 mm are calculated with ANSYS and denoted as spots. It can be noticed that ANSYS's solution lies in surface of Eqn. 16's solution. This surface is monotone to each axis and is almost a plane. Figure 6 shows the same content with load applied at DOF 1 and 6. However，compared with Figure 5，surface in Figure 6 is far from a plane. This is because nodal displacements in Figure 5 are about 2 times of those in Figure 6. With the same amplitude of input error，the output error with smaller nodal displacement shows non-linear property. Generally speaking，from Table 4，Figure 5 and Figure 6，it can be concluded that the larger displacement is caused by loads，the smaller cable force estimation error there will be.
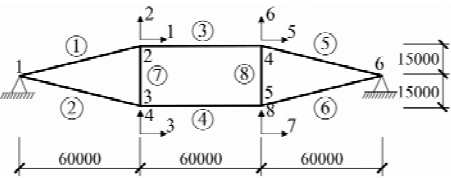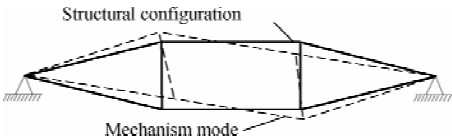

Figure 3　Cable truss of EX. 1
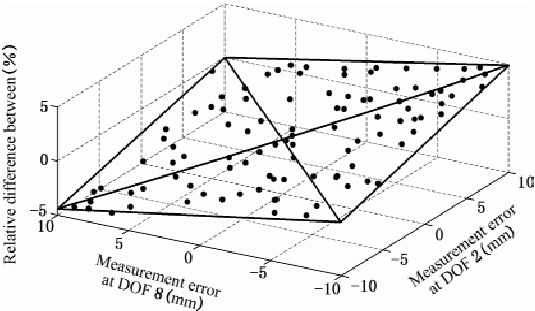

Figure 4　Mechanism mode of cable-truss

Figure 5　－2kN load at DOF 2 and
2kN at DOF 8 in EX. 1
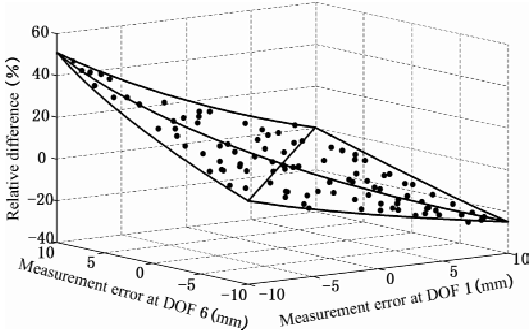

Figure 6　2kN load at DOF 1and
－2kN at DOF 6 in EX. 1

TABLE 1   CROSS AREA OF MEMBERS(mm²)

Element	Area	Element	Area	Element	Area
1, 3, 5	200	2, 4, 6	400	7, 8	1 000

TABLE 2   INTERNAL FORCES OF REAL STRUCTURE(kN)

Element	Pre-stress	Element	Pre-stress	Element	Pre-stress
1, 2, 5, 6	100	3, 4	97.014	7, 8	− 24.253

TABLE 3   LOAD-MEASUREMENT SCHEME AND ITERATION NUMBER OF EX. 1 AND EX. 2

Scheme	Load DOF	Value	Iteration number EX. 1	EX. 2	Scheme	Load DOF	Value	Iteration number EX. 1	EX. 2	Scheme	Load DOF	Value	Iteration number EX. 1	EX. 2
1	2	− 2 kN	6	31	5	2	2 kN	4	24	7	1	2 kN	9	40
2	1	2 kN	9	81		8	− 2 kN				6	− 2 kN		
3	4	− 2 kN	7	31	6	2, 6	− 2 kN	132	163	8	1	− 2 kN	6	29
4	2, 8	− 2 kN	132	163							6	− 2 kN		

TABLE 4   INFLUENCE OF MEASUREMENT ERROR ON EX. 1

Sch.	Load DOF	Value	Realdisp. (mm)	Input Error(mm)	Relative output error ANSYS	Eqn. 16
1	2	− 2 kN	− 114	− 10	− 9.03%	− 8.94%
2	1	2 kN	9	10	− 60.72%	− 60.80%
3	1	2 kN	9	− 6	1 321.40%	1 322.41%
4	2	− 2 kN	− 24	− 3	− 93.88%	− 93.81%
	8	− 2 kN	− 24	0		
5	2	− 2 kN	− 24	10	709.07%	708.65%
	8	− 2 kN	− 24	0		

TABLE 5   INFLUENCE OF MEASUREMENT ERROR ON EX. 2

Sch.	Load DOF	Value	Realdisp. (mm)	Input Error(mm)	Relative output error ANSYS	Eqn. 17
1	2	− 2 kN	− 41	− 10	− 27.75%	− 27.69%
2	1	2 kN	4	10	− 95.58%	− 95.70%
3	1	2 kN	4	− 1	129.79%	129.82%
4	2	− 2 kN	− 22	− 5	− 99.08%	− 99.01%
	8	− 2 kN	− 22	0		
5	2	− 2 kN	− 22	10	287.88%	287.74%
	8	− 2 kN	− 22	0		

Example 2. Cable-truss is the same with Example 1，while there are downwards vertical forces of 10 kN on Node 2 to Node 5. The real internal forces and initial value of iteration is shown in Table 6. The number of iteration before convergence is shown in Table 3. Compared with Example 1，all load-

measurement schemes have similar rule of iteration numbers while it takes more calculation time before convergence. The influence of measurement error on estimation result is shown in Table 5，which is similar with Table 4. However，since the nodal displacement in Example 2 is less than those in Example 1，output errors are larger than Example 1. In companion with Figure 5 and Figure 6，theoretic solution and finite element solution of random input errors are shown in Figure 7 and Figure 8，whose non-linear property is more obvious.

TABLE 6   INTERNAL FORCES OF STRUCTURE IN EX. 2

Element	Real force（kN）	Initial value of iteration（kN）
1，5	300.0	100.0
2，6	380.0	182.5
3	291.0	97.0
4	371.0	177.0
7，8	82.8	34.5

TABLE 7   INTERNAL FORCES OF STRUCTURE IN EX. 3

Member	Internal Force Ⅰ（kN）	Internal Force Ⅱ（kN）
Upper radial cable	100.0	4 000.0
Lower radial cable	100.0	4 000.0
Upper tensing ring	556.6	22 262.3
Lower tension ring	556.6	22 262.3
Flying column	−24.2	−970.2
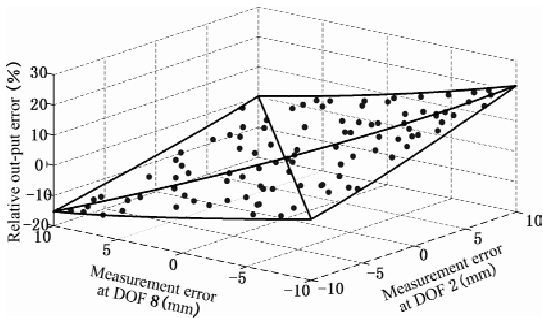
Figure 7   −2kN load at DOF 2 and
2kN at DOF 8 in EX. 2
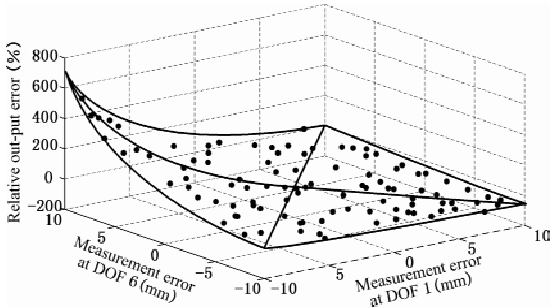
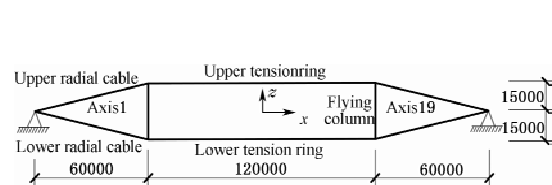Figure 8   2kN load at DOF 1 and
−2kN at DOF 6 in EX. 2

Figure 9   Cable-truss of spoke structure
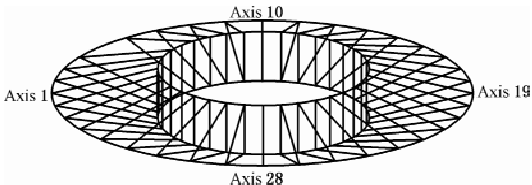

Figure 10   Axis number

TABLE 8   LOAD-MEASUREMENT SCHEMES ANDOUTPUT ERROR OF EX. 3

Scheme	Load		Internal Force	Z Disp.		Relative output error	
	Axis	Value		Max.	Min.	ANSYS	Eqn. 16
1	1~36	2 000	I	− 90	− 90	− 68.25%	− 67.20%
			II	− 14	− 14	− 48.74%	− 47.99%
2	1~18	4 000	I	− 456	279	− 3.69%	− 3.63%
			II	− 23	− 4	− 36.41%	− 35.99%
3	1~9	8 000	I	− 812	342	− 1.63%	− 1.59%
			II	− 32	− 0.003	− 27.23%	− 27.08%

* Negative displacement is downward.

Example 3. A spoke structure of 36 cable-trusses is shown in Figure 9 and Figure 10. Upper radial and tension ring cables have cross-section area of 200 mm^2 and lower radial and tension ring cables 400 mm^2 respectively. Cross-section area of flying columns is 1 000 mm^2. There are no loads before force estimation. Two cases of internal force, denoted as Internal Force I and II are shown in Table 7. A total of 72 kN downwards vertical load is applied with three kinds of distribution, as shown in Table 8. It simulates hanging a number of weights on structures to estimate cable force on construction site. Input error is − 10 mm at every axis where load is applied. The relative output error is the upper boundary error due to monotone relation of input and output errors. It can be seen that the output error in Scheme 3 is the smallest in both internal force cases while the output error in Scheme 1 is the largest. However, since pre-stresses of Internal Force II is larger than those of Internal Force I, the nodal displacement decreases obviously. So the output error increases. This can be explained with Eqn. 16. With the same amplitude of input error, the larger the nodal displacement is, the smaller the output error becomes. So when choosing load-measurement scheme, arrange loads to make nodal displacement at DOFs where loads are applied as large as possible.

CONCLUSION

(1) The method in this paper can obtain real cable forces accurately and its advantage is that only the displacement of degrees of freedom along which loads are applied need to be measured. (2) The less effect the elastic stiffness takes, the larger structural displacement there is; hence the less force estimation error there will be and the faster the numerical iteration will converge. (3) Relation between measurement error and force estimation error is monotone, and if displacement is much larger than measurement error, input-output error relation is linear, otherwise non-linear.

REFERENCES

［1］Sheena, Z., Unger, A. and Zalmanovich, A., "Theoretical stiffness matrix correction by using static test response", Israel Journal of Technology, 1982, 20, pp. 245−253.

［2］Sanayei, M. and Scampoli, F. S., "Structure element stiffness identification from static test data", Journal of Engineering Mechanics, 1991, 117(5), pp. 1021−1035.

［3］Sanayei, M. and Saletnik, J. M., "Parameter estimation of structures from static strain measurements I : formulation", Journal of Structural Engineering, 1996, 22(5), pp. 555−562.

［4］Sanayei, M. and Saletnik, J. M., "Parameter estimation of structures from static strain measurements II : error sensitivity analysis", Journal of Structural Engineering, 1996, 22(5), pp. 563−572.

［5］Banan, M. R. and Hjelmstad, K. D., "Parameter estimation of structure from static response I : computational

aspects", Journal of Structural Engineering，1994，120(1)，pp. 3243-3258.

[6] Banan，M. R. and Hjelmstad，K. D.，"Parameter estimation of structure from static response Ⅱ：computational aspects", Journal of Structural Engineering，1994，120(1)，pp. 3259-3283.

[7] Hjelmstad，K. D.，Wood，S. L. and Clark，S. J.，"Mutual residual energy method for parameter estimation in structures", Journal of Structural Engineering，1992，118(1)，pp. 223-242.

[8] Wei，J. D. and Liu，S. H.，"Tension calculation of cable by its static profile", Engineering Mechanics，2003，20 (3)，pp. 104-107.（in Chinese）

[9] Pellegrino，S. and Calladine，C. R.，"Matrix analysis of statically and kinematically indeterminate frameworks", International Journal of Solids and Structures，1986，22(4)，pp. 409-428.

[10] Tian，G. Y.，Guo Y. L. and Wang K.，"Constraints removal method for form-finding problem of spoke structures", Journal of Xi'an University of Architecture and Technology（Natural Science Edition），2010，42(2)，pp. 153-158.（in Chinese）

[11] Krishna，P.，"Cable-suspended roofs", McGraw-Hill Book Company，1978，pp. 65.

FINITE ELEMENT ANALYSIS ON THE NATURAL FREQUENCY OF A WIND TURBINE TOWER UNDER DIFFERENT BOUNDARY CONSTAINTS

[*] J.J. Wang，G. Shi，Y.J. Shi and Y.Q. Wang

Key Laboratory of Civil Engineering Safety and Durability of China Education Ministry，Department of Civil Engineering，Tsinghua University，Beijing，10084，China
[*] Email：wangjiaojiao922@126.com

KEYWORDS

Wind turbine tower，modal analysis，first-order frequency，boundary constraint，finite element analysis（FEA）.

ABSTRACT

In order to analyze the influence of ground and foundation stiffness on dynamic performance of wind turbine towers，modal analysis is carried out by ANSYS software. Finite element models of the steel tower with and without the concrete foundation are both established. Natural frequency and natural mode of vibration are determined under different boundary constraints including bottom of steel tower fixed，bottom of concrete foundation fixed，bottom and side faces of foundation fixed，bottom of foundation fixed and displacement of two horizontal directions of foundation side constrained，rotational spring and vertical compression-tension spring set at the bottom of foundation，rotational spring and vertical compression-tension spring set at the bottom of foundation and horizontal compression-tension spring set at the side face of foundation. In the finite element model，mass elements of machinery space and impeller are established on top of the tower. Calculation results under different boundary constraints show that flexibility of foundation and ground has a certain effect on natural frequency of the whole structure. Difference between frequency results of foundation and ground stiffness considered or not was about 11.6%. This indicates that stiffness of foundation and ground could not be neglected in the design. The author compared first-order frequency of the tower and 1p，3p of the impeller rotation frequency. The little difference between first-order frequency and upper limit value of 1p shows the unfavorable dynamic properties of the tower.

INTRODUCTION

Nowadays，with the problem of energy shortage，wind power has been used widely due to its mature technology，rapid development and commercialization prospects[1]. The design of wind turbine tower is one of the important issues in wind power industry. Under the dynamic load caused by impeller rotation and random wind load，vibration of the tower would occur. This vibration will not only cause additional

stress of the tower reducing the structure strength，but also affect the deformation and vibration of impeller at the tower top[2]. If the frequency of the impeller is close to the natural frequency of the tower，performance of the wind turbine will be affected due to the resonance. Therefore，in order to ensure the safety of wind turbine，dynamic performance of towers must be analyzed.

Modal analysis is the key issue of the structural dynamic analysis[3]. In the design of the tower，modal analysis must be carried out to find out the natural frequency of the tower and whether it is close to the rotation frequency of the impeller. Therefore，we can determine whether the resonance could be avoided.

In modal analysis，different considerations of boundary conditions have some influence on the results. Liu [4] calculated the natural frequency by ANSYS software considering the tower fixed to the Earth. Zhu[5] and Huang [6] established mass elements at the bottom of the FEA model to consider the effect of the foundation mass. And two rotational springs were connected to the mass nodes so that the effect of the foundation stiffness could be simulated.

In practical engineering，bottom of wind turbine tower is not fixed to the Earth like literature [4]. Concrete foundation is at the bottom of the tower and its bottom and side faces are also not completely rigid. It needs further study whether different boundary conditions have a great influence on dynamic performance of the tower. In this paper，modal analysis is carried out under different boundary constraints with ANSYS software.

TOWER MODEL

Engineering Background

This paper focuses on a cylindrical tower of wind turbine in practical engineering. This tower consists of steel tower of Q345 and concrete foundation of C40. The sketch plan is shown in Figure 1. The steel tower is of hollow cylindrical shape with various wall thicknesses which are from 10 mm to 50 mm. Diameter of the bottom tower is 4.2 m，while the top is 2.737 m. And it is 78.768 m high divided into three parts with flanged connections. The 10.855 m-high concrete foundation consists of cylindrical top，cylindrical bottom and middle hollow cylinder.

Finite Element Model

In the finite element model，outside diameter of the steel tower is 4.2 m from the ground to the height of 1.9 m. And for height of 1.9 m to 78.768 m，the diameter changes from 4.2 m to 2.737 m evenly. The wall thickness is shown in Figure 2. Concrete foundation consists of top cylinder of diameter 4.9 m，height 0.355 m，bottom cylinder of diameter 4.6 m，height 1m and middle cylinder of outside diameter 4.6 m，inside diameter 3.4 m，height 9.5 m as shown in Figure 3.

Mass distribution is considered as following. The material density is 7 850 kg/m^3 for steel tower and 2 500 kg/m^3 for concrete foundation. The tower accessories are 7.8 t weight，only 3% of the whole tower, so they can be ignored. 64 t of machinery space mass and 33.7 t of impeller mass are established at the top of the tower as finite elements of mass 21. Elastic modulus of steel is taken as 2.06×10^5 N/mm^2,

Poisson's ratio as 0.3, and the elastic modulus of concrete C40 as 3.25×10^4 N/mm^2.
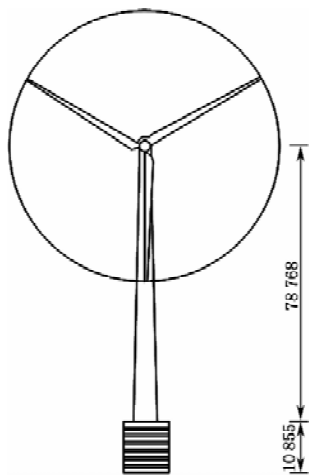

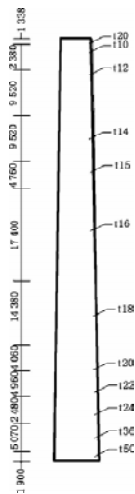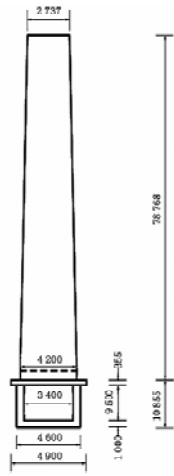| Figure 1 Sketch plan of	Figure 2 Wall thickness	Figure 3 Geometric dimensions
wind turbine tower	of steel tower	of the turbine tower

Flanged connection between three parts of the tower and the connection between steel tower and concrete foundation are simplified as rigid connection in the model.

Solid element (solid 65) is adopted for the concrete foundation while beam element (beam 189) or shell element (shell 181) for the steel tower. The results of two models using different elements are compared.

CALCULATION METHOD

In Ansys software, modal analysis is selected. Modes are obtained by Block Lanczos method using consistent mass matrix.

Natural frequency is calculated for a cantilever beam of single degree of freedom as an example to verify the accuracy of calculation method, as shown in Figure 4.

(a) Calculation diagram   (b) FEA model   (c) First-order mode

Figure 4 Example verification of calculation method

The parameters are as following, $E = 2.06 \times 10^5$ N/mm^2, $m = 100$ kg, $l = 0.5$ m, section dimension

$b \times h = 0.01$ m $\times 0.01$ m. 100 elements of beam 189 are meshed. Mass block m is established at the top of the beam as element of mass 21.

Theoretical value of first-order frequency：

$$\delta = l^3/3EI，k = 1/\delta = 3EI/l^3，T = 2\pi \sqrt{m/k} = 2\pi \sqrt{ml^3/3EI} = 0.978\ 9\ \text{s}，f = 1/T = 1.021\ 6\ \text{s}^{-1}$$

Result of first-order frequency calculated by Ansys is $1.021\ 4\text{s}^{-1}$. That is only 0.02% smaller than the theoretical value which indicates the accuracy of calculation method and effectiveness of the following analysis.

COMPARISON OF BEAM ELEMENT AND SHELL ELEMENT

Results of models using beam element（beam 189）and shell element（shell 181）for the steel tower are compared.

Beam Element Model（Model 1）and Result

In this model，the bottom of the steel tower is considered to be fixed to the Earth（no foundation）. Element of beam 189 is used. 64 elements are meshed along the circumference. 12 parts are divided along the height direction according to the wall thickness and 264 elements are meshed. Roughly equal size of each element is the principle to determine the number of elements each part meshed. First-order frequency is $0.347\ 3\text{s}^{-1}$. FEA model and mode graph are shown in Figure 5.
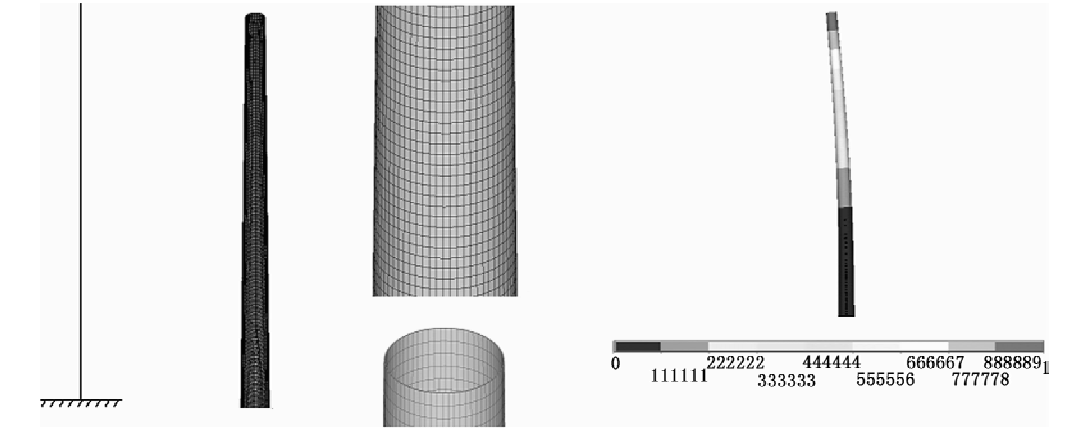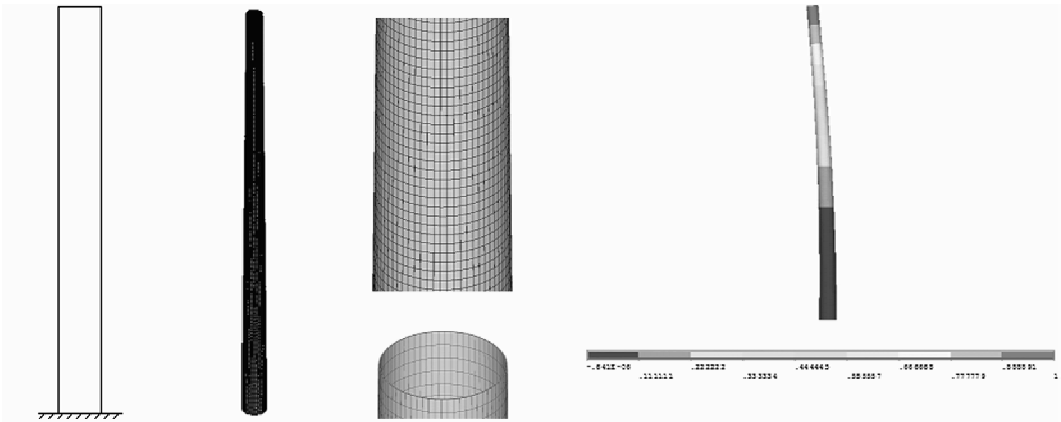

（a）Calculation diagram　（b）FEA model　（c）Details of the model　　　　　（d）First-order Mode

Figure 5　Beam element model and mode graph

Shell Element Model（Model 2）and Result

In this model，the bottom of the steel tower is considered to be fixed to the Earth（no foundation）. Element of shell 181 is used. Area of frustum is established and divided into 12 parts along the height direction according to the wall thickness. Each part is attributed different real constants representing different wall thicknesses. Along the height direction，roughly equal size of each element is the principle

to determine the number of elements each part divided into and there are totally 264 elements. While along the hoop direction，64 elements are divided with mapped meshing. First-order frequency is $0.349\,8\,\text{s}^{-1}$. Figure 6 shows FEA model and mode graph.

a) Calculation diagram　（b）FEA model　　　（c）Details of the model　　　　　（d）First－order mode

Figure 6　Shell element model and mode graph

Comparison of Beam Element Model and Shell Element Model

The difference between results of beam element and shell element models is only 0.7%. Therefore，element type（beam or shell）has little influence on the result of natural frequency. Meantime it also shows the accuracy of FEA model and calculation method of this paper. Shell element is taken in the following analysis.

MODAL ANALYSIS UNDER DIFFERENT BOUNDARY CONSTRAINTS

In practical engineering，the bottom of wind turbine tower is not fixed to the Earth like previous sections. Concrete foundation is at the bottom of the tower and its bottom and side faces are also not entirely rigid. Therefore，in order to analyze the influence of ground stiffness on the dynamic characteristics of wind turbine tower，finite element model of whole structure with steel tower and concrete foundation is established. Overall mode of the tower is studied under different boundary constraints for bottom and side faces of concrete foundation. Figure 7 shows calculation diagrams of model 3 to model 7.

Bottom Face of Foundation Fixed（Model 3）

The bottom of concrete foundation is considered to be fixed to the Earth. Element of shell 181 is adopted for steel tower and solid 65 for concrete foundation. Rigid connection between steel tower and concrete foundation is formed by sharing nodes. Finite element model of the steel tower part is the same with model 2. For concrete foundation，64 elements are meshed along the hoop direction. As to the radial direction，the outside diameter（OD）and inside diameter（ID）of middle part of foundation are taken as the dividing lines as well as the shell face of the steel tower. 2 elements are meshed outside OD，2 elements between OD and face of tower，and 4 elements between face of tower and ID. Along the axial
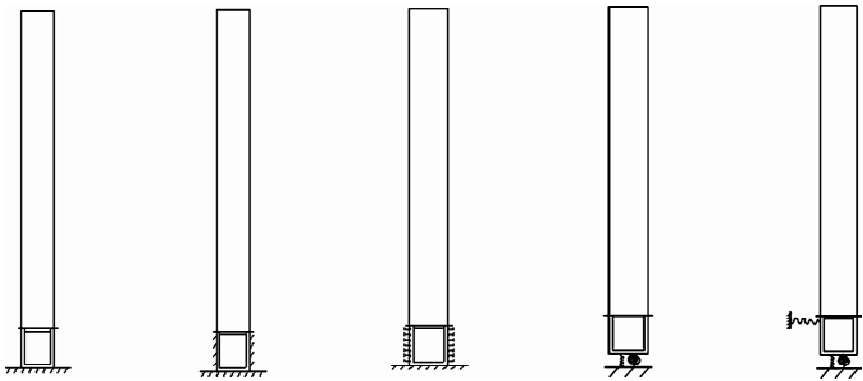
Figure 7　Calculation diagrams

direction，36 elements are meshed（2 for top part，30 for middle part and 4 for bottom part）. The foundation is meshed as body mapped form. First-order frequency is $0.3340\mathrm{s}^{-1}$.

Bottom and Side Faces of Foundation Fixed（*Model 4*）

Bottom and side faces are thought to be fixed to the Earth. Side face of foundation fixed is the only addition compared to model 3. Frequency calculated is $0.3476\ \mathrm{s}^{-1}$.

Bottom of Foundation Fixed and Horizontal Displacement of Side Face Constrained（*Model 5*）

In this model，bottom face of foundation is fixed and displacement of two horizontal directions is constrained for side face. This FEA model is same with model 3 except for constraints. First-order frequency is $0.3442\ \mathrm{s}^{-1}$ which is reasonable between results of model 3 and model 4.

Rotational Spring and Vertical Compression-Tension Spring Set at Bottom of Foundation（*Model 6*）

The influence of ground stiffness could be equivalent to the action of spring. Rotational spring and vertical compression-tension spring are set at the bottom of foundation. Stiffness of rotational spring is 21 GN. m/rad and stiffness of the vertical compression-tension is 108666 kN/m according to geological survey data.（Stiffness value is provided by design group of foundation）. The model is same with model 3 except for elements of combin40 added to the bottom of foundation. The springs are fixed to the Earth. First-order frequency is $0.3031\ \mathrm{s}^{-1}$. Compared to the constraints of bottom entirely fixed（Model 3），the constraints are weaker causing smaller frequency.

Rotational Spring and Vertical Compression-Tension Spring Set at Bottom of Foundation and Horizontal Compression-Tension Spring Set at Side Face of Foundation（*Model 7*）

Taking vertical and side stiffness of ground soil into account，the author established rotational spring and vertical compression-tension spring at bottom of foundation and horizontal compression-tension spring at side face of foundation. 21 GN • m/rad is stiffness for rotational spring，108 666 kN/m for vertical spring and 35 061.2 kN/m for horizontal spring. FEA model is same with model 3 except for elements of combin 40 with fixed end set at the bottom and side faces of foundation. The result turned out to be $0.3092\ \mathrm{s}^{-1}$,

a little larger than model 6 due to more constraints.

Comparison of First-Order Frequency under Different Constraints

The following table lists first-order frequencies under different constraints. In China，result of model 2 is generally used in the design of wind turbine towers. So values of first-order frequencies under different constraints are all compared to the result of model 2.

TABLE 1   FIRST-ORDER FREQUENCIES UNDER DIFFERENT BOUNDARY CONSTRAINTS

Model No.	Constraints	Fist-order frequency	Comparison to result of model 2
3	Bottom face of foundation fixed	$0.334\,0\ \mathrm{s}^{-1}$	-4.5%
4	Bottom and side faces of foundation fixed	$0.347\,6\ \mathrm{s}^{-1}$	-0.6%
5	Bottom of foundation fixed and horizontal displacement constrained	$0.344\,2\ \mathrm{s}^{-1}$	-1.6%
6	Rotational spring and vertical compression-tension spring set at the bottom of foundation	$0.303\,1\ \mathrm{s}^{-1}$	-13.4%
7	Rotational spring and vertical compression-tension spring set at the bottom of foundation and horizontal compression-tension spring set at side face of foundation	$0.309\,2\ \mathrm{s}^{-1}$	-11.6%

It can be seen that the stiffness of foundation has little effect on natural frequency which is less than 5% from comparison between model 3 and model 2.

From comparison of model 3，4 and 5 or model 6 and 7，with same constraints at bottom of foundation，side stiffness of ground soil has little effect on natural frequency of the whole structure.

We can see that stiffness of ground has some influence on natural frequency of whole structure from difference between model 7 and 4. It is 10% different whether to consider vertical and side stiffness of ground soil or not. The frequency is 11.6% lower than that of the model with stiffness of foundation or ground unconsidered.

First-order modes of all models turn out to be curves of bending along the horizontal direction.

CONCLUSIONS

（1）The stiffness of foundation has little effect on natural frequency which is less than 5%.

（2）With same constraints at bottom of foundation，side stiffness of ground soil has little effect on natural frequency of whole structure.

（3）Stiffness of ground soil has some influence on natural frequency. If the ground is taken as elastic material，first-order frequency is 10% lower than ground as rigid material and 11.6% lower than whole foundation taken as a rigid part. This shows that the influence of stiffness of foundation and ground soil cannot be ignored in the design of wind turbine towers.

(4) 1p of the impeller rotation frequency is $0.167 - 0.325$ s^{-1} and 3p is $0.4851 - 0.975$ s^{-1}. First-order frequency of whole structure is 0.3092 s^{-1} which is very close to the upper limit value of 1p indicating the unfavorable dynamic properties of the tower.

REFERENCE

［1］Wang，H.H.，"The Series of Lectures on Wind Power Technology（Part1）Principle and Development of Wind Power Generation"，Machine Building & Automation，2010,39(1),pp.175-178.（in Chinese）

［2］Gong，J.Y. He，D.X. and Sun，R.L.，"Engineering technical Manual of wind farm"，Press of Machinery Industry，2004.（in Chinese）

［3］Jin，X.，He，Y.L.，and Liu，H.，"Vibration analysis of wind turbine based on Pitt-peter theory"，Engineering Mechanics，2008,25(7),pp.28-34.（in Chinese）

［4］Liu，H.Q.，Yu，C.Y.，and Du，Y.，"Wind response analysis under coupling action of the impeller and tower"，Journal of Disaster Prevention and Mitigation Engineering，2010,30 suppl,pp.139-142.（in Chinese）

［5］Zhu，X.H.，Huang，F.L.，and Zhang，L.G.，"Modal and buckling analysis for the tower of large wind turbine"，Journal of Railway Science and Engineering，2010,7(6),pp.86-89.（in Chinese）

［6］Huang，D.S.，Wang，C.S.，Zou，F.S. and Huang，F.L.，"Wind turbine tower modal analysis and application"，Equipment Manufacturing Technology，2009（9）,pp.19-21.（in Chinese）

ANALYSIS ON WIND-INDUCED VIBRATION RESPONSE OF CABLE-STAYED LATTICE STRUCTURE

* G. S. Bian，Y. M. Zhang and B. Guo

School of Civil Engineering，Shandong Jianzhu University，Jinan，250101，China
* Email：bgshseu@163.com

KEYWORDS

Cable-stayed lattice structure，wind-induced vibration，wind speed simulation，coupling analysis，nonlinear analysis，structure response.

ABSTRACT

Based on summary of calculation theory of structural wind engineering and fluctuating wind simulation，the conversion technology from wind speed time interval to wind pressure time interval is studied in this paper. Considering the 3d coherence of the space point，the program of simulating fluctuating wind is compiled based on AR algorithm to select AR（p）and different target wind velocity spectrum freely. Furthermore，the fluctuating wind speed time series under the intended target spectrum can be gained by modifying a small quantity of parameters using the above mentioned programme，and the wind speed time series of many space points are simulated. The analysis of wind-induced response of the awning in Guangzhou University City main stadium is performed by wind loading program，which is compiled by APDL. The analysis results indicate that displacements and the cable forces fluctuate around the average during the process of random wind vibration，and the volatilization doesn't generate. The conclusions are that the instability of cable-mast structure can not happen under wind load，the displacements of cables are small，which guarantee against colliding with the adjacent cables under fluctuating wind，and stress amplitude is very low under wind load，that will not lead to fatigue damage.

Wind load is one of the important factor which leads to structural damage. The situation that airport and stadium roof was blown bad had occurred many times in China. Cable-stayed lattice structure is characterized by small damping，light weight and sensitive to wind effect. The canopy of Guangzhou University Town Center Stadium is different from ordinary cable-stayed lattice structure. It has many masts，many cables，and it is the "double-hinged support" system. The safety of the structure under wind load is worth to study. In this paper，with the background of cable-stayed lattice steel roof of Guangzhou University Town Center Stadium，program is composited to calculate three-dimensional time-related wind speed. Wind load is imposed on the roof calculation model by the APDL language of ANSYS program. The wind-induced vibration response of the structure is studied to ensure the structure safety.

SIMULATION OF AVERAGE WIND AND FLCUTUATING WIND

In this paper，average wind speed was described by A. G. Davenport's exponential law[1] which "Load

code for the design of building structures " GB 50009 (after referred to as" load code ") recommended to adopt.
Eqn. 1.

$$\bar{v}/\bar{v}_s = (z/z_s)^a \tag{1}$$

Where，α is surface roughness index；z is height，$\bar{v}$ is average wind speed at the height；z_s $\bar{v}_s$ is respectively the standard height and average wind speed at standard height.

Kaimal wind spectrum[2] is used to describe the fluctuating wind speed，and the power spectral density function is expressed by the $S_u(z，n)$ express as：
Eqn. 2.

$$nS_u(z，n)/u_*^2 = 200f/(1+50f)^{\frac{5}{3}} \tag{2}$$

Where，n is the frequency (Hz)；f is the Mourning coordinates；z is the ground clearance (m)；u_* is shear wind velocity.

H. A. Panofsky empirical formula[2] according to the measured data is used to descript vertical fluctuating wind speed：
Eqn. 3.

$$S_w(n) = 6kx \cdot \bar{v}_{10}^2/[n(1+4x)^2] \tag{3}$$

Where，$x = nz/\bar{v}_{10}$，$\bar{v}_{10}$ is average wind speed at 10 m height in vertical direction；k is von • Karman constant，the value is usually 0.4；other with equation (2).

Wind speed simulation takes into account the spatial correlation of fluctuating wind. Linear filter method of self-regression (AR method)[3] and the large-scale numerical analysis software MATLAB are used to develop a fluctuating wind simulation program. With the program we can choose the number of autoregressive order p and the calculation accuracy for Wiener-Khinchin formula.

WIND-INDUCED VIBRATION RESPONSE ANALYSIS

Large span cable-stayed grid structures have closely spaced frequencies and requires to consider the horizontal and vertical wind，otherwise there would be a larger deviation[4]. Coupling of the structure and the wind should be taken into account also.

Wind-induced Vibration Analysis Method

Fluctuating wind load is directly added to the structure with time-domain method，and structural dynamic response is obtained by direct integration method. Analysis results and measurement data of wind tunnel experiments and field are more consistent[5]. According to Morison formula，wind load is calculated as following with the relative speed of wind and structure to reflect coupling between wind and structures.
Eqn. 4.

$$p(t) = \frac{1}{2}C_p\rho A[v+v(t)-\dot{u}(t)]^2 \tag{4}$$

Where，$\dot{u}(t)$ is structure of vibration velocity in the same direction as wind，v is the average wind

speed, $\upsilon(t)$ is the fluctuating velocity, C_p is the pressure distribution coefficient, ρ is the air mass density, A is the windward area.

Calculation Model

The cable-stayed lattice roof in East Stand of Guangzhou University Town Centre Stadium has 8 masts, wg1 ~ wg4 and wg1 '~ wg4', and each mast has 10 cables. Mast number is shown in Figure 1. Cable number on the mast wg1 is shown in Figure 2.
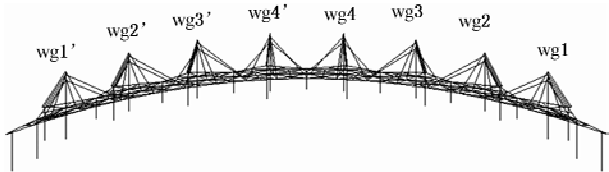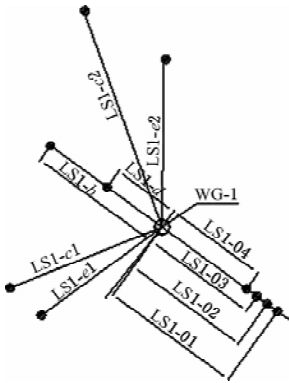

Figure 1   mast number

Figure 2   Cable number (top view)

Modal Analysis

Researchers believe that period of the fluctuating wind simulation should not be greater than the structure of the first natural period of $1/3$[6, 7]. In this paper, structure modal is obtained through modal analytical module of finite element software-Ansys. The first 6 - order modes are shown in Table 1.

TABLE 1   THE NATURAL FREQUENCIES OF CABLE-STAYED GRID STRUCTURES

Order	frequency/Hz	period/s	Order	frequency/Hz	period/s
1	1.272	0.786	4	1.29	0.775
2	1.281	0.781	5	1.298	0.77
3	1.287	0.777	6	1.298	0.77

Analysis shows that low-level modals of lattice structure are mainly lattice vibration, high-level modal are mainly cable vibration. Start-up sequence of cable is related to cable length and cable tension force. The first natural period of this structure is 0.79 s, so the value of fluctuating wind simulation period is taken 0.2 s.

Parameters and Operating Conditions

The average wind speed for 50 years return period in project site: Panyu District of Guangzhou City is $\bar{V}_{10} = 28.3$ m/s corresponding to basic wind pressure, Ground roughness category is B, and the air density $\rho = 1.25$ kg/m^3, prestressing steel damping ratio is taken as 0.02, wind-induced vibration duration $T = 100$ s, the sampling time step $\Delta t = 0.2$ s, ground roughness length $z_0 = 0.03$ m, ground roughness

coefficient $K = 0.04$，the angle between vertical wind and horizontal is $10°$. Horizontal fluctuating wind is simulated by using Kaimal spectrum while vertical fluctuating wind is simulated by using Panofsky spectrum. The shape coefficient of grid structure，mast and cable under the horizontal and vertical wind direction was determined according to the load code for different wind direction.

As loading unit of fluctuating wind load，88 shell elements are generated in the lattice structure. Each mast locas 10 load points and each cable sets nine load points. The wind load is broken down into vertical and horizontal components corresponding to structure symmetrical axis. The time-history wind load is applied to the cable upwind area of the two-axis projection.

Seven load cases are designed，prestressing and structure self-weight is included in any case. Wind load condition of each case is shown in Table 2.

TABLE 2　WIND-INDUCED RESPONSE CALCULATION CONDITIONS

Load case number	Horizontal wind （wind direction）	Vertical wind （wind direction）	cable wind load
Load case 1	$0°$	−	Y
Load case 2	$0°$	−	N
Load case 3	$0°$	↑	Y
Load case 4	$0°$	↓	Y
Load case 5	$180°$	↓	Y
Load case 6	$45°$	↓	Y
Load case 7	$90°$	↓	Y

STRUCTURE OF WIND-INDUCED VIBRATION RESPONSE

By comparing the seven kinds of load case，it is found that the wind suction load case 3 （$0°$ wind direction + vertical wind ↑) is an adverse condition，and the wind press down load case 5 （$180°$ wind direction + vertical wind ↓) is also an adverse condition. The cable strength and structure deformation response under the two conditions are analyzed in the following.

Cable Force Analysis

Cable is most possibly prone to relaxation in load case 3. It shows that the minimum of the time-history cable force was greater than 0 （each cable force is not listed because of the limited space），which guarantees the cable is not out of work under the effect of wind suction. Also it is noted that cable force of those cables with smaller horizontal angle （ls2 − c2，ls − c1，ls − c2，ls − d，ls − e1，ls − e2) is less than 110 kN，so these cables are difficult to maintain tension state in load case 3.

Cable stress is most likely to exceed limit in load case 5. Analysis shows that the cable force is 30% lower than the ultimate bearing capacity，and meets requirements in "Technical Specification for prestressed steel structure" CECS212 − 2006. The force of back cable is mostly small decline than design and the force of front cable is to increase. The reason is strain of front cable because of wind increased，so cable tension increased. Moreover，the bottom of mast can rotate flexibly articulated；the mast has a backward trend under loading so as that cable force decreased slightly.

Time-history cable force of 5 cables under load case 3 is shown in Figure 3. It shows that stress change range of cable is small for cables with larger inclination such as lsa，lsb and lsc while stress change range of cable is larger for cables with small inclination such as lse and lsd. The frequency of maximum cable force is low. This is because the cable with small inclination has smaller original design force，and influence degree by the wind is relatively large. Change amplitude of all cable force does not exceed 10% of cable capacity. As can be seen from Fig 3，cable force changes in the convergence of trends over time，there was no divergence，the structure is stable. Condition in load case 5 is similar to load case 3.
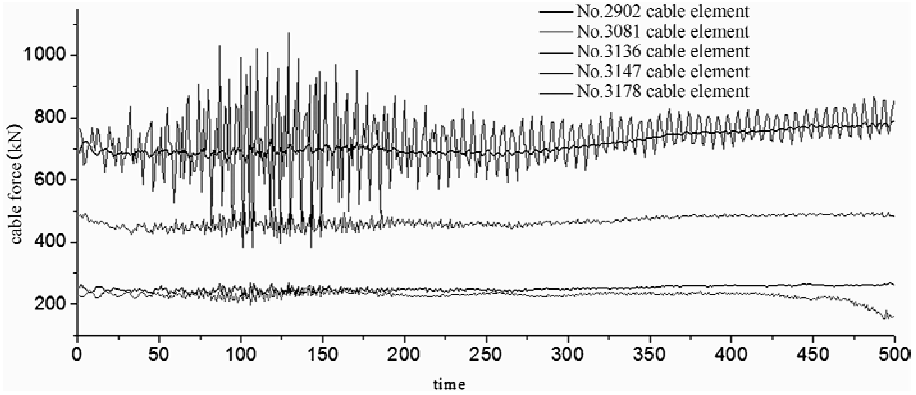
Figure 3   time-history cable force in load case 3

Deformation Analysis

The absolute displacement value of 17 key points on roof overhangs and 8 points on mast vertex is calculated. Deformation value of overhang does not exceed 80.8 mm（load case 3）and 76.3 mm（load case 5）. The largest cantilever length of roof is 33.42 m，cornice deformation is $1/400$ or so to meet the "network structure design and construction procedures"JGJ $7-91$ requirements. Deformation of the top of the mast does not exceed 62.9 mm（load case 3）and 52.4 mm（load case 5），and is about $1/300$ of mast length. It meets the "high-rise structure design specification" requirement. Cable deformation in load case 3 is shown in Figure 4.
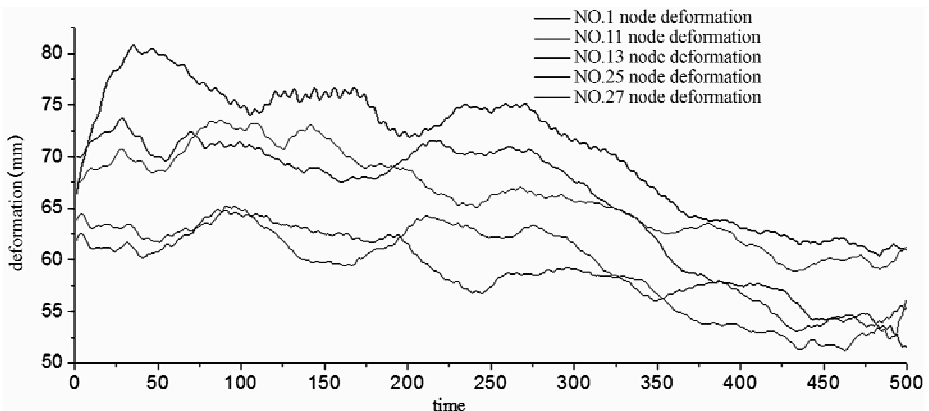

Figure 4   time-history cable deformation in load case 3

CONCLUSION

Through nonlinear time-domain analysis with wind-induced vibration of the cable-stayed lattice canopy，conclusions can be summarized as following：

(1) In the random process of wind-induced，displacement and stress response fluctuates around average and changes no divergence. It indicates cable-mast structure is stable under the action of wind-induced vibration，and will not appear wind-induced instability.

(2) In the project，the cable vibration and cable stress change is small，the steel roof vibration caused by cable vibration is small also. The deformation of key points at mast top is small，and does not cause the large deformation of the grid roof structure.

(3) In the project，the cable strength and structural deformation are within the allowable range，the structure in a safe state.

REFERENCES

［1］Simiu，E.，Robert，H. S.，translate：Liu S. P etc. "Wind effects on structures：an introduction to wind engineering"，Shanghai：Tongji University Press，1992(in Chinese)

［2］Zhang，X. T.，"structure wind engineering"，Beijing：China Building Industry Press，2006(in Chinese)

［3］Xiang，H. F.，"State of the Art and Prospect in Studies on Structural Wind Engineering"，Journal of Vibration Engineering，1997，10 (3)，pp.258–263.（in Chinese）

［4］Li，Y. Q.，and Dong，S. L.，"Random wind load simulation and computer program for large-span spatial structures"，Spatial Structure，2001，7(3)，pp.3–11.（in Chinese）

［5］Aas-Jakobsen，K，Strummen，E.，"Time domain buffeting response calculations of slender structures"，Journal of Wind Engineering and Industrial Aerodynamics，2001，89，pp.341–364.

［6］Rossi，R.，Lazzari，M. and Vitalian，R.，"Wind field simulation for structural engineering purpose"，International Journal for Numerical Methods in Engineering，2004，61(8)，pp.738–763.

［7］Gurley，K. and Kareem，A.，"Analysis interpretation modeling and simulation of unsteady wind and pressure data"，J. Wind Eng. Ind. Aerodyn.1997，71，pp.657–669.

DAMPING IDENTIFICATION FOR CLOSELY SPACED MODES WITH WAVELET-BASED DEMODULATION METHOD

* P. Sun，A. Q. Li，Y. L. Ding and Z. J. Li

Key Laboratory of Concrete and Prestressed Concrete Structures of Ministry of Education，
Southeast University，Nanjing，210096，China
* Email：civil. sunpeng@gmail.com

KEYWORDS

Morlet wavelet，damping identification，closely spaced modes，mechanism，modal coupling，formula derivation，guideline.

ABSTRACT

The time-frequency character of wavelet transform allows adaptation of both traditional time and frequency domain system identification approaches to examine linear structural dynamic systems. However，the identification of closely spaced modes is a well known problem and remains a challenge to dynamics specialists. In particular，the precise definition of closely spaced modes and factors that cause modal overlap require further research. Hence，in order to solve the two specific problems，this article quantifies the concept of closely spaced modes and carries out further researches on the relationship between damping ratios and severity of modal overlap，and the mechanism of modal coupling as well. By formula derivation，the classification method for adjacent modes is proposed. The proposed guideline is based on the demodulation technique with respect to the continuous wavelet transform and Morlet-wavelet function. Finally，numerical simulations demonstrate the validation and applicability of the guideline.

INTRODUCTION

The number of algorithms to estimate modal parameters from measured frequency or impulse response function data is considerable. The modal analysis identification method presented in this paper is based on the use of continuous wavelet transform（CWT）. The wavelet transform has dominant advantages in signal filtering and time-frequency characteristics，which make it applicable to system identification. [1, 2] Using Continuous Wavelet Transform（CWT），the free response of multi-degree-of-freedom system can be divided into free responses of single-degree-of-freedom systems，and in this way modal frequencies and damping ratios can be obtained from every individual free response. [3] However，when it comes to modal identification using Morlet CWT，some issues，such as definition of closely spaced modes and factors that cause of modal overlap，remain be studied. Additionally，with CWT method，frequency identification can be easily and accurately achieved while the accuracy and applicability of damping identification is

limited by some condition. Thus, based on the severity of modal overlap, the adjacent modes can be classified into three types: (1) sparsely spaced modes, (2) closely spaced modes that cannot be demodulated (modal overlap is too severe not to be demoded or not to be accurately identified) (3) closely spaced modes that cannot be demoded. This paper focuses on discussions about these three types.

MODAL IDENTIFICATION USING MORLET WAVELET

For any signal $x(t) \in L^2(R)$, its CWT is defined as:
Eqn. 1.

$$W_g x(a, b) = \frac{1}{\sqrt{a}} \int_{-\infty}^{+\infty} x(t) \varphi^* \left(\frac{t-b}{a} \right) dt \tag{1}$$

where " $*$ " denotes the complex conjugate; a is the scaling factor and b is the translation factor of the wavelet transform and $\varphi(t)$ is the basis wavelet function $\varphi(t) \in L^2(R)$.

For multi-degree-of-freedom system with vicious damping, its free response signal is given by:
Eqn. 2.

$$x(t) = \sum_{i=1}^{n} x_i(t) \tag{2}$$

where $x_i(t) = A_i e^{-\xi_i \omega_{ni} t} \cos(\omega_{di} t - \phi_i)$, $i = 1, 2, \cdots, n$. A_i, ϕ_i, ξ_i, ω_{di}, ω_{ni} are respectively amplitude, phase angle, damping ratio, damped frequency and un-damped frequency of i th mode.

The CWT of the Eqn. 2 is given by:
Eqn. 3.

$$W_g x(a, b) \approx \frac{\sqrt{2\pi a}}{2} \sum_{i=1}^{n} (A_i e^{\alpha_i + j\beta_i}) \tag{3}$$

Where $\alpha_i = -\xi_i \omega_{ni} b - (1/2)[(1 - 2\xi_i^2)\omega_{ni}^2 a^2 + \omega_0^2 - 2\omega_0 \omega_{di} a]$,

$\beta_i = -\xi_i \omega_{ni} \omega_{di} a^2 + \omega_0 \omega_n a \xi_i + \omega_{di} b - \phi_i$
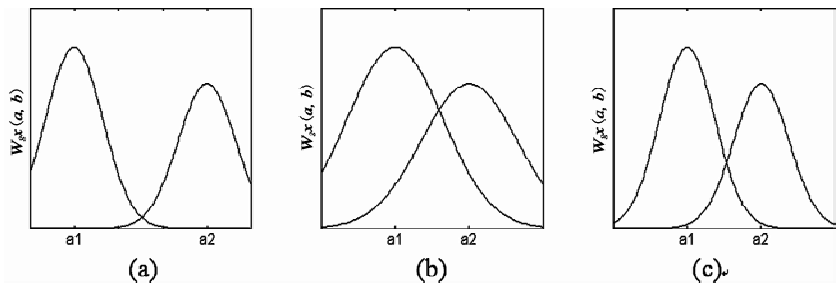

Figure 1   Three types of adjacent modes

Fast algorithm of Continuous Morlet wavelet transform can be deduced either from convolution theory or Parseval's theorem. With the wavelet amplitude the phase curves, the nature frequencies and damping ratios can be obtained. If the frequencies of two adjacent modes are close and the damping ratios are large enough, there may be overlap in frequency domain. Besides, the application of Fourier transform and

band-pass filtering to demodulation would affect the resolution of modal identification for multi-degree-freedom system. Chen et. al [4] adopted a frequency dispersion factor $\gamma = (f_2 - f_1)/(f_2 + f_1)$ to qualify how close two adjacent frequencies are. However, when with two fixed frequencies, modal overlap is closely related to damping ratios. In this case, the relationship between two frequencies cannot necessarily determine the severity of modal overlap.

Using CWT method, frequency identification can be easily and accurately achieved while the accuracy and applicability of damping identification is limited. Thus, based on the severity of modal overlap, the adjacent modes can be classified into three types as Figure 1 shows: a) sparsely spaced modes; b) closely spaced modes that cannot be demoded (modal overlap is too severe not to be demoded or not to be accurately identified); c) closely spaced modes that cannot be demoded. One important objective is to find the distinguishing conditions for the three types and to focus on the research of decoupling condition for the third type. And in this paper, the names—"Type N" and "Type Y" are used to represents the two types of close modes respectively—one that cannot be demodulated and the other that can be demodulated.

THEORETICAL STUDY

Formula Derivation

Although the identification method by the Morlet transform has shown promising results, an issue remains to be studied: the method was based on rough approximation using Taylor series expansion. Because of the rough assumptions, the limitations of the method were not clear. Therefore, a more accurate derivation is needed in this study so as to find the limitations.

Firstly, this paper takes a two-degree-freedom system as an example for research and the wavelet transform of a free response is given by:
Eqn. 4.

$$W_g x(a, b) \approx \frac{\sqrt{2\pi a}}{2} \sum_{i=1}^{2} (A_i e^{\alpha_i + j\beta_i})$$

(4)

Where $\alpha_i = -\xi_i \omega_{ni} b - (1/2)[(1 - 2\xi_i^2)\omega_{ni}^2 a^2 + \omega_0^2 - 2\omega_0 \omega_{di} a]$,
$\beta_i = -\xi_i \omega_{ni} \omega_{di} a^2 + \omega_0 \omega_n a \xi_i + \omega_{di} b - \phi_i$

In order to decouple the wavelet transforms of adjacent modes, the satisfying conditions that $|W_g x_1(a_1, b)| \gg |W_g x_2(a_1, b)|$ and $|W_g x_1(a_2, b)| \ll |W_g x_2(a_2, b)|$ both should hold, where $a_i = \frac{\omega_0}{\omega_{ni}} \frac{\sqrt{1-\xi_i^2}}{(1-2\xi_i^2)}(i = 1, 2)$. [5]

And from Eqn. 4, Eqn. 5-6 can be obtained, where $\omega_r = \omega_{n2}/\omega_{n1} > 1$:
Eqn. 5.

$$|W_g x_1(a_1, b)| = \frac{\sqrt{2\pi a_1} A_1}{2} e^{-\xi_1 \omega_{n1} b + r_1 \omega_0^2}, \quad |W_g x_2(a_1, b)| = \frac{\sqrt{2\pi a_1} A_2}{2} e^{-\xi_2 \omega_{n2} b + (r_1 + r_2)\omega_0^2}$$

(5)

Eqn. 6.

$$|W_g x_1(a_2, b)| = \frac{\sqrt{2\pi a_2} A_1}{2} e^{-\xi_1 \omega_{n1} b + (r_3 + r_4)\omega_0^2}, \quad |W_g x_2(a_2, b)| = \frac{\sqrt{2\pi a_2} A_2}{2} e^{-\xi_2 \omega_{n2} b + r_3 \omega_0^2}$$

(6)

Eqn. 6-a.

$$\text{Where} \qquad r_1 = \frac{\xi_1^2}{2(1-2\xi_1^2)}, \quad r_2 = \frac{(\xi_2^2-\xi_1^2)\omega_r^2}{2(1-2\xi_1^2)^2} - \frac{(\sqrt{1-\xi_2^2}\,\omega_r - \sqrt{1-\xi_1^2}\,)^2}{2(1-2\xi_1^2)} \tag{6-a}$$

Eqn. 6-b.

$$r_3 = \frac{\xi_2^2}{2(1-2\xi_2^2)}, \quad r_4 = \frac{(\xi_1^2-\xi_2^2)}{2(1-2\xi_2^2)^2\,\omega_r^2} - \frac{(\sqrt{1-\xi_1^2}\,\omega_r - \sqrt{1-\xi_2^2}\,)^2}{2(1-2\xi_2^2)\,\omega_r^2} \tag{6-b}$$

From Eqn. 5-6，modal separation conditions are given by：
Eqn. 7.

$$\frac{|W_g x_1(a_1,b)|}{|W_g x_2(a_1,b)|} = \frac{A_1}{A_2} e^{(\xi_2\omega_{n2}-\xi_1\omega_{n1})b - r_2\omega_0^2} \gg 1 \tag{7}$$

Eqn. 8.

$$\frac{|W_g x_2(a_2,b)|}{|W_g x_1(a_2,b)|} = \frac{A_2}{A_1} e^{(-\xi_2\omega_{n2}+\xi_1\omega_{n1})b - r_4\omega_0^2} \gg 1 \tag{8}$$

For close modes，assuming $A_1 = A_2$，because $|(\xi_2\omega_{n2}-\xi_1\omega_{n1})b|$ is too small to count weight，Eqn. 7-8 can be shortened as：
Eqn. 7.

$$\frac{|W_g x_1(a_1,b)|}{|W_g x_2(a_1,b)|} \approx e^{-r_2\omega_0^2} \geqslant 10 \tag{7}$$

Eqn. 8.

$$\frac{|W_g x_2(a_2,b)|}{|W_g x_1(a_2,b)|} \approx e^{-r_4\omega_0^2} \geqslant 10 \tag{8}$$

It is obvious that if $r_2 < 0$ and $r_4 < 0$, the mode separation conditions（Eqn. 7-8）can be achieved by taking ω_0 large enough. Assuming the closely spaced modes can be separated，from $r_2 < 0$ and $r_4 < 0$, the value range of ω_r can be yielded：

1）when $\xi_1 > \xi_2$，$\omega_r > \sqrt{\dfrac{1-\xi_2^2}{1-\xi_1^2}} + \sqrt{\dfrac{\xi_1^2-\xi_2^2}{(1-\xi_1^2)(1-2\xi_1^2)}}$

2）when $\xi_1 < \xi_2$ 时，$\omega_r > \dfrac{\sqrt{1-\xi_1^2}}{\sqrt{1-\xi_2^2} - \sqrt{\dfrac{\xi_2^2-\xi_1^2}{1-2\xi_1^2}}}$
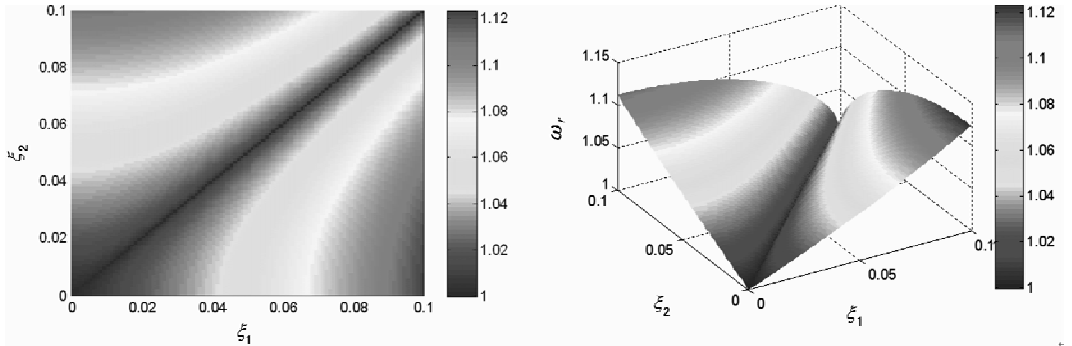

Figure 2 **Relationship between $\omega_{r\min}$ and (ξ_1,ξ_2) under decoupling condition**

Normally，for steel structures，damping ratios vary within $[0.01, 0.02]$; while for reinforced concrete

structures, damping ratios vary within $[0.03, 0.08]$. Hence, to let the research suitable for all the classic civil structures, this paper carry out research on the condition that $(\xi_1, \xi_2) \in [0, 0.1]^2$. As shown in Figure 2, when $\omega_r > 1.12$, decoupling intervals (ξ_1, ξ_2) cover all over $[0, 0.1]^2$; hence the author defines that $\omega_r = 1.12$ is the boundary between sparse modes and close modes for civil engineering structures.

Two Types of Closely Spaced Modes（Type N and Type Y）

Based on the discussions above, when $\omega_r \leqslant 1.12$ the two adjacent modes are closely spaced modes for civil engineering structures. Using CWT method and Eqn. 10–15, the decoupling intervals (ξ_1, ξ_2) at fixed $\omega_r = 1.03$, $\omega_r = 1.02$, $\omega_r = 1.01$ can be obtained (shown in Figure 3). As ω_r decreases, the boundary of decoupling intervals gradually move closer toward the 45-degree angle bisector and decoupling intervals become much smaller. When the damping ratios (ξ_1, ξ_2) fall out of the decoupling intervals, the modal overlap would be too severe to be demodulated (shown in Figure 1(b)).
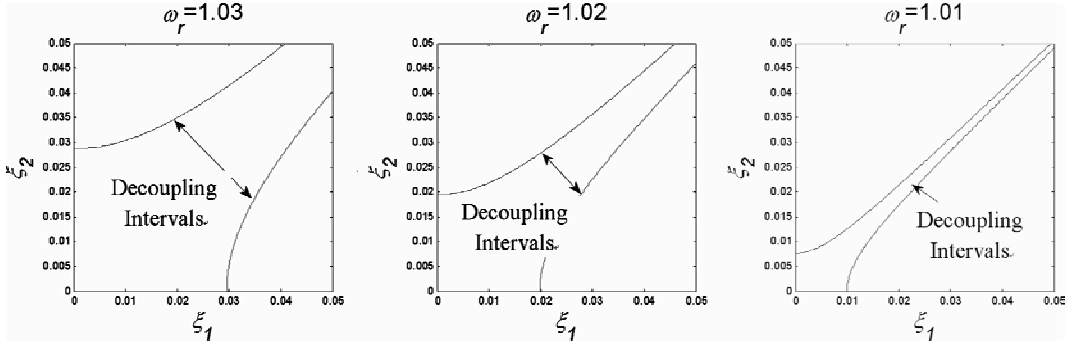
Figure 3　Decoupling Intervals at $\omega_r = 1.03$, $\omega_r = 1.02$ and $\omega_r = 1.01$

The author finds out that given ω_r, the bigger the damping ratios are, the smaller the decoupling intervals are, which means a more strict requirement for decoupling; the bigger the difference between the two damping ratios is, the severer the overlap of the modes is. When Morlet CWT is used to identify modal parameters of structures, it should be taken to notice that only under some circumstance, decoupling becomes possible. Otherwise, even if ω_0 is large enough, CWT method cannot decouple the closely spaced modes.

NUMERICAL EXAMPLE

For closely spaced modes only if ω_r, ξ_1 and ξ_2 hold the conditions that $r_2 < 0$ and $r_4 < 0$, closely spaced modes can be demodulated (Figure 1(c)). Otherwise, they cannot be demodulated or decoupled (Figure 1 (b)). However, the damping ratios of adjacent modes cannot be predicted. It is acceptable to assume the closely spaced modes can be demodulated and use $f_0 = \alpha \sqrt{2} f_{1,2}/(2\pi\Delta f_{1,2})$ $(\alpha = 2)$ [6] to do CWT to the free responses.

Construct two free responses of two degree-of-freedom systems with closely spaded modes as:
Eqn. 9.

$$x(t) = \sum_{i=1}^{2} A_i e^{-2\pi\xi_i f_i t} \cos(2\pi \sqrt{1-\xi_i^2} f_i t - \phi_i) \tag{9}$$

Where for one response $A_1 = A_2 = 1$，$f_1 = 1.10$ Hz，$f_2 = 1.21$ Hz，$\xi_1 = 0.014$，$\xi_2 = 0.012$，$\phi_1 = \phi_2 = 0$；for the other，$A_1 = A_2 = 1$，$f_1 = 1.10$ Hz，$f_2 = 1.21$ Hz，$\xi_1 = 0.014$，$\xi_2 = 0.070$，$\phi_1 = \phi_2 = 0$.
Figure 4 （a）（b） are respectively the wavelet transforms of Type Y （$\omega_r = 1.10 < 1.12$，$\xi_1 = 0.014$，$\xi_2 = 0.012$）and Type N （$\omega_r = 1.10 < 1.12$，$\xi_1 = 0.014$，$\xi_2 = 0.070$）. And the result of the numerical example is shown in Table 1.
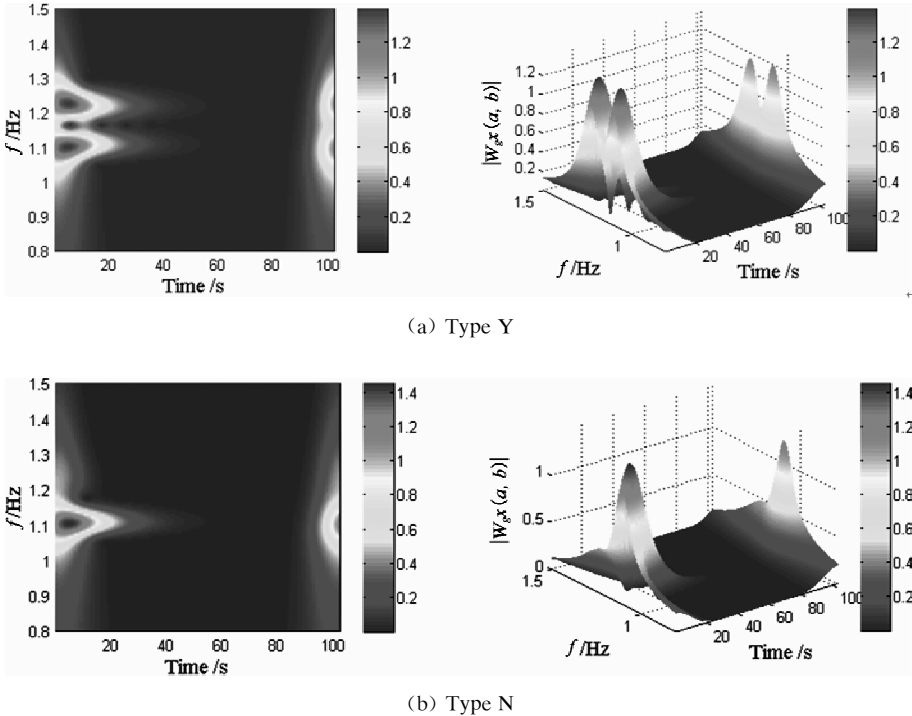
(a) Type Y

(b) Type N

Figure 4　(a) (b) Wavelet transform of Type Y and Type N closely spaced modes

For Type Y，the wavelet magnitude Adjacent peaks can be clearly distinguished，and the magnitude curve is smooth with a stable slope （Figure 4(a)），which indicate an accurate damping identification. While for Type N （see Figure 4(b)），the overlap of the adjacent peaks is so severe that there is quick mutation in the beginning part of the magnitude curve （Figure 5 (b)）. That means that there is strong interference in the two modes. In table 1，deep research finds out that the curve the mode with smaller damping transfer its characteristics to the smaller mode and cause the identification result of second mode to appear to be similar as the first mode. The information from the first mode submerges that of the second one causing contamination.

TABLE 1　MODAL IDENTIFICATION OF THE TWO TYPES OF CLOSELY SPACED MODES

Type		Frequency			Damping ratio		
		Theoretical value/Hz	Identification value /Hz	Error （%）	Theoretical value/%	Identification value/%	Error （%）
Y	1	1.100	1.100	0.000%	1.400%	1.399%	0.057%
	2	1.210	1.210	0.000%	1.200%	1.200%	0.042%
N	1	1.100	1.100	0.027%	1.400%	1.400%	0.007%
	2	1.210	1.100	9.074%	7.000%	1.414%	79.800%

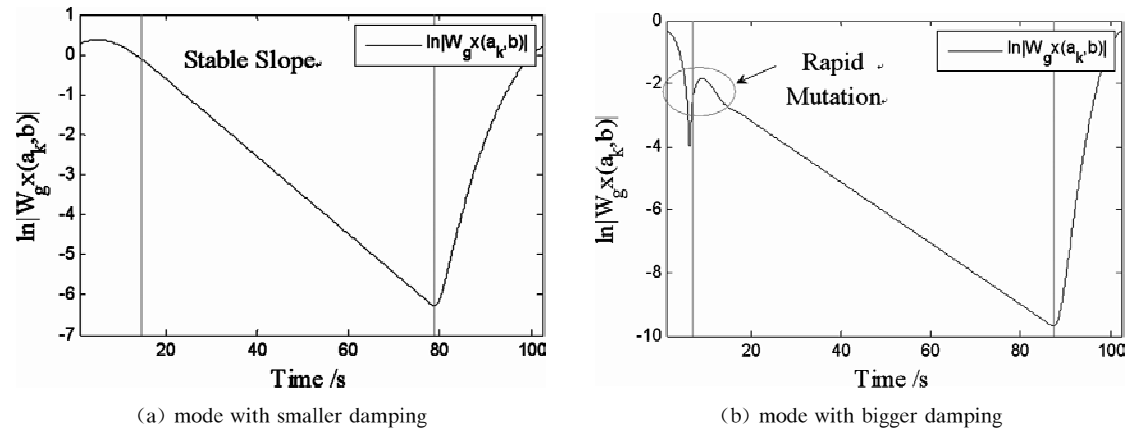(a) mode with smaller damping   (b) mode with bigger damping

Figure 5   Magnitude plot of Type N closely spaced modes

CONCLUSION

This paper analyzes and qualifies the definition of closely spaced modes in civil engineering structures. Secondly，the paper carries out research on the relationship between damping ratios and severity of modal overlap，and the Mechanism of modal coupling as well. Theoretical research shows that $\omega_r = 1.12$ is the boundary between sparse modes and close modes of common civil engineering structures；if two adjacent modes are classified as closely spaced modes，wavelet magnitude curve can be adopted to view whether the modal contamination exists，so that the authenticity of the demodulated results can be obtained.

REFERENCE

［1］Robertson，A. N.，Park，K. C. and Alvin，K. F.，"Extraction of impulse response data via wavelet transform for structural system identification"，Journal of Vibration and Acoustics，ASME，1998，120，pp. 252–260.

［2］Staszewski，W. J.，"Identification of damping in MDOF systems using time-scale decomposition"，Journal of Sound and Vibration，1997，203(2)，pp. 283–305.

［3］Lardies，J，Ta M. N. and Berthither，M.，"Modal parameter estimation based on the wavelet transform of output data"，Archive of Applied Mechanic，2004，73，pp. 718–733.

［4］Chen，J. and Xu，Y. L.，"Hilbert-Huang transform for damping ratio identification of structures with closely spaced modes of vibration"，Advances in Building Technology，2002，2，pp. 1107–1114.

［5］Chen，S. L.，Liu J. J. and Lai H. C.，"Wavelet analysis for identification of damping ratios and natural frequencies"，Journal of Sound and Vibration，2009，323，pp. 130–147.

［6］Kijewski，T. and Kareem A.，"Wavelet Transforms for system identification in civil engineering"，Computer-Aided Civil and Infrastructure Engineering，2003，18，pp. 339–355.

A NOVEL NUMERICAL TECHNIQUE FOR PREDICTING FLUCTUATING WIND LOADS ON A TALL STEEL BUILDING

* C. R. Zheng[1]，Y. C. Zhang[2]，H. Li[1]

[1] School of Civil Engineering，Harbin Institute of Technology，Harbin，150090，China
[2] Department of Civil Engineering，Harbin Institute of Technology at Weihai，Weihai，264209，China
* Email：flyfluid@163.com

KEYWORDS

Tall steel building，fluctuating wind loads，large eddy simulation（LES），inflow turbulence，wind effect，CAARC standard building.

ABSTRACT

Modern tall steel buildings tend to be very vulnerable to wind loads，and the wind-resistance design has gradually become the dominate factor in their structural designs. Therefore，it is significant to investigate the characteristics of flows around tall steel buildings，and to predict the fluctuating wind loads on them. However，the existing techniques of Computational Fluid Dynamics（CFD）have been seldom proved to be effective and reliable in simulating the fluctuating wind loads on building structures. Therefore，in the present paper，a novel numerical technique，which is based on simulation of the "real" inflow turbulence in the atmosphere boundary layer and the turbulence model of Large Eddy Simulation（LES），is constructed to investigate wind effects on the Commonwealth Advisory Aeronautical Council（CAARC）standard tall steel building. The fluctuating wind velocity are generated by the weighted amplitude wave superposition（WAWS）considering the power spectral density and spatial coherence function as targets，and the generated wind velocity series are modified by the divergence-free operation and flux-balance operation to serve as the "real" inflow turbulence. Furthermore，the characteristics of the fluctuating wind loads，such as the pressure coefficients，aerodynamic force coefficients and their power spectral，are analyzed. The numerical results are compared with the corresponding data from the wind tunnel tests，and the feasibility of using the present numerical technique to simulate the fluctuating wind loads on the CAARC standard tall steel building immersed in the atmosphere boundary layer is validated.

INTRODUCTION

As a result of the extensive utility of high-strength and light-weight materials，and emergence of novel structural systems，modern tall steel buildings are often accompanied by increased height and flexibility，and a lack of sufficient inherent damping. Therefore，under the action of strong wind，typical tall steel buildings oscillate significantly in the along-wind，across-wind，and torsional directions（see Solari[1]）. It

has been recognized that for many tall steel buildings，their across-wind responses，result mainly from the aerodynamic pressure fluctuation in the separated zone，may exceed the along-wind responses in terms of both serviceability and survivability designs，and cause serious discomfort to building occupants（see Zhou[2]）. Therefore，it is of great significance to study the characteristics of flows around tall buildings，and to analyze the mechanism of wind effects on them.

As a new branch of Computational Fluid Dynamics（CFD），the Computational Wind Engineering（CWE）has been developed rapidly over the last three decades to evaluate the interaction between wind and structures numerically. The CFD methods，such as the Reynolds Averaged Navier-Stokes Equations（RANS）models and Large Eddy Simulation（LES），have been widely used to predict flows around bluff bodies in wind engineering（see Huang[3] and Zheng[4]）. However，the existing numerical techniques have seldom been approved to be effective and reliable in predicting the fluctuating wind loads on buildings，because the characteristics of the flows around the buildings immersed in turbulent boundary layers are different from those in laminar boundary layers.

Therefore，in order to predict the fluctuating wind loads accurately，it is important to investigate these characteristics of flows observed under oncoming turbulence. However，most of the unsteady computational simulations have used laminar inflows，because the technique of generating turbulent inflow data has not been well established. In recent years，several methods to generate turbulent inflow data have been proposed（see Kondo[5] and Nozawa[6]），Nozawa[6] used the generated turbulent inflow to predict the wind flows around a low-rise building by using the LES method. However，up to now，there have been little studies to develop feasible numerical techniques for simulating the fluctuating wind loads on tall steel buildings immersed in turbulent boundary layers.

In the present study，a novel numerical technique，which is based on simulation of the "real" inflow turbulence and the LES method，is constructed to investigate wind effects on the Commonwealth Advisory Aeronautical Council（CAARC）standard tall steel building immersed in turbulent boundary layers. Moreover，the acquired fluctuating wind loads，such as distribution of the pressure coefficients，aerodynamic force coefficients and the pressure power spectral，are comprehensively compared to previous extensive experimental data to valid the feasibility of the present numerical technique.

NUMERICAL METHODS

Analytical Model and Computational Domain

The analytical model used for the present study is the CAARC standard building. As is introduced by Melbourne[7]，the CAARC building，which is used as a representative tall building for investigating the required modelling accuracy for wind tunnel investigations，has a rectangular prismatic shape with its sides 100 ft by 150 ft and height 600 ft（$B \times D \times H = 30.48$ m $\times 45.72$ m $\times 182.88$ m）in full-scale dimensions. The building is flat-topped without parapets，and its exterior walls are flat without mullions or other geometric disturbances. The CAARC building has been intensively experimented to investigate wind effects on tall buildings since 1969 using wind tunnel tests（see Melbourne[7]，Obasaju[8] and Luo[9]）. It shall be mentioned that the measurements from different wind tunnels for this building model are not consistent，although the experimental techniques and conditions used are almost the same.

To compare with the experimental data from wind tunnel tests by Luo[9] in TongJi University （abbreviated as TJ），the CAARC model which is immersed in simulated turbulence under terrain roughness of D type in Chinese Loading Code，has a length scale of $1/S = 1/300$，so its outline size is $D_x \times D_y \times H = 101.6$ mm $\times 152.4$ mm $\times 609.6$ mm. The incoming velocity at top of the model is set as $V_H = 12.7$ m/s，so the Reynolds number based on the width（or the depth）of the model and the top velocity is about 1.34×10^5（or 0.89×10^5）. Figure 1 shows the local coordinate system and locations of surface pressure test points on the height level $2H/3$（$h = 406.4$ mm）of the CAARC model，where θ denotes the wind direction angle，and only $\theta = 0°$ and $\theta = 90°$ are studied in the present paper.

Figure 1   Distribution of test points on the cross-section $z=2H/3$ of the CAARC model /mm

The computational domain，with a length of $10.5H$（$2.5H$ in the upstream domain and $8H$ in the downstream domain），a width of $3H$ and a height of $3H$，is discretized by the block structured and non-uniform orthogonal mesh，and the mesh near surfaces of the model are locally refined with the minimum mesh size of 2.5 mm. Its overall number of mesh is about 1.15 millions. The inlet boundary conditions for the computational domain are set as the velocity-inlet boundary，with the later-mentioned "real" inflow turbulence being programmed by the UDF（User Defined Function）in the code FLUENT 6.2. The outflow boundary conditions with the turbulence fully developed are used for the outlet conditions. As for the other surfaces，the no-slip wall boundary conditions are used to simulate the wall boundary in the wind tunnel test，where the roughness constant is defined as 0.5.

Solution Strategies

In the present paper，the LES method based on the Smagorinsky-Lilly Model（SLM），Dynamic Smagorinsky-Lilly Model（DSM）and Dynamic Kinetic Energy SGS Model（DKEM）are adopted to compute the fluctuating wind loads respectively. More detailed information about them can be found in Zheng[10].

Discretizations of the spatial-filtered Navier-Stokes equations are accomplished by the code FLUENT 6.2，using the finite-volume method. The pressure-velocity decoupling of the discretized equations is implemented by the PISO algorithm. In order to reduce the time-cost for LES to reach the statistically

stable mode, the steady computation using the RANS-based $k - \omega$ shear-stress transport (SST) model is conducted, and the resultant flow field is transitioned to serve as the initial condition for the LES run. In the LES computation, the second order bounded central differencing scheme and the central differencing scheme are used for discretization of the convective and diffusive terms in the governing equations. The third order QUICK scheme is adopted for discretization of the SGS kinetic energy. For the time discretization, the second order fully implicit scheme is used, and the timestep size is set as 0.001 s. Generally, the flow field will be fully developed after about $1\,000$ timesteps of computation, and an extra $4\,096$ timesteps or more are computed to sample the pressure coefficient for statistics.

SIMULATION OF THE "REAL" INFLOW TURBULENCE

The fluctuating wind velocity series are generated using the weighted amplitude wave superposition (WAWS) method (see Deodatis[11]) considering the power spectral density and spatial coherence function as targets. The Davenport spectrum, which has been adopted in Chinese Loading Code, is used as the targeting spectral density for the fluctuating wind velocity, and the spatial coherence function for two spatial points is expressed as the following formula:

$$Coh(P_i, P_j, \omega) = \exp\left\{-\frac{\omega\left[C_x^2(x_i - x_j)^2 + C_y^2(y_i - y_j)^2 + C_z^2(z_i - z_j)^2\right]^{1/2}}{2\pi(V(z_i) + V(z_j))/2}\right\} \tag{1}$$

where decaying coefficients $C_x = 16$, $C_y = 8$ and $C_z = 10$, (x_i, y_i, z_i) and (x_j, y_j, z_j) are the spatial coordinate of the points P_i and P_j, and $V(z_i)$ and $V(z_j)$ are their mean velocity.

Afterwards, the generated wind velocity series are modified by the mean wind profile in the terrain roughness of D type and the turbulence intensity measured in the wind tunnel of TJ University. Moreover, the divergence-free operation is implemented to satisfy the continuity equation at every timestep and improve the convergence of LES computation. The equations proposed by Shirani[12] to obtain divergence-free velocity field are as follows:

$$u_i^{(S)n+1} = u_i^{(R)n+1} - \Delta t \frac{1}{\rho} \frac{\partial \Delta P^n}{\partial x_i} \tag{2}$$

$$\Delta t \frac{1}{\rho} \frac{\partial^2 \Delta P^n}{\partial x_i^2} = \frac{\partial u_i^{(R)n+1}}{\partial x_i} \tag{3}$$

where, $u_i^{(R)n+1}$ is the fluctuating velocity computed by the WAWS method and then modified by the turbulence intensity, and $u_i^{(S)n+1}$ is the fluctuating velocity acquired after divergence-free operation. To solve the above equations, the Taylor's hypothesis of frozen turbulence is introduced, and the time axis of the inflow turbulence is converted to the spatial coordinate.

Furthermore, the above velocity series should be adjusted to satisfy the flux balance for the inlet and outlet boundary of the computational domain. The flux modified velocity is expressed as follows:

$$\Delta v(t) = -\left(\sum_{i=1}^{n} u_i(t)A_i - S'(t)\right)/A \tag{4}$$

where, $\sum_{i=1}^{n} u_i(t)A_i$ and $S'(t)$ are the overall flux for the inlet and outlet boundary at the timestep t, respectively. A and n is the overall area and mesh numbers of the inlet boundary. The $\Delta v(t)$ is added to achieve the flux-balance operation.

Finally，the"real" inflow turbulence is acquired by adding the mean wind profile and the fluctuating wind velocity after flux-balance operation，to serve as the inlet boundary condition for the LES computation. The above derivation processes are simplified as the restraint of length of the article，and for more detailed information，the readers can refer to the Ph.D. thesis by Zheng[13].

RESULTS AND DISCUSSIONS

Pressure Coefficients

Mean pressure coefficients (C_P) for the 20 test points in Figure 1，acquired by the numerical technique are compared with the experimental data from Melbourne[7] and Luo[9] (surface pressure measurement of the rigid CAARC model) in Figure 2. It can be seen that the numerical results computed by the SLM, DSM and DKEM under the TJ inflow turbulence are almost equal to each other，indicating that the effect of the subgrid-scale stress model on the C_P is little.
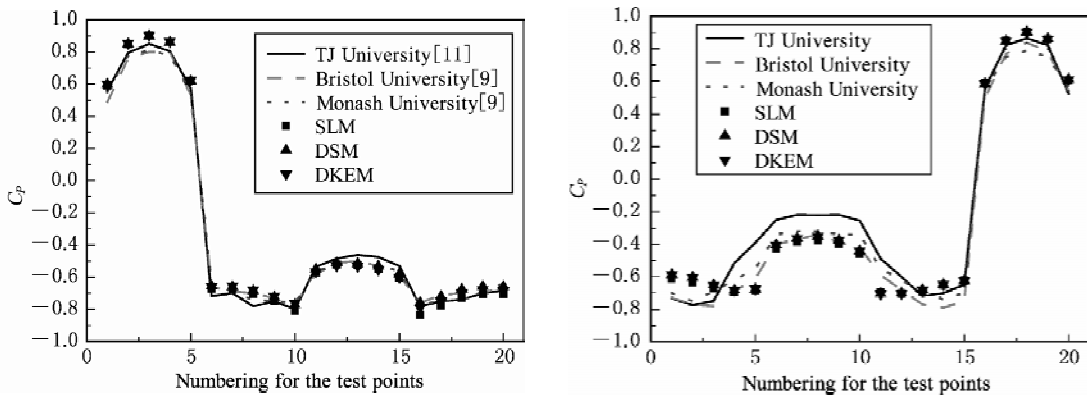
Figure 2　Comparison of the C_P from numerical simulation and experiment (Left：$\theta=0°$，right：$\theta=90°$)

When the wind direction is normal to the wider surface ($\theta=0°$)，the numerical results are slightly bigger than the experimental data for the windward face，with a maximum error of 6.8%. As for the C_P on other faces，the numerical results are quite close to the experimental data，especially for the data from Bristol University (BU) and Monash University (MU). When $\theta=90°$，distinctions of the C_P on side face and leeward face between the numerical results and experimental data from Luo[9] are quite obvious，with a maximum error of 80%. However，agreement between the experiment from Melbourne[7] and the numerical simulation is much better.

Figure 3 shows comparison of the root mean square (rms) values for pressure coefficients ($C_{\sigma P}$) acquired by the numerical simulation and the experimental data from Melbourne[7] and Luo[9]. As is seen，the distribution regularity of $C_{\sigma P}$ from the numerical simulation and experiment is almost the same，though the experimental data are slightly larger. Similarly to the C_P above，the effect of the subgrid-scale stress model on the $C_{\sigma P}$ is also very small.
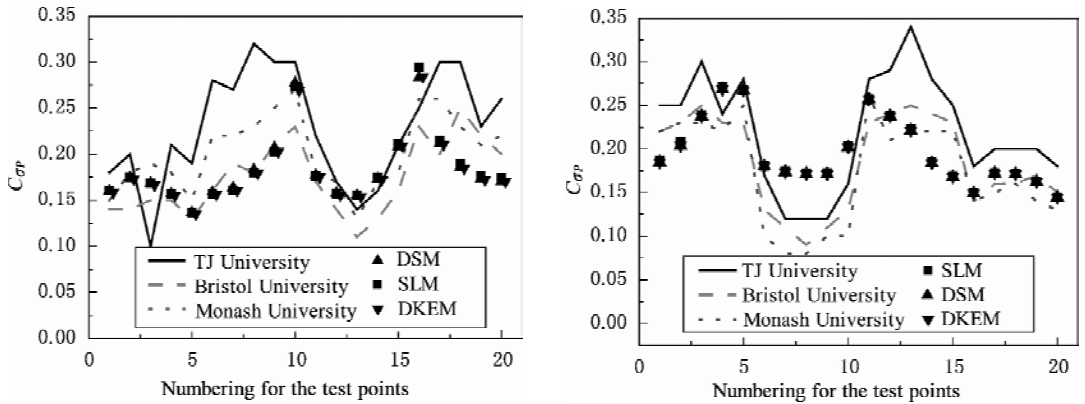
Figure 3   Comparison of the $C_{\sigma P}$ from numerical simulation and experiment (Left: $\theta = 0°$, right: $\theta = 90°$)

When $\theta = 0°$, the numerical results are almost located in the interval of the experimental data from different wind tunnels, and agreement between the numerical results and the experimental data from BU and MU are much better than that from TJ University (with a maximum error of 68.5%). When $\theta = 90°$, compared to the experimental data, the numerical results are more accurately simulated, except for the test points on the leeward face.

Based on the above comparison, the subgrid-scale stress model has little influence on the C_P and $C_{\sigma P}$ under the TJ inflow turbulence, and the numerical results can be assumed to be acceptable. Therefore, it is recommended to use the SLM to compute the wind loads on tall buildings from now on, because of its advantage of less computational consumption. However, if the numerical computations were conducted in laminar layers, the numerical errors would be very significant, and the numerical results computed by three types of SGS model, namely the SLM, DSM and DKEM, would be quite different. The relevant computations have already been implemented by the authors, but are not listed here due to the restraint of length of the article.

Aerodynamic Force/Base-Moment Coefficients

Definitions for the dimensionless aerodynamic force/base-moment coefficients can be referred to in Melbourne[7], Luo[9] and Zheng[13]. Comparison of the numerical results computed by the SLM and the experimental data from Luo[9] are shown in Table 1. As is seen in the table, when $\theta = 0°$, numerical simulation has overestimated mean values of the along-wind force/base-moment coefficients (C_D and C_{Mx}) with the error of 29.0% and 28.1%. It may be attributed to the reason that the experiments are conducted using the high frequency balance tests, while the present numerical model is equivalent to pressure measurement of the rigid CAARC model. Moreover, agreements on mean values of the across-wind force/base-moment coefficients (C_L and C_{My}), and rms values ($C_{\sigma Fx}$, $C_{\sigma Fy}$, $C_{\sigma Mx}$ and $C_{\sigma My}$) are quite satisfying, with the maximum error less than 16%. When $\theta = 90°$, the numerical simulation has also overestimated the C_L and C_{My} in the along-wind direction with the error of 36.1% and 40.7%. However, very good agreement is evident for other aerodynamic coefficients.

TABLE 1   COMPARISON OF THE RESULTS FROM NUMERICAL SIMULATION AND EXPERIMENT

Data source	θ	C_D	$C_{\sigma Fx}$	C_L	$C_{\sigma Fy}$	C_{Mx}	$C_{\sigma Mx}$	C_{My}	$C_{\sigma My}$
Numerical simulation	$0°$	1.232	0.204	0.001	0.217	0.661	0.103	0	0.092
Experimental data[9]	$0°$	0.955	0.188	0.002	0.206	0.516	0.098	-0.004	0.109
Numerical simulation	$90°$	0.012	0.217	0.698	0.133	0.006	0.118	0.394	0.071
Experimental data[9]	$90°$	-0.004	0.211	0.513	0.114	0.014	0.12	0.28	0.063

According to the overall comparison，it can be concluded that the present numerical technique is able to acquire exact fluctuating wind loads on the CAARC model，and feasibility of the numerical technique to simulate tall buildings immersed in the atmosphere boundary layer is validated.

Power Spectral Analysis

The numerical results of pressure power spectral for the test points 3 and 13（see Figure 1）of the CAARC model under $\theta=0°$，computed by the SLM are compared to the experimental results（see Melbourne[7]）and the power spectrum of the inflow turbulence（Davenport spectrum）in Figure 4. As is shown in the Figure，a good agreement is evident for the pressure power spectral for the test point 3，while the numerical results for the test point 13 are slightly smaller than the experimental results at low frequency. As compared to the Davenport spectrum，the pressure spectrum for point 3 is slightly lower at the high frequency，due to the mesh filter of LES computation. However，the pressure spectrum for point 13 at high frequency is quite close to the Davenport spectrum，the reason can be attributed to the significant signature turbulence in the leeward face.
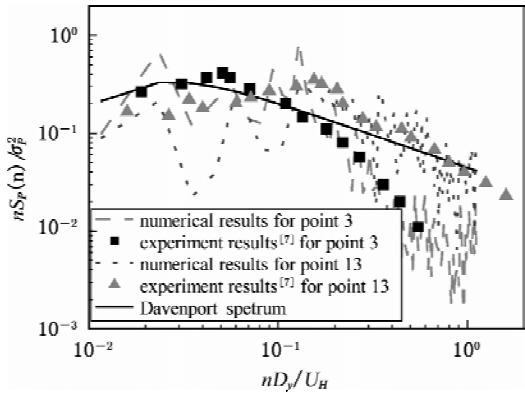
Figure 4   Comparison of the pressure power spectral

CONCLUSION

Based on simulation of the "real" inflow turbulence in the atmosphere boundary layer，the LES method，using the SGS stress model of the SLM，DSM and DKEM respectively，is adopted to investigate the characteristics of fluctuating wind loads on the CAARC standard tall steel building. Comparison of the numerical results，such as the pressure coefficients，dimensionless aerodynamic force/base- moment coefficients and pressure power spectral，and corresponding experimental data are conducted，and the feasibility of the numerical technique to simulate the fluctuating wind loads on tall buildings immersed in the atmosphere boundary layer is validated.

ACKNOWLEDGEMENT

REFERENCE

［1］Solari，G.，"Mathematical model to predict 3-D loading on buildings"，Journal of Engineering Mechanics，ASCE，1985,111(2),pp. 254-275.

［2］Zhou，Y.，Kijewski，T. and Kareem，A.，"Aerodynamic loads on tall buildings：Interactive database"，Journal of Structural Engineering，ASCE，2003,129(3),pp. 394-404.

［3］Huang，S.，Li，Q. S. and Xu，S.，"Numerical evaluation of wind effects on a tall steel building by CFD"，Journal of Constructional Steel Research，2007，63,pp. 612-627.

［4］Zheng，C. R. and Zhang，Y. C.，"Numerical investigation on the drag reduction properties of a suction controlled high-rise building"，Journal of Zhejiang University SCIENCE A，2010,11(7),pp. 477-487.

［5］Kondo，K.，Murakami，S. and Mochida，A.，"Generation of velocity fluctuations for inflow boundary condition of LES"，Journal of Wind Engineering and Industrial Aerodynamics，1997,67 & 68,pp. 51-64.

［6］Nozawa，K. and Tamura，T.，"Large eddy simulation of the flow around a low-rise building immersed in a rough-wall turbulent boundary layer"，Journal of Wind Engineering and Industrial Aerodynamics，2002,90,pp. 1151-1162.

［7］Melbourne W. H.，"Comparison of measurements of the CAARC standard tall building model in simulated model wind flows"，Journal of Wind Engineering and Industrial Aerodynamics 1980,6,pp. 78-88.

［8］Obasaju，E. D.，"Measurement of forces and base overturning moments on the CAARC tall building model in a simulated atmospheric boundary layer"，Journal of Wind Engineering and Industrial Aerodynamics，1992,40,pp. 103-126.

［9］Luo P.，"Investigation on standard models using wind tunnel tests"，Master Thesis，Tongji University，Shanghai，China，2004,pp. 11-87.

［10］Zheng，C. R.，Zhang，Y. C. and Zhang，W. Y.，"Large eddy simulation of separation control over a backward-facing step flow by suction"，International Journal of Computational Fluid Dynamics，2011,25(2),pp. 59-74.

［11］Deodatis，G.，"Simulation of ergodic multivariate stochastic processes"，Journal of Engineering Mechanics，ASCE，1996,122(8),pp. 778-787.

［12］Shirani，E.，Ferziger，J. H. and Reynolds，W. C.，"Mixing of a passive scalar in isotropic and sheared homogeneous turbulence"，Report TF-15，Mechanics Engineering Department，Standford University，1981.

［13］Zheng，C. R.，"Numerical investigation of wind loads on high-rise buildings controlled by suction/blowing"，PhD Thesis，Harbin Institute of Technology，Harbin，China，2010，pp. 141-180.

WIND TUNNEL TEST ON AEROELASTIC MODEL OF 500 kV TRANSMISSION LINE SYSTEM

* C. Y. Duan[1]，H. Z. Deng[1]，X. H. Jin[2] and Z. H. Wang[2]

[1] Department of Building Engineering，Tongji University，Shanghai，200092，China
[2] Guangdong Electric Power Design Institute，Guangzhou，510663，China
* Email：duanchengyin@126.com

KEYWORDS

Transmission line system，aeroelastic model，wind tunnel test，wind-induced response，mean displacement，acceleration RMS.

ABSTRACT

In order to investigate the wind-induced vibration of 500 kV double-circuit transmission line system，an aeroelastic model was designed with discrete stiffness method according to the characteristics of transmission tower structure. Under multiple wind attack angles and wind velocities，wind tunnel tests on the model of single tower and tower-line system consisting of five towers and four spans of conductors were performed respectively in turbulent flow. The time history of both displacement and acceleration of the model was obtained. The experimental results show that the wind attack angle greatly affects the mean displacement. The mean displacement of tower-line system in along-wind direction is much greater than that of single tower. The conductors influence the acceleration root mean square（RMS）oppositely in two directions：in X-direction the acceleration RMS of tower-line system is larger than that of single tower while in Y-direction the acceleration RMS of tower-line system is less than that of single tower，which indicates that conductors significantly constrain the vibration in Y-direction. The same conclusion is evidenced in study of the power spectrum of acceleration. It can also be observed that the acceleration RMS in along-wind direction is as same order of magnitude as that in transverse direction for all cases. The crosswind vibration should not be neglected.

INTRODUCTION

With the features of both long-span structures and high-rise structures，transmission line system is sensitive to wind loads. On the other hand，because of the uncertainty of natural wind，the variety of mechanical property of members，the complexity of fluid-structure interactions，and the unique structure of transmission tower，it is hard to analyze wind-induced vibrations of transmission line system through purely theoretical means. Therefore，aeroelastic model tests in the boundary layer wind tunnel are of great importance in researches and engineering practices. Loredo-Souza and Davenport[1-3] have researched the dynamic behaviour of transmission lines. They have also proposed a modelling approach

for transmission lines which has been widely used in related studies. References[4-5] have designed aeroelastic models of long span transmission line systems using different methods and conducted wind tunnel tests with these models. Other researches[6-7] have investigated wind-induced responses of lattice towers taking an ultra-high-voltage transmission line as background. In this study, a 500 kV double-circuit transmission line system with five lattice towers and four spans of conductors is assumed as the prototype. The tower, which is made up of angular and tubular steel members, has a 72–meter nominal height and 101–meter total height. The cross section is square with 2.4 meters width at the top and 18.92 meters width in the bottom. The transmission lines consist of six electric conductors and two lightning conductors. The span length is 630 meters.

DESIGN OF THE AEROELASTIC MODEL AND SIMULATION OF THE WIND FIELD

Design of the Aeroelastic Model

Similarity parameters followed in designing the aeroelastic model are Cauchy number (Ca), Strouhal number (St), density ratio and damping ratio (ζ). A geometric scale $\lambda_L = 1/80$ and a wind velocity scale $\lambda_v = 1/3$ are chosen and other scales are set according to the given similarity parameters (Table 1). The frame of transmission tower model is made of brass of which the elastic modulus is 103 000 Mpa. Deviations in axial stiffness of main members are less than 5% so that the overall dynamic behavior is not significantly changed. The profile of each member is simulated by using well-shaped ABS plastic for angular members and foam cylinders for tubular members.

TABLE 1   MAIN SCALES FOR THE MODEL

Scale	Ratio	Scale	Ratio
Length λ_L	1/80	Mass $\lambda_m = \lambda_L^3 \cdot \lambda_{\rho_f}$	1/512 000
Wind velocity λ_v	1/3	Axial rigidity $\lambda_{EA} = \lambda_L^2 \cdot \lambda_v^2 \cdot \lambda_{\rho_f}$	1/57 600
Air density λ_{ρ_f}	1/1	Frequency $\lambda_f = \lambda_v / \lambda_L$	26.67/1
Structure density $\lambda_{\rho_s} = \lambda_{\rho_f}$	1/1	Displacement $\lambda_y = \lambda_L$	1/80
Area $\lambda_A = \lambda_L^2$	1/6 400	Acceleration $\lambda_{\ddot{y}} = \lambda_v^2 / \lambda_L$	8.89/1

Because of the difficulty to simulate the span length of conductors with geometrical scale $\lambda_L = 1/80$, a factor $\gamma = 0.4$ is adopted to adjust the span length, as is suggested by Loredo-Souza[2]. Since the natural frequency of the conductor depends on the sag, it is necessary to keep the sag of each conductor the same in order to have the same dynamic behavior, together with the total mass and wind load area. Main scales for transmission lines are shown in Table 2. The model is built using a steel wire as the basic cable and a plastic hose as the cloths. The test view of the model is shown in Figure 1.

TABLE 2   MAIN SCALES FOR CONDUCTORS

Scale	Ratio	Scale	Ratio
Span $\lambda_L^* = \gamma \cdot \lambda_L$	1/200	Mass per unit length $\lambda_{\bar{m}}^* = \lambda_L^2 \cdot \lambda_{\rho_f} / \gamma$	1/2 560
Diameter $\lambda_d^* = \lambda_L / \gamma$	1/32	Axial rigidity $\lambda_{EA}^* = \gamma \cdot \lambda_L^2 \cdot \lambda_v^2 \cdot \lambda_{\rho_f}$	1/144 000
Sag $\lambda_s^* = \lambda_L^2 / \lambda_v^2$	1/711.11	Frequency $\lambda_f^* = \lambda_v / \lambda_L$	26.67/1

The natural frequencies and damping ratios in X-direction (normal-to-line) and in Y-direction (parallel-to-line) are measured using artificial excitation method (Table 3). Deviations of the frequencies are less

Figure 1　Test view of the model

than 7.4% and the frequency in X-direction is slightly less than that in Y-direction. Damping ratios are also among 1% to 2% which is widely accepted for steel structures.

TABLE 3　DYNAMIC CHARACTERISTICS OF THE MODEL

Frequency X (Hz)		Frequency Y (Hz)		Damping ratio	
Required	Measured	Required	Measured	X	Y
34.75	32.2	34.91	33.0	1.4%	1.4%

Simulation of the Wind Field

The wind tunnel test has been conducted in TJ－3 Boundary Layer Wind Tunnel. The wind tunnel has a test section 15 m wide，2 m high and 14 m long. The maximum wind velocity attainable in a turbulent flow is about 12 m/s. The simulated mean velocity profile is matched to a B-category profile in Load Code for the Design of Building Structures (GB 50009－2001) of which the power index is 0.16. The turbulence intensity profile follows the suggestion of International Wind Load Standard (ISO4354－2009) that the turbulence intensity at 30 m height is 16%. The turbulent flow is generated using grilles，spires and roughness elements. The arrangement of wind field is shown in Figure 2 and the mean velocity and turbulence intensity profiles simulated in the wind tunnel are shown in Figure 3.

Figure 2　Arrangement of the wind field
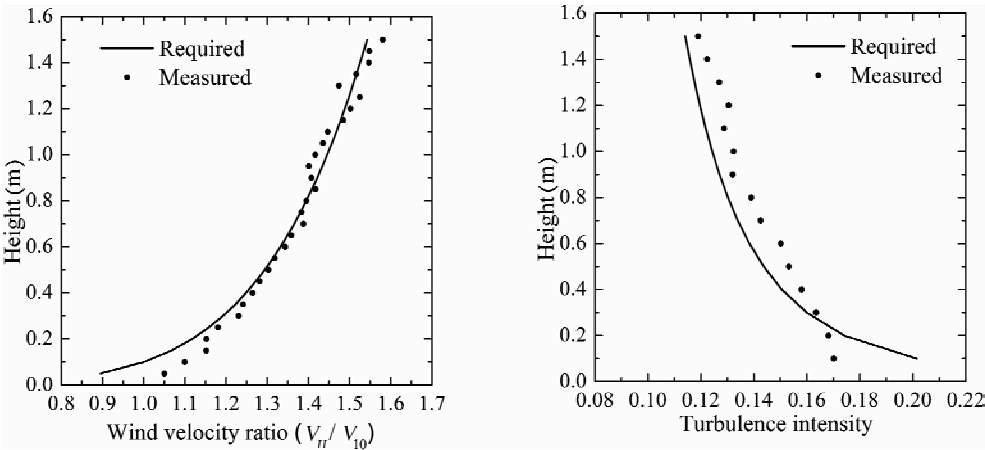
Figure 3   Simulated mean velocity and turbulence intensity profiles

WIND TUNNEL TEST AND ANALYSES OF EXPERIMENTAL RESULTS

Model Instrumentation

Asis shown in Figure 4，X-axis is defined as the direction normal to conductors and Y-axis parallel to conductors，and the wind attack angle is defined as the angle between flow direction and Y-axis. Seven laser transducers（D1，D3，D5，D7 in Y-direction and D2，D4，D6 in X-direction）and two accelerometers（A1 in Y-direction and A2 in X-direction）are mounted at three heights on the tower, as is indicated in Figure 4. Furthermore，the wind velocity is measured by a pitot-tube micro-manometer and the turbulence intensity is measured by a hot wire anemometer.
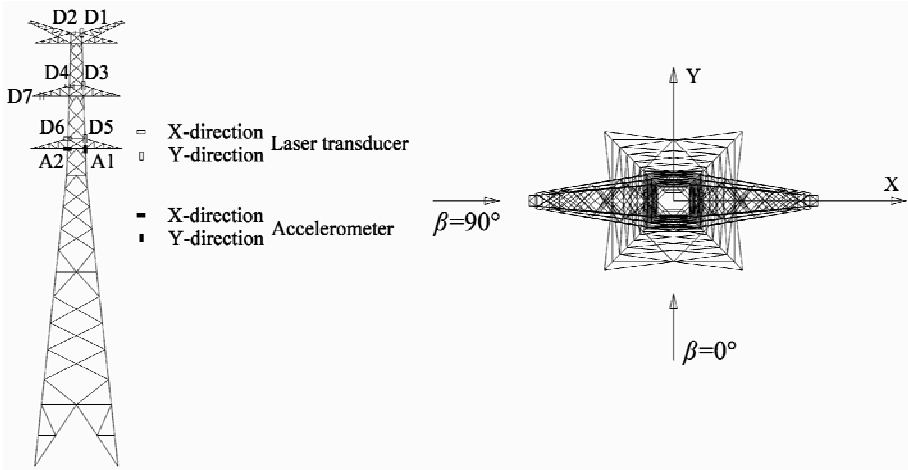
Figure 4   Model instrumentation and coordinate definition

The wind tunnel test concludes the test of a single tower and of a tower-line system. The single tower is tested under 0，15，30，45，60，75，90° of wind attack angle and the nominal wind velocity at the height

of 1.263 m ranges from 2.53 to 10.25 m/s. The tower-line system is tested under 75 and 90° of wind attack angle and the nominal wind velocity ranges from 2.53 to 7.69 m/s. Both displacement and acceleration responses are recorded for 69.632 seconds at a sampling frequency of 250 Hz.

Analyses of Experimental Results

Relationships between mean displacement，which is recorded by D1 and D2，and wind attack angle are shown in Figure 5 and Figure 6 for single tower and tower-line system，respectively. Wind attack angle has a significant effect on mean displacement for single tower. The displacement increases from 0 to 90° in X-direction while the opposite trend is evidenced in Y-direction. As to tower-line system，mean displacement at 90° is slightly larger than that at 75° in X-direction. In Y-direction no apparent trend is observed and all the values of mean displacement are around 0，which suggests that the cross-wind displacement response is zero mean vibration.
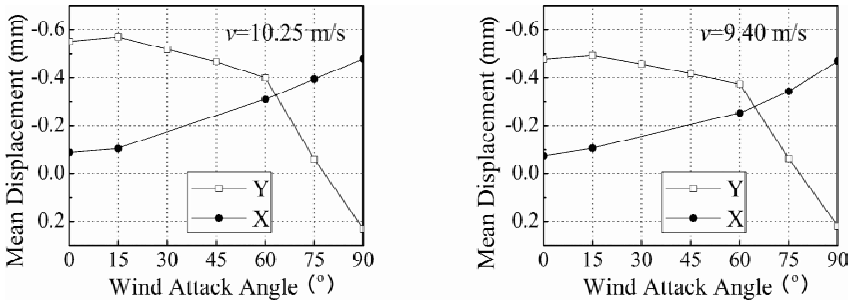
Figure 5   Mean displacement recorded by D1 and D2 for single tower
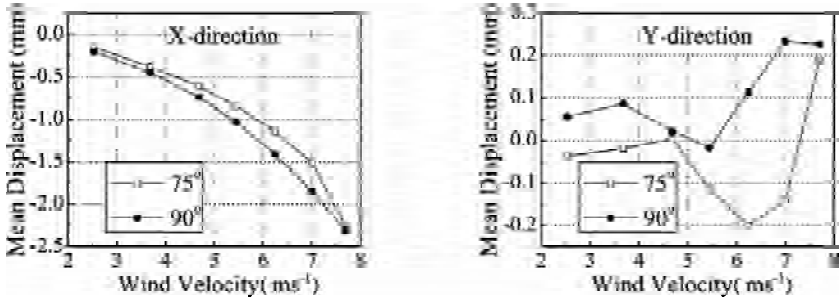
Figure 6   Mean displacement recorded by D1 and D2 for tower-line system

Relationships between acceleration root mean square（RMS），which is recorded by A1 and A2，and wind attack angle are shown in Figure 7 and Figure 8 for single tower and tower-line system. There is no obvious trend of acceleration RMS with the variation of wind attack angle for single tower. And it is evidenced that acceleration RMS in X-direction is as same order of magnitude as that in Y-direction. Therefore，cross-wind vibrations should not be neglected. For tower-line system acceleration RMS in Y-direction at 90° is obviously larger than that at 75°. The reason is that conductors in both sides of the tower have symmetric tension at 90° so that vibrations in Y-direction are restricted.

Comparisons about mean displacement recorded by D1 and D2 between single tower and tower-line system
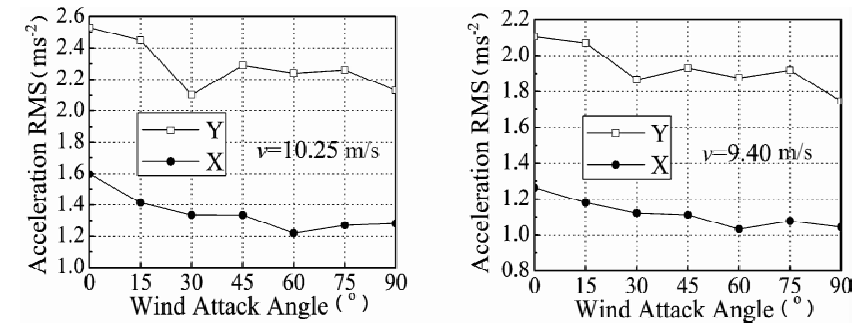
Figure 7   Acceleration RMS recorded by A1 and A2 for single tower
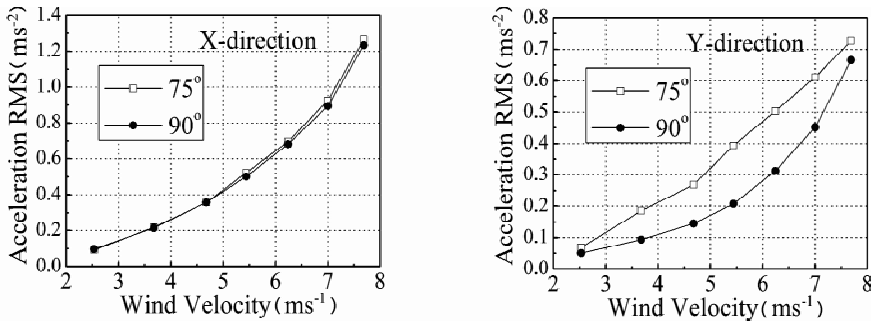
Figure 8   Acceleration RMS recorded by A1 and A2 for tower-line system

are shown in Figure 9，where ST represents single tower and TL represents tower-line system. Tower-line system has much larger mean displacement compared with single tower in X-direction，which suggests that conductors greatly increase wind loads in this direction.
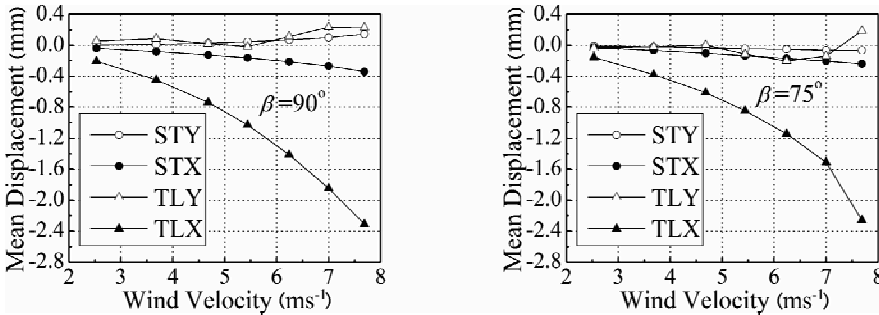
Figure 9   Comparisons about mean displacement between single tower and tower-line system

Comparisons about acceleration RMS recorded by A1 and A2 between single tower and tower-line system are shown in Figure 10. It is observed that acceleration RMS of tower-line system is larger than that of single tower in X-direction（normal-to-line）while the former is less than the latter in Y-direction（parallel-to-line）. Apparently，conductors provide strong constraint in Y-direction and on the contrary increase wind loads in X-direction.

Load case 1（the condition that a few of pedestrians walk fast）

In this load case，the condition that 90 persons walking at the vertical natural frequency，2.788 6 Hz，is taken into account. It is most unfavorable to dynamic responses of the entire structure when the exciting loads are located at the middle piece of the truss structure where the main sidewalk sites intermediately between the two middle pieces trusses. Therefore，90 persons are distributed uniformly at the floor plate with an area of 9 m × 60 m.

Human-induced Dynamic Loads are adopted as IABSE（International Association for Bridge and Structural Engineering）[5] recommended（as shown in Figure 3）. As to the details，the step frequency is 2.79 Hz，and the assumption is that all the persons walking at the same phase and frequency. The individual weight is taken as 70 kg per person following the reference [7]，and the damping ratio is taken as 0.05，taking the damping effectiveness of partition walls，seats on the floors and people into account，referring to [8].

Load case 2（the condition that a large amount of people stand up at the same time）

In this load case，the condition that 5 500 persons stand up together is considered，with the assumption that the standing-up motion lasts one minute. The impact load induced by stand-up motion is simulated as the sinusoid，and the elevation difference of the center of gravity is assumed to be 0.4 m. The individual weight is taken as 70 kg per person following the reference [7]. The number of seats in the convention center is about 5 500，which distributed on the floor with the area of 81 m × 54 m. The equivalent uniformly distributed load is calculated as 0.7×5 500/（81×54）= 0.88 kPa. The impact load curve is represented in Figure 3.

Load case 3（the condition that a large number of people walk slowly）

In this load case，the condition that a large number of people walk slowly only in the sidewalk is taken into consideration，whose step frequency is 1.5 Hz. Referring to the domestic Load Code，the pedestrians' equivalent uniformly distributed load is considered as 2 kPa，which will be cut half walling on sidesteps. The other basic assumption that all the pedestrians are walking at the same frequency and phase，and the simulation of human-induced dynamic loads are similar to Load Case 1，except the less step frequency. The area of the main plane sidewalk taken as 330 m², the equivalent uniformly distributed load is calculated as 2×330/（81 m×27）= 0.302 kPa. The human-induced dynamic load is shown in Figure 3.

Load case 4（the condition that a few people jump）

This load case is about the condition that 30 persons jump at the frequency of 2.788 6 Hz，the same as the natural frequency of the floor system. This load case is likely to occur when the meeting hall is used as an acting venue. The range of human activities is the central plate of the meeting hall（12 m × 9 m = 108 m²），and the impact load is simulated by sinusoids which also can be seen in Figure 3. The individual weight is taken as 70 kg per person following the reference [7]，so the equivalent uniformly distributed load of the central plate is 0.70×30×/（12×9）= 0.292 kPa.

Load case 5 （*the condition of concerts*）

This condition talks about the interaction between the participants and the performers during a concert. Taking [7] as a reference，the exciting frequency is taken as 1.5 Hz，and the exciting uniformly distributed load is 1.5 kPa. In addition，the impact load is considered as the sinusoid as shown in Figure 3 as well. The peak acceleration responses in these five load cases are shown in Figure 5.

Location Optimization For Multiple TMD （*MTMD*）[9]

As indicated in Table 4，the peak acceleration responses in Load Case 1，Load Case 3，and Load Case 4 exceed the limits of human comfort which the code requires. Meanwhile，based on the results from the modal analysis，the vibration responses depend on the first two vertical modes of this large-span floor system. Thus，TMD1 and TMD2 are installed to control the vibration of the first two vertical modes respectively. Since the TMDs should be set on locations where the amplitudes reach the largest in each mode shape to utmost their performances；Correspondingly，TMD1 are assembled around the middle of the floor system，and TMD2 are set on the spots at the one third length of the span. Parameters of both kinds of the TMD systems are represented in Table 2.
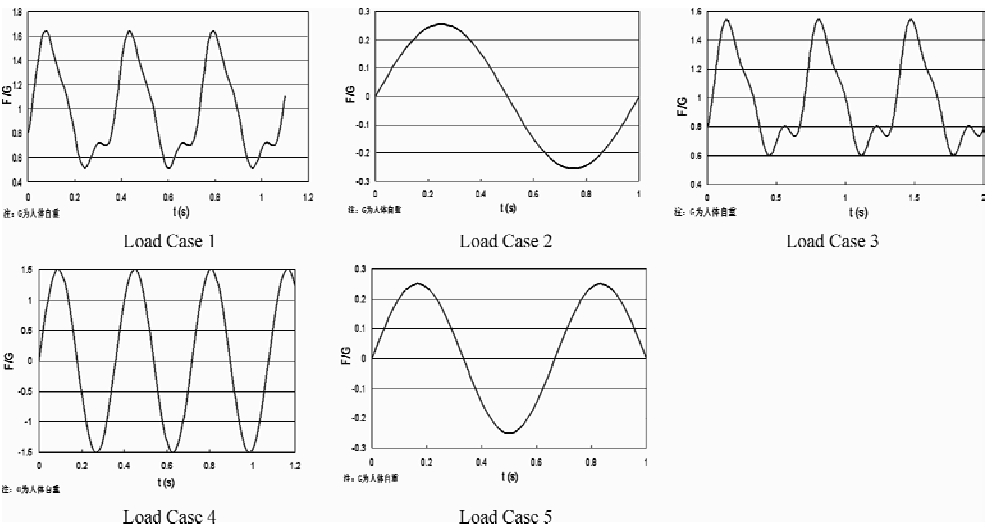
Figure 3   Human-induced dynamic loads

TABLE 2   CALCULATING PARAMETERS OF THE MASSES AND SPRING DASHPOTS

TMD system	Stiffness of springs(N/m)	Mass （kg）	Damping ratio of TMD
TMD1	47 016.5	580	1.0
TMD2	70 456.8	580	1.0

Aimed at the location optimization of MTMD involved in this project，it's feasible to apply genetic algorithm to reduce excessive calculating workload which other calculating methods may bring about. As the group algebra of evolution increases，an optimal value was gradually approached. In this paper，a specially designed toolbox for genetic algorithm and direct search，which the MATLAB program version 7.0 contains，was used. By programming the fitness function on our own to realize the call of command

flow from the ANSYS program in the MATLAB toolbox，and to improve the optimization algorithm，the interaction between the optimizing program and the finite element program is realized，which ensures high reliability of analyzing results and allows the calculation high efficiency.

Study on location optimization of TMD

Considering the floor system is symmetrical，firstly the points where are likely to be installed TMD on the one fourth part of the floor，thus to obtain the plan of TMD arrangement the entire floor.

The effect of vibration control in different load cases and with varying amounts of TMDs are shown in Figure 4，in which the horizontal coordinate stands for the amount of TMD and the vertical coordinate is for the vibration reduction ratio. The vibration reduction ratio equals the ratio of the peak accelerations' difference between without and with TMD to the peak accelerations without TMD.

（a）Load Case 1

（b）Load Case 2

（c）Load Case

（d）Load Case 4
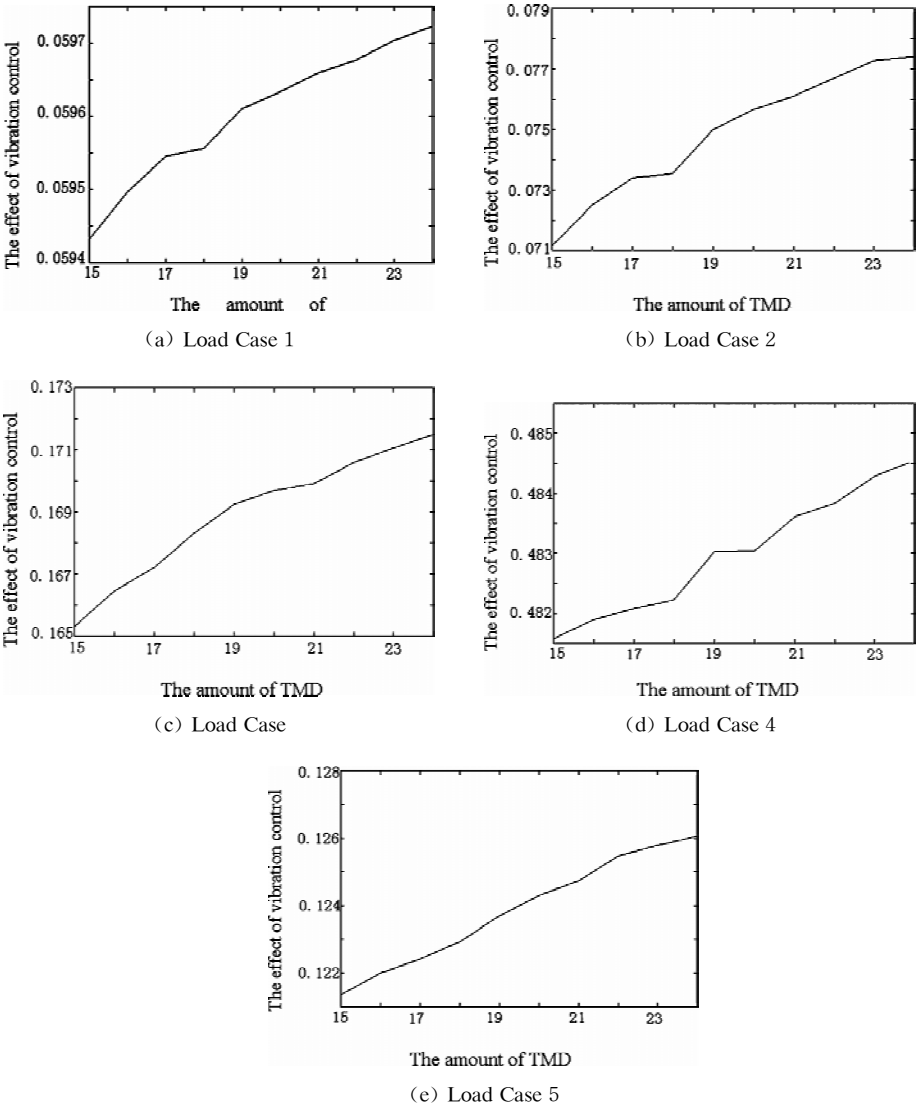
（e）Load Case 5

Figure 4　The vibration reduction effect graph

As indicated in Figure 4，the inflection points in five load cases concentrate in two intervals，which are around the point on behalf of 19 sets and 21 sets respectively. Both these two amounts of TMD can meet the requirements of human comfort. Consequently from the economic point of view，the optimal amount of TMD is determined as 19 sets，that is，for the entire floor，the amount will be 72 sets（$19 \times 4 - 4 = 72$）.

Location preference of TMD

The optimal location of TMD varies in different loads cases. On the account that the peak accelerations in Load Case 1，Load Case 3，and Load Case 4 exceed the limits of human comfort in relevant codes，the weighing of these three load cases are raises during the location preference of TMD. The weighing of all load cases are listed in Table 3. The final arrangement of TMD are decided by calculating the weighing sum of each objective location based on the weighing coefficients in Table 3 and selecting adequate locations according to the weighing successively，from large ones to small ones. The final determination of the TMD arrangement is shown in Figure 5.

TABLE 3 THE WEIGHING OF FIVE LOAD CASES

Load Case	Load Case 1	Load Case 2	Load Case 3	Load Case 4	Load Case 5
Weighing	0.3	0.1	0.25	0.25	0.1
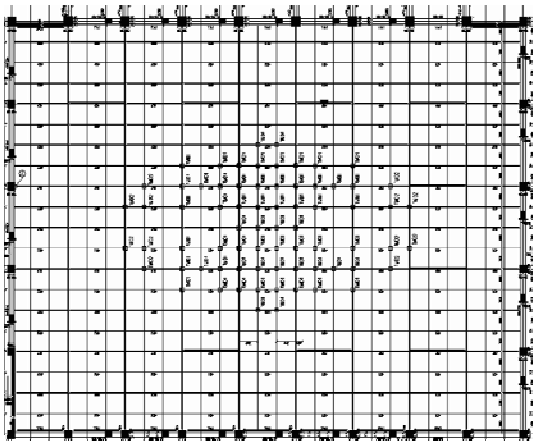
Figure 5   The optimal plan of TMD arrangement

Parameter Optimization of MTMD [9]

Theoretically，with the structural damping not being considered，the vibration reduction effect is the idealists when the natural frequency of TMD equals that of the structure. However，in engineering practice，it's no easy to determine the frequency ratio when taking the structural damping into account. The optimal frequency ratio is supposed to fluctuate around 1.0，and the fluctuating range varies with different loads cases. In consequence，the range for optimizing is set as $1.1 \sim 1.15 \sim 1.2$ initially，and the step length is still 0.01，though. Figure 6 is for the peak accelerations graph with various frequencies in different load cases.

（a）Load Case 1

（b）Load Case 2

（c）Load Case 3

（d）Load Case 4

（e）Load Case 5
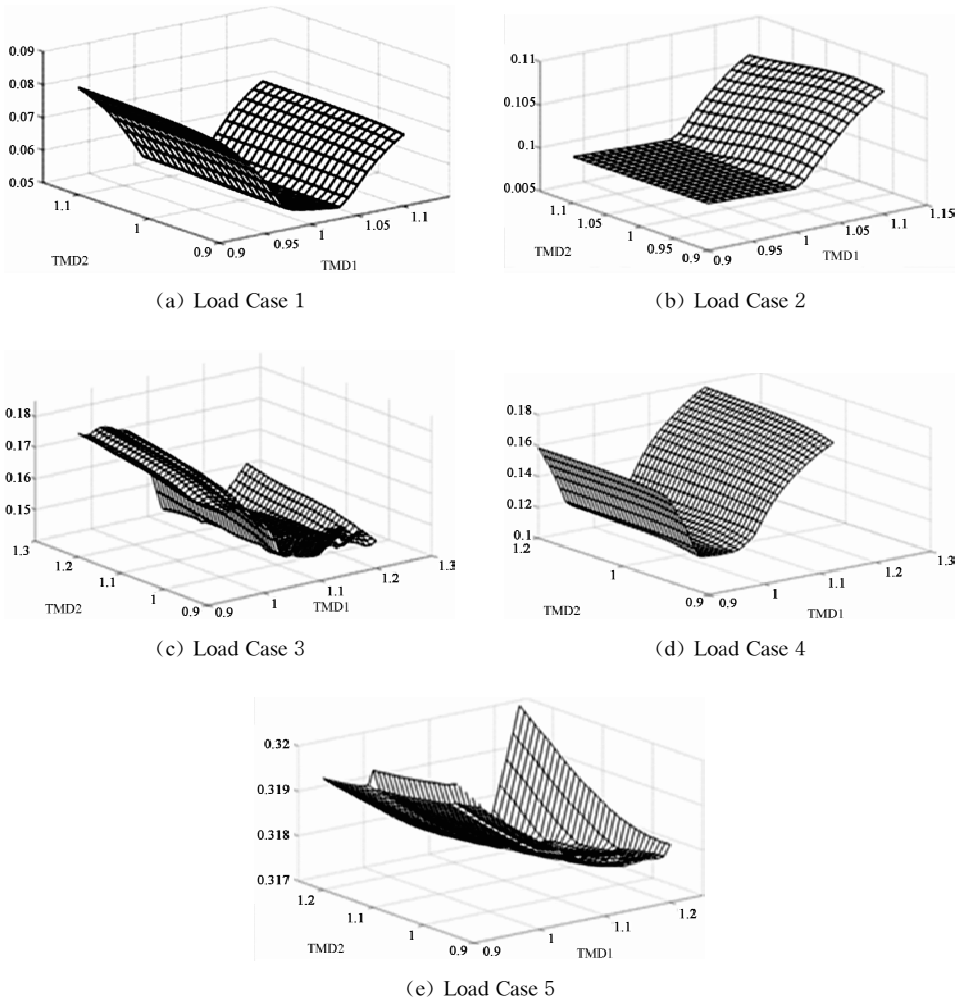
Figure 6   The peak accelerations graph

It is implied in Figure 8 that altering the frequency ratio of TMD1 affects the peak accelerations more significant than that of TMD2. The curves of peak accelerations shows obvious valleys as the frequency ratio of TMD1increases，while in the case of TMD2，there are no obvious valleys.

Because the TMD system isn't able to approach the self-adapting state，there is only a single frequency composite value to be selected to make the vibration reduction effect of all load cases acceptable. Hence，after analyzing the peak acceleration curves of all loads cases comprehensively，the curves are more intensive when the frequency ratio ranges from 1.03 to 1.08 and the frequency ratio varies between 0.9 and 1.2. The RMS value of the acceleration ratio in each load case is chosen to be the evaluating indicator，which is kind of the effective value，that is，the square root of the average of the square sum of a set of statistics. The frequency combination is fixed as 1.06 for TMD1 and 0.90 for TMD2，which is the optimum with the least RMS value.

Using the optimal parameters，the comparison of the peak vertical accelerations between with and without MTMD is represented in Figure 7，and the results are shown in Table 4.

637

(a) Load Case 1

(b) Load Case 2

(c) Load Case 3

(d) Load Case 4
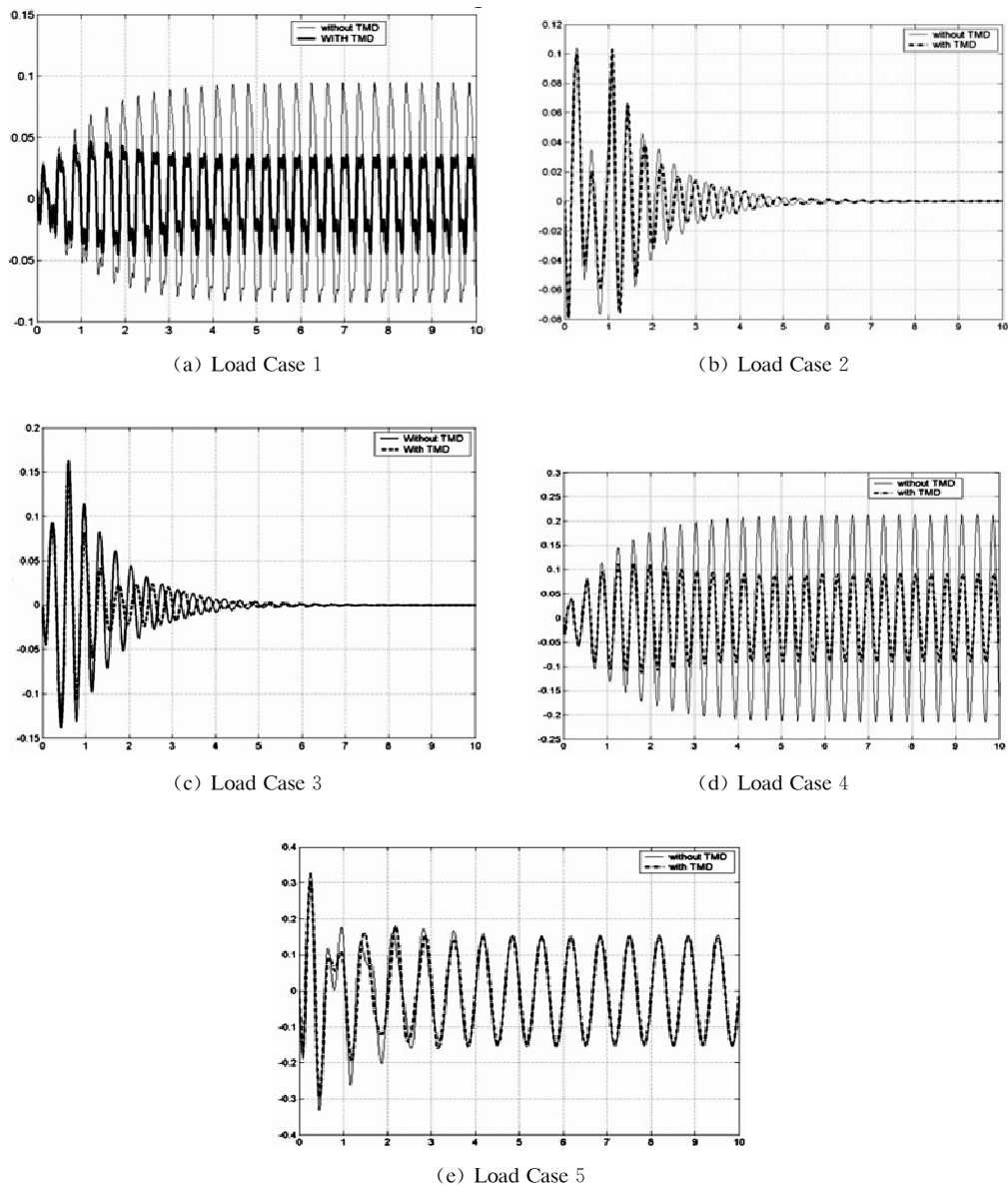
(e) Load Case 5

Figure 7   Comparison of the peak vertical accelerations between with and without MTMD

TABLE 4   COMPARISON OF THE PEAK VERTICLE ACCELERATION

Load Case	Without TMD	With TMD	Vibration reduction ratio	Acceleration limits
LC 1	0.009 69 g	0.004 94 g	49.1%	0.005 g(offices)
LC 2	0.010 6 g	0.010 5 g	1.3%	0.015 g (Stores)
LC 3	0.018 5 g	0.015 2 g	17.4%	0.015 g(Stores)
LC 4	0.021 9 g	0.011 7 g	46.7%	0.015 g(Stores)
LC 5	0.033 9 g	0.032 5 g	4.2%	0.04 g(only rhythmic activities)

CONCLUSION

Without vibration reduction measures，the floor cannot satisfy the limits for human comfort in most load cases. In the walking or jumping case，the vertical vibration probably is beyond the level that occupants can accept. Through calling the genetic algorithm toolbox，the location optimization was carried out with the minimum peak accelerations as the objective function. The optimal amount and locations of TMD is determined based on the effect of the TMD system. The results indicate that the final arrangement of TMD perform well in vibration reduction obtaining by genetic algorithm. The optimal frequency ratio combination is achieved by parameter optimizing aimed at the TMD system in optimal arrangement. The vibration reduction ratio reached 49.1% to the most，and the least one is 1.3%，which depends on the difference between the natural frequency of the excitation and that of the floor system. The closer the two are，the more effective the vibration reduction is. With the optimal vibration reduction scheme applied，the acceleration responses of the floor satisfy the requirements of human comfort in general. During the parameter analysis，the frequency of TMD plays an important role in vibration control；thus，the in-situ test on the dynamic characteristics of the floor system can ensure the vibration reducing effect.

ACKNOWLEDGEMENT

REFERENCE

［1］Ohlsson，S. V.，"Ten years of floor vibration research—a review of aspects and some results". Proceedings of the Symposium/Workshop on Serviceability of Buildings（movements，Deformations，Vibrations），Vol.1，Ottawa，Canada，1988；419–434.

［2］Ellingwood，B.，MASCE and Tallin，A.，"Structural Serviceability：Floor Vibrations"［J］，Journal of Structural Engineering，VOL.110，No.2，1984；401–418.

［3］Ebrahimpour，A. and Sack，R. L.，"Modeling dynamic occupant crowd harmonic movements"［J］，ASCE，1992，118(2)：1121–1136.

［4］National Standards of the People's Republic of China，"Technical specification of urban pedestrian overcrossing and underpass（CJJ69–95）"，Beijing，China Construction Industry Press，1996.

［5］Zhu，M.，Zhang，Z. Q.，Ke，C. H.，Zhang，X. and Li，A. Q.，"Study on improvements of vertical vibration comfort issue with large-span steel floor system"，Building Structure：2008，Jan.

［6］ENV1991–1："Basis of design and actions on structures"，European Committee for Standardization.

［7］Canadian Institute of Steel Construction. "Floor Vibrations Due to Human Activity（Steel Design Guide Series 11）"，American Institute of Steel Construction，1997

［8］Applied Technology Council. "Minimizing Floor Vibration（ATC Design Guide 1）"，1999.

［9］Huang，M. Y.，"Vibration control of large-span floor system under human-induced loads"，Nanjing：Master thesis in SEU，2009.

WIND-INDUCED RESPONSE ANALYSIS IN STRONG WINDS FOR MONOLAYER CABLE NET CURTAIN WALL

* L. F. Yin[1]，G. Tang[1, 2]，J. Cui[1] and B. J. Wang[1]

[1] Southeast University，Key laboratory of concrete and pre-stressed concrete structures of the Ministry of Education，Nanjing，210096，China

[2] Department of Civil Engineering，Nanjing University of Aeronautics and Astronautics，YuDao Street 29，Nanjing，210016，China

* Email：eking@seu.edu.cn

KEYWORDS

Monolayer cable net，wind-induced vibration analysis，multi-input non-linear time history analysis.

ABSTRACT

Owning to the wind-sensitivity of the monolayer cable net curtain wall，wind-induced vibration analysis is a key issue in the design work of construction using these curtain walls. In this paper，the multi-points input nonlinear time history method is used to have a wind-induced vibration analysis of the curtain wall in the CNPC Xinjiang Command Center under frequent fluctuating wind，by choosing average wind pressure location as the initial location. Its dynamic characteristics are further analyzed. The study shows that as the size of the monolayer cable net gets larger，the net subjects to the strong wind more with a larger displacement and a bigger range of cable tension. Under characteristic combination，the maximum displacement was controlled in 1/50 of the span；under fundamental combination，the tensions of lateral string cable do not exceed 0.5 times of the minimum breaking force while the tensions of vertical net cable do not exceed 0.44 times of the minimum breaking strength. It is concluded that this cable net design under fluctuating wind has a good performance and security. Thus a precise wind-induced vibration analysis is the key to ensure the safety of a building with the monolayer cable net curtain wall in the strong wind.

INTRODUCTION

The monolayer cable net system，because of its excellent architectural features，has been applied in multiple building including New York TW Center [4]，Harbin International Sports Exhibition Center [5]，Beijing Poly Plaza project [6] and CNPC Xinjiang Command Center in recent years. The design and construction of many huge projects have promoted the research of the monolayer cable net structure and research in related areas[7-9]，yet the current research far lags behind the market's needs. CNPC Xinjiang Command Center was built in the south-eastern suburbs of Karamay city，Xinjiang province. The location

PROJECT BACKGROUND CALCULATIONS

ANSYS is used to build the CNPC Xinjiang Command Center monolayer cable net finite element model in this project. In the model，LINK10 is used for cable net，COMBIN14 for the buffer spring and Mass 21 in the finite element model for the quality of the glass and claw pieces. As the supporting frame has weak edges and the lateral cables carry the horizontal load，the deformation will directly effect the force distribution of the cable. Therefore，it is crucial for us to ensure that the cable net and the supporting frame work together. In order to solve this problem，the combination of SHELL63 and Beam44 are used to establish the 3d frame model based on shell elements，as shown in Figure 2.
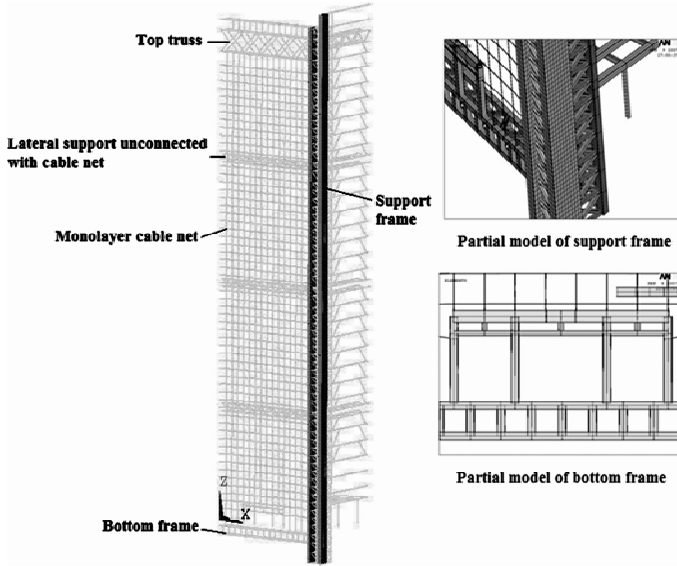
Figure 2　Finite element model

It had taken on the work of form-finding and pre-tension optimization of the finite element model built，to help the first design of the cable net. And the stiffness and strength of the cable net is analyzed under various conditions and the best diameter and pre-stress number is finally chosen. The results and related data available in this paper are based on the analysis of the best solution we have chosen.

Natural Vibration Characteristics Analysis

The cable net system went through big deformations in this project. Thus its model analysis is not the same as the ordinary undamped modal analysis. So the pre-stressed modal analysis is conducted after the large deformation static analysis. The specific steps are：1）opening the stress stiffening and large deformation to conduct the Geometric nonlinear static analysis；2）consider the effect of pre-stress and conduct mode analysis. When conducting the vibration characteristics analysis，the stiffness of the glass was not included. And the Mass21 is used as the glass and claw pieces in the finite element model. Typical results are shown in Figure 3.

In terms of vibration mode，it is concluded that the maximum amplitude of first mode occurs in the lower part of monolayer cable net，a typical half-wave vibration mode，similar to one-way plate type structure vibration. With the vibration modes number increasing，the frequency of the structure gradually

increased，but the frequency of vibration mode is relatively intense in similar cycle，reflecting the typical monolayer cable net structure dynamic characteristics.

| The first mode | The second mode | The third mode | The fourth mode | The fifth mode |
| (Period 0.6925s) | (Period 0.6745s) | (Period 0.6471s) | (Period 0.6471s) | (Period 0.6471s) |
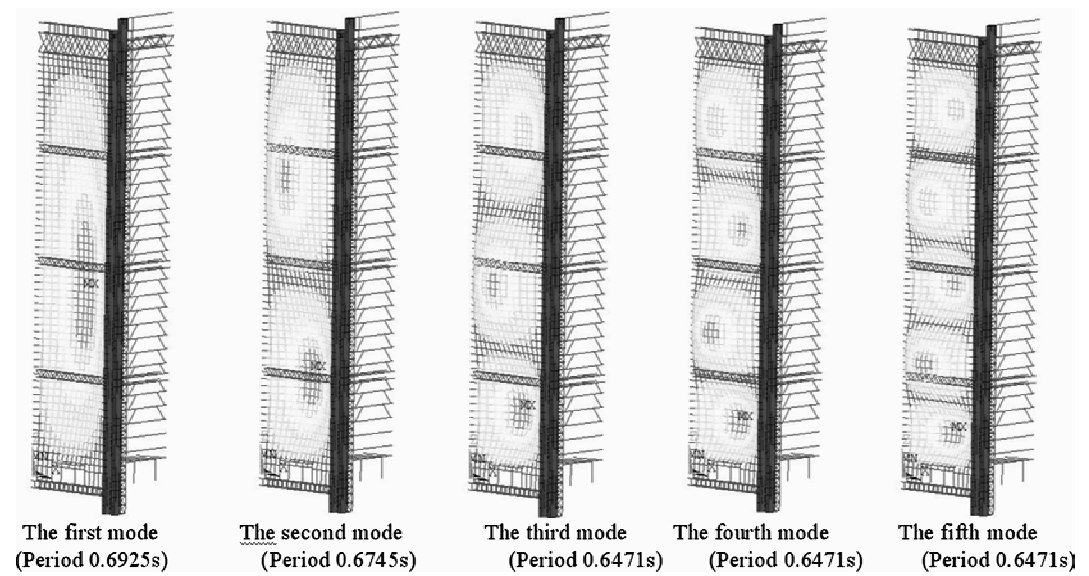
Figure 3   The first five orders of vibration mode of the monolayer cable net curtain wall structure

The Value of Wind Load

In the "wind tunnel report" [9]，the ratio of curtain wall wind tunnel test model is 1∶200(the height of pilot is 100 cm，equivalent to 200 m of the actual building height)；the wind speed is about 7.9 m/s；the sampling time is 13.1 s；the actual sampling frequency is 313 Hz；The tests are carried out at interval of 15° in 24 the wind directions and the measuring point are shown in Figure 4. The height of the test reference point that converted to corresponding actual height of the building is 101 m（the height from top building）.

According to wind tunnel report，converting the data in proportion，basic parameters of wind speed are available. The standardized wind speed is 38 m/s at 10 m height while it is classified as B class landscape. The time-length of time history of the actual structure is 337 s after conversion. Considering the vibration period of the monolayer cable net is 0.692 5 s，in order to save computation，120 s are chosen as the wind-induced vibration excitation input，when wind pressure drop or change in a larger scale，and 0.016 s as time step. The cable net vibration modes damping ratio is 0.02. The other points' pressure can be got by intersection algorithm.

Through comparison，it is seen that the distribution angles of larger wind pressure coefficient are 0 degrees，15 degrees（negative Y direction），285 degrees and 300 degrees（positive Y to the wind）. From the calculation results，it can also be seen that the structure responses are relatively large under 0 degrees wind direction（negative Y to the wind）and 300 degrees wind direction（positive Y to the wind）. This paper presents wind-induced vibration analysis results of the two wind direction. The fluctuating wind pressure time history curve of a typical measurement point of is shown in Figure 5.
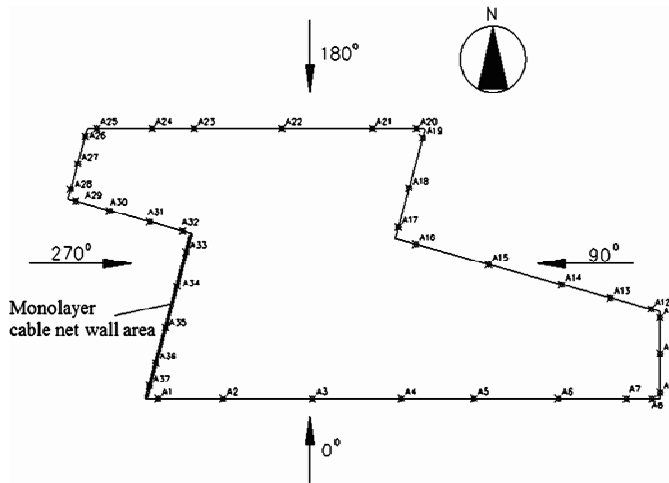
Figure 4   The measuring points layout of wind tunnel test
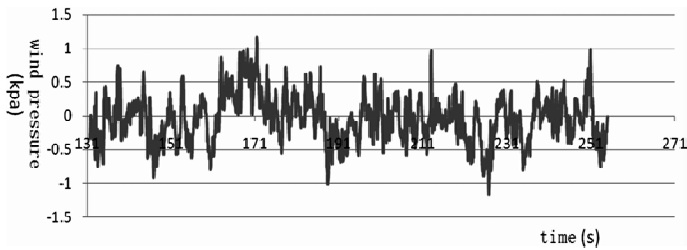
（a）0 degrees wind direction（point A33）
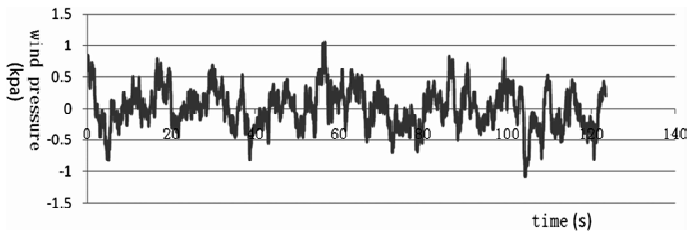
（b）300 degrees wind direction（point H1）

Figure 5   The time-history curves of fluctuating wind pressure on typical pressure-measuring points

Wind-induced Vibration Analysis

The results of the characteristic combination

The paper，in case 1（1.0×PRESTRESS + 1.0×DEAD + 1.0×WIND（+）） and case 3（1.0×PRESTRESS + 1.0×DEAD + 1.0×WIND（-）），takes the static analysis results to study the deformation of the structure. The positive pressure takes 300 degree wind angle while the negative pressure takes 0 degree. Results of typical wind-induced vibration analysis under characteristic combinations are shown in Figure 6 and Figure 7.

The typical results are shown in Figure 2 to Figure 5，and the full lines show the results of the geometrical

nonlinear analysis and the dotted lines show the results of the double nonlinear analysis.
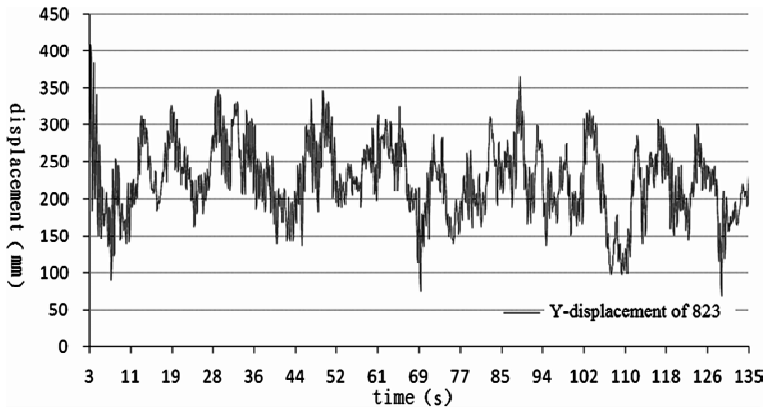
（a）Case 1
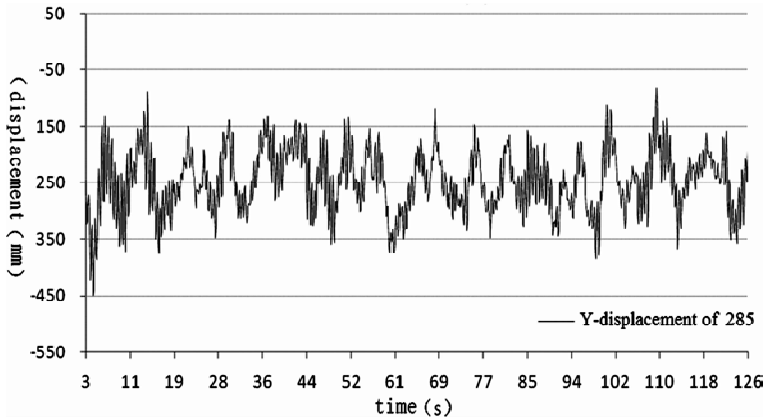
（b）Case 3

Figure 6   The time-history curves of Y-direction（out of plane）displacement on
points with the largest displacement under nominal combination
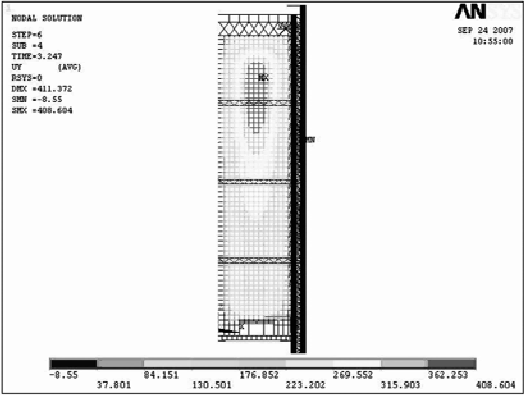
（a）Case 1
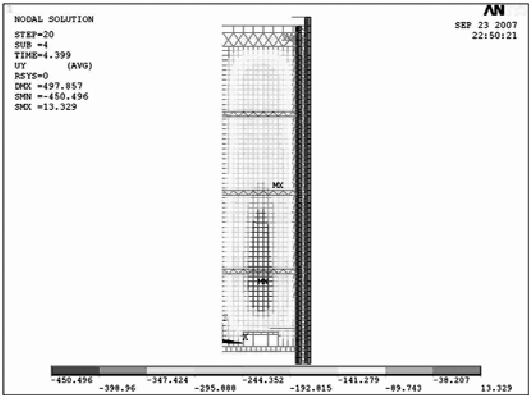
（b）Case 3

Figure 7   Under the standard combination, the Y direction（outer-plane）displacement distribution（mm）

The Results of the Fundamental Combination

The paper takes the results of case 5 (1.0×PRESTRESS + 1.2×DEAD + 1.4×WIND (+)) and case 9 (1.0×PRESTRESS + 1.2×DEAD + 1.4×WIND (−)) to know whether the strength of the structure meet the design and specifications or not. Results of typical wind-induced vibration analysis under fundamental combinations are shown from Figure 8 to Figure 12.
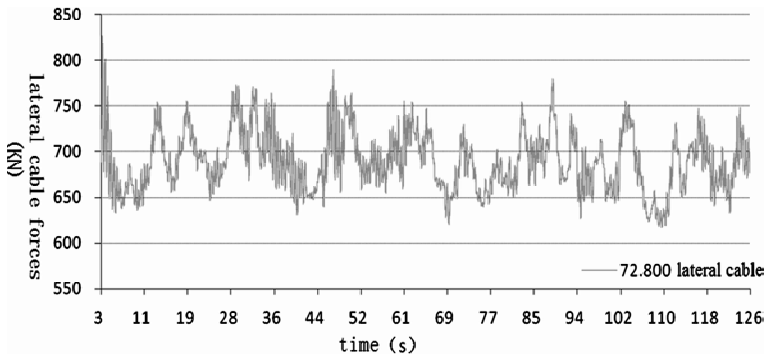
(a) Case 5
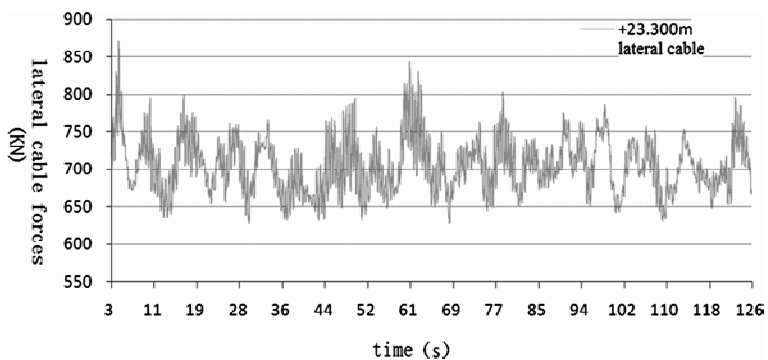
(b) Case 9

Figure 8   The time-history curves of cable tension on the largest transverse cable under fundamental combination
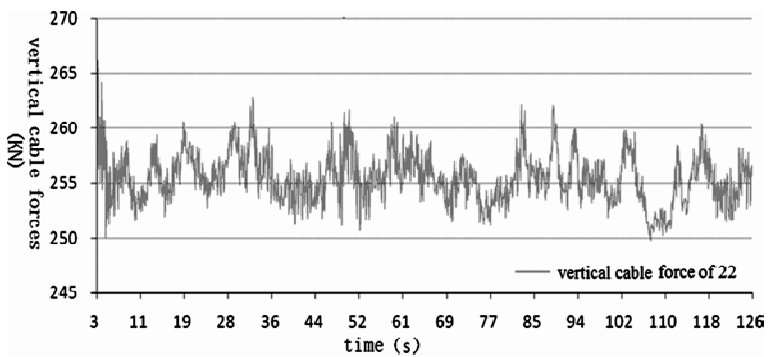
(a) Case 5

EXPERIMENTAL STUDY ON FATIGUE BEHAVIOR OF SRC BEAM-TO-CFRHS COLUMN CONNECTIONS IN HIGHSPEED RAILWAY STATION

* Q.J. Xian, L.W. Tong, L.Y. Zhou, Y.Y. Chen and E. Xie

State Key Laboratory for Disaster Reduction in Civil Engineering,
Tongji University, Shanghai, 200092, China
Department of Building Engineering, Tongji University, Shanghai, 200092, China
* Email: xianqj@126.com

KEYWORDS

SRC beam-to-CFRHS column connections, constant-amplitude fatigue experiment, fatigue behavior, crack propagation, redistribution of internal force, fatigue failure mode.

ABSTRACT

Due to lack of study on fatigue behavior of steel reinforced concrete (SRC) beam-to-concrete filled rectangular hollow section (CFRHS) column connections, three 1 : 4 beam-to-column connection specimens were investigated by means of two-stage constant-amplitude fatigue experiment. In first stage the specimen was under cyclic loading for two million times according to design load amplitude, so as to provide basis for fatigue design of the connections. In second stage fatigue failure of the specimen occurred eventually with bigger load amplitude, so as to investigate its fatigue behavior and damage characteristics. The research shows that three specimens meet fatigue design requirements. The top tensile flange of H-shaped steel in certain beam fractures completely where the flange width changes. The crack traverses the weld toe of stud and stirrup hole, and then propagates downward along web, but the top longitudinal tensile reinforcements do not fracture. The fracture of top tensile flange in certain beam can be regarded as the sign of fatigue failure of beam-to-column connections. Before the fracture of flange, the redistribution of internal force mainly occurs among top tensile flange, top longitudinal tensile reinforcements and bottom compressive concrete in beam, but integral stiffness of the connection does not decrease obviously. After the fracture of flange, fatigue cumulative damage aggravates in beam, so integral stiffness of the connection decreases gradually.

INTRODUCTION

Steel reinforced concrete (SRC) structure can be regarded as a new steel-concrete composite structure which is composed of internal profile steel, external reinforcements and concrete, and a certain number of stud connectors. SRC structure is widely used in practical projects now because of its good characteristics. In recent years express railway develops rapidly in our country, so a large number of

express railway station buildings are required correspondingly. In some large multi-functional traffic hubs，express railway station building is constructed to use SRC beams and concrete filled rectangular hollow section（CFRHS）columns，which involves a large number of SRC beam to CFRHS column connections. This type of beam-to-column connections are directly affected by frequent train loads because of daily operation of express railway trains. So in the design lifetime，fatigue strength of these connections must be considered.

At present more research has been done on SRC beams at home and abroad，but it is mainly about static behavior of the most basic solid-web SRC beams（Cai[1]，Shao[2]，Liu[3]）. The current *Technical specification for steel reinforced concrete composite structure* in China only gives static calculation regulations of SRC beam，column，connection（[4]）etc. Now the fatigue research related to SRC beam is almost a blank at home and abroad except the only literature that fatigue comparison experiment of a small number of SRC beams and RC beams under torsion and bending moment conditions was done in Japan in 1990 (Izumi[5]). However，there is no fatigue research concerning SRC beam to CFRHS column connections.

Based on the needs of construction of express railway station buildings，fatigue experiments of three 1∶4 models of SRC beam to CFRHS column connections have been done in order to achieve two purposes (Tong[6]，Zhou[7]). First，the designed SRC beam to CFRHS column connections are examined whether to reach fatigue life of 2 million times or not. Second，if the connections can not reach fatigue life of 2 million times，how to improve the design is considered. If they can reach fatigue life of 2 million times，fatigue failure will be further promoted by increasing fatigue load so as to investigate their fatigue behavior and damage characteristics.

EXPERIMENTAL PROGRAM

Specimen Design

A 1∶4 model of SRC beam to CFRHS column connection is taken as specimen BC as shown in Figure 1.

(a) Plan drawing of the specimen　　　　(d) Section drawing of the beam
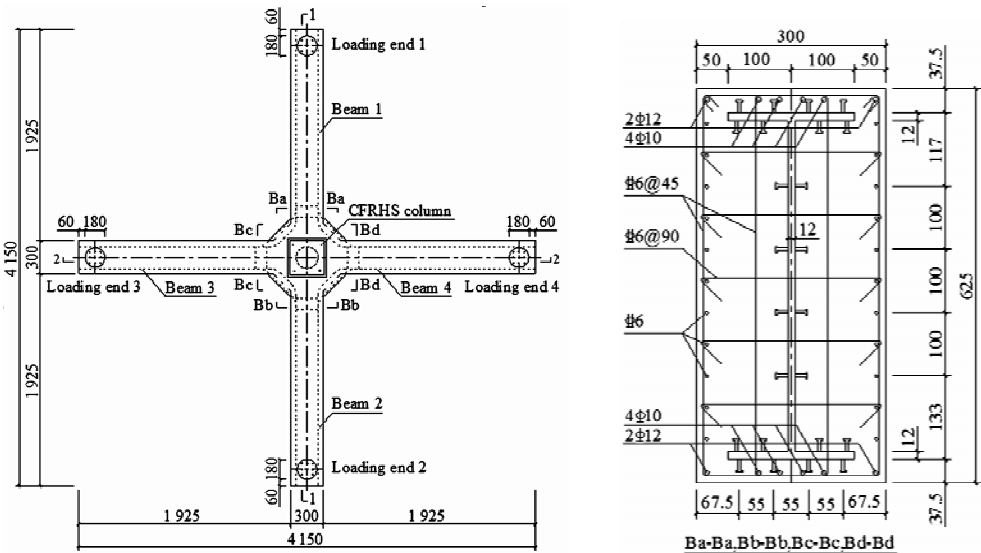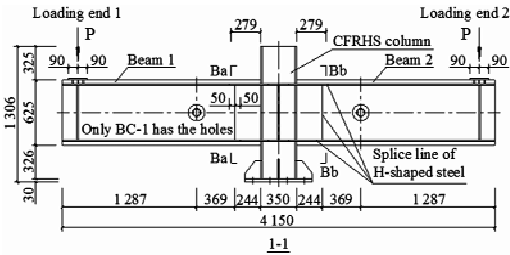
（b）Elevation drawing of beams 1 and 2   （c）Elevation drawing of beams 3 and 4
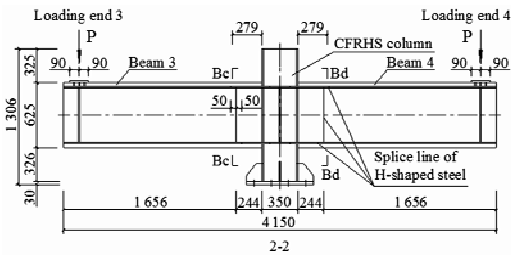
Figure 1   Plan drawing, elevation drawing and section drawing of the specimen

Beam section and column section of the specimen are obtained according to $1 : 4$ scale of actual sections of beam-to-column connection in express railway station building. The shear and moment values of beam section in beam and column interface of connection zone are calculated from actual internal force design values in the light of similarity principle. Then the length of beam can be determined according to loading capacity of fatigue testing machine. In beam-to-column connection specimen BC, SRC beams 1 to 4 are cantilever beams to serve as loading ends 1 to 4, the bottom end of CFRHS column is fixed but the top end is free. The specimen is fabricated with continuous beams and disconnected column. Due to the needs of actual piping arrangement, two holes are made in the webs of H-shaped steel of beam 1 and 2 away from connection zone in specimen BC-1.

TABLE 1   TEST RESULTS OF MATERIAL PROPERTIES

| Specimen number | H-shaped steel of the beam | | Steel plate of the column | | Longitudinal reinforcements of the beam | | | | Concrete in beam | Concrete in column |
| | | | | | Φ 12 | | Φ 10 | | | |
	f_y/MPa	f_u/MPa	f_y/MPa	f_u/MPa	f_y/MPa	f_u/MPa	f_y/MPa	f_u/MPa	f_{cu}/MPa	f_{cu}/MPa
BC-1									27.1	37.2
BC-2	359	533	359	507	367	531	351	495	44.4	49.3
BC-3									38.3	51.6

Note: The symbols f_y, f_u mean average yield strength and average tensile strength, and f_{cu} means average value of cubic concrete compressive strength.

The specimen uses C35 concrete in beams and C50 concrete in column, HRB335 longitudinal reinforcements, Q345 steel and Q235 studs. Test results of related material properties are shown in Table 1. Reinforcement ratio of longitudinal tensile reinforcements is 0.30%, and steel ratio of H-shaped steel is 5.93% in beam.

Loading Scheme

Figures 1（b）and （c）show that the distance between loading center of beams 1 to 4 and beam and column interface is 1.75 m. Loading ends 1 to 4 achieve simultaneous loading through two distribution beams. Loading values of fatigue experiment are shown in Table 2.

TABLE 2   LOADING VALUES OF FATIGUE EXPERIMENT

Loading value	P_{max}/kN	P_{min}/kN	M_{max}/M_u	M_{min}/M_u
First stage fatigue experiment	200	128	0.319	0.204
Second stage fatigue experiment	200	95	0.319	0.151

Note：P_{max}，P_{min} mean maximum load and minimum load of loading end. M_{max}，M_{min} mean maximum bending moment and minimum bending moment of section Ba-Ba. M_u means design value of flexural strength of section Ba-Ba.

Testing Scheme

The main measurement contents in experiment include loading end deflections of beam 1 to 4，strains of tensile flange，longitudinal tensile reinforcements and compressive concrete surface in the sections near splice line of H-shaped steel in beam which include sections Ba-Ba，Bb-Bb，Bc-Bc and Bd-Bd，and the strain of tensile flange in beam and column interface. In addition，output loads of fatigue testing machine are kept track of from second stage fatigue experiment to final fatigue failure of the specimen. Because layout scheme of strain gauges in sections Bb-Bb，Bc-Bc and Bd-Bd is the same as section Ba-Ba，the layout scheme in section Ba-Ba is only given here，as shown in Figure 2.
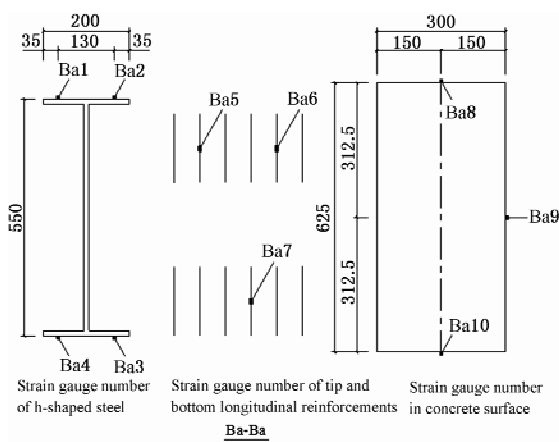
Figure 2   Layout scheme of strain gauges in beam section of the specimen

EXPERIMENT RESULTS

Experiment Phenomena

Fatigue failure occurs in three specimens eventually，and experiment phenomena of BC-3 which is taken for example are to be described here. In static experiment before fatigue experiment of BC-3，top surface and two lateral surfaces of beams 1 to 4 near connection zone have already appeared tiny cracks. In subsequent first stage fatigue experiment process，the existing cracks continue to propagate，while some new tiny cracks also appear. Crack width and deflection of loading ends 1 to 4 do not increase obviously，the maximum crack width is less than 0.1mm after cyclic loading of 2 million times and meets design requirement. At the end of second stage fatigue experiment，top surface and two lateral surfaces of beam 2 near connection zone craze severely and deflection of loading end 2 becomes very large，as a result

fatigue failure occurs in BC-3. After the concrete is got rid of，top flange in beam 2 fractures completely where flange width changes. The winding crack traverses weld toe of stud and stirrup hole，then propagates downwards along wed until the distance from top surface of flange is about 120 mm，at the same time the crack slants in direction of connection zone，but top longitudinal tensile reinforcements in beam 2 do not fracture.

Experiment phenomena of BC-2 are similar to BC-3，but its fatigue failure occurs in the section of beam 3 near connection zone. Compared with BC-3，because the concrete strength of beams in BC-1 has not reached design strength，surfaces of beams appear many tiny cracks. Fatigue failure occurs in the section of beam 1 near connection zone. In addition，during fatigue experiment process，cracks are not found around the web hole in beam 1 or 2，and the location of the hole is also far away from connection zone，so the construction detail has no effect on fatigue behavior of BC-1. The comparison of locations where top flange fractures is shown in Figure 3.
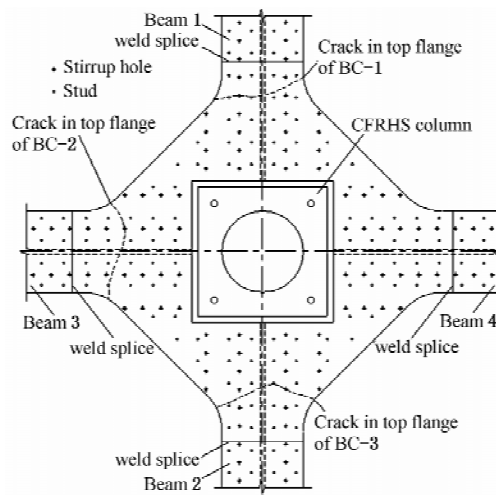
Figure 3　Location where H-shaped steel fractures in every connection

Analysis of Experiment Results

Strains of various materials and deflection of loading end 1 of beam 1 in BC-1

Final fatigue failure occurs in beam 1 of BC-1. In second stage fatigue experiment，the development situations of strains of various materials，deflection of loading end 1 and fatigue load with cyclic number are shown in Figures 4 to 6. What can be shown from Figures 4 to 6 are as follows：

(1) After cyclic loading of 3.1 million times，the strain of top longitudinal reinforcement Ba5 increases sharply to yield. It is indicated that adjacent top flange of H-shaped steel fractures suddenly because of unstable crack propagation.

(2) After cyclic loading of 2.74 million times before top flange fractures，the strain Ba1 in one side of adjacent top flange decreases gradually till zero and the strain Ba2 in the other side increases slightly，at the same time the strain Ba5 of top longitudinal reinforcement increases gradually and the strain Ba10 of

bottom concrete surface do not varies obviously. It is indicated that the crack is propagating from one side of top flange Ba1 to the other side of Ba2 gradually until it traverses the whole flange，and meanwhile，slow internal force distribution is caused mainly between top flange and top longitudinal reinforcements. During the process，the deflection of loading end 1 do not varies obviously and fatigue maximum load almost remains unchanged. It is indicated that the phenomenon of internal force distribution does not reduce the overall stiffness of BC-1.

（3）After top flange fractures，the strain Ba2 in the other side of adjacent top flange decreases gradually till zero due to release of internal force，the strain Ba5 of top reinforcement reaches and remains yield state，and the strain Ba10 of bottom concrete surface increases obviously. It is indicated that after the crack traverses the whole flange，beam 1 can be regarded as reinforced concrete（RC）beam and continues to bear loads. During the process，the deflection of loading end 1 increases obviously while maximum load decreases obviously. It is indicated that the overall stiffness of BC-1 decreases gradually.
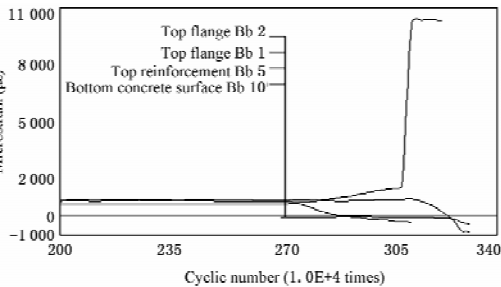
Figure 4　Development of strains of various materials in beam 1 with cyclic number in BC-1
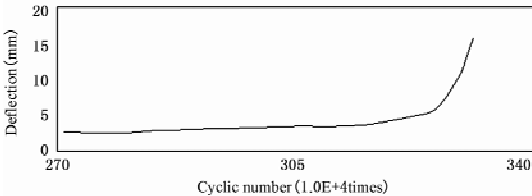
Figure 5　Development of deflection of loading end 1 with cyclic number in BC-1
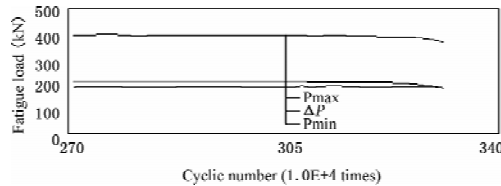
Figure 6　Development of fatigue load with cyclic number in BC-1
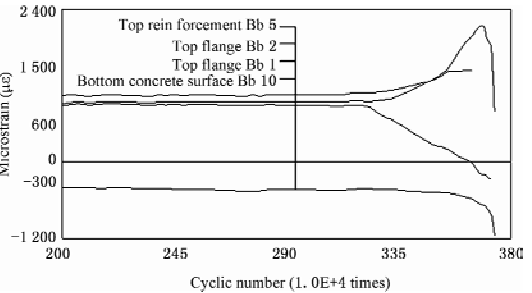
Figure 7　Development of strains of various materials in beam 2 with cyclic number in BC-3
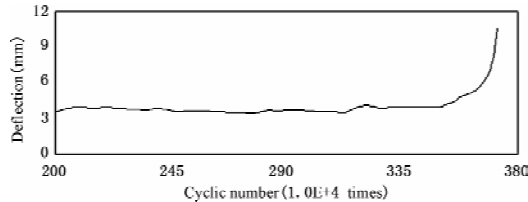
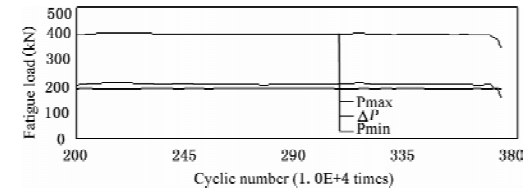Figure 8　Development of deflection of loading end 2 with cyclic number in BC-3

Figure 9　Development of Fatigue load with cyclic number in BC-3

Strains of various materials and deflection of loading end 2 of beam 2 in BC-3

Final fatigue failure occurs in beam 2 of BC-3. In second stage fatigue experiment，the development situations of strains of various materials，deflection of loading end 2 and fatigue load with cyclic number are shown in Figures 7 to 9. What can be shown from Figures 7 to 9 are as follows：

（1）When cyclic loading reaches 3.64 million times，the strain Bb5 of top reinforcement maximizes and then yields. It is indicated that adjacent top flange of H-shaped steel fractures suddenly.

（2）After cyclic loading of 3.23 million times before top flange fractures，the strain Bb1 in one side of adjacent top flange decreases gradually till zero and the strain Bb2 in the other side increases gradually，at the same time the strain Bb5 of top longitudinal reinforcement also increases gradually and the strain Bb10 of bottom concrete surface increases slightly. It is indicated that the crack is propagating from one side of top flange Bb1 to the other side of Bb2 gradually until it traverses the whole flange，and meanwhile，slow internal force distribution is caused mainly among top flange，top longitudinal reinforcements and bottom concrete. During the process，the deflection of loading end 2 increases slightly and fatigue maximum load almost remains unchanged. It is indicated that the phenomenon of internal force distribution does not reduce the overall stiffness of BC-3.

（3）After top flange fractures，the strain Bb2 in the other side of adjacent top flange decreases obviously due to release of internal force，the strain Bb5 of top reinforcement reaches and remains yield state，and the strain Bb10 of bottom concrete surface increases obviously. It is indicated that after the crack traverses the whole flange，fatigue damage accumulation of RC beam 2 aggravates. During the process，the deflection of loading end 2 increases obviously while maximum load decreases obviously. It is indicated that the overall stiffness of BC-3 decreases gradually.

Sign of Fatigue Failure

After top flange of H-shaped steel in certain beam of beam-to-column connection fractures，the connection isn't applicable in structural engineering bearing fatigue loads any more. Therefore，the fracture of top flange in certain beam can be regarded as the sign of fatigue failure of the connection，and the cyclic number at this moment can be regarded as its fatigue life. Fatigue life and total cyclic number of every specimen are shown in Table 3.

TABLE 3 FATIGUE LIFE AND TOTAL CYCLIC NUMBER OF EVERY SPECIMEN

Specimen number	First stage fatigue	Second stage fatigue		Fatigue life/E+4	Total cyclic number/E+4
	Actual number/E+4	Flange fractures /E+4	Actual number/E+4		
BC-1	200	109.5	131.0	309.5	331.0
BC-2	200	120.3	123.6	320.3	323.6
BC-3	200	164.2	173.4	364.2	373.4

Note：The column "Flange fractures" means the cyclic number when top flange in certain beam fractures.

CONCLUSIONS

According to two-stage constant-amplitude fatigue experiments of three beam-to-column connection

specimens，some conclusions can be drawn as follows：

(1) In first stage fatigue experiment of the specimen，crack width，strains of various materials and deflection of loading ends 1 to 4 do not increase obviously，the maximum crack width is less than 0.1 mm after cyclic loading of 2 million times and meets design requirement.

(2) At the end of second stage fatigue experiment of the specimen，top surface and two lateral surfaces of certain beam near connection zone craze severely and deflection of corresponding loading end becomes very large，as a result fatigue failure occurs. After the concrete is got rid of，top flange in certain beam fractures completely where flange width changes. The winding crack traverses weld toe of stud and stirrup hole，then propagates downwards along wed，at the same time the crack slants in direction of connection zone，but top tensile reinforcements in certain beam do not fracture.

(3) On the basis of experiment phenomena，the fracture of top flange of H-shaped steel in certain beam can be regarded as the sign of fatigue failure of the beam-to-column connection，and the cyclic number at this moment can be regarded as its fatigue life.

(4) Before top flange in certain beam fractures，when the crack is propagating from one side of top flange to the other side gradually，the strain in one side of top flange decreases gradually till zero and the strain in the other side increases gradually，at the same time the strain of top longitudinal reinforcements increases gradually and the strain of bottom concrete surface increases slightly. Internal force distribution is caused mainly among top flange，top longitudinal reinforcements and bottom concrete，but the overall stiffness of the specimen do not reduce obviously.

(5) After top flange in certain beam fractures，the strain of adjacent top flange decreases till zero，the strain of top longitudinal reinforcements reaches yield state，and the strain of bottom concrete surface increases obviously. Fatigue damage accumulation of certain beam aggravates，so the overall stiffness of the beam-to-column connection decreases gradually.

ACKNOWLEDGMENTS

REFERENCES

［1］Cai，J.，Zheng，Y.，Yang，C.，He，J. G. and Chen，H. F.，"An Experimental Study on the Box Steel Reinforced Concrete Beam"，Journal of South China University of Technology (Natural Science Edition)，2002，30(7)，pp. 52 – 56.

［2］Shao，Y.J. and Zhao，H. T.，"Comparative study on the calculation theory for the flexural capacity of steel reinforced concrete beams"，J. Xi'an Univ. of Arch. & Tech. (Natural Science Edition)，2006，38(3)，pp. 374 – 378.

［3］Liu，J. R.，Hu，X. M. and Xue，W.，"STUDY ON THE BOND-SLIP OF SRC STRUCTURES"，Steel Construction，2008，23(8)，pp. 26 – 30.

［4］Ministry of Construction of the People's Republic of China. "JGJ 138—2001 Technical specification for steel reinforced concrete composite structures"，Beijing：China Architecture & Building Press，2002.

［5］Izumi，M. and Yamadera，N.，"Behavior of Steel Reinforced Concrete Members under Torsion and Bending Fatigue"，International Association for Bridge and Structural Engineering，IABSE Symposium，Brussels，1990，vol. 60，pp. 265－266.

［6］Tong，L. W.，Chen，Y. Y.，Zhou，L. Y.，Xian，Q. J. and Xie，E.，"Fatigue experiment report of SRC beam-to-column connections in Shanghai hongqiao station of Beijing-Shanghai express railway"，Research Group for Steel and Lightweight Structures in Department of Building Engineering，Tongji University，2009.

［7］Zhou，L. Y.，"Experimental Study on Fatigue Behavior of Steel Reinforced Concrete（SRC）Girders and Connections for Beijing-Shanghai Express Railway"，Master dissertation of Tongji University，2009.

APPLICATION PROGRESS OF FIBER REINFORCED PLASTICS IN CIVIL ENGINEERING

* K. Fu and W. Wang

Department of Building Engineering，Tongji University，Shanghai，200092，China
* Email：eric. fukai@gmail. com

KEYWORDS

Fiber reinforced plastics，decks，composite structures，bridges.

ABSTRACT

FRP（Fiber Reinforced Plastics），with its high strength，small specific gravity，high resistance to corrosion and chemical as well as the advantages of ease in fabrication，manufacturing，handling，and erection are attracting more and more attention as a new structural material in civil engineering and has been widely used. In this paper，an introduction is given on the properties and different forms of FRP and the application progress of FRP bridge decks and FRP tendons are introduced.

Fiber reinforced plastics（FRP）from the 20th century，40 years since the advent of aviation，aerospace，automotive，chemicals，machinery，and other fields of medicine and a wide range of applications. In recent years，FRP materials for its high strength，small specific gravity，good corrosion resistance as well as the advantages of good design more and more attention by the engineering profession to become a new type of civil engineering structural material（Bakis[1] and Douglas[2]）. The main products include FRP materials：FRP tendons，FRP plates，FRP sheets and FRP profiles.

APPLICATION PROGRESS OF FRP BRIDGE DECKS

FRP bridge decks have significant advantages：① light weight. The weight of hollow FRP bridge deck panels or sandwich is about 20% to 40% of the weight of conventional concrete bridge deck. FRP bridge decks which used instead of the traditional FRP bridge decks or bridge deck concrete bridge deck，can improve the carrying capacity of the bridge；② anti-fatigue performance. The general strength of the metal fatigue tensile strength of 40% to 50% while 70%～80% for FRP materials；③ excellent chemical resistance. FRP bridge deck has a good ability of acid，alkali，salt and other chemical erosion which can be applied to the bridge construction in special environment；④ to facilitate construction. FRP bridge decks can be manufactured in the factory，on-site installation. Because of its light weight，even without lifting equipment and heavy machinery，pedestrian bridge has been built abroad（Fu[3] and Bank[4]）.

Application Progress of FRP Bridge Deck System

FRP bridge deck system from the structural form can be divided into two types: one is the bridge plate,
that is the direct use of FRP bridge decks leap; the other is the beam bridge, FRP bridge decks will be
shelved in the steel beam or concrete beams, can also with FRP beam or FRP composite beam. FRP
bridge deck system can also be used to repair the old bridge, on the one hand reduce the structural
weight, even improve the load rating, and the other hand enhance the corrosion resistance of the bridge
structure.

In 1990, an all FRP test bridge was built in Japan (shown in figure 1). Columns, beams, slabs and
handrails were made of GFRP pultrusion profile, CFRP sheet was used for local strengthening, inclined
cables were made of CFRP and foundation was made of concrete (Xue[5]).

Figure 1   FRP bridge in Japan

Figure 2   Aberfeldy bridges

In 1992, an all FRP cable-stayed pedestrian bridge was built in Britain (shown in figure 2). Box section
GFRP pulltrusion profiles were applied in bridge towers, beams, decks and handrail. Inclined cables were
made of AFRP. This was the first all FRP structural bridge all over the world (Thornburrow[6]).

In 1997, Pontresina, Switzerland's scenic spots built a full-GFRP footbridge. The bridge which is two-
span continuous truss span of 12.5 m, width of 1.50 m, the design live load 5 kN/m², made by bonding
GFRP pultruded profiles. It is very easy installation and removal for its light weight, so it can be installed
in the tourist high season, and up in low season (Ye[7]).

In 2008, the United Kingdom has been located across the railway line Standen Hey bridge deck
replacement for the whole FRP bridge decks dealers. The bridge became the first all-FRP bridge deck
Dealers Bridge (Hollaway[8]).

In 2009, Haibo Si shows a strong company with 200 tons of large FRP composite materials pultrusion
technology, color footbridge (shown in figure 3) in 12th Beijing High-Tech meeting. The bridge is
currently located in Shanghai Normal University.

In order to repair and reinforce activities of the world's seventh largest bridge - Broadway Bridge (shown
in figure 4), the engineers used Dura Span FRP bridge deck panels replaced the original steel bridge

（Xue[5]）.

Figure 3   FRP color footbridge

Figure 4   Broadway Bridge

Application Progress of FRP-concrete Composite Bridge

FRP-concrete composite beam（slab）was a reasonable FRP-concrete composite structure style，it can take fully used of high tensile strength，good durability of FRP and high compressive strength of concrete.

In 1994，Bond Mill Bridge（shown in figure 5）which was built by the use of a combination of GFRP pultruded profiles in Britain. The length of bridge is 8.22 m，wide of 4.27 m，and the six FRP box beam composed of beam 0.85 m（Hollaway[9]）.

Figure 5   Bond Mill Bridge in Britain

Figure 6   FRP Highway Bridge in Australia

In 2003，Australia's first FRP bridge（shown in figure 6）was built，its design concept from the traditional plank bridge design patterns，stringer for the pultruded GFRP-concrete composite beams，concrete thickness of 100 mm，total height box beam 350 mm. Compared with the traditional bridge，the bridge saves 90% of the traffic control costs；construction took only 5 days，while ordinary bridge will need 8-10 weeks；save transport costs by 75%（Van[10]）.

In 2003，a bridge span of 21.3 m combination - Fairfield Bridge was built in Maine States，which substructure using FRP profiles，the upper pouring concrete，set at the interface of the shear key spacing 152 mm. Panoramic view of the bridge and the bridge cross-section dimensions as shown in Figure 7

（Xue[5]）.
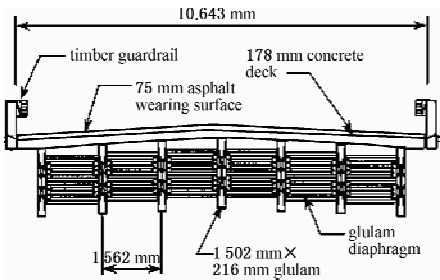
Figure 7   Fairfield Bridge in the USA

APPLICATION PROGRESS OF FRP TENDONS

FRP tendons in civil engineering applications can be summarized as follows: as the enhancement tendon in concrete structures, as prestressed reinforcement for prestressed concrete structures, as the main cable bridge force bearing structures（Mei[11]）.

FRP Tendons As the Enhancement of Reinforced Concrete Structures

Replacement of reinforcement tendons in reinforced concrete structures, mainly for erosion of environmental conditions, the use of FRP tendons with excellent corrosion resistance characteristics, to improve durability of the structure.

FRP reinforced concrete structures has many applications in foreign countries, the United States' first bridge using CFRP tendons for the Bridge Street Bridge, Michigan（Bridge Street Bridge）, the main beams and bridge deck, respectively, in the use of non-prestressed reinforcement Linear grid CFRP reinforcement and tendons.

In 1988, Japan adopted the construction of CFRP tendons that Mia St. Bridge（shinmiya）, the bridge width 7.0 m, a span of 5.76 m（Zeng[12]）.
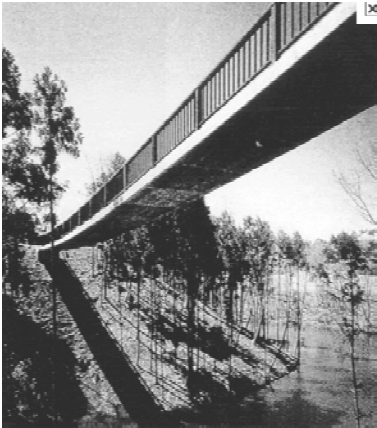
Figure 8   Shinmiya bridge in Japan

In 2002，Morristown Bridge was built in Vermont（shown in figure 9）. Top and bottom of the bridge deck in two horizontal directions were configured in the GFRP bar diameter of 19 mm，the short side direction of GFRP tendons spaced 100 mm，the long side direction is 150 mm. Morristown Bridge did not use any reinforcement，is the first full-GFRP reinforced concrete bridge deck project（Feng[13]）.

Figure 9   Morristown Bridge in the USA

In the municipal tunnel project（shown in figure 10）in 2010 Shanghai Expo area which is responsible by Tongji University，GFRP tendons is used in part of the tunnel section instead of steel as its good resistance of corrosion（Hu[14]）.
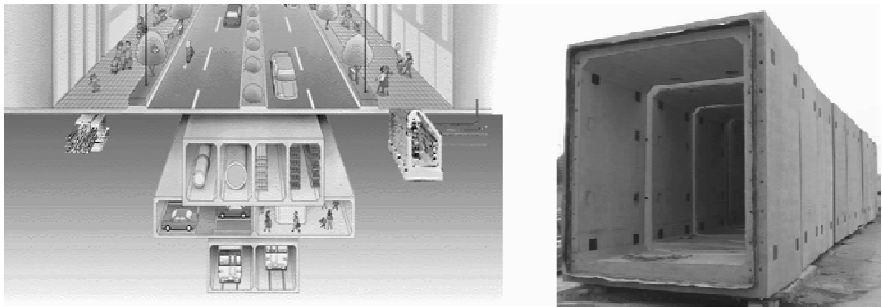
Figure 10   Precast municipal tunnel sketch

FRP Tendons As Prestressed Reinforcement For Prestressed Concrete Structures

To take full advantage of the strength characteristics of FRP tendons，FRP tendons can be used as prestressed reinforcement for prestressed concrete structures. Currently，the application of FRP tendons as prestressed reinforcement in interior is relatively larger than as the application of external prestressed reinforcement.

Japan is the country which is the first use CFRP wire and AFRP tendons as prestressed reinforcement in concrete bridge. From 1989 to 1992，Japan had developed the application of FRP materials as concrete bridge tendons of the necessary technology，different types of FRP tendons were experimental studied and had completed the required anchorage system. These results were used to develop FRP reinforced concrete bridge design and construction guidelines（Zhang[15]）.

In 1989，a footbridge was constructed with post-tensional double T type continuous beams and seven

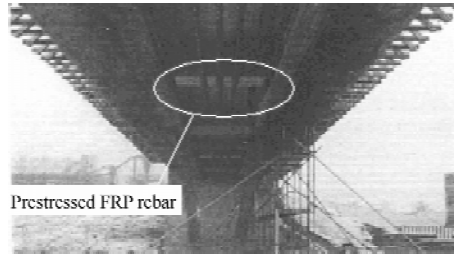external prestressed FRP tendons in Germany(shown in figure 11).

Figure 11   Eadolf‐Berlin Arequipa Stewart footbridge

Street Bridge，the first prestressed FRP reinforcement bridge（shown in figure 12），was designed by Grace etc. under the background of cooperation of US and Japan in 2002.
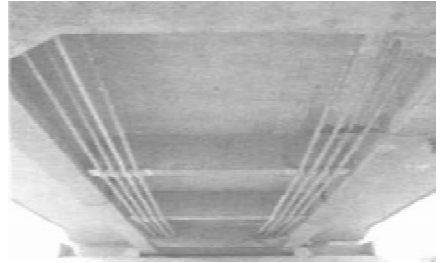

Figure 12   Street Bridge　　　　　　　　**Figure 13   He Wei Bridge**

In 2006，China's first bridge He Wei Bridge（shown in figure 13）which is use of CFRP tendons as prestressed reinforcement was built in Jiangsu province（Wang[16]）.

FRP Tendons As the Main Force Component For Cable Supported Bridge

In cable supported bridge（including suspension bridges，cable-stayed，tied arch bridge）in the main cable，cable-stayed，and the cable boom and other materials used in FRP reinforcement can improve the durability of the cable，and enhance efficiency and increase the bridge carrying bridge span. Currently，foreign CFRP cable-stayed bridge in the research more，and there are many medium and small span of the FRP bridge application.

In 1986，in Dusseldorf，Germany built a PC with a glass fiber reinforced plastic cable Highway Bridge，the world's first use of the noose of post-tensioned FRP highway bridge（Zhou[17].）

Denmark's first large-scale bridge using CFRP materials for the construction of Heming bridge with length of 80 m，which is used in all so far the longest completion of CFRP cable-stayed bridge.

In 2005，Southeast University designed and built China's first high-performance CFRP cable stayed bridge（total length of 51.5 m），the bridge span of 30 m ＋18.4 m，width of 6.8 m，concrete single and double cable planes inclined tower Bridge，pier beam consolidation system using tower，tower 4 on each side of the layout of cables，cable with Lead line CFRP cable（Mei[18]）.

Figure 14　China's first high-performance CFRP cable stayed bridge

CONCLUSIONS

In summary，FRP materials has been widely applied in civil engineering，especially in bridge engineering，and FRP materials have great potential for use in infrastructure and other civil engineering applications，the advantage of FRP materials has been understood by engineers and technicians，but there are still some pending further works，including：

(1) FRP technology standardization work；

(2) FRP Laminates reinforced structure form and technology work（including concrete structure、Masonry structure、wood structure and steel structure）；

(3) Studies on structure performance、anchorages technology and construction technology for FRP tendons reinforced concrete structure；

(4) Studies and application of FRP—concrete composite structure in long span bridge；

(5) Application of high performance FRP in Intelligent structures.

REFERENCES

［1］Bakis，C.，"Fiber-reinforced polymer composite for construction state-of-art-review"，Journal of Composite for Construction，ASCE，2002，6(2)，PP. 73–87.

［2］Douglas，A.，"An all fiber-reinforced-polymer-composite bridge：design，analysis，fabrication，full-scale experimental structural validation，construction and erection"，Newark：Central for Composite Materials，University of Delaware，2001.

［3］Fu，H.X. and Xue，Y.D.，"Research of Pultruded FRP Bridge Deck. Fiber Reinforced Plastics/Composite"，2003，(6)，pp.45–48.

［4］Bank，L.C. and Xi.Z.，"Pultruded FRP grating reinforced concrete slabs. Fiber-Reinforced Plastic for Concrete Structures — Int. Symposium"，A. Nanni and C. W. Dolan，eds.，SP-138，American Concrete Institute，Farmington Hills，Mich.，1993，pp.561–583.

［5］Xue，W.C. and Zhang，S.L. "Sate-of-art-report on field applications of the FRP bridge decks"，Proc. 11th Conference on Applications and development FRP，Da Lian，2006，pp.197–202.

［6］Thornburrow，P.R.，"Working together to build bridges". In：Antonio Miraveteed. Proceedings of ICCM/9. Madrid：University of Zaragoza，Wood-head Publishing Limited，1993，pp.200–207.

［7］Ye，L.P. and Feng，P. "Applications and development of fiber-reinforced polymer in engineering structures". China Civil Engineering Journal，2006，(3)，pp. 24–36.

［8］Hollaway，L.C.，"A review of the present and future utilisation of FRP composites in the civil infrastructure with reference to their important in-service properties". Construction and Building Materials，2010，24(12)，pp.2419

-2445.

［9］Hollaway，L. C.，"The evolution of the way forward for advanced polymer composites in the civil infrastructure"，the International Conference on FRP Composites in Civil Engineering. Hong Kong：Elsevier Science Ltd，2001，pp.27-40.

［10］Van，Erp，Gerard and Cattell，Craig and Ayers，Stephen.，"A fair dinkum approach to fibre composites in civil engineering"，Construction and Building Materials，2006，20（1），pp.2-10.

［11］Mei，K.H.，"Introduction and review of FRP applications in bridge engineering"，Journal of China & Foreign Highway，2007，（7），pp.12-15.

［12］Zeng，X. T. and Che，H. M.，"Application of FRP Composite Material to Bridge Works and its Prospect". Bridge Construction，2000，（2），pp.66-70.

［13］Feng，P. and Ye，L. P.，"Review and new proposals for performance indices of flexural members"，8th International Symposium on Structure Engineering for Young Experts. Science Press，2004，pp.121-130.

［14］Hu，X. and Xue，W. C.，"Experimental study of mechanical properties of PPMT"，China Civil Engineering Journal，2010，43(5)，pp.29-37.

［15］Zhang，Q. and Zhu，H. M.，"Application of FRP Composite Material to Japan's prestressed concrete bridge construction and other constructions"，World Bridges，1996，（4），pp.31-35.

［16］Wang，P.，Ding，H. S. and Lü，Z. T.，"Application study of external prestressing by CFCC in bridge"，Journal of Southeast University（Natural Science Edition），2007，37(6)，pp.1061-1065.

［17］Zhou，L.，"Application of FRP to prestressed concrete"，World Bridges，1994，（1），pp.52-55.

［18］Mei，K.H. and Lü，Z. T.，"Static characteristic analysis of CFRP cables"，China Journal of Highway and Transport，2004，17(2)，pp.43-45.

EXPERIMENTAL STUDY ON FRACTURE TOUGHNESS OF BUTT WELD OF Q460C HIGH-STRENGTH CONSTRUCTION STEEL

Y.Q. Wang[1]，[*] Y. Lin[2]，Y.N. Zhao[2]，Y.J. Shi[1]

[1] Key Laboratory of Civil Engineering Safety and Durability of China Education Ministry，
Tsinghua University，Beijing，100086，China
[2] School of Civil Engineering，Shenyang Jian Zhu University，Shenyang，
Liaoning，110168，China
[*] Email：never－flinch_ly@163.com

KEYWORDS

Q460 steel structure，low temperature，fracture toughness，butt weld，heat affected zone，crack tip opening displacement（CTOD）.

ABSTRACT

Weld directly affects their fracture toughness of welded steel structure，causing its heat affected zone becoming a weak link in the fracture especially at the low temperature. In this paper，a three-point-bending fracture toughness test of weld zone and that of heat affected zone of 14 mm thick Q460C constructional high-strength steel at distinct low temperature is determined. And the values of CTOD for weld zone and heat affected zone of Q460C steel are obtained. Then making use of a regression analysis with Boltzmann equation，the ductile-brittle transition temperature and variation with temperature are acquired. Furthermore analyze the scanning electronic microscope of the TPB specimen fracture surfaces with five temperature points. And the results show that low temperature impacts the fracture toughness of Q460C steel in a large part；with the temperature dropping，there is a downward trend on the fracture toughness. Compared with the CTOD of base metal Q460C，that of its weld zone is unstable and that of its heat affected zone is at lowest. The ductile-brittle transition temperature for weld zone of Q460C is around－53.6℃，that for its heat affected zone of Q460C is about －40.3℃. Besides，the fracture appearances of TPB specimens of weld zone and heat affected zone of Q460C，which fractured at －20℃ have already shown their brittle characteristics significantly.

INTRODUCTION

High strength steel structure，mostly as large-scale welding structure，from chemical petroleum engineering to bridge construction project，from ancient times to modern times，home and abroad，it was obtained widespread application gradually. But due to the increased intensity of steel plate and its attachment weld，effects of stress concentration，complicated stress and strain condition，and crack

sensitivity increasing rapidly，it was easy to brittle fracture；Simultaneously since the welding process and quality got bad in the attachment weld，it also resulted in initiation of the brittle crack and going on expanding. Besides，the heat affecting from welding produces of high strength steel structure will make the welded joint and the nearby steel plates properties bad，and produce crack after weld cooling[1-5]. There is large area of cold region in domestic land springing up the high strength steel structure with its welding structure members. Therefore it was significant to research the fracture toughness property of high strength steel structure and its welded joint. Then experiment of fracture toughness parameter and the fracture behavior of the butt weld of Q460C high strength structure steel was carried out in this article under low temperature，and crack tip opening displacement（CTOD）of three point bending（TPB）specimen was selected as the index of fracture toughness. For obtaining regularity for change of the CTOD value with low temperature changing and tough-brittle transition characteristic，it was required to get samples with the position vertical to the direction of the welded steel plate and be executed at the different low temperature spots.

OVERVIEW OF THREE POINT BENDING TEST

Material and Method

According to GB 4161—2007 Metallic Materials-determination of Plane-strain Fracture Toughness and GB/T 21143—2007 Metallic Materials-unified Method of Test for Determination of Quasistatic Fracture Toughness，which are test standards in Chinese，three point bending（TPB）test of weld zone and heat-affected zone（HAZ）specimen of Q460C(14 mm at thickness) steel was carried out at five temperature points containing respectively 20℃，0℃，－20℃，－40℃ and －60℃. Selected fifteen samples each other，three at each temperature point，and thirty samples were selected in all. Q460C steel，the high-strength construction-structure steel，the newly developed steel at home presently，was delivered at rolling status. Moreover，their technical conditions were in line with GB／T 1591—2008 "high-strength low-alloy structural steel," carbon equivalent Ceq was equal to 0.468%，and the main chemical components were as Table 1.Welded specimens adopted full penetration gas shielded arc welding with V-groove，whose welding procedure had been assessed. Parameters of the welding procedure were shown in Table 2，sizes of butt weld zone and heat-affected zone samples were shown in Figure 1（a）and（b）respectively，and sizes of TPB specimen were shown in Figure 1（c）. Make sure that center line of gap of weld zone sample and geometric centre line of the sample overlap. Furthermore，make the center line of gap of heat-affected zone specimen five millimeter distance from the vertical beveled edges，and ensure that the crack was in base steel district.

TABLE 1 CHEMICAL COMPOSITION OF Q460C STEEL / %

Carbon	Sulfur	Phosphorus	Silicon	Manganese	Copper	Aluminum	Nickel	Vanadium	Chromium
0.190	0.004	0.013	0.220	1.510	0.070	0.035	0.030	0.045	0.050

TABLE 2 PARAMETER OF WELDING PROCEDURE / %

welding method	welding position	welding wire type	Gas and welding flux	Diameter of welding wire/mm	electricity /A	Voltage /V	Velocity cm/min
gas shielded arc welding	downhand welding	JM-60	CO220% + Ar80%	φ1.2	250-300	28-35	30-45

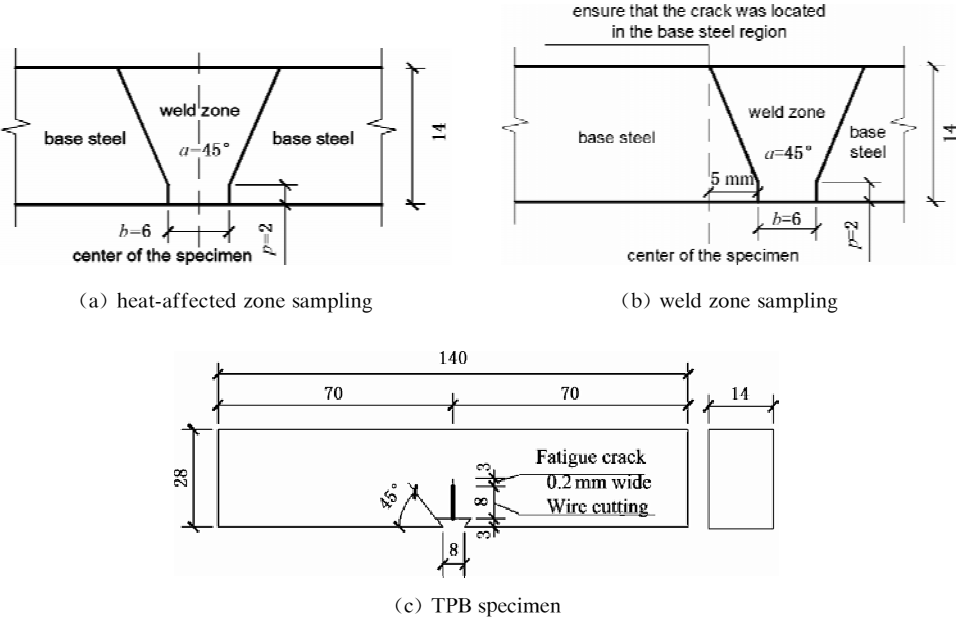（a）heat-affected zone sampling　　　　　（b）weld zone sampling

（c）TPB specimen

Figure 1　The size of sampling and TPB specimen

The Device Equipment

Three point bending test was took in the incubator to cool the tensile specimen through steaming a mixture of liquid nitrogen and air. Test performed in the Strength Mechanical Laboratory of the School of Aerospace of Tsinghua University，which has a full set of low-temperature three point bending test equipment，and "INSTRON" type of fatigue tester to create pre-fatigue crack.

EXPERIMENTAL RESULT

Trend of the CTOD Value Responding to the Temperature Change

The maximum upload CTOD value δ_m was adopted as the CTOD representative value. And the δ_m value can be utilized under a series of fractures. It can be measured precisely and had low discreteness. And it is also easy to be compared and analyzed. The CTOD values for experiment results of weld zone and heat affected zone specimens of Q460C the high-strength steel were plotted as in Figure 2（a）and（b）respectively.

（1）Except discrete value at −40 ℃，CTOD value of weld zone of Q460C steel decreased with temperature decreasing，which can be seen from Figure 2（a）.（2）The CTOD value almost presented linear decrease from 0℃，observed in Figure 2（b）. The minimum value measured at −60 ℃ was 87.84% less than the maximum value measured at 0 ℃. That had finished the switch from the plastic fracture to the brittle fracture. It can be deduced that low temperature had a negative impact on the fracture toughness of heat affected zone of Q460C steel. CTOD value at 20℃ was a bit lower，probably owing to inherent defects in the weld zone or complex force characteristics of heat affected zone.
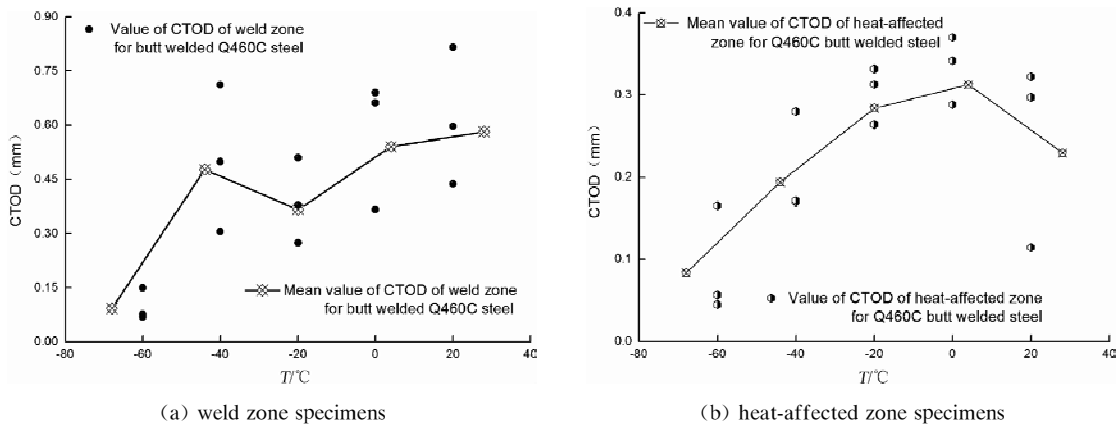
(a) weld zone specimens   (b) heat-affected zone specimens

Figure 2   Trend of CTOD value with temperature

Compared with Base Metal of Q460C Steel

The CTOD value δ_m of weld zone specimens，heat affected zone specimens of Q460C butt welded steel and base metal specimens of Q460C steel were Compared and analyzed[6]． The experiment data was plotted in Figure 3.
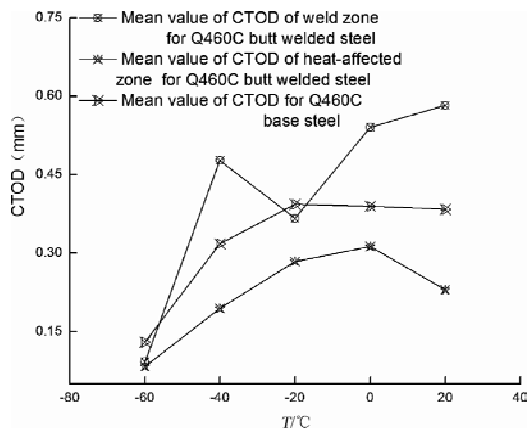

Figure 3   Comparison of CTOD value of weld zone with heat-affected zone and base steel

Figure 3 showed that the lowest CTOD value of Q460C steel was the value of welding heat affected zone，and that of weld zone was higher than the base metal on the whole． However，from－40 ℃ to－60 ℃，the decreasing amplitude of that value of weld zone was significantly greater than the other two． It indicated that low temperature influenced the toughness of weld zone of Q460C steel to a great degree，which made fracture toughness of heat-affected zone of Q460C welded steel relatively worst．

Brittle Transition Temperature

Because of dispersion of the experimental data was great，by fitting with an appropriate function to attain brittle transition temperature of weld zone and heat-affected zone samples was more reasonable． Using the form Eq. 1 of the Boltzmann function to analyze the dependence of the fracture toughness on

temperature，smaller residuals and better correlation can be achieved，and the physical meaning of each parameter was well described[7, 8].

$$\delta = \frac{\delta_1 - \delta_2}{1 + e^{(T-x_0)/dx}} + \delta_2 \qquad (1)$$

In Eqn. 1，δ represented CTOD value，T as temperature，δ_1(mm) as down-platform energy，δ_2(mm) as up-platform energy，x_0(℃) as transition temperature of toughness-brittleness，and dx（℃）as range of transition temperature. When the value of dx decreased，the more narrow range of transition temperature became，the much easier changed from plasticity to brittleness for steel's property. Test results showed in Figure 4 were analyzed with regression by using Boltzmann function. The fitting results were well consistent with regression coefficient，which were shown in Table 3 and the fitting function curve of the weld zone and the heat-affected zone was shown in Figure 4.

TABLE 3　PARAMETERS OF BOLTZMANN FUNCTION

Type of sample	Parameters for Boltzmann			
	δ_1	δ_2	x_0	dx
Weld zone	2.16	0.50	− 53.58	4.52
HAZ	0.08	0.27	− 40.28	0.89
Base steel	0.13	0.39	− 40.94	0.97
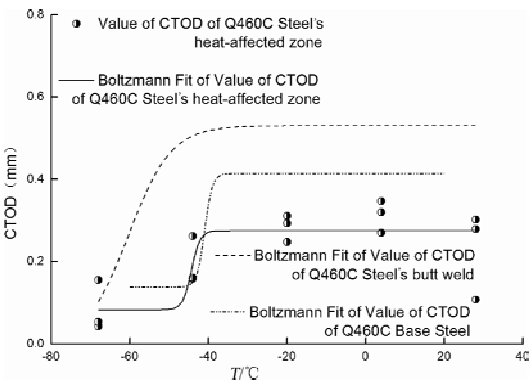
Figure 4　Value of weld zone，heat-affected zone and base steel with its Boltzmann fitting curve

（1）Compared to the base metal and the heat affected zone（the CTOD value of base metal of Q460C steel was researched by paper[6]），the platform energy of the weld zone was greater as well as larger for range of transition temperature，while the lower for ductile-brittle transition temperature，which was -53.58 ℃，which was shown in Table 3. It indicated that the properties of fracture toughness of weld zone for Q460C welded steel itself was not a controlling factor. （2）Figure 4 can be observed that heat-affected zone of Q460C welded steel showed relatively poor fracture toughness property. Besides the value of platform for the heat-affected zone was lower，and the transition temperature range was smaller than the base metal，while the ductile-brittle transition temperature，which was − 40.28℃ was higher than that of base metal，which was − 40.94 ℃. It further conformed that the fracture toughness of heat-affected zone of Q460C welded steel had deteriorated，which was the weakest link.

Scanning Electronic Microscope of Fracture

In order to obtain a preliminary understanding of the fractures，macro-analysis of them was necessary，

but for intensive study，micro-structure analysis of fracture was indispensable and important. The fractography of three-point bending specimen of welded Q460C steel was observed by scanning electronic microscope（SEM）shown in Figure 5 which were specimen of weld zone，and that of heat-affected zone were shown in Figure 6 These taken photographs were near the center part of the fracture with amplification of 300 and 2 000 times，respectively.
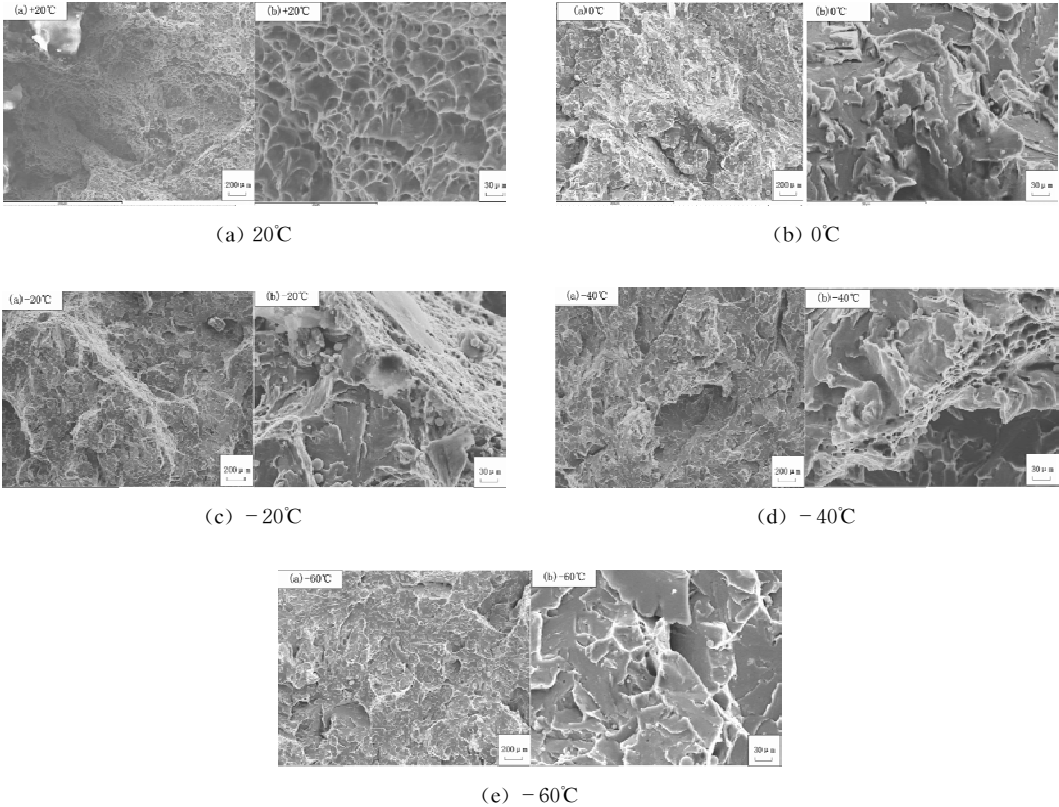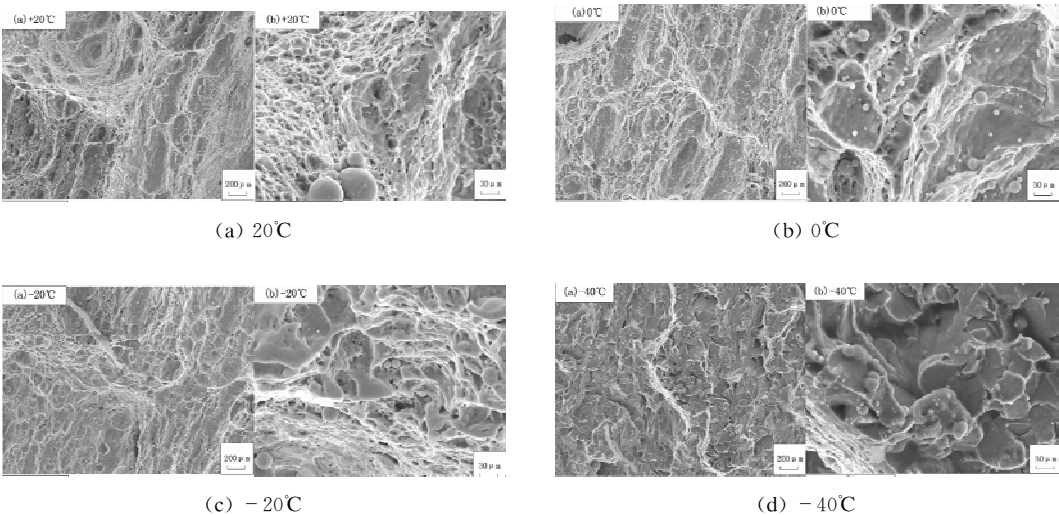

（a）20℃   （b）0℃

（c）－20℃   （d）－40℃

（e）－60℃

Figure 5   Scanning electron micrographs of fracture surface of weld zone at 5 temperature points

（a）20℃   （b）0℃

（c）－20℃   （d）－40℃

（e）－60℃
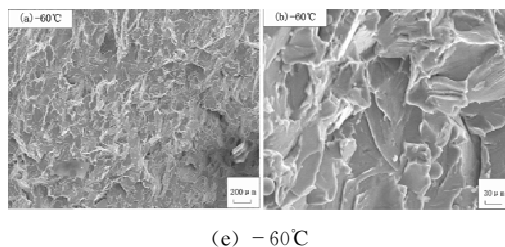
Figure 6   Scanning electron micrographs of heat-affected zone at 5 temperature points

（1）Figure 5 and Figure 6 showed that the fracture appearance of weld zone as well as heat-affected zone for Q460C steel had a large number of torn edges and dimples at 20℃. Dominated by ductile deformation，they took on transgranular fracture at room temperature.

（2）The shapes of stripes of fractures were mainly like river pattern and cleavage steps at －60℃，which turned on the significant property of brittle fracture along the grain at low-temperature，where plastic deformation was extremely small.

（3）With the temperature declining，the quantity of torn edges and dimples of weld zone as well as heat-affected zone of fracture surface was decreasing；besides the toughness deformation became smaller and smaller，where the brittle characteristic was increasing.

Summary and Conclusions

（1）The value of CTOD of weld zone of Q460C steel was fluctuated，which reflected the instability of its fracture toughness to low temperature changing. And that value of heat-affected zone was relatively lower than that of base steel，which signified that as weak links，weld heat-affected zone of Q460C steel deteriorated its performance，whose toughness was gradually brittle at low temperature. As a whole，the CTOD values both showed the trend of decreasing，having worse fracture ductility with temperature declining.

（2）The result of Boltzmann function fitting showed that ductile-brittle transition temperature of heat-affected zone was highest，compared with that of base Q460C steel，that of weld zone was higher，so that heat-affected zone of Q460C steel more easily transformed to brittle form toughness.

（3）SEM analysis showed that，specimen fracture of weld zone and heat affected zone which ruptured at －20 ℃，appeared a mechanism of quasi-cleavage fracture，where there was plastic deformation mixed with brittle deformation；While temperature fell to －40 ℃，the fractures presented characteristics of brittle cleavage fracture.

ACKNOWlEDGEMENT

REFERENCES

［1］Shi，G. and Shi，Y. J.，"Engineering Application of Ultra-high strength steel"，Progress in Steel Building

Structure，2008，10(4)：pp.32-38.

［2］Heinila，S. and Marquis，G. B.，"Observations on Fatigue Crack Paths in the Corners of Cold Formed High Strength Steel Tubes"，Engineering Fracture Mechanics，2008，75：pp.833 – 844.

［3］Wang，Y. Q. and Lin，Y.，"Experimental study on the mechanical properties of Q460C the high strength construction steel at low temperature"，Journal of Shenyang Jianzhu University (Natural Science)，2011，27(4)：pp. 646-652.

［4］Lin，Y. and Wang，Y.Q.，"Progress on research of high-strength steel and weld fracture toughness"，Steel，2010 (Supplement)：pp.105-114.

［5］Günther H. P.，"Use and application of high-performance steels for steel structures"，International Association for Bridge and Structural Engineering (IABSE)，2005，vol. 8.

［6］Wang，Y. Q. and Lin，Y.，"Experimental study on the fracture toughness of Q460C the high-strength construction steel at low temperature"，Applied Mechanics and Materials，2011，vol.71-78，pp. 890-897.

［7］Zhao，J.P. and Zhang，X.M.，"On the method of data processing for ductile-brittle transition temperature"，Petro-chemical Equipment，2004，33(4)：pp.29-32.

［8］Wu，Y.M. and Wang，Y.Q.，"Effects of low temperature on properties of structural steels"，Journal of University of Science and Technology Beijing，2004，11(5)：pp. 442-448.

THE ANALYSIS ON MECHANICS PERFORMANCE OF CFRP LAMINA REINFORCE IN MULTI-FUNCTION BRIDGE UNDER HIGH TEMPERATURE ENVIRONMENT

* X. Yuan[1, 2], J. W. Zhang[1], S. T. Song[1] and Z. P. Feng[1]

[1] College of Civil Engineering，Southeast University，Nanjing，210096，China
[2] College of Civil Engineering，Panzhihua University，Panzhihua，617000，China
* Email：yuanxin9988@163.com

KEYWORDS

High temperature effect，reinforcement，CFRP，SMA，static test，fatigue test.

ABSTRACT

The length of Bangabandhu bridge in Bangladesh is 4 800 m，which is a cross section of continuous box girder multi-function bridge，with the highway，railway and power line transiting it. In the influence of the frequent drought and tropical cyclone such as various climate disaster，as the surface temperature stress which lead to the Bangabandhu bridge deck appear longitudinal crack. Grouting epoxy resin on the Bangabandhu bridge is made after the restoration，the preliminary design for the bridge deck crack is to coat with CFRP lamina in transverse in order to constraint the longitudinal cracks development. It is made level up layer，waterproofing，insulating layer and 5 cm thick Matrix Asphalt（SMA）with a wear protection layer and providing corrosion resistant layer. It is the first time so large area CFRP lamina pasted on bridge panel and the construction of Matrix Asphalt layer in the world. In order to research the rationality of the design scheme and durability of new part after reinforcement of CFRP lamina on multi-function box girder-bridge under the environment of high temperature. The effective simulating test is made to study the mechanics performance of CFRP lamina reinforcement on multi-function box girder-bridge under the environment of high temperature according to the design scheme.

OVERVIEW

The bridge is completed in June 1998 in Bangladesh. At that time it was the world 11th longest bridge，while now which is the sixth longest bridge in South Asia. This bridge is located at between the Asian highway and the Trans-Asian railroad，which uninterruptedly communicates northeast Central Asia and Europe's transportation. The bridge was open to traffic，in which there was many obviously crack. The lapse of time，the quantities，the length and the width of crack were expanding.

In the influence of the frequent drought and tropical cyclone such as various climate disaster，as the surface temperature stress which lead to the Bangabandhu bridge deck appear longitudinal crack. Grouting epoxy resin on the Bangabandhu bridge is made after the restoration，the preliminary design for

the bridge deck crack is to coat CFRP lamina in transverse in order to constraint the longitudinal cracks development. It is made level up layer，waterproofing，insulating layer and 5 cm thick Matrix Asphalt （SMA）with a wear protection layer and providing corrosion resistant layer. It is the first time so large area CFRP lamina pasted on bridge panel and the construction of Matrix Asphalt layer in the world. In order to research the rationality of the design scheme and durability of new part after reinforcement of CFRP lamina on multi-function box girder-bridge under the environment of high temperature. The effective simulating test is made to study the mechanics performance of CFRP lamina reinforcement on multi-function box girder-bridge under the environment of high temperature according to the design scheme.

REINFORCEMENT DESIGN SCHEME

Section of rectangle beam size is length × width × highly ＝4 000 mm×650 mm×280 mm. CFRP plate specification：1.4 mm（thickness）× 100 mm（width）. The detail of reinforcement design is shown in Figure 1.
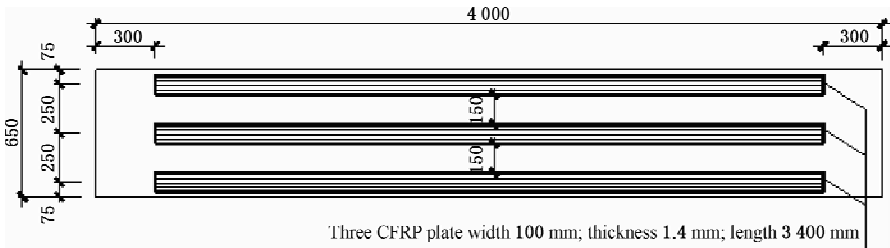
Figure 1   Planar graph of CFRP reinforcement design（mm）

Steel Rebar and Concrete

The design concrete of Test slab is C45，of which the steel rebar in the tension zone is HRB400 with the diameter of 12 mm while the steel rebar in pressure area is HRB400 with the diameter of 12 mm.

CFRP and Adhesive

The main performance index of CFRP and adhesive is shown in Table 1 and Table 2.

TABLE 1   MAIN PERFORMANCE INDEX CFRP

Thickness（mm）	Longitudinal strength（MPa）	Tensile modulus（GPa）	Elongation at break（%）
1.4	≥2 300	≥150	≥1.4

TABLE 2   MAIN PERFORMANCE INDEX OF CFRP ADHESIVE

model	Tensile strength（MPa）	Tensile elastic modulus（MPa）	Bending strength（MPa）
K-801	≥25	≥2 500	≥30

REINFORCEMENT DESIGN SCHEME

This test takes the method of two points of symmetric loading to observe the bearing capacity improving
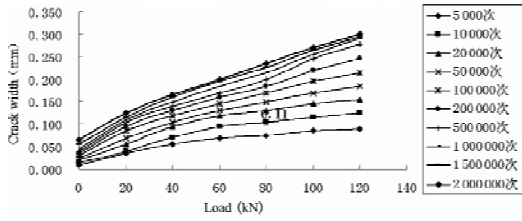
**Figure 8　Extending of the cracks along
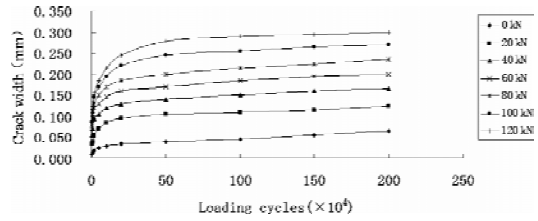with the loading increase**

**Figure 9　Extending of the cracks along
with loading times increase**

According to the Figure 8 and Figure 9，the cracks of CFS-N‑10 beam increase gradually as loading increase and loading times increase. The cracks increase faster in initial loading stage while increase relatively slow in later stage. After the fatigue load level which are 120 kN are carried on 2 million time，the maximum crack is 0.3 mm.

Cracks appear very early in where the moment is MAX，and in the original damage position cracks appear in the first. Because of the constraints of CFRP plate the cracks extension are relatively slow，after unloading the cracks will basic closed. The space of cracks are small，while the amount is more. According to above figure，the cracks increase faster in initial loading stage while increase relatively slow in later stage. After the fatigue load level which are 120 kN are carried on 200 thousand times[5]，the cracks are stable. The normal use fatigue lifetime of beams improves to some extent which is mainly because CFRP reinforcement plate improve tensile role of concrete and have better inhibition action with cracks and CFRP can constraint the development of cracks. Thus CFRP has good improvement to beam anti-cracking performance.

Deflection Research of Fatigue Test

Through the test of load-displacement by the percent meter，the arrangement of the percent meter is the same as static research.
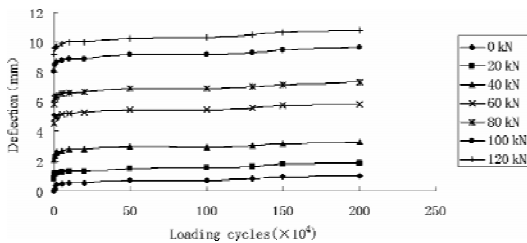

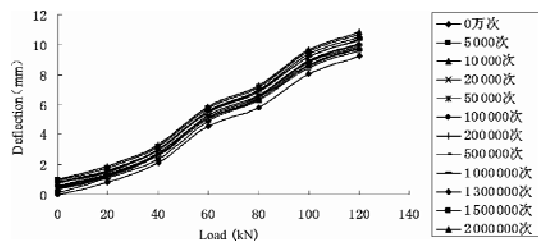**Figure 10　Deflection of CFS-N‑10 beam increase along
with loading increase curves**

**Figure 11　Deflection of CFS-N‑10 beam increase
along with loading times increase curves**

According to Figure 10 and Figure 11，the deflection of CFS-N‑10 beam increase gradually as loading increase and loading times increase. The deflection increase faster in initial loading stage while increase relatively slow in later stage. After the fatigue load levels which are 120 kN are carried on 2 million times，the maximum deflection is 10.83 mm which indicate that the CFRP participate in work with concrete section can restrict the improving speed of deflection. When fatigue load is up to 2 million times，the deflection in mid-span section gradually become stable. One reason is the deflection increase faster in initial loading stage while increase relatively slow in later stage. The other reason is in the early

fatigue loading progress the concrete elastic modulus decrease relatively fast，leading to a relatively fast growth of deflection in mid-span section. Thus when fatigue loading progress comes to a certain time，the elastic modulus of concrete gradually tend to be relatively stable，so the cross section deflection and stiffness tend to be stable.

Deflection Research of Fatigue Test

Through pasting strain tablets in mid-span of the tension position of the beam，we can measure variation of steel strain as load level increases. After designated fatigue load，static load is fractionally carried on to measure the strain of steel. The load -strain curve of steel bar is shown in Figure 12.

According to Figure 12，the steel strain of CFS-N-10 beam increase gradually as load increase and load times increase. The strain increase shower in initial loading stage while increase relatively faster in later stage. Along with the increase of cyclic loading，the strain of steel bar in CFS-N-10 also increases.

Because the CFRP is involved in tension zone，actually the fatigue stress peak-to-peak value of steel bar in CFS-N-10 is relatively small. Therefore to achieve the same steel bar strain value，the fatigue cyclic loading which reinforced beams can withstand is much more than beams not being reinforced. When uninstall the loading back to zero，the strain of CFS-N-10 beam mainly is residual strain under which CFRP is not involved in the tension while the tension is mainly for steel bar. Along with load enlargement the bottom concrete cracking and beam deformation is great. Therefore the pulling force of CFRP is becoming bigger and bigger.
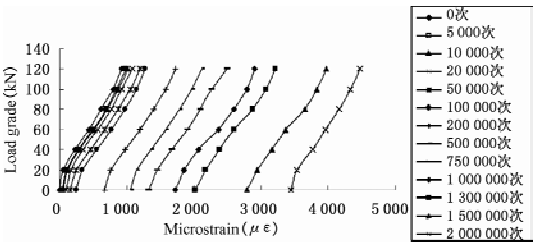

Figure 12　CFS-N-10 load -strain curve of steel bar

Breast Concretes Load-strain Curve

After certain times of load progress separately and the load limit comes to fatigue classification，we may test the strain of concrete. Conclusion can be drawn that the concretes strain assumes the linear distribution. Although after the function of redundant load，the section strain still conforms to the horizontal section assume[6]. The concrete of CFS-N-10 beam load-strain diagram of curves is shown in Figure 13.

According to Figure 13，the concrete strain of CFS-N-10 beam increase gradually as loading increase and loading times increase. After the fatigue load level which are 120 kN are carried on 2 million time，the maximum concrete strain is 1 761 μ_ε. When pasting CFRP plate to the concrete the strain of which is reduced indicate that CFRP can greatly improve the pressure of the concrete pressure area. This is of great significance to compression structure of concrete.
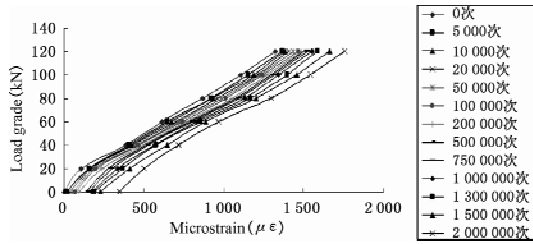
Figure 13   CFS-N-10 beam load-strain curve of concrete

CONCLUSION

This article takes research of 2 concrete contrasting beam and 4 beams reinforced by CFRP under high temperature effect of the SMA. Mechanical properties of 4 beams reinforced by CFRP are studied under cyclic loading and static load. This article also takes analysis of strain in the tension zone of the steel bar and the strain of bottom concrete and changing of cracks along with static load level increases and fatigue load times enlargement as well as the observation of crack development and deflection. It has indicated that:

For the first time in domestic the article takes research of fatigue and static experiment of beams reinforced by CFRP under high temperature effect of the SMA and being crushed. From the perspective of the material and deflection and crack development，study found that the strength，stiffness and the limit of crack development of reinforced beams obviously increased than those not reinforced by CFRP and the strain of steel bar，deflection and cracks are further less than those not reinforced by CFRP.

Beams reinforced by CFRP under the high temperature effect of the SMA and being crushed can withstand 2 million times of fatigue loading. The cracks increase faster in initial loading stage while increase relatively slow in later stage. CFRP under the high temperature effect of the SMA and being crushed has good improvement to beam anti-cracking performance.

The strain of concrete is reduced when pasting CFRP in the tension zone which indicated that CFRP can improve limit bending bearing capacity under the fatigue load. Under high temperature effect of the SMA，compressive strength Beams reinforced by CFRP still increased.

REFERENCES

［1］Xu，G. H.，Hu，M. Y. etc，"Highway and bridge and culvert design manual- girder bridge"，China Communication Press，1992，pp. 63.

［2］Zhan，R. S.，Hu，Z. F. and Shuai，C. B.，"Highway bridge reinforcement technique and examples"，China Communication Press，1992，pp. 106.

［3］Max，S. and Eugen，B.，"Fatigue of existing reinforced concert bridge desk slabs"，Engineering Structures，1998；20(11)，pp. 991-998.

［4］Kwa，K.-H. and ParK，J. -G.，"Shear-fatigue behaviour of high strength reinforced concrete beams under repeated loading"，Structural Engineering and Mechanics，2001，11(3)，pp. 301-314.

［5］Li，H. N.，Zhao，Y. H. and Huang，C. K.，"Fiber reinforced materials in geotechnical engineering research and

application［C］. The academic exchanges conference proceedings of the second session on national civil engineering with fiber reinforced polymer application technology"，Peking，Tsinghua University Press，2002：pp. 43-50.

［6］ Cheng，K. L.，"CFRP materials in the application of bridge reinforcement engineering［J］"，Bridge construction，2001(1)，pp. 44-46.

FLEXURAL STRENGTH ANALYSIS OF HYBRID GIRDERS FABRICATED FROM HIGH PERFORMANCE STEEL

L. Duan, L. Zheng, * C. S. Wang and J. M. Wang

Key Laboratory for Bridge and Tunnel of Shaanxi Province, College of Highways,
Chang'an University, Xi'an, 710064, China
* Email: wcs2000wcs@163.com

KEYWORDS

Steel girder, high performance steel, hybrid design, flexural strength, rotation capacity, ductility.

ABSTRACT

As high performance steel (HPS) plates are used in highway bridges, the steel types and articles in bridge codes should be modified. To make the HPS wide and secure application in highway bridges, testing study and finite element parameter analysis were performed on hybrid I-girders fabricated from HPS plates in this paper, in addition, the failure mechanism had been studied. Based on test and parameter analysis results, the following design rules are proposed for hybrid HPS girders. Firstly, flange slenderness is a major factor affecting plastic rotation capacity. Normalized flange slenderness λ_f from 0.2 to 0.25 is proposed in hybrid HPS 485W I girder design to obtain sufficient ductility. Secondly, both flexural strength and ductility will decrease with the increase of web slenderness. Appropriate normalized web slenderness λ_w from 3.78 to 5.7 is proposed to attain plastic moment. Thirdly, it is found that the flexural strength and ductility will increase with the descent of aspect ratio (h_w/b_f). Finally, for the design of hybrid girder, the strength gap between flanges and web should not beyond two steel grades to avoid early web buckling and greater residue deformation.

INTRODUCTION

High performance steel (HPS) has several advantages such as high strength, good weldability, greater toughness, and corrosion resistance. Thus, HPS bridges are economical for saving material, reducing fabrication cost and eliminating corrosion maintenance. With increasing notification of saving limited resource and protecting our environment, sustainable engineering, like HPS bridges, are proposed and encouraged nowadays. So far, there are over two hundred and fifty HPS bridges in service in the U. S., which demonstrated good serviceability and economic cost in whole life cycle[1].

With the quick development and widely application of HPS for highway bridges worldwide, HPS bridges must be closely studied to be included in current standard highway bridge design provisions to ensure safe use of HPS in bridge structures. This paper focus on inelastic bending behaviour HPS girders fabricated

685

HPS 485W and traditional steel. Three hybrid HPS girders were designed and tested by mid-span loading[2, 3]. After checking by the testing result，finite element mode was used for parameters analysis，including flange slenderness，web slenderness，material matching，section aspect ratio，lateral bracing arrangement and initial imperfection.

BENDING TEST PROGRAM

Test Program

Three welded I-girders，with symmetrical cross section，were designed to study the flexural ductility of hybrid HPS girders，dimensional shown in Figure 1 and Table 1. HPS 485W was employed in the flanges while lower strength grade steel Q235 for the webs. Each specimen was loaded at mid-span with five lateral bracing arranged at mid-span，two mid-span nearby sections and two end supporting sections.
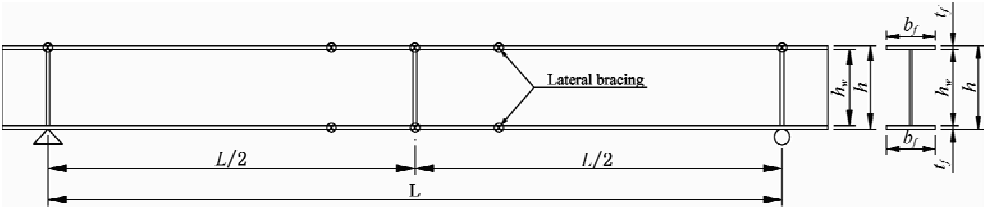

Figure 1   Test specimen dimension.

TABLE 1   DIMENSION OF BENDING SPECIMENS

No.	b_f	t_f	h_w	t_w	L
1	140 mm	13.2 mm	280 mm	7.5 mm	2 400 mm
2	130 mm	13.2 mm	280 mm	7.5 mm	3 000 mm
3	130 mm	13.2 mm	350 mm	7.5 mm	3 000 mm

Test Results Analysis

At the initial loading phase，the vertical deformations increased linearly with loading in this elastic stage. With load increasing，the compressive web near mid-span turned yielding before higher strength flange，and then the yielding field expanded from compressive web to high strength flanges quickly. In this yielding stage，the deformation grew continuously while load increased very slowly. Then the mid-span section turns completely plastic and plastic moment was attained. After that，this plastic region expanded nearby，corresponding to the growing vertical deformations and attaining ultimate capacity. As plastic rotation joint formed in mid-span，the girder became unloading and deformation still grows. The bending behaviours of three tested girders were shown by moment and rotation curve in Figure 2.

After the test，it was found that the failure modes of three girders were both local buckling in compressive flange and compressive web local buckling near mid-span. The web buckling field in test girder 3 was greater than that of girder 1 and 2，since its slender web. Compared with girder 1，the compressive flange local buckling was more obvious and web buckling field was greater in girder 2. Because the bigger span length in girder 2 caused greater plastic field.
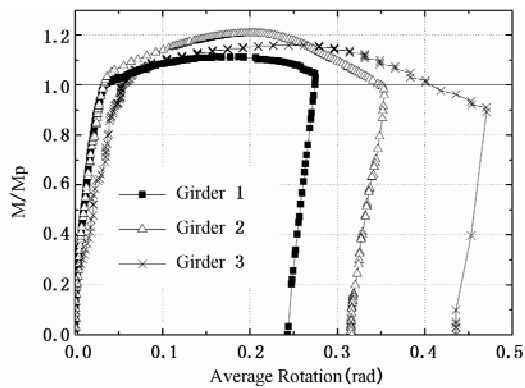
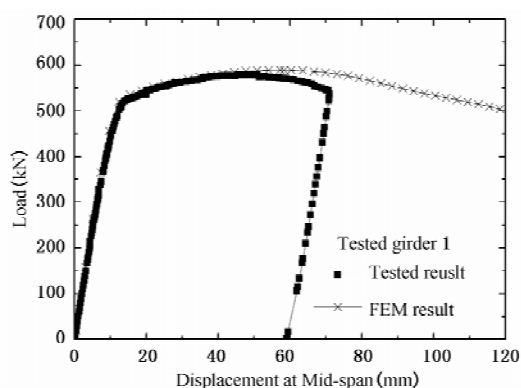**Figure 2   Moment and rotation curves of test girders**

Figure 3   Comparative results for test girder No. 1

FINIT ELEMENT MODLE CHECKING

Software ANSYS was used to build models for hybrid steel I girder，considering lateral bracing，initial imperfection，and residual stress[4]. The model girder was verified by comparing with test results. In this paper，test girder number 1 was chosen for checking finite element model（FEM），and the comparative calculation results was shown in Figure 3 and 4. Learn from Figure 3 and 4，the FEM could modulate the bending behaviour and failure mode in test precisely.
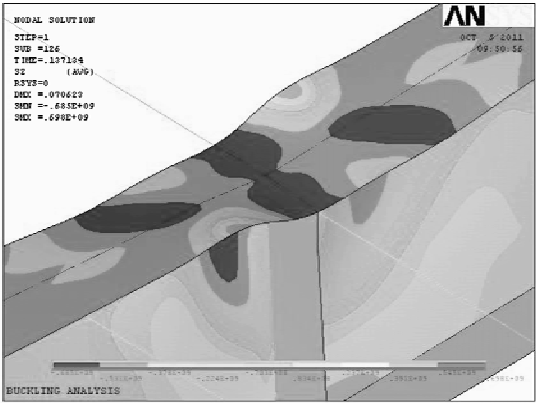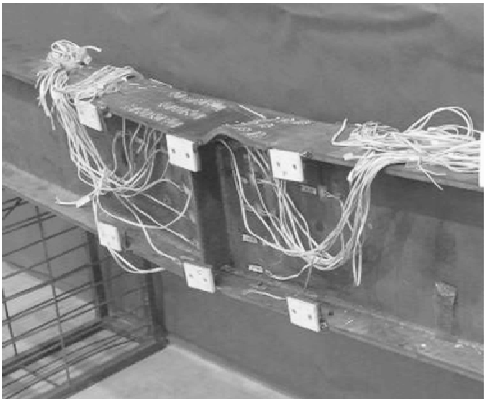

Figure 4   Failure model for No. 1 test girder

PARAMETER ANALYSIS

The verified FEM was used for flexural behaviour and ductility study for high performance steel hybrid I steel girders. Several critical parameters were study including flange slenderness ratio（λ_f），web slenderness ratio（λ_w），section aspect ratio（h_w/t_w），material matching，initial imperfection and lateral bracing. In all model girders below，high performance steel HPS 485W（with minimum yield stress of 485 MPa）was used for flanges，while tradition steel Q420（with minimum yield strength of 420 MPa）was employed for web.

Flange Slenderness Ratio

In the model girders，HPS 485 W was adopted in flanges while traditional steel grade Q420 was used for web. While the same compact web was used in model girders，only normalized flange slenderness，$\lambda_f = (b_f/2t_f) \times (\sigma_{yf}/E)^{0.5}$，was changed in non-compact field ranging from 0.5 to 0.15. The calculation result is shown in Figure 5. The results show that the bending capacity will increase from 0.97 Mp to 1.1 Mp as λ_f is decreasing from 0.5 to 0.2. However，the ultimate capacity will drop to 0.67 Mp as λ_f is decreasing from 0.2 to 0.15. For failure mode，local buckling in compressive flange will control bending capacity and ductility when λ_f is greater than 0.45，while both local buckling in compressive flange and web buckling control failure if λ_f belong to the field of 0.2 to 0.382. With decreasing of λ_f，web buckling turn more obvious. As λ_f is smaller than 0.15，web buckling controls bending capacity and ductility. In a world，for the design of high performance hybrid steel I girder，the normalized flange slenderness is suggested from 0.2 to 0.25.
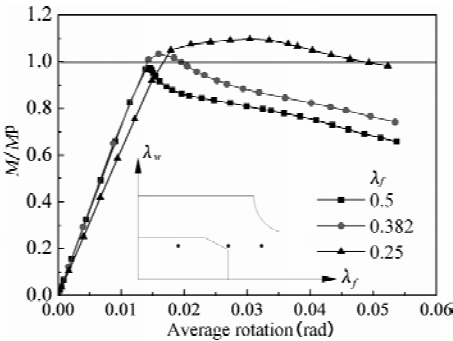

Figure 5   Middle span moment and average rotation curve

Web Slenderness Ratio

In the model girders，it was used the normalized web slenderness ratio ($\lambda_w = (h_w/t_w) \times (\sigma_{yw}/E)^{0.5}$) of 2.83, 3.78, 4.5 and 5.5，while the λ_f value of 0.382 and 0.25 were used，respectively. Figure 6 shows the calculation results. Learning from Figure 6, if λ_f equals to 0.382，as λ_w is increasing from 2.83 to 5.5，the capacity of girder will decrease from 1.03 Mp to 1.0 Mp，while rotation capacity will descend from 0.33 to 0.07. If 0.25 is adopted for λ_f，as λ_w is increasing from 2.83 to 5.5，the capacity of girder will decrease from 1.1 Mp to 1.02 Mp，while rotation capacity will descend from 1.92 to 0.51. Because of flange local buckling，the capacity and ductility are higher than that of $\lambda_f = 0.382$.

Web buckling will be brought forward as λ_w increasing，and then bending moment will transform to flange，which promote local buckling in compressive flange. As a result，both the capacity and ductility will decrease with the increasing of web slenderness ratio.

Section Aspect Ratio

Using compact web in all the model girders，section aspect ratio (h_w/b_f) adopted was 2, 2.5, 2.7, 3 and 3.5，respectively，while flange slenderness of 0.382 and 0.25 was considered. Figure 7 shows the moment at mid-span and average rotation curves. Learn from Figure 7，with the decrease of aspect ratio，the bending capacity and plastic rotation capacity are enhanced obviously.
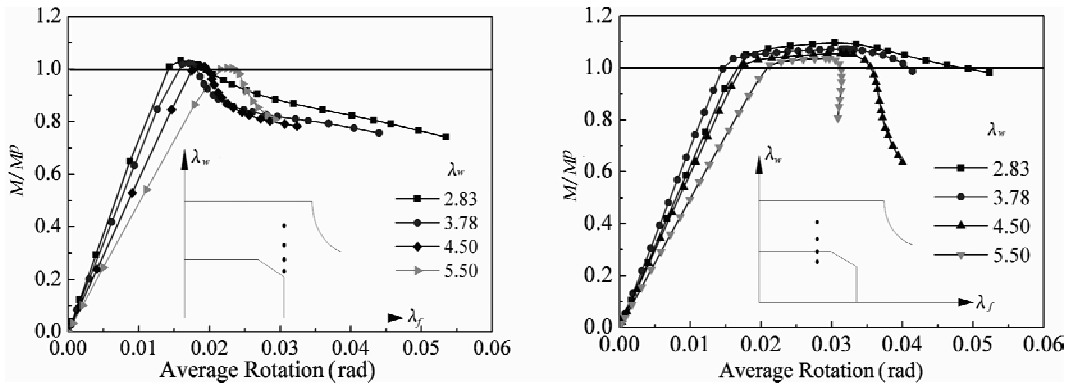
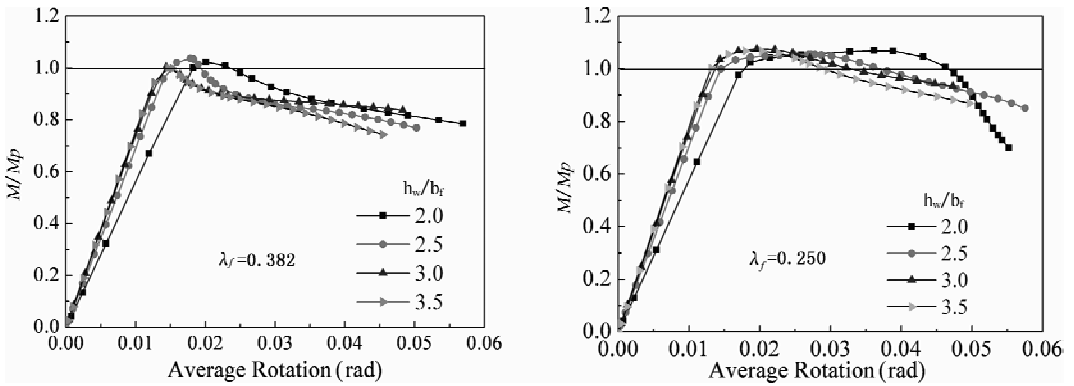**Figure 6   Middle span moment and average rotation curve**

Figure 7   Middle span moment and average rotation curve

Material Matching

In all the models, while HPS 485W was used for flanges, different steel grades were used for webs, including Q235, Q345, Q370 and Q420. Bilinear material model was used for web. The normalized flange slenderness of 0.382 and 0.25 were adopted respectively for different webs. All the web slenderness was the same ($h_w/t_w = 62.675$), but the normalized web slenderness λ_w was different. The value of λ_w for Q420, Q370, Q345 and Q235 was corresponding to 2.83, 2.66, 2.56 and 2.12, respectively. Learning from the analytical results shown in Figure 8, both the flexural strength and ductility are enhanced as minimum web yield strength is dropping from 420 MPa to 235 MPa. For models of $\lambda_f = 0.382$, when the web strength is descending from 420 MPa to 235 MPa, the flexural strength is increasing from 1.03 Mp to 1.05 Mp, and the rotation capacity is improving from 0.33 to 0.47. For models of $\lambda_f = 0.25$, when the web strength is descending from 420 MPa to 235 MPa, the flexural strength is increasing from 1.1 Mp to 1.12 Mp, and the rotation capacity is improving from 1.92 to 2.62. With the decrease of web strength, normalized web slenderness ratio is decreasing, thus enhancing the compactness of web. Learning from analytical results, when strength gap between flange and web is range from 10% to 50%, one seventh to one half of web height would yield before flange yielding, the web rigidity is decreased obviously and the residual deformation is relatively large. As a result, to ensure the serviceability of bridges, it was suggested that the strength gap between flanges and web should not belong two steel grades to avoid yield
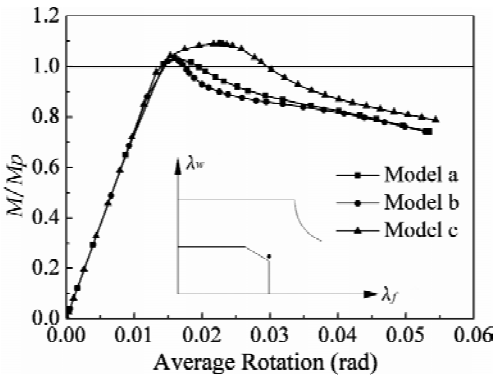
Figure 10   Moment and rotation curves for different imperfection distributions

demonstrated that the apparent inverse relationship between flexural capacity and initial imperfection peak value. As a result，the imperfection should be controlled as far as possible during welding and fabrication phase.
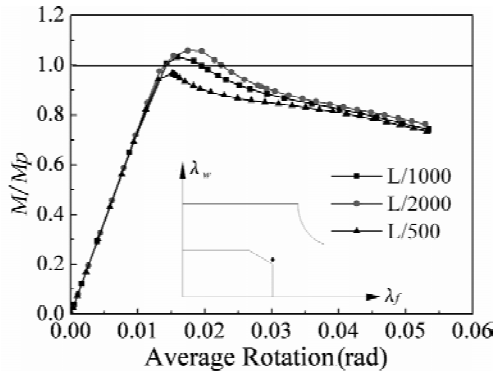

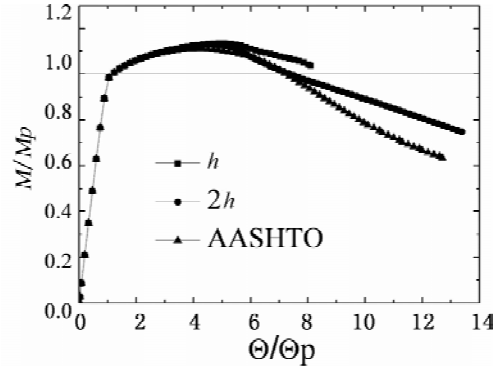**Figure 11   Moment and rotation curves with different imperfection peak value**

Figure 12   Moment and rotation curves with different imperfection peak value

Lateral Bracing

Three types of lateral bracing configuration are considered for the same hybrid model. Firstly，the first

691

lateral bracing is one height of cross section（h）away from mid-span. Secondly，the first lateral bracing is twice height of cross section（2h）away from mid-span. Thirdly，distance between the first lateral bracing point and mid-span is calculated according to AASHTO LRFD[4]. The analytical results are shown in Figure 12. Learning from analytical results，compare with the third bracing，model with the first and second bracing type have greater flexural capacity and ductility，but not obvious.

CONLUSIONS

This paper focus on the flexural behaviour of hybrid I girder fabricated by high strength HPS 485W flanges and low strength web. Three simple girders were designed and tested loading at mid-span. After the test，the bending behaviour and failure mode was analyzed. Based on the tested results，finite element model is established considering lateral bracing，initial imperfection，and residual stress. By checking the flexural strength and failure mode of finite element model with test result，the finite element is verified having capacity of modulating the test girder accurately. Major parameters are analyzed and following design rules are proposed for hybrid HPS girders. Firstly，flange slenderness is a major factor affecting plastic rotation capacity. Normalized flange slenderness λ_f from 0.2 to 0.25 is proposed in hybrid HPS 485W I girder design to obtain sufficient ductility. Secondly，both flexural strength and ductility will decrease with the increase of web slenderness. Appropriate normalized web slenderness λ_w from 3.78 to 5.7 is proposed to attain plastic moment. Thirdly，it is found that the flexural strength and ductility will increase with the descent of aspect ratio（h_w/b_f）. Finally，for the design of hybrid girder，the strength gap between flanges and web should not beyond two steel grades to avoid early web buckling and greater residue deformation.

ACKNOWLEDGEMENTS

REFERENCES

［1］Lwin，M. M.，"High Performance Steel Designers' Guide（Second Edition）"，San Francisco：U. S. Department of Transportation，Federal Highway Administration，Western Resource Center，2002.
［2］Wang，C. S.，Duan，L.，Wei，M.，Liu，L. X. and Hu，J. Y.，"Bending Behavior of Hybrid High Performance Steel Beams"，Advanced Materials Research，2011，vols. 163-167，pp492−495.
［3］Guo，T.，Wei，M. and Liu，L. X.，"Development of New Type Atmospheric Corrosion Resisting Steel A709M - HPS 485W for Bridge"，Journal of Steel Structure，2009，24，pp17−20.（in Chinese）
［4］AASHTO，"AASHTO LRFD Bridge Design Specification"，Washington，D. C.，AASHTO，2007.

STATIC TEST OF A FULL-SCALE ORTHOTROPIC STEEL DECK MODEL

* C. S. Wang[1, 2]，B. N. Fu[1]，Q. Zhang[1] and Y. C. Feng[1]

[1] Engineering Research Center for Large Highway Structure Safety of Ministry of Education，College of Highways，Chang'an University，Xi'an，China
[2] Key Laboratory for Bridge and Tunnel of Shaanxi Province，College of Highways，Chang'an University，Xi'an，China
* Email：wcs2000wcs@163.com

KEYWORDS

Orthotropic steel deck，static test，out-plane deformation，fatigue stresses.

ABSTRACT

An orthotropic deck has different stiffener in perpendicular directions，and the asymmetry enables the complicated stress of the deck's components. Before the fatigue test of a full-scale orthotropic deck model designed based on typical steel orthotropic deck of the long-span cable-stayed bridges，static test was conducted at the bridge laboratory of Chang'an University. The static test results showed that the local out-of plane deformation induced high local flexural stresses in the deck details under vehicle load. Furthermore，high stress gradient was found in the part of rib-to-diaphragm. The closer to the joint, the higher stress was produced. The high in-plane stress was found at the bottom corner of the diaphragm cut-out. However，the stress at the top corner of cut-out was influenced by the out-plane deformation of the diaphragm. Then，the finite element method was used to simulate the orthotropic steel deck under vehicle load，and the results from calculation and experiments were in good agreement. As a result，a comprehensive understanding of the stress distribution in the orthotropic steel deck was obtained according to the full-scale static test and finite element analysis，which makes a solid foundation for the further fatigue performance study.

INTRODUCTION

Due to the most important advantages of orthotropic decks such as high loading capacity，light weight，manufactured in workshop and short installation time，it has been widely used in medium and long span bridges. However，orthotropic decks are more prone to fatigue failure under the wheel load[1-9]. It is more important to know the stress distribution to determine the fatigue strength. But the stress distribution of orthotropic decks is more complex. So，the static test of a full-scale orthotropic bridge deck is required to study the stress distribution of the decks.

THE TEST SPECIMEN

The full-scale orthotropic deck in this study was fabricated by Q345 grade steel. It consists of six trapezoidal ribs supported by the transverse floor beam. The specimen dimensions and the details at the diaphragm cutout are shown in Figure 1. The dimensions of the deck are 1 800 mm in the longitudinal direction and 3800 mm in the transverse direction.

As shown in the Figure 1，the thickness of the deck plate is 14 mm. The cross section of the rib is 300 mm （top width）× 280 mm（height），and the thickness of the rib is 8 mm. The longitudinal ribs with the thickness of 10 mm are continues through the diaphragm. And the spacing between the longitudinal ribs is 600 mm. This specimen is a symmetrical structure with respect to the diaphragm.
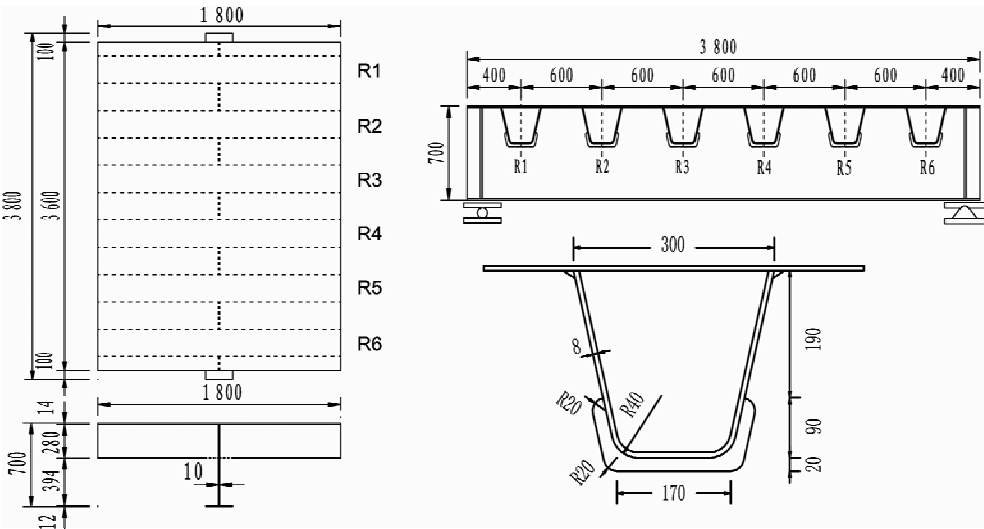

Figure 1　Size of full-scale model and rib （unit：mm）.

TEST SETUP AND LOADING SCHEME

Without considering the effect of surfacing，two-point loading was applied on the deck plate through block rubber. The load distribution areas are 200 mm （longitudinal）× 300 mm （traverse） and 200 mm （longitudinal）× 600 mm （traverse）. The spacing of loading area from center to center are 1 500 mm and 1 200 mm. In this test，loads are moved in transverse direction of the model to simulate the different locations of the wheel loads. For this purpose，several load cases were used in this test. The transverse location of the loading cases is shown in Table 1. The load was gradually applied by 50 kN to the maximum of 400 kN and Figure 2 shows the test device of static test. Strain gauges and strain rosettes were instrumented to measure the strain of the deck. The measure points of static test are shown in Figure 3.
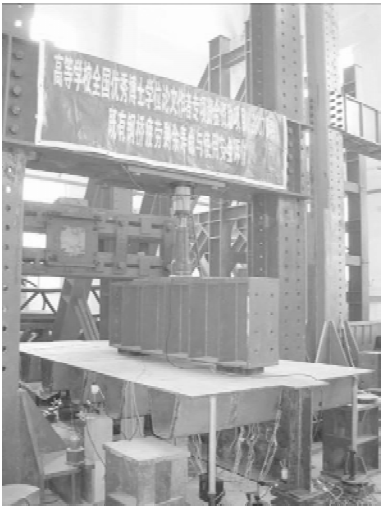
Figure 2　Loading equipment of test

（a）Measure Points of Rob

（b）Measure Points of bottom Deck

（c）Measure Points of digphragin
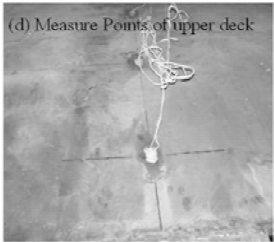
（d）Measure Points of upper deck

Figure 3　Assign of measure points

TABLE 1　LOADING CONDITIONS

Loading conditions	Loading area （mm²）	Center distance （mm）	Movement distance of cross direction（mm）	Movement distance of longitudinal direction（mm）	Schematic View
H4	200×600	1 200	0，150，300，450，600，900	—	

<div align="right">continued</div>

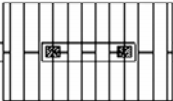| Loading conditions	Loading area (mm²)	Center distance (mm)	Movement distance of cross direction(mm)	Movement distance of longitudinal direction(mm)	Schematic View
H2	200×300	1 500	−600，−450，−300，−150，0，150，300，450，600，750，900	—	
HZ4	200×600	1 200	—	0，10，20，30	
Z2	200×300	1 300	0，300，600，750，900，1 050，1 200，1 500	—	

TEST RESULTS AND FINITE ELEMENT ANALYSES

In order to comprehensively study the stress distribution of orthotropic deck under the action of wheel loads，31 load cases were applied and 125 strain gauges were stick on the important zones of the orthotropic deck during the static test. During the static test of full-scale specimens，it is necessary to preload on the model. Static resistance strain indicator was used to record the information of strain gauges.

Stress of the Deck Plate

In orthotropic decks，the deck plate is directly supported the wheel loads，and is not supported between the longitudinal rib webs. The out-plane bending in the deck plate result in high local flexural stress causing the fatigue cracks along the longitudinal weld[6]，as shown in Figure 4. Because of the rain and other harmful substances can easily enter into the steel box girder through these fatigue cracks，these cracks are very harmful to the deck plate[5]. These fatigue cracks result from high transverse stress of the deck plate.
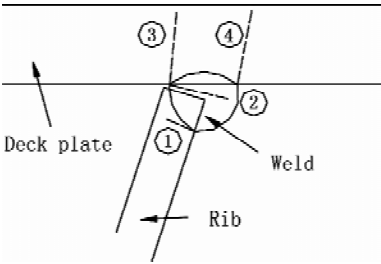

Figure 4　The fatigue failure models

Test value and calculation results of measure points are shown in Figure 5. The Figure 5 shows that the closer to rib-to-deck connections，the higher stress of the transverse stress. In addition，the transverse

stress of measure points reach to its maximum when the load was applied right above of the points. Therefore，the stress distribution of deck is prone to affect by local effect of load and the deck bending effect.
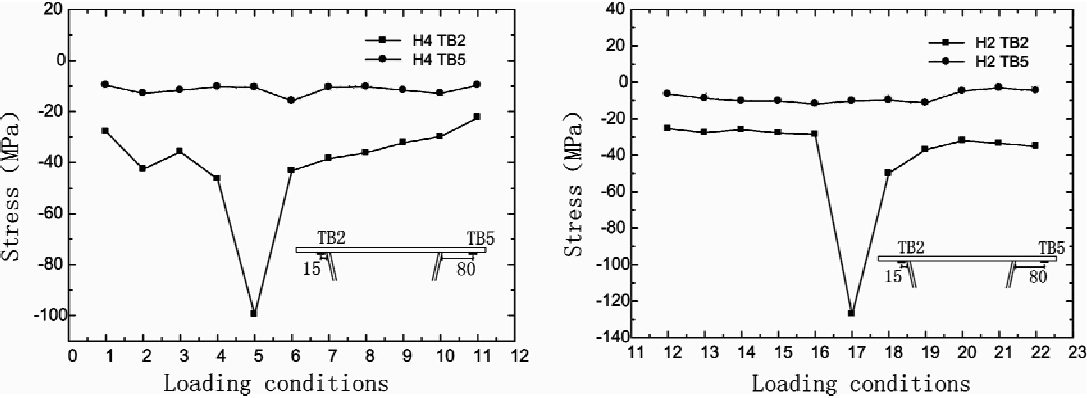
Figure 5　Stress test results of the desk plate

Stress of the Longitudinal Rib

Rib webs of orthotropic decks are supported by diaphragm. As the end of rib-to-diaphragm connection subjected to out-plane distortion，weld-induced residual stress and geometric stress concentration under the wheel loads，these fatigue cracks initiate from the weld toe and expand longitudinally on the rib web[7-9]. Therefore，combination welding is suggested using at the rib-to-diaphragm connections to improve the fatigue level in the structure design.

It was found that fatigue cracks of rib-to-diaphragm connections mainly initiates from weld toe and expanded in the rib web. The vertical stress and stress gradient were all measured during the static test and test results of the measure points under the 200 kN load are shown in Figure 6. It can conclude that the closer to connection，the more vertical stress may cause. When the distance is 5 mm，the vertical stress is 160 MPa and it decrease to 20 MPa at the distance of 40 mm.

Figure 6　Stress test results of the rib

Stress of the Cut-out

Due to cutout of the diaphragm，the stiffness of the diaphragm decreased and it is more easily to find out-of-plane distortion on the diaphragm[7-9]. Main stress which perpendiculars to the free edge of the cutout may be very high as well. As a result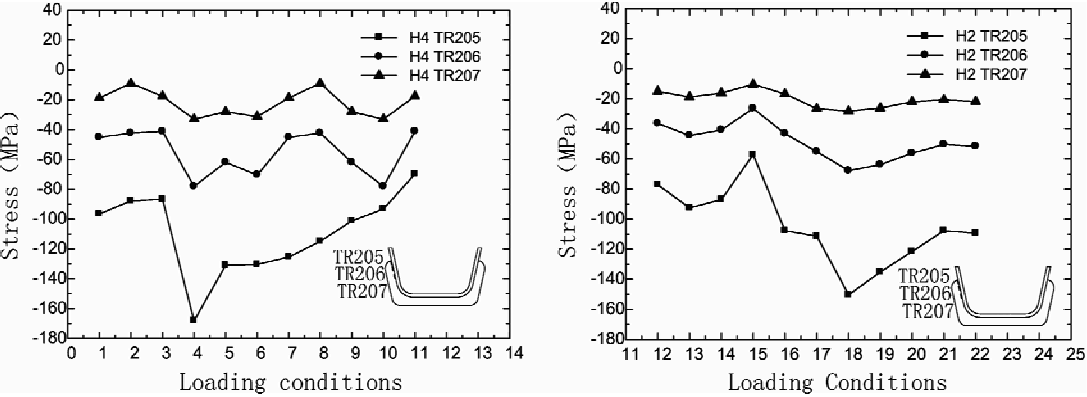，the free edge of the cutout is sensitive to fatigue. The geometry stress concentration，similar crack defects at the free side of the cut-out and out surface deformation of the diaphragm are main factors to affect its fatigue failure. The stress distribution of the cut-out is shown in Figure 7. The high in-plane stress was found at the bottom corner of the diaphragm cut-out. However，the stress at the top corner of cut-out is influenced by the out-plane deformation of the diaphragm.
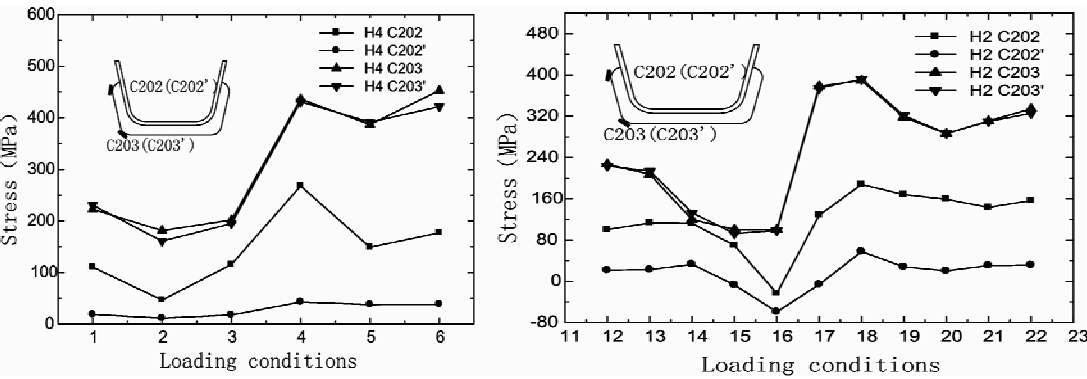
Figure 7   Stress test results of the cutout

FINITE ELEMENT MODEL STUDY

To study the stress distribution of the orthotropic decks，a finite element model of full-scale orthotropic decks is created with linear elastic shell63 element using FE software ANSYS 11. 0. The finite element model is intended to simulate the test specimens，and the dimension of the FE model is accord with test specimens. The FE model of the orthotropic decks and the mesh of the cutout are shown in Figure 8.

Figure 8   Full size finite element model

Stress of the Deck Plate

In order to deeply study the stress distribution of the deck plate，movement load were acted on the FE

surface deformation of deck plate. There are high stress gradient at the rib-to-diaphragm connections.

3. A high in-plane stress was found at the bottom corner of the diaphragm cut-out. However，the stress at the top corner of cut-out 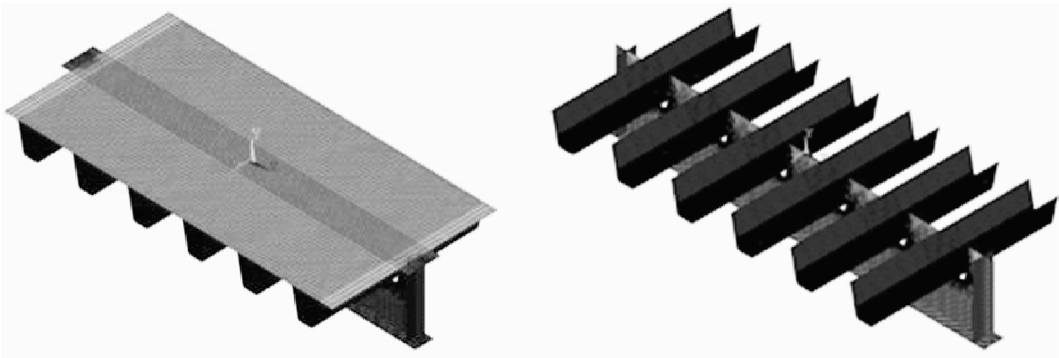is influenced by the out-plane deformation of the diaphragm. The cut-out stress could decrease by increasing the radius of the bottom hole，and it may not cause negative influence to the stress of rib.

ACKNOWLEDGEMENTS

REFERENCES

［1］ Gurney，T.，"Fatigue of steel bridge decks"，TRL State of the Art Review 8，1992.

［2］ AISC Design Manual，"Design Manual for Orthotropic Steel Plate Deck Bridges"，American Institute of Steel Construction Inc，New York，United States of America，1963.

［3］ Wolchuk，R.，"Lessons from weld cracks in orthotropic decks on three European bridges"，J. Structural Engineering，ASCE，1992，116(1)，pp.75-84.

［4］ Wang，C.S. and Feng，Y.C.，"Review of the fatigue behaviors and finite element analysis of orthotropic steel bridge decks"，2008 Orthotropic Bridge Conference，Sacramento，California，USA，2008，pp.290-304.

［5］ Xu，W. and Zhang，X.N.，"Analysis distress charactors and design of steel orthotropic bridge decks pavement in China"，2008 International Orthotropic Bridge Conference，Sacramento，California，USA，Aug.2008，pp.184-192.

［6］ Xiao，Z.G. and Yamada，K.，"Stress analyses and fatigue evaluation of rib-to-deck joints in steel orthotropic decks"，International Journal of Fatigue，2008，30(8)，pp.1387-1397.

［7］ Corte，W.D. and Bogaert，P.V.，"Improvements to the analysis of floorbeams with additional web cutouts for orthotropic plated decks with closed continuous ribs"，Steel and composite Structures，2007，7(1)，pp.1-18.

［8］ Kolstein，M.H.，"Fatigue classification of welded joints in orthotropic steel bridge decks"，Delft University of Technology，Netherlands，2007.

［9］ Choi，J.H. and Kim，D.H.，"Stress characteristics and fatigue crack behavior of the longitudinal rib-to-cross beam joints in an orthotropic steel deck"，Advances in Structural Engineering，2008，11(2)，pp.189-198.

FATIGUE OF CFRP STRENGTHENED STEEL CONNECTIONS UNDER COMBINED ACTIONS

H. B. Liu and * X. L. Zhao

Department of Civil Engineering，Monash University，Melbourne，VIC 3800，Australia
* Email：ZXL@monash. edu

KEYWORDS

CFRP（Carbon Fibre Reinforced Polymer），steel connections，fatigue，combined loads，cyclic load，crack propagation.

ABSTRACT

In this paper a series of experiments was performed to investigate the effectiveness of composites on preventing fatigue crack propagation and extending the fatigue life of steel connections under combined loads，including a cyclic mode I load and a tensile static load. Each specimen is formed by two steel plates joined together by single-sided girth welds. To prevent premature failure，an initial notch was machined. The steel connections were reinforced with single-sided CFRP sheets. Different numbers of CFRP overlays were applied. All the specimens were tested to failure under a constant amplitude tensile cyclic load combined with varied tensile static load，which are perpendicular to the cyclic load. The experimental results reveal that the presence of tensile static load is able to reduce the fatigue crack growth rate and hence results in a longer fatigue life. This observation is true for the steel connections with and without CFRP overlays. The effect of tensile static load on the number of fatigue cycles at varied layers of CFRP sheets was evaluated by the comparison of their fatigue lives.

INTRODUCTION

Examination of previous structural failures has revealed that many failures are due to fatigue fracture，which is the most significant failure behaviour for metal structures. Composite repair has been verified to be an efficient and cost-effective means to reduce crack growth rate and extend the service life of cracked metallic components（Ratawani et al.[1]，Domazet[2]，Suzuki[3]，Bocciarelli et al.[4]）. However studies in this area to date have been very limited and many issues remain unclear（Hollaway and Cadei[5]，Zhao and Zhang[6]）. For example，fatigue fracture is a key issue for the girth welded connections in subsea pipelines，which have been used to carry oil or gas produced from fields that lie under the sea to shore（e. g. Busby[7]，Macdonald & Maddox[8]，Xiao and Zhao[9]）. These connections are subjected to combined stresses in most of their service life，which include the fluctuating axial stress normal to the girth welds and the hoop stress that can be viewed as static stress. Little research was carried out on the repair

efficiency of composites reinforced steel connections under combined actions，even though composite sheets have been shown to have great advantages in the repair of structures with curves or complex shapes （Haedir et al.[10]，Shaat and Fam[11]）.

This paper deals with the testing of CFRP sheets reinforced steel connections under combined actions. Each connection is formed by two steel plates connected by single-sided girth welds. Three or five layers of CFRP sheets were applied on one side. All the specimens were tested to failure under a uniform Mode I cyclic load combined with varied tensile static loads，which is perpendicular to the cyclic load. The comparisons of experimental results disclose that the application of tensile static load in the perpendicular direction to the cyclic load is able to prolong the fatigue live of CFRP reinforced steel connection. The effect gets more noticeable with the tensile load increasing. The reinforcement of CFRP sheets can also extend the fatigue life of steel connections under combined loads and the improvement gets more obvious with the number of CFRP sheets increasing.

MATERIALS，SPECIMENS AND TEST PROCEDURES

Specimen Geometries

To investigate the fatigue behavior of CFRP reinforced steel connections under combined loads，a set of specimens were designed and prepared. Each specimen is formed by two steel plates connected by a complete penetrated girth welding. Some specimens were reinforced with CFRP sheets on one side. To prevent premature failure，each specimen was machined with an initial notch sitting on one of the weld toes centrally. The initial notch consists of a 5 mm hole and two initial slots，which were wire cut with dimensions of 1 mm long and 0.3 mm wide. It was designed according to ASTM E‑647 specifications （[12]）. Additional two holes with diameter of 21 mm were fabricated for the application of tensile static load. Typical geometry and configuration of the specimen is shown in Figure 1，together with details of girth weld and initial notch. In this figure，CFRP sheets are highlighted in pattern.

Material Properties

All the steel plates used in this experimental program have a uniform thickness of 10 mm. There are two batches of steel plates used. The mechanical properties of the steel plates were determined through tensile coupon tests according to AS1391 （[13]）. For steel type 1，its mean yield stress，tensile strength and elastic modulus are 224 MPa，346 MPa and 203 GPa，respectively. For steel type 2，its mean yield stress，tensile strength and Young's modulus are 298 MPa，411 MPa and 195 GPa，respectively.

Previous work of the authors （Liu et al.[14]） had proved that the carbon fibre of MBrace CF530 is able to produce outstanding effects in the strengthening and repair of steel members. Therefore MBrace CF530 was adopted as patching system in this study. An optimal bond length of 120 mm was proposed for five layers of MBrace CF530 and the width was proposed be sufficient to cover the whole potential path of crack growth （Liu et al.[15]）. The CFRP sheets with dimensions of 200 mm in longitudinal direction and 135 mm in vertical direction was then applied. The carbon fibre sheets were provided in rolls with a width of 300 mm and a thickness of 0.19 mm. As reported in the technical datasheet provided by the producer，MBrace CF530 has an elastic modulus of 640 GPa，ultimate tensile strength of 2 650 MPa and ultimate tensile elongation of 0.4%.

Structural adhesive，Aradite 420，was used to bond the composite overlays. This room temperature curing structural epoxy is characterized with high shear and peel strength. It is an extremely tough and resilient adhesive and can resist moisture adequately. Based on the technical data provided by the manufacturer，its tensile strength，lap shear strength on CFRP，elastic modulus and ultimate strain are 32 MPa，36 MPa，1 900 MPa and 4% at 23℃，respectively. The Poisson's ratio was assumed to be 0.35，which is a typical value for this type of adhesive (Baker et al. [16]，Matta[17]).
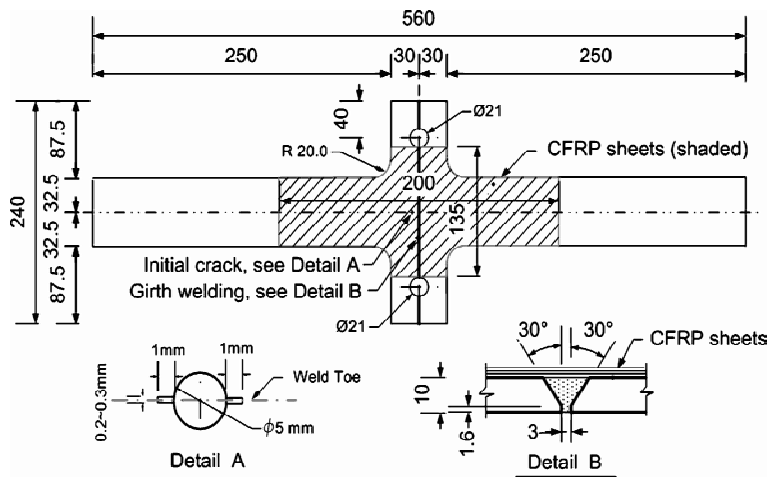
Figure 1   Dimensions and details of the specimens

Specimen Preparations

The girth welds used to connect the steel plates were prepared according to AS/NZS 1554 ([18]). As the performance of the bond between the steel and CFRP is significantly affected by the steel surface condition，it is important to prepare the steel surface in an efficient way. For a complete contact between the steel and CFRP，the raised welding beads at the joint were grinded to create a flat surface，as shown in Figure 2(a). The surfaces of the steel plates were then sandblasted to remove the rust and create a rough surface ensuring a better mechanical interlocking，as shown in Figure 2 (b). After these treatments，the substrates were cleaned with acetone to remove grease，oil and dust to expose a fresh chemically active surface. When the surfaces were dry completely，the adhesive of Aradite 420 was applied uniformly using a brush，and one layer of CFRP sheet was laid onto the adhesive-coated steel plates. At the moment a roller was used to apply uniform pressure over the CFRP sheet until the sheet

(a) Weld after grinding   (b) Sand blast surface   (c) Ready-to-test specimens

Figure 2   Preparation of the specimens

was immersed in the resin and extra epoxy and air pockets were forced to bleed out. In the same way, other CFRP sheets were applied. The ready-to-test specimen is shown in Figure 3(c). The specimens were cured until the epoxy achieved full strength.

Test Procedures

Figure 3(a) shows the experimental setup in the fatigue test. The loading regime is shown in Figure 3(b), in which, F_1 represents the cyclic loading in longitudinal direction; F_h represents the tensile static load in the direction perpendicular to the cyclic loading. A universal testing machine, Instron 1 342, was used to apply cyclic load. The servo-hydraulic controlled machine has a load capacity of 100 kN. The static tension load was applied using the hydraulic of Enerpac RCH 120, which has a load cell capacity of 120 kN. The load from hydraulic was transferred to the specimen through a loading frame, which was designed to apply the force on two sides of the specimen equally. In this experimental program three varied static loads were tested, 0 kN, 40 kN and 80 kN. The value of zero represents the specimen being tested under cyclic load alone. All the cyclic loads have a constant frequency of 10 Hz and a stress ratio of 0.1 until fracture failure occurred. Fracture was set to occur when the displacement of the actuator runs out of the regular displacement range by 1 mm.

(a) Fatigue Test Setup   (b) Loading regime
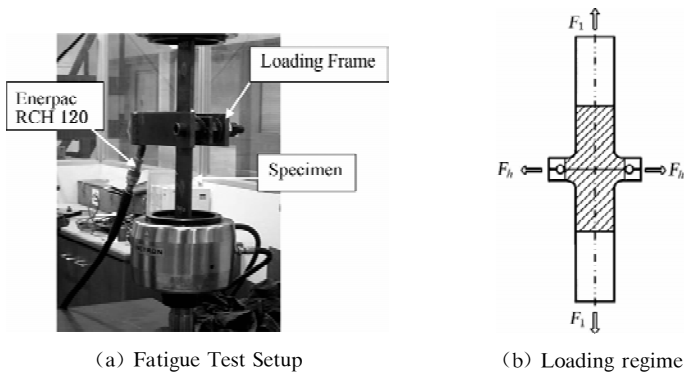
Figure 3   Experimental setup and loading regime

FATIGUE TEST RESULTS AND DISCUSSIONS

Experimental details and results were listed in Table 1. This table includes the variables of steel type, CFRP layer number, maximum value (F_{1max}) and minimum value (F_{1min}) of the cyclic load, tensile static load (F_h), fatigue cycle number (N), fatigue life increase ratio (N/N_{H0}) and crack length. The fatigue cycle number was counted until fracture failure occurred. N_{H0} represents the fatigue cycle number of the specimen tested by cyclic load only, such as S1C0H0, S2C0H0, S2C3H0 and S2C5H0. The crack length is the direct distance between two crack fronts. Comparing the crack length of the specimens made of steel type two, the value sits in the range of 81 – 88 mm when there is no CFRP, in the range of 100–102 mm when there are three layers of CFRP and 127–137 mm when there are five layer of CFRP. Obviously the crack length at fracture gets longer as the number of CFRP layers increasing.

TABLE 1   EXPERIMENTAL DETAILS AND RESULTS

Items No.	Steel Type	CFRP Layer No.	F_{1max} (MPa)	F_{1min} (MPa)	F_h (kN)	N (million)	N/N_{H0}	Crack Length (mm)
S1C0H0		0	100	10	0	1.447	1.00	104.80
S1C0H40	Type 1	0	100	10	40	1.639	1.13	107.73
S1C0H80		0	100	10	80	1.933	1.34	98.64
S2C0H0		0	150	15	0	0.458	1.00	81.87
S2C0H40	Type 2	0	150	15	40	0.524	1.14	88.38
S2C0H80		0	150	15	80	0.549	1.20	87.91
S2C3H0		3	150	15	0	0.623	1.00	100.36
S2C3H40	Type 2	3	150	15	40	0.678	1.09	102.38
S2C3H80		3	150	15	80	0.779	1.25	101.32
S2C5H0		5	150	15	0	0.811	1.00	137.07
S2C5H40	Type 2	5	150	15	40	0.844	1.04	127.88
S2C5H80		5	150	15	80	0.742	0.92	134.57

There are a total of twelve specimens included in Table 1. Each specimen was given a name according to its steel type (S), CFRP layer number (C) and the value of tensile static load (H). The specimens can be divided into four groups by steel type and CFRP layer number. Each group includes three specimens which are uniform except for the tensile static load applied. In each group there is one specimen tested by cyclic load only. Its result was represented by N_{H0}, which can be used as a control data in its group. The fatigue life of each specimen was compared with the control data in its group and the ratio between them was defined as fatigue life increase ratio (N/N_{H0}). For example，the fatigue life of S1C0H0 was referred as N_{H0}, which is equal to 1.447 million. When the fatigue lives of S1C0H0, S1C0H40 and S1C0H80 were compared with it，the fatigue life increase ratios are equal to 1.00，1.13 and 1.34，respectively. There is an increase of 13% in fatigue life when the tensile load is 40 kN and 34% when the tensile load is 80 kN. Similarly the fatigue life increase ratios of S2C0H0, S2C0H40 and S2C0H80 are equal to 1.00，1.14 and 1.20，respectively. It is obvious that the application of tensile static load is able to extend the fatigue life of steel connection，and the effect gets more obvious when a higher value of static load was applied.

Figure 5 shows the effect of tensile static load on the number of fatigue cycles at varied layers of CFRP sheets. The vertical coordinate represents the number of fatigue cycles. This figure only includes the specimens made of steel type 2. The data can be divided into three groups according to the number of CFRP layers，the first group without any CFRP，the second group with three layers of CFRP，and the third group with five layers of CFRP. Each group includes three uniform specimens tested by three varied tensile static loads，0 kN，40 kN and 80 kN，respectively. The fatigue life increase ratio (N/N_{H0}) was marked above each column. Obviously the fatigue life of steel connection was obviously increased by the reinforcement of CFRP sheets. Analysis of the first and second groups indicated that the application of tensile static load has a considerable effect on the extension of fatigue life and the effect gets more noticeable with the tensile load increasing. In the third group，the increment in fatigue life is 4% when the tensile load is 40 kN but a decrement of 8% when the tensile load is 80 kN. This is not consistent with the observation in the first two groups. More research on the effect of tensile static loads on CFRP reinforced steel connections needs to be carried out in the future.

Figure 6 illustrates the effect of CFRP layer on the number of fatigue cycles at varied static loads. The
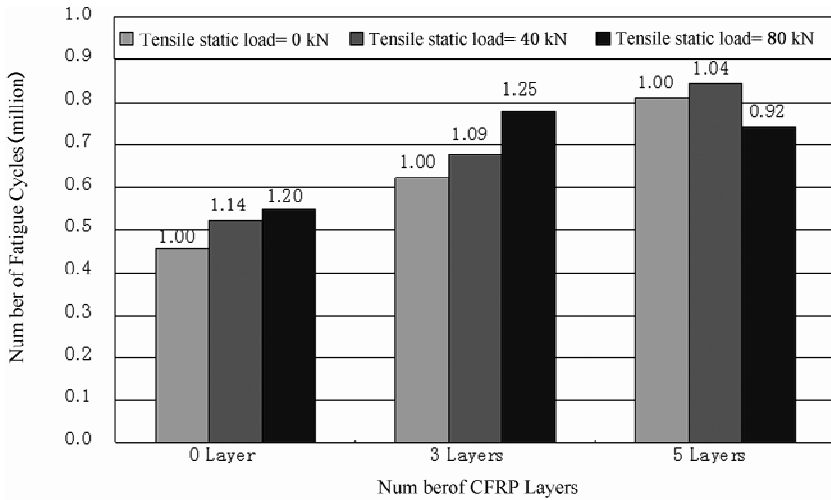
Figure 4   Effect of tensile static load on fatigue life at varied numbers of CFRP layers
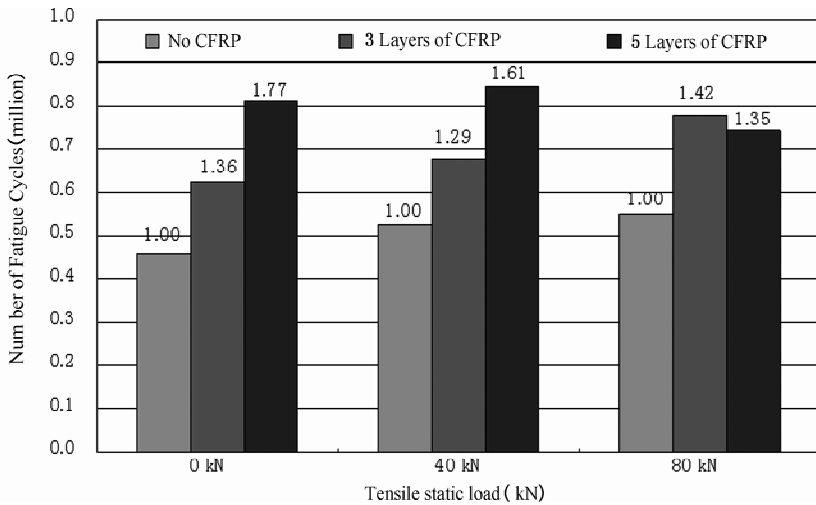
Figure 5   Effect of CFRP layer numbers on fatigue life at varied tensile static loads

twelve data in Figure 4 was plotted in Figure 5 in a different way. The vertical coordinate still represents the number of fatigue cycles. However the horizontal coordinate represents tensile static load. In Figure 5 the data was divided into three groups by tensile static load，the first group without any tensile loads，the second group with 40 kN tensile loads and the third group with 80 kN tensile loads. Each group still includes three uniform specimens except for the number of CFRP sheets，one specimen without any CFRP sheets，one specimen with three layers of CFRP and the other one with five layers of CFRP sheets. In each group the specimen without CFRP was set as the control panel. The fatigue life of other specimen is compared with it and the ratio between them is listed above each column. When there is no tensile static load，as shown by the first group in Figure 5，the fatigue life has an increment of 36% by three layer of CFRP and 77% by five layer of CFRP. When the tensile load of 40 kN was applied，as shown by the second group in Figure 5，the increment in fatigue life is 29% by three layers of CFRP and 66% by five layer of CFRP. The analysis of these two groups indicated that the application of CFRP

sheets is able to prolong the fatigue life of steel connections considerably. The improvement gets more obvious with the number of CFRP sheets increasing. However in the third group the increment of fatigue life is 42% by three layer of CFRP and dropped to 35% by five layer of CFRP. The inconsistent results proposed that more study needs to be carried out on the steel connections reinforced by five layers of CFRP sheets in the future.

All the experimental results demonstrated that the tensile static load is able to extend the fatigue life of steel connections under combined loads. This is owing to the fact that with the application of tensile static load，a retaining effect is introduced at the crack front to reduce the crack opening displacement. Therefore the stress intensity factor gets smaller in mode I and the crack propagation rate is slowed down. With the propagation of fatigue crack，the crack front opens wider. To prevent larger deformation the restrain effect from the tensile static load was forced to increase. The continuous effect from tensile static load is able to slow down the crack growth rate and leads to an enhanced fatigue life. When the steel connection is reinforced by CFRP sheets，the applied loads are carried by both the steel plate and composite at the repaired zone. As the crack propagates more loads are transferred to the composites due to the retaining effect of the mobilised CFRP patch. Therefore crack opening displacement is significantly reduced and longer fatigue life is achieved. When CFRP reinforced steel connection is tested to fracture failure under cyclic mode I load and perpendicular tensile static load，the restraining effect is introduced by both CFRP sheets and tensile static load. Therefore a longer fatigue life is expected.

CONCLUSIONS

This paper has reported on experimental investigations of the fatigue behavior of CFRP reinforced steel connections under combined actions. All the steel connections were tested to failure under a constant amplitude tensile cyclic load combined with varied tensile static loads，which are perpendicular to the cyclic load. The following conclusions were reached：
(1) The application of tensile static load has a considerable effect on the extension of fatigue life and the effect gets more noticeable with the tensile load increasing.
(2) The reinforcement of CFRP sheets is able to prolong the fatigue life of steel connections considerably. The improvement gets more obvious with the number of CFRP sheets increasing.

REFERENCES

［1］Ratwani，M. M.，Kan，H. P.，Fitzgerald，J. H. and Labor，J. D.，"Experimental investigation of fibre composite reinforcement of cracked metallic structures"，Composite materials：testing and design（Sixth conference），ASTM STP 787，1982.
［2］Domazet，Z.，"Comparison of fatigue crack retardation methods"，Engineering Failure Analysis，1996，3，pp. 137-147.
［3］Suzuki，H.，"Experimental study on repair of cracked steel member by CFRP strip and stop hole"，Proceedings of 11th European Conference on Composite Materials，Rhodes，Greece，2004.
［4］Bocciarelli，M.，Colombi，P.，Fava，G. and Poggi，C.，"Fatigue performance of tensile steel members strengthened with CFRP plates"，Composite Structures，2009，87，pp. 334-343.
［5］Hollaway，L. C. and Cadei，J.，"Progress in the technique of upgrading metallic structures with advanced polymer composites"，Progress in Structural Engineering and Materials，2002，4(2)，pp. 131-148.
［6］Zhao，X. L. and Zhang，L.，"State-of-the-art review on FRP strengthened steel structures"，Engineering

Structures，2007，29(8)，pp.1808-1823.

［7］Busby，R.F.，"Underwater inspection/testing/monitoring of offshore structures"，Ocean Engineering，1979，6 (4)，pp.355-491.

［8］Macdonald，K.A. and Maddox，S.J.，"New guidance for fatigue design of pipeline girth welds"，Engineering Failure Analysis，2003，10(2)，pp.177-197.

［9］Xiao，Z.G. and Zhao，X.L.，"Stress analysis of free spanning subsea pipelines with finite element method"，10th International Symposium on Structural Engineering for Young Experts，Changsha，China，2008，pp.971-980.

［10］Haedir，J.，Bambach，M. and Zhao，X.，"Bending strength of CFRP-strengthened circular hollow steel sections"，3rd international conference on FRP composites in civil engineering，Miami，USA，2006，pp.701-704.

［11］Shaat，A. and Fam，A.，"Axial loading tests on short and long hollow structural steel columns retrofitted using carbon fibre reinforced polymers"，Canadian Journal of Civil Engineering，2006，33(4)，pp.458-470.

［12］American Society for Testing and Materials，A.I.，"ASTM designation：E 647. Standard test method for measurement of fatigue crack growth rates"，Annual book of ASTM standards，ASTM International，2001.

［13］Australia Standards 1391，"Methods of tensile testing of metals"，Standards Australia，Sydney，1991.

［14］Liu，H.B.，Al-Mahaidi，R. and Zhao，X.L.，"Experimental study of fatigue crack growth behaviour in adhesively reinforced steel structures"，Journal of Composites Structures，2009，90(1)，pp.12-20.

［15］Liu，H.B.，Zhao，X.L. and Al-Mahaidi，R.，"Boundary element analysis of CFRP reinforced steel plates"，Journal of Composite Structures，2009，91(1)，pp.74-83.

［16］Baker，A.A.，"Fatigue crack propagation studies on aluminium panels patched with boron/epoxy composites"，International conference on aircraft damage assessment and repair，Melbourne，Australia，1991，pp.209-215.

［17］Matta，F.，"Bond between steel and CFRP laminates for rehabilitation of metallic bridges"，Ph.D Thesis，University of Padua，Padua，2003.

［18］AS/NZS 1554：4，"Structural steel welding - Welding of steel structures subject to high levels of fatigue loading"，Standards，Australia，2010.

FULL-SCALE FATIGUE TEST OF ORTHOTROPIC STEEL DECK

* C. S. Wang[1, 2]，B. N. Fu[1]，Q. Zhang[1] and Y. C. Feng[1]

[1] Engineering Research Center for Large Highway Structure Safety of Ministry of Education，College of Highways，Chang'an University，Xi'an，China
[2] Key Laboratory for Bridge and Tunnel of Shaanxi Province，College of Highways，Chang'an University，Xi'an，China
* Email：wcs2000wcs@163.com

KEYWORDS

Orthotropic steel deck，fatigue test，cycle stress，fatigue crack，fatigue strength.

ABSTRACT

Orthotropic steel deck with closed trough ribs has been widely used in steel bridges due to lightweight construction，large capacity for heavy loads，fast erections and so on. Except for their excellent behavior，steel orthotropic bridge decks have experienced a variety of fatigue problems due to high cycle stress，stress concentration and residual stress in welding connections. In bridge engineering，the common damage parts include the weld of deck-to-rib，the weld of rib-to-rib，the weld of rib-to-diaphragm and so on. Therefore，a full scale fatigue test was carried out for investigating the behavior of orthotropic deck. Based on the typical orthotropic deck plate of the long-span cable-stayed bridges，fatigue test of a full-scale model was carried out for researching the fatigue behavior of orthotropic steel deck. Static and dynamic measurements as well as visual inspection were conducted during the fatigue test. Test results revealed that visual fatigue cracks were detected in the rib-to-diaphragm. The fatigue strength of the rib-to-diaphragm is more than the D degree in the AASHTO and the 63 degree in EUROCADE.

INTRODUCTION

Orthotropic steel deck with closed trough ribs has been widely used in steel bridges due to lightweight construction，large capacity for heavy loads，fast erections and so on. The application of orthotropic deck has become a sign of a country steel bridge design and manufacture level[1-2]. In China，orthotropic deck was used in most long-span steel bridge under construction. Because of the complex of structure and stress，orthotropic deck is apt to fatigue failure under the directly repeated actions of vehicles[3-7].

In modern steel bridge，cut-out of crossbeam，rib-to-diaphragm and rib-to-deck connections are more susceptible to fatigue failure. There is complex in and out surface combination stress due to the outside surface deformation of diaphragm and rib web under the action of vehicles. In addition，the closed stiffen

rib can only be welded outside，which is difficult to guarantee the quality of welding，so it is easy to fatigue failure. At present，the fatigue behavior study of orthotropic deck in China and full-scale fatigue test date，used for the engineering design，is very limited. To some extent，it restricted the application of orthotropic deck. Therefore，as a long-span cable-stayed steel bridge for engineering background，a full-scale fatigue test of orthotropic deck is conducted in this article. The aim of this fatigue test is to confirm the fatigue strength of typical fatigue detail and provide date basis for orthotropic deck reasonable design.

THE TEST SPECIMEN

The full-scale deck specimen used in this study consists of six trapezoidal ribs supported by the transverse floor beam. Q345C steel is used in the deck plate and ribs of deck，while Q345B steel used in other elements. The specimen dimensions and the details at the diaphragm cutout are shown in Figure 1. The dimensions of the deck are 1 800 mm in the longitudinal direction and 3 800 mm in the transverse direction.

As shown in the Figure 1，the thickness of the deck plate is 14 mm. The cross section of the rib is 300 mm (top width)×280 mm(height)，and the thickness of the rib is 8 mm. The longitudinal ribs are continues through 10 mm thick diaphragm. And the spacing of the longitudinal ribs is 600 mm. This specimen is a symmetrical structure with respect to the diaphragm.
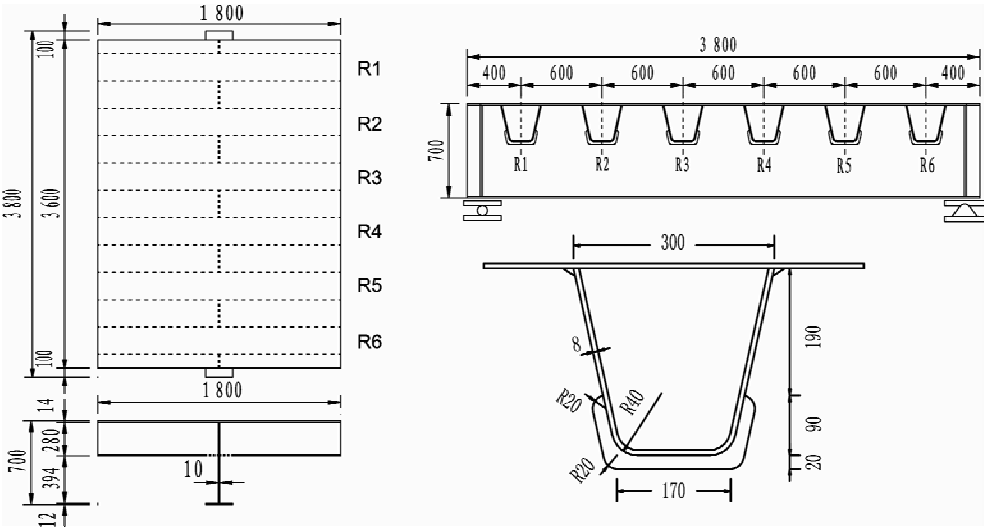
Figure 1　Size of full-scale model and rib (unit：mm).

TEST SETUP AND LOADING SCHEME

Without considering the effect of loading surfacing，two-point loading was applied on the deck plate through block rubber. The loading area was 200 mm(longitudinal)×300 mm(traverse) and the loading spacing was 1 200 mm in traversal direction. During the fatigue test，the deck was supported on two hinge supports. Figure 2 shows the test setup with an actuator locating on the deck.

Strain gauges and strain rosettes were instrumented. The measure points of fatigue test are shown in

Figure 3. The load amplitude adopted in the test was 200 kN，with the load ranging from 250 kN to 50 kN. Dynamic test was conducted with a loading frequency of 1Hz. After every 1million cycles，static test and visual inspections were carried out，and it was recorded the measurement from strain gauges and the information of fatigue cracks.
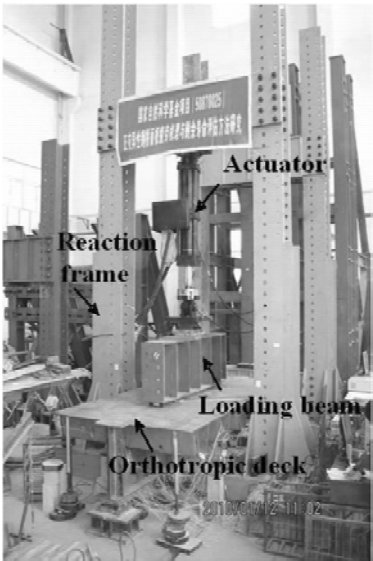
Figure 2   Test Setup of fatigue test.
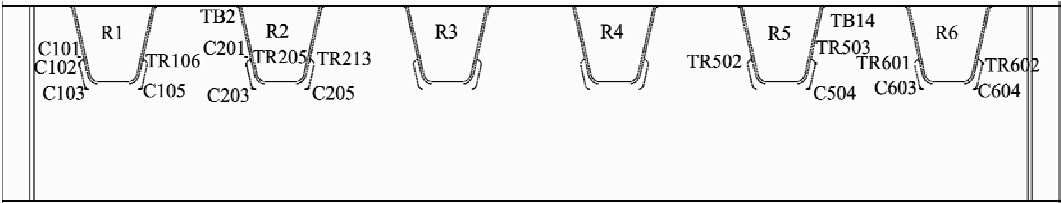
Figure 3   Measure points of fatigue test

FATIGUE CRACKS INVESTIGATED IN TESTING

Visual inspection with magnifying glass was conducted during the fatigue testing at the every end of 200 thousands loading cycles. Main elements prone to fatigue were investigated，including rib-to-deck，rib-to-diaphragm and cut-outs of crossbeam.

Crack In the Rib-To-Diaphragm

In vehicle loading action，the largest vertical stress of rib web is in the weld end of rib-to-diaphragm，combined with the effects of the welding residual stress and complex stress in and out of the diaphragm，making this location is very sensitive to fatigue crack. This kind of fatigue cracks mainly initiate from weld toe，and the crack growth directions include：extend in the diaphragm，in the rib web or extend along the vertical weld. Some fatigue cracks，desired from weld toe of rib-to-diaphragm connection and

expanded in rib web，were found during the test. At the end of rib-to-diaphragm connection of rib 5，the stress amplitude is 90 MPa. As is shown in Figure 4，fatigue cracks were found when the loading cycle up to reach 5 millions. When the fatigue test is finished，the fatigue crack of rib 5 and rib 6 are 54mm and 31mm，respectively.

Crack In the Cutouts

Fatigue cracks in the cutouts of diaphragm are generally perpendicular to the free edges and further expanded in the diaphragm. Geometric stress concentration and crack-like defects are the main reason for the initiation and expansion of these fatigue cracks. Strain test results indicated that there is larger strain in the corner of cutouts，but it did not change widely during the fatigue test. At the end of the test，no visual fatigue cracks were found in cutouts of the crossbeam.
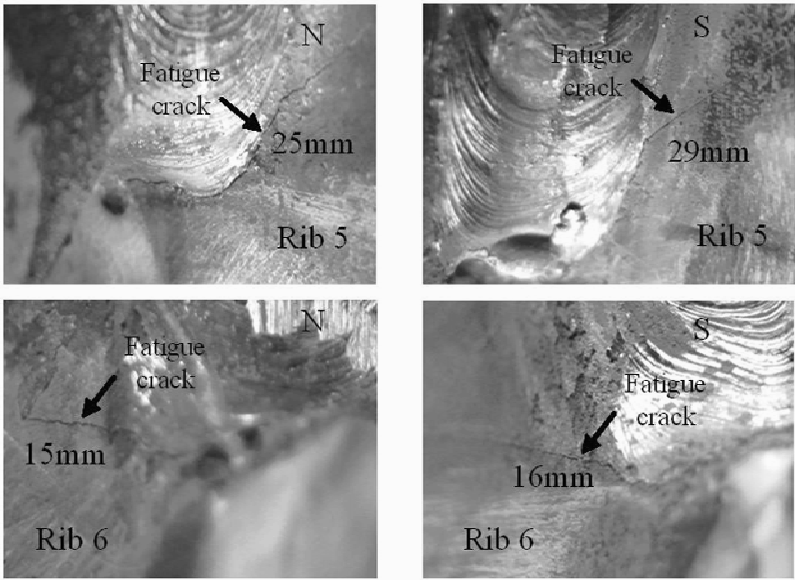
Figure 4   Typical crack development in rib-to-diaphragm connection

RESULTS OF THE FATIGUE TEST

Length Analysis of Fatigue Cracks

Visual inspection was conducted during the fatigue test. From the information of cracks length，We can conclude that the crack within the web of Rib 5 was firstly detected and this crack was longest. By comparing the cracks length between 10 million and 10.2 million，the cracks length at the Rib5 and Rib6 expanded nearly 10 mm. The change law of fatigue crack length with loading cycle was showed in Figure 5. In the Figure 5，it shows that the first as well as the longest fatigue crack is found at the web of rib 5，which is loaded directly. The fatigue cracks of the rib 5 web grow faster as the cycle increases. As the load cycles changed from 10 millions to 10.2 millions，it is found that the fatigue crack grow almost 10mm near the rib 5 web. From the information of Figure 5，it can confirm that fatigue cracks growth rate significantly increased when the loading cycle number accumulated up to a certain value，and

structure stays in an unstable stage of fatigue failure.
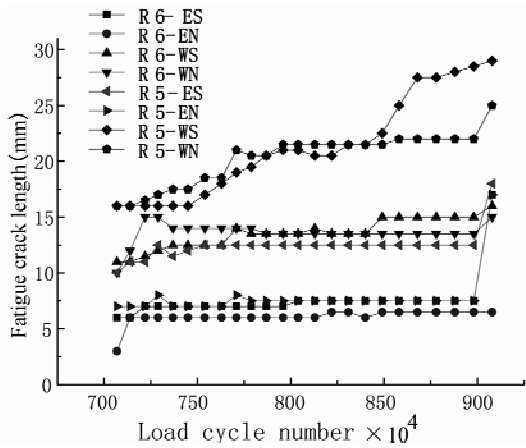
Figure 5   Curve of fatigue crack growth

Stress Analysis of Measure Points

The main parts stress of structure was measured by the dynamic strain meter during the fatigue test. The test results show that many measure points stress changed with the increase of the loading cycles. The curve of stress with the cycle number of the cutouts of the crossbeam measure points are respectively shown in Figure 6. Moreover，the numerical value of the greatly changed points is listed in Table 1. According to the analysis of the measured strain result，both of the measured and calculated strain at the rib-to-diaphragm connection of rib 5 and 6 showed that these sites were in compressive zone. However，the fatigue crack expends as a result of the welding residual stress，which make the welding residual stress can not be ignored in the fatigue performance analysis. The strain analysis of measure points near the fatigue crack suggests that strain of the strain will be changed suddenly and subsequent strain will decrease with the increasing of loading cycles，when the loading cycles accumulate to a certain number. Figure 7 (a) and Figure 7(b) show the location of measure points in S-N curve when the points stress changed or crack was visible. It can confirm that the fatigue strength of the rib-to-diaphragm is more than the D degree in the AASHTO[8] and the 63 degree in EUROCADE[9].
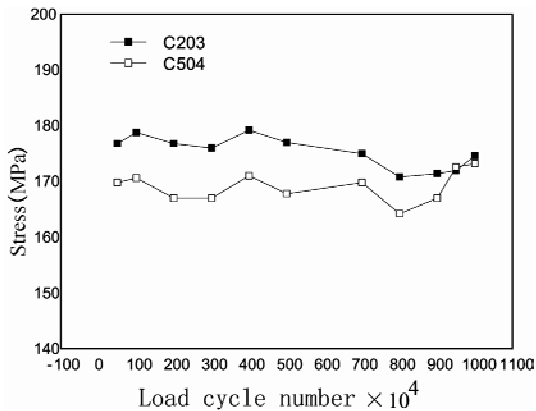
Figure 6   Stress at cutout

TABLE 1   STRESS OF MEASURE POINTS (NUIT: MPa)

Cycle number (million)	C501	C605	TR213	TR502	TR503	TR601	TR602	TC6
0	16.4	125.4	130.8	195.8	− 131.6	165.4	− 139.8	− 63.6
0.5	31	109.6	131.4	186	− 130	200	− 136.2	92.8
1	31.8	100.4	130.8	183	− 126.6	206	− 150.8	32.8
2	25	58.2	128.6	181.4	− 111.4	189.8	− 143.6	− 14
3	19.8	28.4	130.4	20.6	− 67.6	191.6	− 145.2	24.6
4	20.4	15.4	131.4	0.4	− 32.4	204	− 103.6	98.6
5	15.4	8.8	125.2	− 6.4	− 15.8	195	− 58.6	140.2
7	6	3.8	128.4	− 3.4	− 1.4	194.4	− 20.2	206.8
8	− 0.4	1.4	111.2	− 8.2	− 3.6	174.2	− 18	− 48
9	− 2.6	− 0.2	59	− 8.6	− 3.8	141.6	− 17.6	− 63.8
9.5	− 1.6	− 1.6	42.8	− 6.2	− 4.2	152.4	− 17	− 67
10	− 3.4	− 0.8	2.8	− 6.4	− 4.2	149.6	− 1.2	− 61
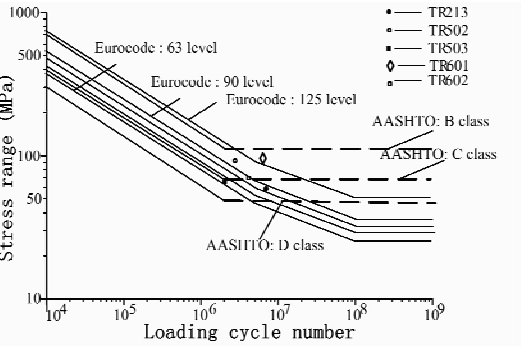
a. Test result of the points stress changed.   b. Test result of the crack is visible.

Figure 7   Fatigue test results of rib-to-diaphragm details

CONCLUSION

This paper describes the results of a full scale fatigue test of orthotropic steel deck. Fatigue test had an accumulation of 10.2 millions cumulative loading cycles and load amplitude was const as well as loading frequency. In this testing, fatigue cracks, initiated from the end of rib-to-diaphragm connection, and could be detected through naked eye. Static and dynamic test results indicate that the fatigue strength of the rib-to-diaphragm is more th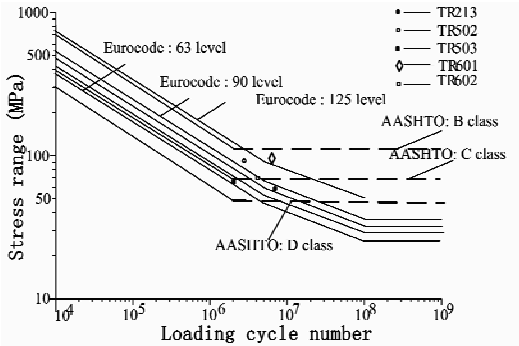an the D degree in the AASHTO and the 63 degree in EUROCADE. Fatigue cracks grew slowly at the early stage, but as the loading cycle accumulating to a certain number of cycles, cracks expanded rapidly.

ACKNOWLEDGEMENTS

and the China West Transportation Development Research Projects（Grant No. 20113185191410 and No. 200831849452）.

REFERENCES

［1］Gurney，T.，"Fatigue of steel bridge decks"，TRL State of the Art Review 8，1992.

［2］Tsakopoulos，P. A. and Fisher，J. W.，"Full-Scale Fatigue Tests of Steel Orthotropic Decks for the Williamsburg Bridge"，Journal of Bridge Engineering. 2003.

［3］Wang，C. S. and Feng，Y. C.，"Fatigue review of orthotropic steel bridge deck"，Steel Construction，2008，24（9）：10-13，32.

［4］Wang，C. S. and Feng，Y. C.，"Fatigue damage evaluation and retrofit of steel orthotropic bridge decks"，Key Engineering Materials. 2009.

［5］Xu，W. and Zhang，X. N.，"Analysis distress characters and design of steel orthotropic bridge decks pavement in China"，2008 International Orthotropic Bridge Conference，Sacramento，California，USA，Aug. 2008；184-192.

［6］Wang，C. S. and Feng，Y. C.，"Review of the fatigue behaviors and finite element analysis of orthotropic steel bridge decks"，2008 Orthotropic Bridge Conference，Sacramento，California，USA，2008；290-304.

［7］Feng，Y. C.，"Fatigue behavior research of orthotropic steel bridge deck"，Xi'an，Chang'an University，2009.

［8］AASHTO.，"LRFD bridge design specifications"，5th edition，Washington，D. C.，2010.

［9］Eurocode 3.，"Design of steel structures—Part 1-9，Fatigue"，2005.

EXPERIMENTAL STUDY OF FATIGUE PERFORMANCE OF TEMPERED GLASS PANELS UNDER CYCLIC LOADING

* G. P. Shu[1], H. Y. Li[1, 2], R. H. Lu[1]

[1] School of Civil Engineering, Southeast University, SiPaiLou 2, Nanjing, 210096, China
[2] School of Civil Engineering, Shijiazhuang Tiedao University, SShijiazhuang, 050043, China
* Email: sgp0818@vip.sina.com

KEYWORDS

Cyclic loading, tempered glass panels, fatigue strength, *S-N* curves, Goodman method.

ABSTRACT

The strength of the material is dependent on the distribution of cracks or surface flaws. These factors, coupled with the inherent brittleness, complicate the fatigue strength of tempered glass panels. This paper is concerned with fatigue performance of tempered glass panels under cyclic loading in room environment. It was found that the fatigue strength of glass panels depend very strongly on their static strength. And the experimental results give the evidence that they deserve the same high degree of scatter of strength. However, the linear *S-N* curves were used to fit the experimental data, and the Goodman method was employed to approximately account for the effect of mean load.

INTRODUCTION

Recently, a substantial increase in demand of point-supported curtain walls has occurred owing to its transparency, aestheticism and flexibility of construction. Composed by tempered glass panels, bolted connections and supporting system, point-supported curtain walls have outstanding performance in the use as a part of the building envelope. The main point to be noted is that the glass is generally vulnerable to failure compared to other components of the curtain walls due to a number of reasons, including its relatively lower tensile strength, high degree of scatter of strength and property of brittleness, etc. An additional problem with broken tempered glass in overhead applications is its tendency not to break into small parts. It may rather fall in large clumps, which could lead to serious human injuries and possible life threats. For the structural use of glass, it is required to meet serviceability conditions taking into account the possibility of any potential failure of glass element.

Several experimental and theoretical investigations have been conducted over the years, largely focusing on the strength of glass plates subjected to both static and dynamic loading[1-7]. However, there is a little attention to be focused on the fatigue strength of the tempered glass plates for its high scatter in the results under cyclic loading. Tests performed by Kaja Boxheimer and Johann-Dietrich Wörner[8] showed

that only four of the ten specimens failed before they reached 2 million load cycles. In their study，all specimens with different thickness of 4 mm，8 mm and 12 mm are 500 mm in length and 100 mm in width. Prior to the recognition that brittle solids exhibit fatigue effects，Evans，A. G. and Fuller，E. T. [9] have developed a method to compute the time-to-failure due to cyclic loading as a function of the static crack growth curves. For brittle materials，Jacobs，D. S. ，Chen，I. W. [10] have been proposed a modified Paris Law for cyclic crack growth that expresses crack growth as a function of the maximum stress intensity factor and the difference between the maximum and minimum stress intensity during a cyclic load. Using these studies in ceramics，Keith B. Doyle and Mark A. Kahan[11] indicated that predicting the strength of the glass subjected to dynamic or cyclic stress levels is more complicated and the conservative estimates of glass strength are recommended. A subsequent report by SHI Yongjiu and HE Xiaoping，etc[12] produces some high frequency fatigue tests on monolithic and laminated glass panels. It shows that no fatigue phenomenon appears on the specimens with real size under actually cyclic loading conditions.

In this paper，the bending fatigue performance of the tempered glass plates with real size has been investigated under cyclic loading at room temperature. The *S-N* curves are derived from results on samples of the material to be characterized where a regular sinusoidal load is applied by a testing machine which also counts the number of cycles to failure，and the Goodman method was employed to approximately account for the effect of mean load. Also the relationship about static strength and fatigue strength is investigated to demonstrate the bending fatigue property of the tempered glass plates.

EXPERIMENTAL PROCEDURE

Preparation of Glass Specimens

Commercial tempered glass panels were used in these experiments（Shanghai Yaohua Pilkington Glass Co.，Ltd.）. The glass was procured in the form of 1 000 mm×1 000 mm×12 mm plates. To enhance the probability of surface defects at edges all specimens had polished edges. The composition of the glass was 72.5 wt% SiO_2，13.0 wt% Na_2O，0.3 wt% K_2O，9.3 wt% CaO，3.0 wt% MgO，1.5 wt% Al_2O_3，0.1 wt% Fe_2O_3. The mechanical properties adopted by Design Standard[13] are as follows：young's modulus，0.72×105 MPa，Poisson's ratio 0.2.

Test Facility

The test used to apply the static and cyclic loading to the glass panels is schematically shown in Figure 3，with a servo-hydraulic testing machine of 30kN dynamic capacity being the major apparatus. Particular care was taken to ensure precise contact at the load application points to avoid unequal load transfer to the glass panels. In particular，flexible rubber with 2mm thickness was inserted between actuator and glass panel to avoid any frictional contact which could probably cause additional damage on the surface of glass panel.

Test Procedure

For the simulation of positive wind pressure and saving the tests cost，the load wave was sinusoidal with constant amplitude with frequency of 2 Hz. The fatigue tests were performed in tension-tension. For the

some specimens at higher load levels in the fatigue tests. This may be attributed to the special fatigue properties of tempered glass panels determined by the static strength and the high degree of scatter in strength. It should be pointed out that all specimens failed during the fatigue tests were withstanding no more than 5×10^4 cycles.

TABLE 2   FATIGUE EXPERIMENTAL RESULTS

Sample	Load range（kN）	Cycle range（kN）	Ratio	Cycles	Remark
DC-1a	2～10	8	0.20	949	failed
DC-1b	2～10	8	0.20	407	failed
DC-1c	2～10	8	0.20	1 512	failed
DC-2a	2～9	7	0.22	34 340	failed
DC-2b	2～9	7	0.22	0	failed
DC-2c	2～9	7	0.22	12 626	failed
DC-3a	2～8	6	0.25	6 185	failed
DC-3b	2～8	6	0.25	500 000	did not fail
DC-3c	2～8	6	0.25	500 000	did not fail

Constant Amplitude S-N Curve

To predict the fatigue life of tempered glass panels under this cyclic loading condition，it is necessary to establish the corresponding constant amplitude *S-N* curves where *S* is maximum cyclic load and *N* is number of cycles to failure. The number of load cycles at the fatigue strength limit is defined to be 5×10^4 cycles，according to fatigue testing done in this paper. The *S-N* curves can be obtained by fitting constant-amplitude fatigue test results into the following equation：

$$N = cS^b \tag{1}$$

Where *c* and *b* are the constants to be determined.

Using linear regression analysis of the constant-amplitude repeated load test results，the *S-N* curve for the tempered glass panels is found to be

$$S^{21.645} N = 2.836\ 7 \times 10^{24} \tag{2}$$

Where *S* is in kN.

The *S-N* curve for tempered glass panels is plotted in Figure 5. It should be noted that all the loading ranges used in the constant-amplitude load tests were from 2 kN to various maximum loads. However，the simulation of positive wind pressure can start from various minimum loads to various maximum loads. Therefore，*S-N* curves that can take the effect of various mean levels into account should be found.

In this paper，the Goodman method，which is widely used to account for the effect of mean stress，is analogically used to approximately account for the effect of mean load. For a given load range and load ratio，an equivalent load range with different load ratios can be concluded using this method. The equivalent ranges given by the Goodman methods are based on the following equations：

$$\frac{S_r}{S_{re}} + \frac{S_m}{S_u} = 1 \tag{3}$$

Where S_r is load range，S_m is mean load，S_u is ultimate load of tempered glass panel，and S_{re} is equivalent load range with zero mean level.

Using the Goodman method，the *S-N* curves with different load ratios for tempered glass panels are concluded，respectively：

$$S^{16.812} N = 3.351\ 3 \times 10^{19}，\text{ for } r = 0 \tag{4}$$

$$S^{19.516} N = 4.696\ 1 \times 10^{17}，\text{ for } r = -1 \tag{5}$$
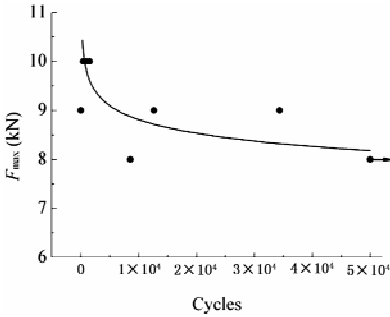
Figure 5   S-N curve for tempered glass panel   **Figure 6   S-N curves with different load ratios**
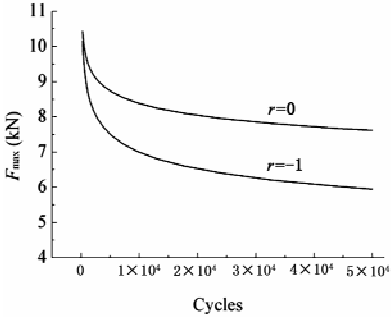
Relationship between Static Strength and Fatigue Strength

Several previous studies showed that the cyclic fatigue strength appears to be very close to the static strength of tempered glass panels. In this paper，the relationship between static strength and fatigue strength has been investigated on the basis of static and fatigue experiment results. The maximum load of load ranges normalized with respect to mean ultimate static strength versus the number of cycles is shown in Figure 7(a). The started load levels for cyclic loading in this paper could be selected at 95% of mean ultimate static strength. Fatigue strength was found to be approximately of 75% of mean ultimate static strength at 5×10^4 cycles. Therefore，the fatigue phenomenon of tempered glass panels could only occur within a narrow zone of load levels at approximately 75%~95% of mean ultimate static strength. Using the Goodman method，the relationship between the fatigue strength and static strength with different load ratios can be concluded，as illustrated in Figure 7(b) − (c). It can be shown that the values are
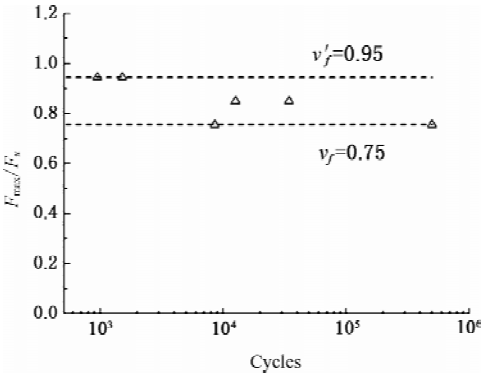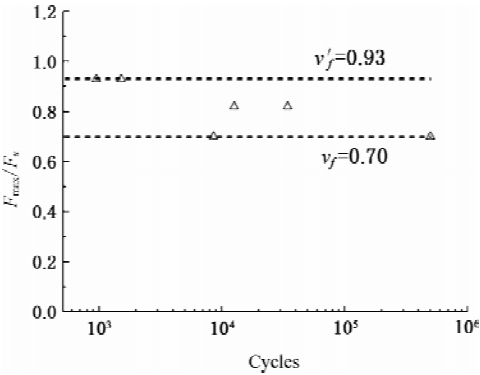
(a) Test results   (b) Load ratio($r = 0$)
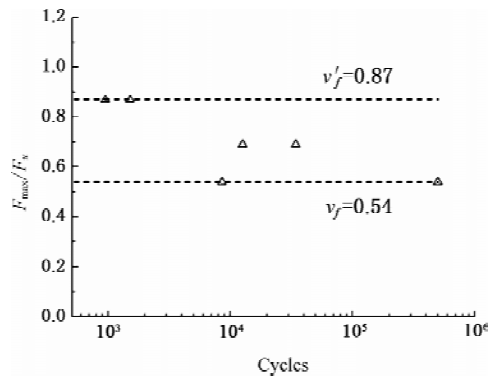
(c) Load ratio ($r = -1$)

Figure 7   Relationship between fatigue strength and static strength

different with different load ratios for the effect of various mean levels. These correlations can only be used for the qualitative descriptions of fatigue behaviour due to lack of more cyclic testing results with different load ratios. However, it's still helpful for understanding the fatigue performance of tempered glass panels.

CONCLUSION

A series of constant-amplitude repeated load tests was performed on the full-size tempered glass panels with realistic support conditions. In the load levels studied here, the linear *S-N* curves were used to fit the experimental data, and the Goodman method was employed to approximately account for the effect of mean load. The test results show that the tempered glass panels exhibit a high degree of scatter both in static strength and fatigue strength. It is interesting to notice that all specimens failed during the fatigue tests was withstanding no more than 5×10^4 cycles. In the fatigue tests, the started load levels for cyclic loading in this paper could be selected at 95% of mean ultimate static strength. Fatigue strength was found to be approximately of 75% of mean ultimate static strength at 5×10^4 cycles. Therefore, the fatigue phenomenon of tempered glass panels could only occur within a narrow zone of load levels at approximately 75% ~ 95% of mean ultimate static strength. So, the test results show that fatigue behaviour of tempered glass panels was found to be largely dependent on their static strength which was quite different from metals.

ACKNOWLEDGEMENT

REFERENCES

[1] Wang, Y.Q., Yang, W., Liang, Y.F. and Shi, Y.J., "Analysis of load bearing properties of four point-supported glass plate in point-supported glazing building", Engineering Mechanics, 2002, 19(6), pp. 63–66.

[2] Shi, Y.J., Deng, X.W. and Wang, Y.Q., "Study on overlap-connected glass curtain wall and bearing capacity of its glass panel", Industrial Construction, 2005, 35(2), pp. 11–15.

［3］Wang，Y.Q.，Liang，Y.F.，Shi，Y.J. and Ma，Y.，"Failure stress analysis around the hole in point supported glass panels"，Engineering Mechanics，2005,22(5),pp.147-152.

［4］Hong，T.H. and Li，H.N.，"Study on dynamic performance of monolayer cable net point-supporting glass curtain wall under wind load"，Journal of Disaster Prevention and Mitigation Engineering. 2008,28(2),pp.156-162.

［5］Norville H Scott and Conra Edwan J.，"Blast-resistant glazing design"，Journal of Architectural Engineering，2006,12(3),pp.129-136.

［6］Azouaoui K.，Rechak S. and Azari Z.，"Modelling of damage and failure of glass/epoxy composite plates subject to impact fatigue"，International Journal of Fatigue，2001(23),pp.877-885.

［7］Lhymn C.，"Impact fatigue of PPS/glass composites-theoretical analysis"，Journal of Materials Science Letter，1985(4),pp.343-350.

［8］Kaja Boxheimer and Johann-Dietrich Wörner.，"Fatigue strength of glass panels under cyclic loading"，Structural Engineering International，2004(2),pp.126-128.

［9］Evans，A.G. and Fuller，E.R.，"Crack propagation in ceramic materials under cyclic load conditions"，Met. Trans，1974(5),pp.27-33

［10］Jacobs，D.S. and Chen，I.W.，"Cyclic fatigue in ceramics：a balance between crack shielding accumulation and degradation"，J. Am. Cer. Soc，1995(78),pp.513-520.

［11］Keith B. Doyle and Mark A. Kahan.，"Design strength of optical glass"，SPIE Vol. 5178(4)，San Diego，CA，Aug2003.

［12］Shi，Y.J.，He，X.P. and Wang，Y.Q.，etc. "Fatigue tests of single layer and laminated glass plates with point supports"，Journal of Tsinghua University (Science and Technology)，2010,50(3),pp.346-350.

［13］"Technical specification for point-supported glass curtain wall"，CECS 127：China Association for Engineering Construction Standardization，2001.

［14］"Research of endurance capability of glass and the key link site of point-supported glass curtain"，Master's Degree Thesis of Southeast University，China，2008

TEST ON STAINLESS STEEL WELDED I-COLUMNS

[*] G. P. Shu[1]，B. F. Zheng[1]，X. M. Shen[2]

[1] School of Civil Engineering，Southeast University，Sipailou 2，Nanjing，210096，China
[2] Suzhou Industrial Park Design & Research Institute，Suzhou，215020，China
[*] Email：sgp0818@vip.sina.com

KEYWORDS

Stainless steel，welded I-section，flexural-buckling，columns，test.

ABSTRACT

In this paper a series of tests on welded I section columns of Grade 304 were conducted. FEM model were then developed considering nonlinear material properties，geometric imperfections and residual stress. Effects of cold working enhancement of the shearing edge and residual stress due to welding were evaluated. The flexural buckling strength of the welded I-columns increased by 2%～3% when taking shearing edge enhancement into consideration，and decreased by 6%～7% for buckling in minor axis due to the existence of residual stress. Welding has considerable influence on the buckling resistance of columns，especially for stub columns. Comparisons between the tests results collected and the predictions of the American，European specification and the formula proposed by Zheng were carried out. These comparisons point out that：predictions of the European specification for minor axis and the formula of Zheng could fit the result of tests well，and could be used to design stainless welded I-columns.

INTRODUCTION

Stainless steel is an ideal structural material. Its excellent corrosion-resistance，long-lasting property and perfect appearance of architecture satisfy both structure engineers and architects at one time. The amount of stainless steel used as structural material has increased sharply in resent years. Although the predominant type of members used in buildings is still thin-walled members，welded members will be the competitive selection in corrosive environment with high demand in load resistance（such as Water treatment work）.

In this paper，tests on welded I-columns were described，and ANSYS were employed to study the effects of residual stress and shearing edge enhancement. At last test results from other researchers were collected and compared with strengths calculated using the American[1] and European[2] specifications and the formula proposed by Zheng[8].

TEST PROGRAM

In this test，Austenitic 304 was selected for its wide use in construction. The surface of the plate was No.

1 with color in silvery white. Firstly the plates were cut into strips using shearing machine，and then strips were welded into I-sections using TIG welding. The test program consisted of 6 material coupons in tension，2 stub columns and 7 long columns. 4 of these columns were designed to buckle in major axis and others were designed to buckle in minor axis. Prior to the test，geometric imperfections were measured including local imperfections and overall imperfections in both major axis and minor axis. Table 1 summarizes the geometric information.

TABLE 1   MEASURED DIMNSIONS AND IMPERFECTIONS

Test Type	Specimens	Length L(mm)	Depth H(mm)	Width B(mm)	Thickness t(mm)	Imperfection(mm) Major	Minor	Ultimate Load F(kN)
Stub column	H-S-a	400				1.17	1.08	530
	H-S-b	400				1.51	0.44	548
Major axis	H-L-1500 M	1 580				0.79	1.33	341
	H-L-2000 M	2 080				2.39	1.39	297
	H-L-2500 M	2 580	100	100	5.85	2.39	2.35	284
	H-L-3000 M	3 080				1.81	2.73	224
Minor axis	H-L-1500 R	1 580				2.01	1.87	268
	H-L-2000 R	2 080				1.97	1.17	209
	H-L-2500R	2 580				0.99	11.45	136

Material Tests

Stainless steel is sensitive to cold working，especially for Austenitic stainless steel. As introduced formerly，the plates were cut using shearing machine. Therefore，the material property around the shearing edge may be different from the virgin plate. Coupons from the central part of web（HZ-x）and that from the shearing edge（HB-x）were extracted from the untested columns using Spark Cutting. The coupons were tested in a 100 kN capacity MTS displacement controlled testing machine using friction grips. The load rate was 1 mm/min controlled by the machine automatically. A pair of stain gauges was pasted on each face of the coupon，so the stain-stress curve could be available till the stain gauge peeled off from the coupon. Figure 1 gives test assignment and details of the coupons. Test results were analyzed according to Eqn. 1 proposed by Gardner[3]. In this equation，σ and ε are engineering stress and strain respectively，E_0 is the initial Young's modulus，$\sigma_{0.2}$ is the 0.2% proof stress（also called yield strength），n is a strain hardening exponent，$\sigma_{1.0}$ is the 1.0% proof stress and $n_{0.2,\ 1.0}$ is a strain hardening coefficient representing a curve that passes through $\sigma_{0.2}$ and $\sigma_{1.0}$. Table 2 shows the material properties from tension tests.

We can see from the test result that the proof strength and ultimate strength of the coupons from the shearing edge was 20 Mpa higher than those of the center of the web. Other parameters of Eqn. 1 were kept the same.

$$\begin{cases} \varepsilon = \dfrac{\sigma}{E_0} + 0.002\left(\dfrac{\sigma}{\sigma_{0.2}}\right)^n & \sigma \leqslant \sigma_{0.2} \\ \varepsilon = \dfrac{\sigma - \sigma_{0.2}}{E_{0.2}} + \left(0.008 - \dfrac{\sigma_{1.0} - \sigma_{0.2}}{E_{0.2}}\right)\left(\dfrac{\sigma - \sigma_{0.2}}{\sigma_{1.0} - \sigma_{0.2}}\right)^{n'_{0.2,\ 1.0}} + \varepsilon_{t0.2} & \sigma_{0.2} \leqslant \sigma \leqslant \sigma_{2.0} \end{cases} \tag{1}$$
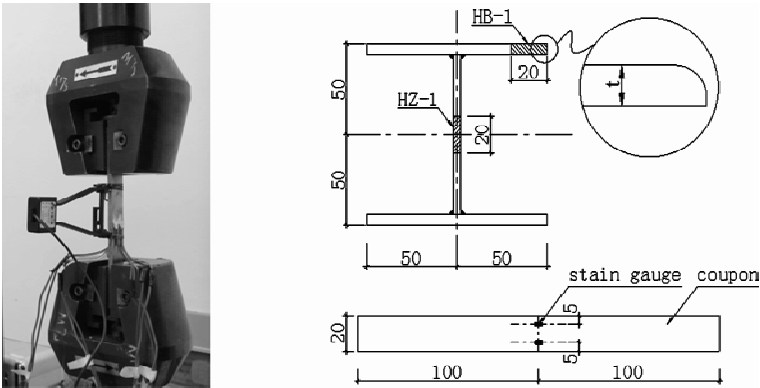
Figure 1   Sketch of the test and details of the coupon

TABLE 2   MEASURED MATERIAL PROPERTIES

Specimens	E_0	$\sigma_{0.01}$	$\sigma_{0.2}$	$\sigma_{1.0}$	$\sigma_{max.}$	$e_{t0.2}$	$e_{t1.0}$	n	$n_{0.2}$
HB − 1	189 347	91.13	249.30	298.88	708.77	0.003 2	0.011 6	2.98	2.00
HB − 2	181 645	104.33	267.89	307.19	700.17	0.003 7	0.011 7	3.18	1.70
HB − 3	184 405	118.69	271.02	325.23	687.55	0.003 5	0.011 8	3.63	2.30
AVG. HB	185 132	104.72	262.74	310.43	698.83	0.003 4	0.011 7	3.26	2.00
HZ − 1	192 295	93.23	235.76	283.96	674.84	0.003 0	0.011 5	3.23	2.30
HZ − 2	190 535	107.32	242.51	283.86	671.49	0.003 3	0.011 5	3.67	1.80
HZ − 3	184 632	103.49	247.10	291.45	672.08	0.003 3	0.011 6	3.44	2.00
AVG. HZ	189 154	101.35	241.79	286.43	672.80	0.003 2	0.011 5	3.45	2.03

Stub Column Tests

Stub column tests were conducted in a 300 kN capacity SCHENCK testing machine. Prior to the tests，all the ends of the stub columns were milled flat to ensure full contact with the load plate of the test machine. Eight stain gauges settled in edge and the center of the web and flange were used to install the specimens to ensure concentric loading. Four displacement transducers（LVDT）were used to measure the axial shorting of the specimens，and the average value was used as end-shorting. The full image of the test arrangement is shown in Figure 2. The test strengths are listed in Table 1. Full range load-displacement curves are presented in Figure 3.

All specimens failed in local buckling. Although the local imperfections of the stub column in this test were large（Avg. = 1.05 mm），plates of the section could keep flat until the load step just before the ultimate load（about 450 kN）. The deformation of the distorting of the flange and the end shoring happened in large amount at the load step around the ultimate load. Material properties from stub column tests are shown in Table 3. The initial elastic module from stub column tests is lower than that from tension tests due to the existence of the residual stress. The proof strength from stub column test is close to that from tension tests of shearing edge.
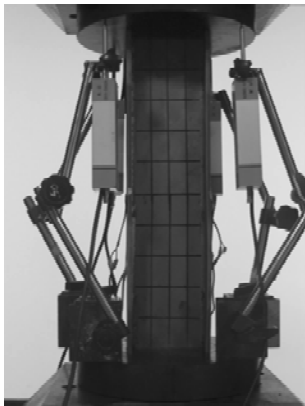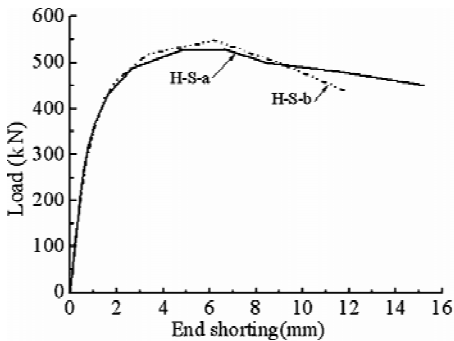
Figure 2　Sketch of the Stub column tests　　**Figure 3　Load-End shorting Curves of stub column**

TABLE 3　MEASURED MATERIAL PROPERTIES

Specimens	E_0	$\sigma_{0.01}$	$\sigma_{0.2}$	n
H-S-a	174 737	119.92	265.75	3.76
H-S-b	179 987	131.26	256.14	4.48
AVG.	177 362	125.59	260.95	4.12

Long Column Tests

The long column specimens were tested in a 5 000 kN capacity hydraulic test machine with the maximum length up to 5 m. Test arrangement is shown in Figure 4. Columns were tested in pinned end condition. One way knife edge was used to realize pinned end condition in one direction and fixed end in the other condition. The knife edges were settled at both the end of columns. There was no rig settled at the middle of the specimens to restrain the lateral deformation in fixed direction. Clamps were designed to prevent the unwanted sliding. On the other side，they can be adapted to fit different section easily. Details of the clamps are given in Figure 5.

Tests were performed in a displacement-control model using screw jack. The use of displacement control allowed the tests to be continued into the post-ultimate range. Screw jack was placed on the ground plate of the test machine. A LVTD fixed under the end pate of the column helped to control the rate of loading. Figure 6 shows the loading system in detail.

Four LVTDs were located at each corner of the end plate both at the bottom and top respectively. So the rotation and the end-shorting of the column could be obtained. Three LVTDs were assigned at the middle height of the column，two in the pinned direction and one in the fixed direction. At the top of the column a load cell was used to obtain the accurate load.

The ultimate loads are given in Table 1. In Table 1，the length of the column is the distance between the hinges，which includes the thickness of the end plate. Figure 7 and Figure 8 presents the load-lateral displacement curves and load-end shorting curves respectively.

All the test specimens failed in the flexural buckling，and no local buckling was detected before ultimate strength. In general，at the beginning of test in the major axis，displacement increased both in the pinned direction and the fixed direction. As the load increased，the displacement in pinned direction increase in a

high speed compared to that in fixed direction. However，there was no displacement in major direction appearing for tests in minor axis. After tests the deformation of the column recovered in large degree.
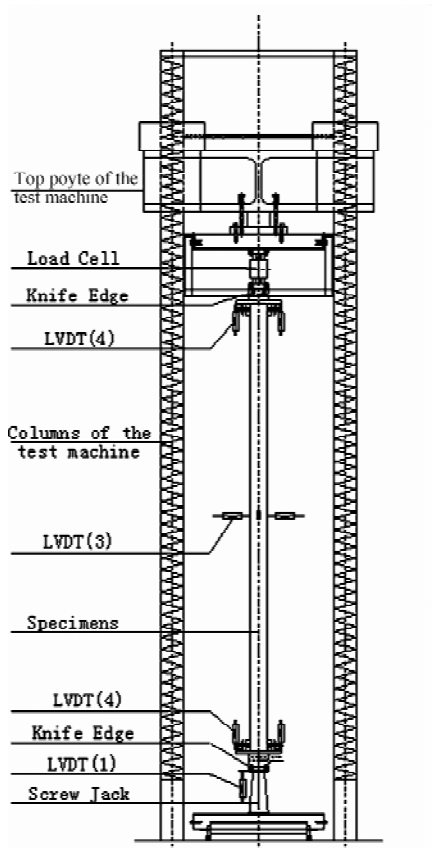
Figure 4   Sketch of the long column tests
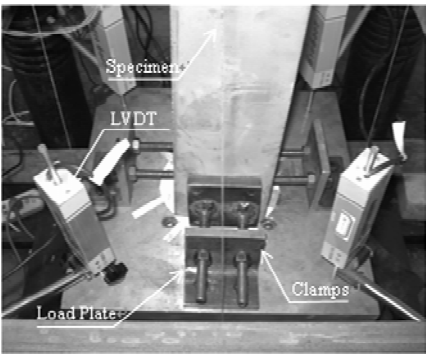
Figure 5   Fixture of the specimens
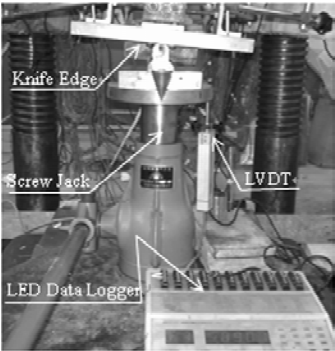
Figure 6   Detail of the loading system
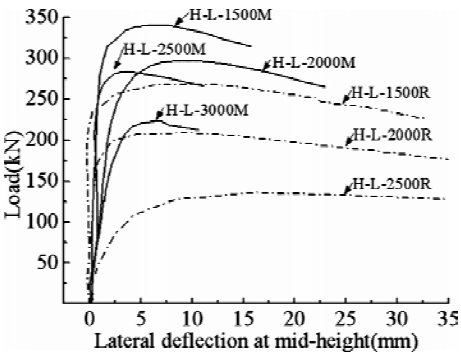
Figure 7   Load-lateral deflection curves
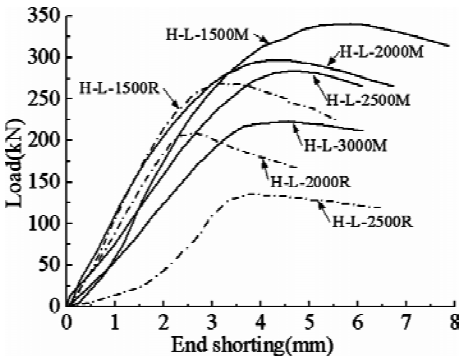
Figure 8   Load-end shorting curves

FEM ANALYSIS

In this section，ANSYS was employed to analysis the specimens using the information obtained from tests

including material and geometric properties. The effects of material enhancement at the shearing edge and residual strength were investigated.

Material Model

Material model proposed by Gardner[3] was used. Prior to applying material curve into the FEM model，the normal stress and strain were transferred into real stress and strain. Material curves used in FEM model are shown in Figure 9.

Geometric Imperfection

Both the local and the overall imperfections were taken into consideration. The model of Eigenvalue buckling analysis was employed as the pattern of the imperfection. Measured imperfection was used as the amplitude of the overall imperfection. The amplitude of the local imperfection was 1.05 mm that was the average value of test result of stub columns.

Residual Stress

Wang[7] studied the residual stress in the stainless steel welded I-section. He tested the residual stress in welded I-section of Grade 316 and modified the distribution model for stainless steel. So the residual model proposed by Wang was used in this paper. Figure 10 shows the residual model and the residual stress distribution in FEM model.
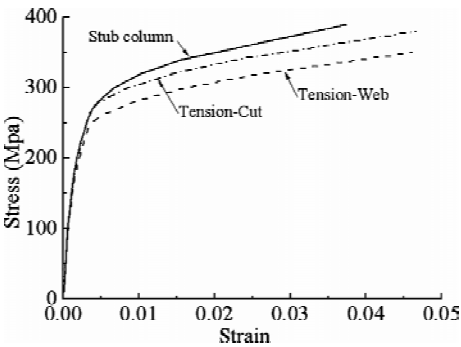
Figure 9   Material curves in FEM
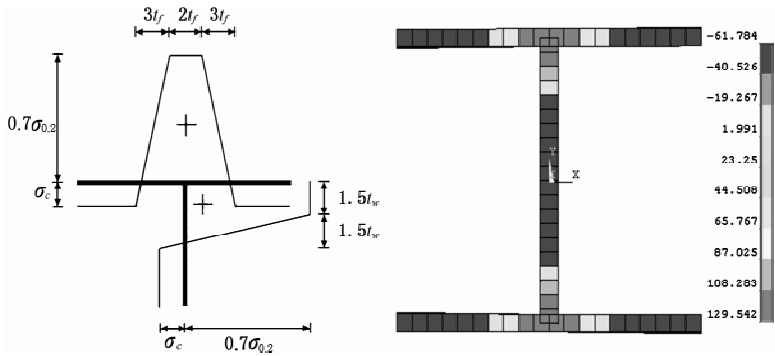
Figure 10   Residual stress distribution model proposed by Wang

Analysis Result

Using the FEM model developed，five models for each specimen were analyzed. These are：the model using material properties of web coupons（F_w），the model considering the strength enhancement of the shearing edge（F_c），the model considering residual stress but no strength enhancement（F_r），the model considering residual stress and strength enhancement（F_{r+c}）and the model using material property of stub column test（F_s）. The results are listed in Table 4.

From Table 4，we can see that the ultimate strength can be obtained accurately using FEM，and the average deviations were lower than 5%. As the differences among those five models were concerned，those conclusions below could be dawn：

1. The ultimate strength increases by 2%～3% when the shearing edge enhancement is taken into consideration.

2. The influence of the residual strength is different between the columns buckling in major axis and minor axis. Residual stress has no effect on the ultimate strength of columns buckling in major axis. However，the ultimate strength for columns buckling in minor axis would decrease by 6%～7% when residual stress was considered. This is due to the residual stress model where compression stress exists at the far end of the neutral axis.

3. The ultimate strength calculated using material properties from stub column test are higher than the test strengths and the ultimate strength of stub column from FEM analysis is lower than the test in large degree which also be mentioned by Gardner[4] and Bredenkamp[5]. That maybe attribute to the welding. On one hand，the area of the section increases，and more important welding is made of duplex stainless steel with high strength. On the other hand，the heart expressed in the welding process changes the micro structure of the region alongside welding which improves the material strength of the heat affected zone.

TABLE 4   COMPARISON AMONG THE RESULTS OF FEM ANALYSIS

Test Type	Specimens	Ultimate Load F(kN)	F_w/F_t	F_c/F_t	F_r/F_t	F_{r+c}/F_t	F_s/F_t
stub columns	H-S-a	530	0.846	0.870	0.845	0.868	
	H-S-b	548					
major axis	H-L-1500 M	341	1.086	1.111	1.084	1.109	1.160
	H-L-2000 M	297	1.034	1.055	1.039	1.064	1.099
	H-L-2500 M	284	0.941	0.967	0.948	0.959	1.000
	H-L-3000 M	224	1.045	1.063	1.061	1.079	1.128
minor axis	H-L-1500 R	268	0.964	0.994	0.905	0.937	1.026
	H-L-2000 R	209	0.980	1.004	0.897	0.925	1.048
	H-L-2500 R	136	0.875	0.896	0.817	0.842	0.929
	Avg.		0.989	1.013	0.964	0.988	1.056
	S. Dev		0.071	0.071	0.099	0.098	0.080

COMPARISONS

In this section，comparisons between test result and design specification were carried out. Test results around the world were collected. Little test results of stainless steel welded section is available around the

world. Bredenkamp[5] reported column tests on welded I $140 \times 70 \times 4.0 \times 3.5$ and I $180 \times 90 \times 6.0 \times 4.5$, and the material was 3CR12. Burgan[6] reported tests on welded I $160 \times 80 \times 6 \times 10$ and I $160 \times 160 \times 10 \times 6$, and the material were austenitic 1. 403 1 （S304） and duplex 1. 446 2 （S31803）. It is necessary to mention that the test results from Bredenkamp[5] need to determine the effective width before calculation of ultimate strength. To clarify the point，results from Bredenkamp[5] were not included in comparison. Test results from Burgan[6] together with those in this paper were compared with predictions of the European，American specifications and formula proposed by Zheng[8]. Comparison results are given in Figure 11.

European specification adopted Perry formula as the basic design expression to design columns. Curves for different section were identified by a series of parameters （imperfection factor α and limiting slenderness λ） in Perry formula. For welded I column buckling in major axis and in minor axis，these parameter are （$\alpha = 0.49$, $\lambda = 0.20$） and （$\alpha = 0.76$, $\lambda = 0.20$），respectively. American specification adopted Tangent Elastic Modulus Method，and curves varied for different material properties. Iteration would be encountered in the solution of buckling stress. Formula proposed by Zheng was based on FEM analysis and the concept was similar to that in the paper by Kim Rasmussen[9]. It took Perry formula as the basic expression，and a new expression for slenderness λ was proposed to account for the nonlinear properties of stainless steel. Design formulas in American code and Zheng need three parameters （E_0, $\sigma_{0.2}$, n） of Osgood-Ramberg equation. Material properties from web coupon tension tests were used in these formula （$E_0 = 189\ 154$ Mpa, $\sigma_{0.2} = 241.79$, $n = 3.45$）. In all these calculations，the partial factors （such as γ_m in European code） were set to 1.0.
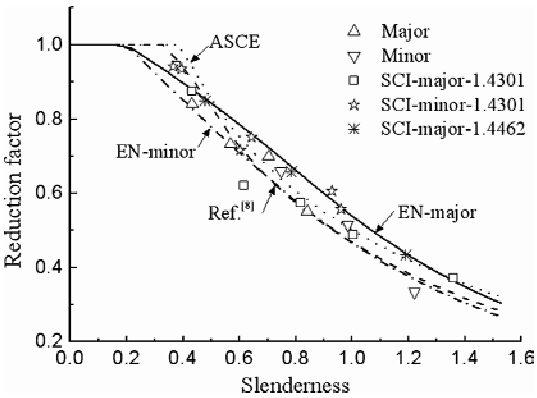
Figure 11   Comparisons between test results and predictions of the codes

From Figure 11，those conclusions below could be dawn：
1. Test results of columns buckling in major axis mixed with that of minor axis，and there are no sign that column buckling in major axis owns higher strength than one buckling in minor axis when their slenderness is the same.
2. According to European code，predictions of the formula for major axis is higher than test results. And prediction curve for minor axis almost along the down side of test result could be used as the design formula.
3. Predictions of the American code lie between prediction curves of European code for the major axis and that for the minor axis for the intermediate slenderness specimens. For the specimens with small slenderness，predictions of American code were unconservative. However it should be mentioned that American code is design specification only for cold formed members.

4. Predictions from formula proposed by Zheng could fit test results well in the full range，and could be used as the design formula for welded I-columns.

CONCLUSIONS

Tests on welded I-section were reported. And comparisons among tests results，FEM analysis and design specifications were conducted. The following conclusions could be obtained：

1. Material alongside the shearing edge was enhanced during the cutting process. That enhancement improves the strength of welded I-columns by 2%～3%.

2. The strength of welded I-columns buckling in minor axis decrease by 6%～7% due to the residual stress.

3. It is unnecessary to develop design formula for major axis and minor axis separately，when taking the effect of shearing edge enhancement and residual stress into consideration.

4. Formula in European code for column buckling in minor axis and formula proposed by Zheng could be used as the design formula for stainless steel welded I-columns.

REFERENCES

［1］ASCE.，"Specification for the design of cold-formed stainless steel structural members"，American Society of Civil Engineers，SEI/ASCE-8-02，Reston，Virginia，2002.

［2］EC3.，"Eurocode 3：Design of steel structures—Part 1. 4：General rules—supplementary rules for stainless steels"，European Committee for Standardization，ENV 1993-1-4，CEN，Brussels，2006.

［3］Gardner，L. and Nethercot，D. A. "Experiments on stainless steel hollow sections-part 1：material and cross-sectional behavior"，Journal of Constructional Steel Research，2004,60(9),pp.1291-1318.

［4］Ashraf，M.，Gardner，L. and Nethercot，D. A. "Finite element modeling of structural stainless steel cross-sections"，Thin-Walled Structures，2006 44(10),pp.1048-1062.

［5］Bredenkamp，P. J. and Van den Berg，G. J.，"The Strength of stainless steel built-up I-section columns"，Journal of Constructional Steel Research，1995,34(2-3),pp.131-144.

［6］Burgan，B. A.，Baddoo，N. R. and Gilsenan，K. A.，"Structural design of stainless steel members-comparison between Eurocode 3，Part 1.4 and test results"，Journal of Constructional Steel Research，2000,54(1)，pp.51-73.

［7］Wang，Y. Q. and Guan，J.，"Experimental study on the residual stress of austenitic stainless steel 316 at I-section"，Industrial Building，2011（In Press in Chinese）.

［8］Zheng，B. F.，"Theoretical and experimental investigations on cold-formed stainless steel columns and beam-columns"，Master Thesis，School of Civil Engineering，Southeast University，2010.（In Chinese）.

［9］Rasmussen，K. J. R. and Randall，J.，"Explicit approach to design of stainless steel columns"，Journal of Structural Engineering，ASCE，1997,123(7),pp.857-863.

RESIDUAL STRESS INFLUENCE ON MULTIPLE CONTACT FATIGUE

[*] M.J. Pazdanowski

Faculty of Civil Engineering，Cracow University of Technology，
ul. Warszawska 24，31-155 Cracow，Poland
[*] Email：plpazdan@cyf - kr. edu. pl

KEYWORDS

Cyclic load，rolling contact，contact fatigue，residual stresses，mechanical model，fatigue criterion，fatigue strength，numerical techniques.

ABSTRACT

Multiple contact fatigue（MCF）constitutes an important aspect of safe operations for any metallic structure subject to cyclic loads. It may have various forms（plastic deformations，macro and micro pitting，spalling，crack initiation from inclusions，etc.）and is interacting with wear[1, 2]. Such kind of fatigue may occur when service（contact）loads arising in the structure exceed elastic bearing capacity of the material. In order to correctly estimate the fatigue limit one has to be able to determine the stresses in considered body in any moment in time. A mechanical model to evaluate residual stresses in an elastic perfectly plastic body subject to cyclic loads remaining within load envelope known had been developed some time ago[3, 4]，thoroughly tested[5]，generalized to the case of material exhibiting kinematic hardening[6] and applied successfully to determine residual stresses in railroad rails and wheels[7, 8]. Estimated residual stresses added to momentary elastic stresses，computed as if the considered body deformed purely elastically，will yield an accurate estimate of total stresses existing in the body at any moment in time. The study[9] has shown that for the so called "hard" metals（including steels）fatigue criteria belonging to the group of approaches using averages of stress quantities within an elementary material volume yield the results closest to experiment. Therefore for further analyses Dang Van criterion[10] has been selected. The analysis performed so far indicates that residual stresses developing in steel structure during service may significantly affect its resistance to contact fatigue.

INTRODUCTION

Rolling contact fatigue，followed by cracking and fracture，may occur when the loads in the wheel/rail interface exceed elastic bearing capacity of the material. In order to decrease the risk of catastrophic wheel failure during service，an initial hoop compression in the wheel rim is introduced during manufacture，via heat treatment. This beneficiary residual stress may revert its sign during service due to

contact loads，introducing local high level stresses in the wheel thread zone，and high speed braking，which in turn creates repeated high intensity thermal loads on the wheel thread，which in turn lead to cracking（Figure 1，2）．

Figure 1   Thermal cracks on 32" diameter commuter car wheels of New York metropolitan area[11]
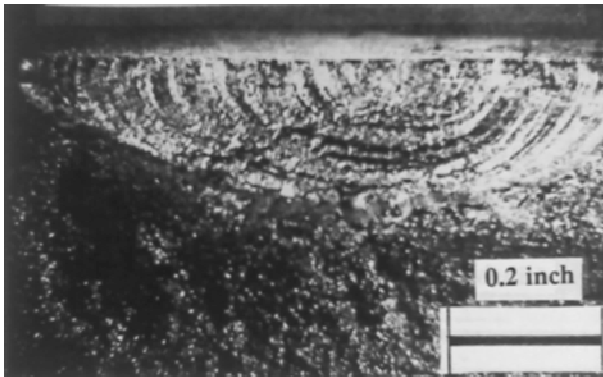
Figure 2   Exposed crack face on a commuter car wheel[11]

In order to correctly estimate the fatigue limit of the wheel one must know the total stresses at any moment in time. If the wheel shakes down elastically[12] to the applied loading program，these stresses may be decomposed into two components：elastic stresses，changing with every revolution of the wheel and residual stresses，independent of time. Elastic stresses may be found using standard FEM analysis，while residual ones may be computed using direct approach[13] (i. e. incremental analysis)，or a shakedown based calculations. The second method，though being at a disadvantage of giving only an estimate of residual stresses really existing in a considered body，offers a substantial speedup of calculations[7, 8]. This is especially true，if the initial plastic zone is small with respect to the whole considered body. The disadvantage of having only an estimate of residual stresses is not as bad，as it may seem，since it was shown on several examples that it is of remarkably good quality[14]，and besides that the loading program is not known precisely anyway，because of the nature of analyzed phenomenon（wheel wandering，varying axle load，dynamic effects）．

According to[9] high cycle fatigue criteria may be classified into three categories：
  · critical plane approaches，
  · approaches based on the stress invariants，

- approaches using averages of stress quantities within an elementary material volume.

This study has also shown，that for the so called "hard" metals，criteria belonging to the third group yield the results closest to the experiment. Therefore Dang Van criterion[10, 15]，belonging to this group，has been selected here，in spite of criticism[16]，stating that there is a problem with calibrating the constants of this criterion，and especially so for negative stress ratios.

MECHANICAL MODEL USED TO ESTIMATE RESIDUAL STRESSES

The mechanical model dealing with development of residual stresses due to repetitive contact loads in elastic-plastic material exhibiting kinematic hardening[6] may be presented as the following two step procedure：

I compute the correlation matrix A_{ijkl} :

$$\sigma^r_{ij} = A_{ijkl} \cdot \varepsilon^p_{kl} \tag{1}$$

solving the following nonlinear constrained optimization problem for self equilibrated stresses σ^r_{ij} as a function of plastic distortions ε^p_{ij} :

$$\min_{\varepsilon^p_{ij}} \Theta(\sigma^r_{ij}), \ \Theta(\sigma^r_{ij}) = \int_V \sigma^r_{ij} \cdot C_{ijkl} \cdot \sigma^r_{kl} \cdot dV - \int_V \varepsilon^p_{ij} \cdot \sigma^r_{ij} \cdot dV \tag{2}$$

at：

$$\sigma^r_{ij,j} = 0, \text{ in } V \text{ — internal equilibrium conditions,} \tag{3}$$

$$\sigma^r_{ij} \cdot n_j = 0, \text{ on } \partial V \text{ — static boundary conditions,} \tag{4}$$

II find plastic distortions ε^p_{ij}, which minimize the following total complementary energy functional：

$$\min_{\varepsilon^p_{ij}} \Psi(\varepsilon^p_{ij}), \ \Psi(\varepsilon^p_{ij}) = \int_V \varepsilon^p_{gh} \cdot A^T_{ghij} \cdot C_{ijkl} \cdot A_{klmn} \cdot \varepsilon^p_{mn} \cdot dV \tag{5}$$

at：

$$\Phi(A_{ijkl} \cdot \varepsilon^p_{kl} + c \cdot \varepsilon^{pc}_{ij} + \sigma^E_{ij} + \sigma^T_{ij}) - 1 \leqslant 0, \text{ in } V \text{ — yield conditions,} \tag{6}$$

$$c = \frac{E \cdot H}{E - H} \text{ — kinematic hardening parameter.} \tag{7}$$

where：σ^r_{ij} — residual stresses induced in the considered body by the applied cyclic loading program，ε^p_{ij} — plastic distorsions，ε^{pc}_{ij} — plastic distorsions assumed to have constant spatial distribution during iteration，σ^E_{ij} — elastic stresses（calculated as if the body deformed purely elastically during considered cyclic loading program），σ^T_{ij} — thermal stresses（calculated as if the body deformed purely elastically during service induced heating），A_{ghij} — correlation matrix linking plastic distorsions and residual stresses，C_{ijkl} — elastic compliance matrix，E — Young modulus，H — elastic plastic tangent modulus.

In order to insure convergence of computer routines plastic distortions have to be determined using the iterative approach：

$$^n\varepsilon^{pc}_{ij} = \lambda \cdot {}^{n-1}\varepsilon^{pc}_{ij} + (1-\lambda) \cdot {}^{n-2}\varepsilon^{pc}_{ij}, \ \lambda \in (0, 1), \tag{8}$$

where，during iteration 0 initial plastic distortions $^0\varepsilon^{pc}_{ij} = 0$，and during subsequent iterations the above formula is used to determine current level of plastic distortions. Numerical tests have shown[8] that such iterative procedure is convergent，and while any value of λ belonging to the interval $(0, 1)$ may be used，$\lambda = 0.5$ led to the final，stable spatial distribution of plastic distorsions in the lowest number of iterations.

This number of iterations never exceeded 19, though numerical solutions of sufficient quality have been obtained in as low as 7 iterations[8].

FATIGUE CRITERION

The Dang Van fatigue limit criterion[10, 15] condenses the time histories of six stress tensor components into a load path defined by two parameters, thus simplifying the fatigue damage calculations[17]. The criterion combines hydrostatic pressure σ_H and momentary maximum shearing stress τ_a calculated according to Tresca criterion:

$$\tau_a(t) = \frac{1}{2} \cdot \left[s_I^v(t) - s_{III}^v(t) \right] \tag{9}$$

evaluated on the part of stress deviator tensor varying in time, defined as:

$$s_{ij}^v(t) = s_{ij}(t) - s_{ij}^c = \left[\sigma_{ij}(t) - \delta_{ij} \cdot \sigma_H(t) \right] - s_{ij}^c \tag{10}$$

where s_{ij}^c is the solution of the following minimization problem:

$$s_{ij}^c = \min_{s_{ij}^*} \max_t (s_{ij}(t) - s_{ij}^*) \cdot (s_{ij}(t) - s_{ij}^*) \tag{11}$$

i. e. constitutes a value of the time independent stress deviator s_{ij}^* minimizing over time the maximum of the norm $(.) \cdot (.)$. The shearing stress and hydrostatic pressure are then combined linearly, to yield an equivalent scalar:

$$\tau_{eq, DV} = \max_t (\tau_a(t) + \alpha \cdot \sigma_H(t)) \tag{12}$$

which may be used to estimate the fatigue damage in combination with the material's S-N curves to calculate the fatigue damage[17]. The constant α is determined as:

$$\alpha = 3 \cdot \left(\frac{\tau_D}{\sigma_D} - \frac{1}{2} \right) \tag{13}$$

where τ_D and σ_D represent fatigue limits in torsion and tension-compression, respectively. It is worth to notice, that according to Dang Van criterion, time independent residual stresses do not affect the momentary maximum shearing stress (8), they only affect the hydrostatic stress term[17].

APPLICATION

The contact load acting on the wheel thread has been simulated by biparabolic pressure distribution spanned over rectangular contact area applied at a discrete contact location in the case solved. The peak pressure p_0 and patch size $a \times b$ have been determined using elastic Hertz contact formulae to compute the contact ellipse area for a contact load and later on to determine a rectangle with equivalent area and biparabolic pressure distribution balancing this contact load (Figure 3).
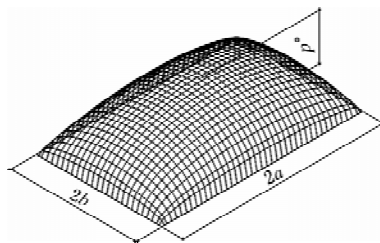
Figure 3　The surface tractions, as applied to the wheel running surface

737

For the purpose of calculations presented here the following material data have been assumed：

Wheel：	32" MU（US type），
Young modulus：	$E = 206$ GPa，
Poisson's ratio：	$v = 0.3$，
Yield limit：	448 Mpa，
Contact load	$P = 78$ kN.
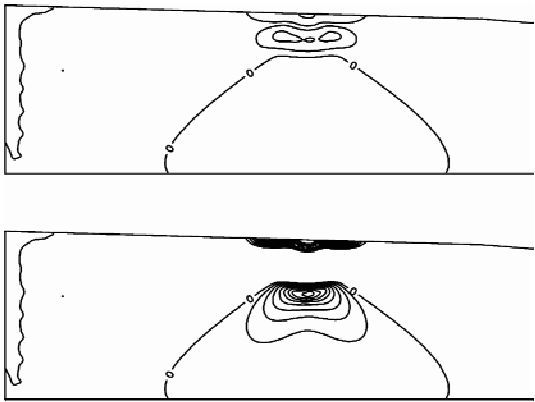
Figure 4　Hoop residual stress in the vicinity of wheel tread.

The distribution of hoop residual stresses due to simulated contact load in the tread area of a wheel is shown on the Figure 4. The highest hydrostatic pressure level induced in the wheel by residual stresses due to the considered contact load is in the range of 30 Mpa，and is much lower，than the residual stress induced hydrostatic pressure due to manufacturing and braking[11]，Table 1. This hydrostatic pressure level is important，as it directly affects the resistance to rolling contact fatigue，as determined by the Dang Van criterion.

TABLE 1　EVOLUTION OF RESIDUAL STRESS INDUCED HYDROSTATIC PRESSURE

Point	Hydrostatic pressure ［Mpa］			
	Load 1	Load 2	Load 3	Load 4
1	28 378	169 740	154 825	159 190
2	19 237	177 908	162 758	163 980
3	19 740	177 634	162 450	167 654

Loads 1，2，3，and 4 in the Table 1 above denote residual stress pressure level due to contact load only，thermal load due to braking only，thermal load due to manufacturing and braking combined and all considered loading cases combined，while points 1，2，and 3 have been selected as to yeld extreme values of hydrostatic pressure for all considered loading scenarios.

CONCLUSIONS

Initial calculations performed so far indicate，that at least for the passenger car wheels，subject to relatively minor service loads，residual stresses which do indeed form at the wheel rail interface due to contact forces are of a low magnitude. In fact these stresses are totally dominated by the residual stresses induced during manufacturing （beneficiary hoop compression），and later on by hoop tension due to

thermal loads. The most up to date results and updated conclusions will be presented at the conference.

REFERENCES

［1］Ciavarella M., Monno F. and Demelio G., "On the Dang Van fatigue limit in rolling contact fatigue". International Journal of Fatigue 28, 2006, pp.852-863.

［2］Bernasconi A., Filippini M., Foletti S. and Vaudo D., "Multiaxial fatigue of railway wheel steel under non-proportional loading", International Journal of Fatigue 28 , 2006, pp.663-672.

［3］Orkisz J. and Harris A., "Analysis of Residual Stresses at Shakedown", A Hybrid Approach, Theoretical and Applied Fracture Mechanics, 9, 1988, pp.109-121.

［4］Orkisz J., et al., "Discrete Analysis of Actual Residual Stresses Resulting from Cyclic Loadings", Computers and Structures, 35, 1990, pp.397-412.

［5］Pazdanowski, M., "An application of the generalized Finite Difference Method to the residual stress analysis in bodies subject to cyclic loads", Ph.D. Thesis, SMI CUT, Cracow, 1994 (in polish).

［6］Orkisz J. and Cecot W., "Prediction of actual residual stresses resulting from cyclic loading in kinematic hardening material", In: Proceedings of International Conference COMPLAS V, Barcelona, 1997, pp.1879-1891.

［7］Perlman, A.B. and Gordon, J.E., "Application of the constrained minimization method to the prediction of residual stresses in actual rail sections". In: Residual Stress in Rails Ⅱ — O. Orringer, J. Orkisz, Z. Świderski (eds), Kluwer Academic Publishers, Dordrecht, 1992, pp.151-177.

［8］Pazdanowski M., "Prediction of residual stresses in railroad rails by the constrained complementary energy minimization shakedown method", Final Report to the US DOT, FRA, Washington DC, to be published.

［9］Papadopulos I.V., Davoli P. and Gorla C., Filippini M., Bernasconi A., "A comparative study of multiaxial high-cycle fatigue criteria for metals", International Journal of Fatigue 19, 1997, 3, pp.219-235.

［10］Dang Van K., Griveau B. and Message O., "On a new multiaxial fatigue limit criterion: theory", application. In: Biaxial and multiaxial fatigue EGF, M.W. Brown, K.J. Miller (eds), 3, 1989, pp.479-496.

［11］Gordon, J. and Perlman, A.B., "Estimation of Residual Stresses in Railroad Commuter Car Wheels Following Manufacture", Final Report to the US DOT, FRA, Washington, 2003.

［12］Martin, J.B., "Plasticity-fundamentals and general results", The MIT Press Publ., 1975.

［13］Zienkiewicz, O.C. and Taylor, R.L.; "The Finite Element Method", Buttrworth Heineman, 2000.

［14］Pazdanowski, M.J., "On Estimation of Residual Stresses in Rails Using Shake-Down Based Method", The Archives of Transport, 3, 2010, pp.319-336.

［15］Dang Van K., "Macro-micro approach in high cycle fatigue". In: Advances in multiaxial fatigue, ASTM STP 1191 — D.L. McDowell, R. Ellis (eds), Philadelphia ,1993, pp.120-130.

［16］Desimone H., Bernasconi A. and Beretta S., "On the application of Dang Van criterion to rolling contact fatigue", Wear 260, 2006, pp.567-572.

［17］Bernasconi A., Davoli P., Filippini M. and Foletti S, "An integrated approach to rolling contact sub-surface fatigue assessment of railway wheels", Wear 258, 2005, pp.973-980.

FATIGUE CRACKING MONITORING AND EVALUATION USING AE SENSORS FOR EXISTING STEEL BRIDGES

* C. S. Wang，L. Tian and B. N. Fu

Engineering Research Center for Large Highway Structure Safety of Ministry of Education，College of Highways，Chang'an University，Xi'an，Shaanxi Province，710064，China
* Email：wcs2000wcs@163.com

KEYWORDS

Steel bridge，acoustic emission，fatigue，crack monitoring，safety evaluation，bridge maintenance

ABSTRACT

The existing railway steel bridges are often required to carry an increasing volume of traffic，higher speed and heavier trains，so China railway bridge owners pay more attention to the actual fatigue life and service safety of such structures. Recently fatigue cracks were found at web gaps between vertical stiffeners and main girder webs，and the low flange connection plates between end cross-frames and main girders for each span of Wei River Bridge，a railway girder bridge built in 1982. In order to prevent crack propagation，stop holes were drilled in front of the crack tips. However，the new cracks have been detected beyond the stop holes during the recent inspection. In this paper，Acoustic Emotion（AE） sensors are used to monitor and evaluate the fatigue cracking of Wei River Bridge，which is the first field AE monitoring using Physical Acoustics Company equipment and sensors in China. This AE sensor has fine frequency bandwidth of interest to bridge monitoring，which is applicable to local cracking position and can monitor fatigue crack in close-range. In the filed inspection，healthy monitoring was conducted at several locations，including the cracking web gaps，non-cracking web gaps and low flange connection plates using AE sensors. Based on AE monitoring data，the fatigue behavior of cracking zones was analyzed in order to propose theoretical basis and the rational advices for Wei River Bridge renovation.

INTRODUCTION

The safety of bridges in China is becoming worse and worse. Even though the load tests are carried out to examine the behavior of bridges，they only inspect bridges at particular moment. The current state of bridges in China calls for the implementation of a continuous bridge monitoring system that can aid in timely damage detection and help extend the service life of these structures. A typical monitoring system would be one which enables non-invasive，continuous monitoring of the structure. The characteristics of the acoustic emission（AE） make it as a choice to serve the purpose. Although the AE technique has been successfully used for decades for damage detection in bridge engineering and other fields worldwide[1-7]，

its potential in bridge monitoring has not yet been fully used in China.

AE testing is a nondestructive testing tool for real time examination of the behavior of materials[1]. When bridges are under load conditions, the materials of bridges like concrete and steel will emit energy in the form of elastic waves because of various material-relevant damage mechanisms. These waves are picked up by the sensors attached to the surface of the material[2–7]. The further evaluation of the collected data can give a result about the healthy condition of the bridge and help prioritize repair and maintenance[7]. This paper mainly focuses on the AE monitoring of the fatigue crack in the existed steel bridge. By analyzing the collected data, the information of the fatigue crack activities can be obtained and the bridge conditions can be evaluated.

BACKGROUND OF THE INSPECTION FOR WEI RIVER BRIDGE

Wei River Bridge (as shown in Figure 1) is an important railway bridge on Longhai Railway Line from Xi'an to Xianyang. It is a 12-span steel girder bridge opened to traffic in 1982 with span length of 26.15 m. In bridge service stage, fatigue cracks were found at several positions of the steel bridge. In 2006 and 2008, the Bridge Department of Chang'an University carried out inspections of the stress and strain in some key positions under the normal operation of the train for several hours. According to the analysis of the result of the inspection, the servicing and maintenance suggestions were given for Bridge Management Department of Xi'an Railway Bureau. Thereafter, the Bridge Management Department took measures to reinforce and renovate some key positions, such as drilling stop holes and adding steel stiffened plate.

In fact, neither the test of stress and strain nor reinforcement and renovation can describe the actual activity of fatigue crack. The characteristic of Acoustic Emission is just to monitor the transient behaviour of crack propagation, so AE monitoring is a valuable supplement for stress and strain monitoring. AE also can examine the effect of reinforcement and renovation effectively. Therefore, the Bridge Department of Chang'an University and Bridge Management Department decided to reconduct the inspection of stress and strain in the field test. However, compared with the previous two tests, it is the first time that the AE equipment is brought in the structural healthy monitoring in China. The monitoring is conducted for more than 60 hours from 20：30 on April 26, 2011 to 11：00 on April 29, 2011.

BASIC PRINCIPLE OF ACOUSTIC EMISSION MONITORING

AE signal is a transient elastic stress wave produced by the release of material internal local energy[1–2]. As shown in the Figure 2, under the condition of tension, compression, impact and so on, the internal crack tip of the structure will lead to a transient release of stress that can produce stress waves. When the crack propagates, the stress waves spread in all around directions. Then these waves would be picked up by the AE sensors attached to on the surface of the structure.

AE locating is the most important link in the Acoustic Emission structural healthy monitoring. Another important characteristic of the AE technology is crack locating. As shown in Figure 3, two AE sensors are set at a distance of L. When the crack propagation between two sensors and is at a distance of l to the sensor 1, the time of reaching sensor 1 and sensor 2 can be measured as τ_1 and τ_2 respectively. As for the same AE signal, according to the different time of reaching the two sensors and the speed v in particular material, the acoustic source can be located in the form of Eqn. 1.

Figure 1   The Wei River Bridge
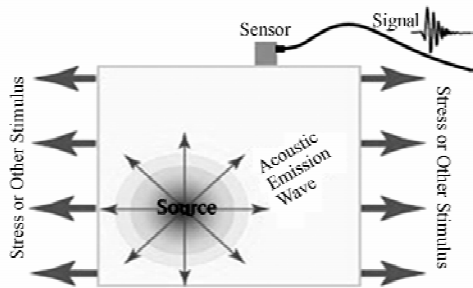
Figure 2   The model of the AE production and spread

$$l = \frac{L - (\tau_2 - \tau_1) \cdot v}{2} \tag{1}$$
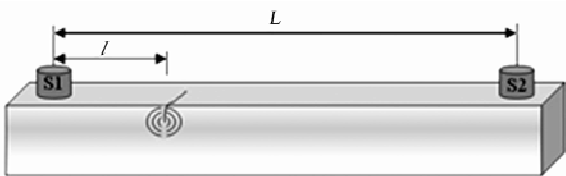
Figure 3   The model of the AE locating

Based on the same principle，three sensors can be used to locate the crack propagation of plane structure in two-dimensional coordinate. As lots of noise would occur during the Acoustic Emission monitoring，which can have an effect on judging the crack propagation signals，the AE locating will have an important role in confirming the features of the crack propagation signals.

FIELD CONDITIONS OF ACOUSTIC EMISSION MONITORING

The monitoring site is at the ninth pier of Wei River Bridge. The simplified model of the bridge and the four monitoring positions are shown in the Figure 4. The basic information of the four monitoring positions is described as following：The first position is low position of left web，using sensor 1 to 3，having a visible crack and drilling the stop hole two years ago. The second position is low position of right web，using sensor 4 to 6，having no visible cracks. The third position is front base，using sensor 11 to 13，having no visible cracks. The fourth position is the back base，using sensor 14 to 16，having visible cracks two years ago and reinforced by drilling stop holes.
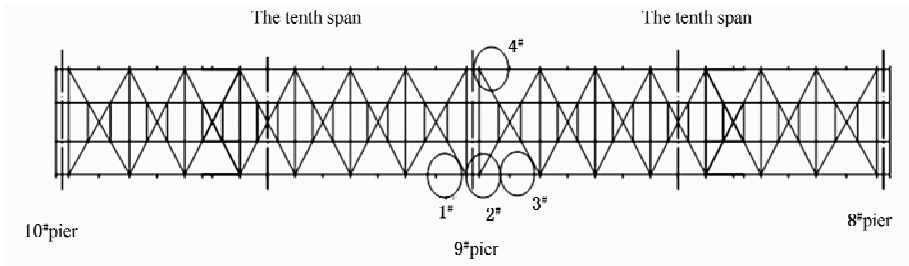
Figure 4   The simplified model of the bridge and the four monitoring positions

742

Three sensors were placed in each position form a plane locating group，which was totally independent with each other. Because of the particularity of bridge structure，AE equipment in this monitoring has the following characteristics. Firstly，AE sensors are integrating and have high frequency[3-7]. Secondly，AE equipment needs a set of equipments independent on the computer. Thirdly，the distance is the shortest from AE equipment to sensors. Fourthly，the monitoring can last for 24 hours or longer，which will greatly increase the reliability of monitoring results. Fifthly，there is a large capacity of storage space，which will ensure the data no break，no lost and storage in time. Sixthly，AE sensors are waterproof and can work in all weather conditions.

Monitoring equipment made by the Physical Acoustics Company were used in Wei River Bridge Acoustic Emission monitoring. It includes the 150 KHz-resonant-frequency and 40－decibels R15I sensors and high performance independent AE system—MicroII. The equipment is small，light and has a 500 GB hard disk for saving the data. The equipment also can be connected to a laptop to realise the remote control by an Internet line，which is suitable for bridge in situ monitoring.

ANALYSIS OF ACOUSTIC EMISSION MONITORING DATA

Figure 5 shows the scatter plot of the 5－hour AE signal amplitude，from 00:00 April 27 to 05:00. When a train passes through the monitoring zone，many amplitude signals appear at that moment. Besides，the sensors also can receive some other scattered signals that are from random and uncertain noise，such as wind，sand collision，the release of temperature stress and so on. Because these signals have low energy，low quantity and low frequency，it has little influence on the monitoring results.
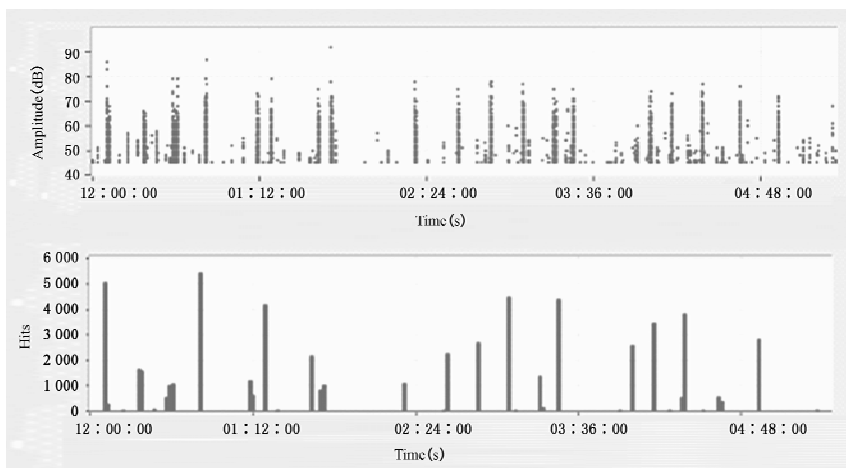
Figure 5   AE amplitude and total number of the hit

A train load for example is chosen to analyse the features and process of AE signals. In Figure 6，it is shown some AE characteristic graphs which reflect the AE signals at the moment pointed in the Figure 5. These graphs provide the following information of the field inspection. First，the train arrived at about 04 : 35 : 39 and lasted 22 seconds through the monitoring zone. Second，the sensors placed in position 3 and position 4 （Channel 11 to Channel 16 ）received the signals first and the sensors placed in position 1 and position 2 （Channel 1 to Channel 6）received later. Third，the majority signal amplitudes are under 55 decibels，as shown in the Figure 6. Fourth，the signal amplitude peak is about 76 decibels，but the

number of the signals over 65 decibels is limited. Fifth，when a train just entered or left the monitoring zone，the signals were in larger amplitude and at higher average signal level as shown in the Figure 6. Sixth，the 12 sensors totally received 1 400 impact signals.
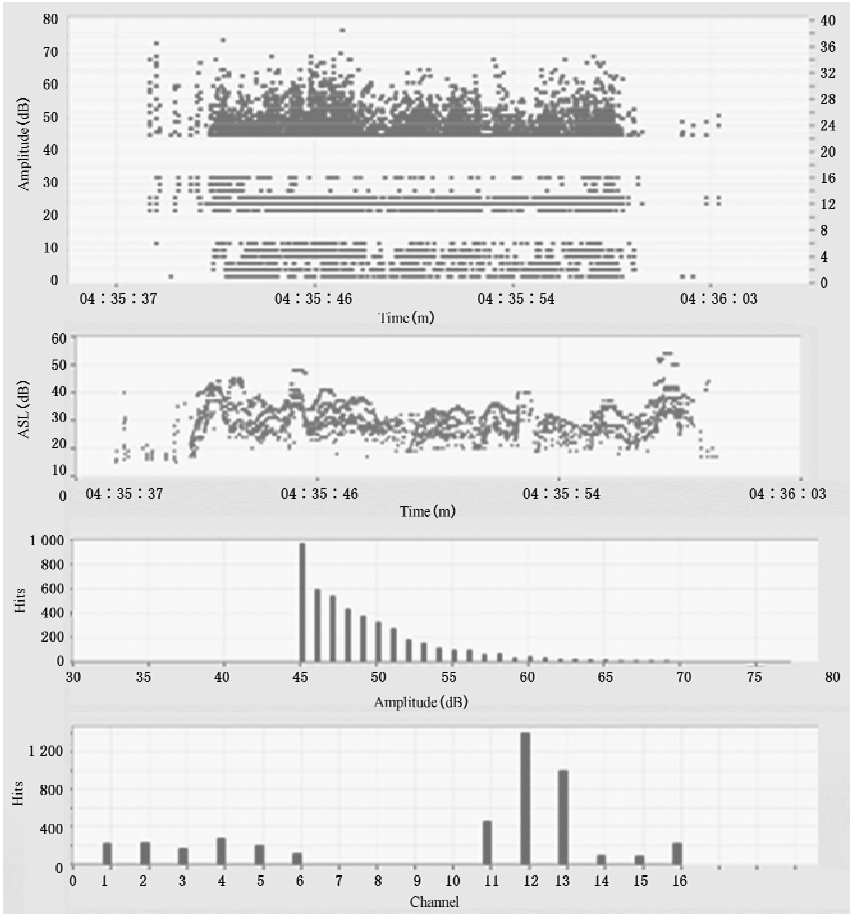
Figure 6　Some characteristics of the AE signals

Bridge monitoring inevitably appears much noise as a train running is a dynamic process. The above basic information is actually a mixed reflection of all influences，including crack propagation as well as other noise. In order to acquire the information contained in the signals effectively the characteristics of the signal waveforms should be analysed. However，in fact，even if the noise can be filtered by analysing the characteristics of frequency and waveform，it is uncertain whether the AE signals is caused by the crack activities. Therefore，AE locating is the most valuable technology in judging the signal source and the crack activities. The more signals there are in the locating zone and the more concentrated they are，the more reliable the evaluation of crack activity is. Take the position 1 for example，from the Figure 7，it can be found a bit of locating signals，and they are not concentrated in the monitoring zone. So the conclusion can be drawn that there is no crack activity in the position 1 during the train passes this zone.

$$\frac{\varepsilon_{csm}}{\varepsilon_y} = \frac{0.4}{\bar{\lambda}_p^{3.2}} \quad \text{but} \quad \frac{\varepsilon_{csm}}{\varepsilon_y} \leqslant 15 \quad \text{for} \quad \bar{\lambda}_p \leqslant 0.748 \tag{2}$$

in which $\varepsilon_y = f_y/E$ is the yield strain of the material, E is the Young's modulus, and ε_{csm} is the CSM limiting strain of the section. The base curve was generated as described in[4] by means of stub column test data collected from previous studies[5-11]. In interpreting the test data, for stocky sections (i. e. $\bar{\lambda}_p \leqslant$ 0.748), the CSM limiting strain ε_{csm} is related to the local buckling strain $\varepsilon_{lb} = \delta_u/L$, defined as the end shortening at ultimate load δ_u normalised by the stub column length L. For materials that exhibit a well defined yield stress, such as hot-rolled sections, the strain ratio $\varepsilon_{csm}/\varepsilon_y = \varepsilon_{lb}/\varepsilon_y$ and for materials that exhibit a more rounded, non-linear stress-strain response, such as with cold-formed sections, the strain ratio involves the subtraction of the plastic strain at the 0.2% proof stress, giving $\varepsilon_{csm}/\varepsilon_y = (\varepsilon_{lb} - 0.002)/\varepsilon_y$. The above also applies to slender sections ($\bar{\lambda}_p > 0.748$) in cases where the ultimate test load N_u is greater than the yield load N_y, while for $N_u < N_y$, $\varepsilon_{csm}/\varepsilon_y$ is taken simply as N_u/N_y.
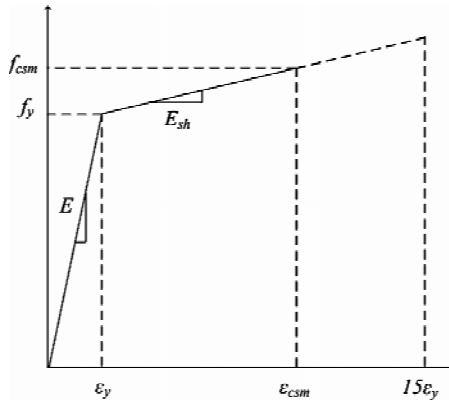
Figure 2 Bi-linear material model

Having calculated the strain ratio of the cross-section, the stress at any point can be determined directly, based on the assumption of plane strain, from the elastic-linear hardening material model given in Figure 2, which has an initial slope E for stresses up to f_y and a strain hardening slope $E_{sh} = E/100$, as recommended in EN 1993-1-5[2], for stresses beyond f_y. Thus, the limiting stress f_{csm} corresponding to ε_{csm} is determined from Eqn. 3:

$$f_{csm} = f_y + E_{sh}(\varepsilon_{csm} - \varepsilon_y) \qquad \varepsilon_{csm} \geqslant \varepsilon_y \tag{3}$$

COMPRESSIVE RESISTANCE

For pure compression (i.e. uniform axial strain), the cross-section resistance N_{csm} is given by Eqn. 4 as the product of the gross cross-section area A and the limiting stress f_{csm}.

$$N_{csm} = A f_{csm} \tag{4}$$

In Table 1, numerical comparisons of ultimate test load N_u for 77 documented test specimens[5-11] show that the mean and coefficient of variation of N_{csm}/N_u are 0.945 and 0.073 9, respectively, whereas for the Eurocode 3[12] predictions, the mean and coefficient of variation of N_{EC3}/N_u are 0.899 and 0.105, respectively. The results show that the CSM offers more accurate prediction of the test data and a reduction in scatter.

TABLE 1   COMPARISON OF CSM AND EC3 PREDICTIVE MODELS TO COLLECTED TEST DATA

Loading	No. of tests：		EC3/ Test	CSM / Test	CSM / EC3
Axial	77	Mean	0.899	0.945	1.05
		COV	0.105	0.074	—
Bending	68	Mean	0.864	0.908	1.05
		COV	0.084	0.069	—
Axial + Bending	6	Mean	0.890	0.920	1.03
		COV	0.135	0.068	—

BENDING RESISTANCE

For a symmetric section，assuming plane sections remain plane and normal to the neutral axis in bending，and with strain ratio $\varepsilon_{csm}/\varepsilon_y \geqslant 1$ (hence $f_{csm} \geqslant f_y$ and the moment capacity $M_{csm} \geqslant M_{el}$)，[4] provides Eqn. 5，which is a general design expression for the major axis moment capacity M_{csm}，in terms of the elastic section modulus W_{el} and plastic section modulus W_{pl}. Analytical and design expressions have also been developed for circular hollow sections，and I/box sections bending about the minor axis.

$$\frac{M_{csm}}{M_{pl}} = 1 + \frac{E_{sh}}{E} \frac{W_{el}}{W_{pl}} \left(\frac{\varepsilon_{csm}}{\varepsilon_y} - 1 \right) - \left(1 - \frac{W_{el}}{W_{pl}} \right) \left(\frac{\varepsilon_{csm}}{\varepsilon_y} \right)^{-2} \tag{5}$$

Comparison of the CSM predictions with the ultimate test moment M_u of simply supported major axis bending tests[6, 7, 13, 14] are shown in Figure 3 where the CSM design expression is displayed for a shape factor of 1.25，which is approximately the mean value of the data set. The maximum strain ratio of $\varepsilon_{csm}/\varepsilon_y = 15$, gives a cap to M_u/M_{pl} for slenderness values below 0.32. In Table 1，numerical comparisons against the 68 documented bending test specimens show that the mean and coefficient of variation (COV) of M_{csm}/M_u are 0.908 and 0.069 1 respectively for the CSM，while for the Eurocode 3 predictions a mean value of M_{EC3}/M_u of 0.864 and a COV of 0.083 9 are found，showing the CSM to provide a more accurate prediction of the test data and a reduction in scatter.
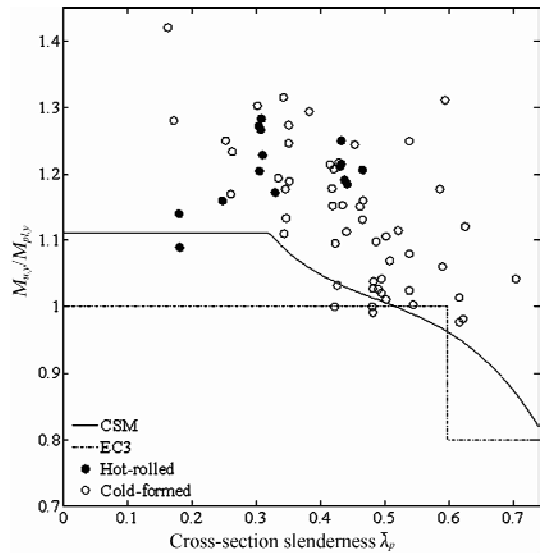

Figure 3   Bending test data and comparison with design models

AXIAL + BENDING RESISTANCE

For combinations of axial force and bending moments about either axes, a numerical model has been employed due to the complexity of an analytical approach. This model is based upon the plane strain distribution of Eqn. 6, which can describe the strain distribution under any combination of axial load and bending moments. I-sections, box sections and circular hollow sections have been examined.

$$\frac{\varepsilon}{\varepsilon_{csm}} = \frac{\varepsilon_A}{\varepsilon_{csm}} + \frac{\varepsilon_B}{\varepsilon_{csm}}\left(\frac{2y}{h}\right) + \frac{\varepsilon_C}{\varepsilon_{csm}}\left(\frac{2z}{b}\right) \tag{6}$$

where ε_A is a uniform strain acting across the entire cross-section, ε_B is the value at $y = h/2$ of a linearly varying strain associated with bending about the major axis and ε_C is the value at $z = b/2$ of a linearly varying strain associated with bending about the minor axis. The combination of strains can be increased up to the limiting strain ε_{csm}, and for doubly symmetric sections, the distances y and z are taken from the geometric centroid. For a given cross-section and strain ratio, the stress distribution can be obtained from the bi-linear material model of Figure 2. Integrating the stresses over the area of the cross-section yields the axial and moment resistances N, M_y and M_z, which define points on an interaction surface. A suitable fit to this surface, normalizing by the individual CSM resistances, has been found in the form of Eqn. 7, where α, β, γ are defined as functions of cross-section geometry.

$$\left(\frac{N}{N_{csm}}\right)^\alpha + \left(\frac{M_y}{M_{csm,\,y}}\right)^\beta + \left(\frac{M_z}{M_{csm,\,z}}\right)^r \leqslant 1 \tag{7}$$

Slices through these surfaces can be taken at fixed values of axial load level $\psi = N/N_{csm}$ to produce the interaction curves shown in Figure 4. With the assumed strain hardening modulus of $E_{sh}/E = 1/100$, the model predicts approximately a 10% increase in capacity over Eurocode 3 for a strain ratio of 15. For the case of combined loading, cross-section slenderness, which is required to determine the cross-section's strain ratio, may be calculated based on an elastic stress distribution under N, M_y and M_z.
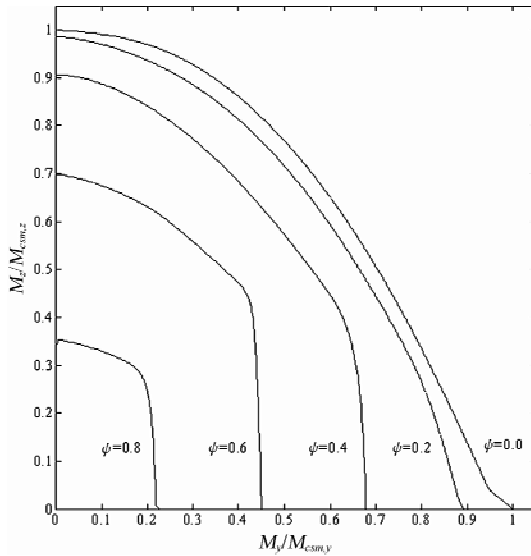

Figure 4   **Contour representation of interaction surfaces (I-section)**

Table 2 provides the proposed values of the exponents α, β and γ for cases where one of the loading

components N，M_y or M_z is equal to zero. The term A_w/A，is the web area $h_w t_w$ divided by the total cross-sectional area A，t_w is the web thickness（taken as twice the wall thickness for box sections）and h_w is the web height measured between the flanges. The term $W_{pl, y}/W_{pl, z}$ is the ratio of the major to minor axis plastic section module. For cross-sections with a strain ratio less than 3，bending about either the major or minor axis，a conservative linear interaction（$\alpha = \beta = \gamma = 1$）is proposed. Work is underway to determine expressions for α，β and γ when all 3 loading components are present.

TABLE 2   PROPOSED VALUES OF EXPONENTS α, β, γ

	$\varepsilon_{csm}/\varepsilon_y$	α	β	γ
I/Box sections（$M_z = 0$）	3–15	$A_w/A + 1.2$	0.82	—
Box sections（$M_y = 0$）	3–15	$A_w/A + 1.2$	—	0.82
I-sections（$M_y = 0$）	3–7	2	—	1
	7–15	$4.5A_w/A + 2$	—	0.7
Box sections（$N = 0$）	3–15	—	$1.6 - 0.15(W_{pl, y}/W_{pl, z} - 1)$	$1.6 + 0.05(W_{pl, y}/W_{pl, z} - 1)$
I-sections（$N = 0$）	3–5	—	2	1
	5–15	—	$2 + 0.15 W_{pl, y}/W_{pl, z}$	$0.8 - 0.015 W_{pl, y}/W_{pl, z}$

Comparisons of the proposed model with the results of 6 axial plus bending tests on square hollow sections[15] are shown in Figure 5. 'Data（a）' corresponds to test results on 2 Class 1 cross-sections（$\varepsilon_{csm}/\varepsilon_y \approx 3.8$），while 'EC3（a）' and 'CSM（a）' are the corresponding Eurocode 3 and CSM design curves；the CSM may be seen to provide a closer prediction of these test data. 'Data（b）' corresponds to test results on 4 Class 3 cross-sections（$\varepsilon_{csm}/\varepsilon_y \approx 1.6$），with 'EC3（b）' and 'CSM（b）' being the corresponding Eurocode 3 and CSM design curves；although both methods employ a linear interaction for these sections，the more accurate end points results in CSM providing a better prediction of the test capacity. Table 1 provides the ratio of mean predicted to test capacity and coefficient of variation for these test results；the CSM offers an improved mean and a reduced scatter.
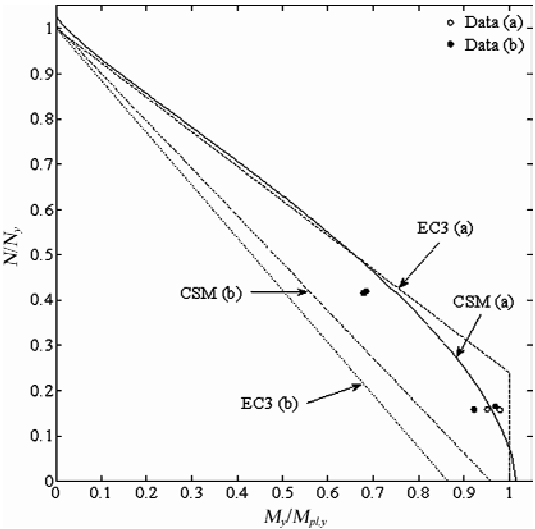

Figure 5   Axial plus bending test data and comparison with design models

CONCLUSIONS

The importance of strain hardening to the response of structural steel elements has been highlighted in this paper. It was shown through analysis of existing axial and bending test data，that the limiting resistances adopted in present design practice of the yield load in compression for stub columns and the plastic moment capacity in bending for beams are conservative in the case of stocky sections，due to the influence of strain hardening. The Continuous Strength Method is a deformation based design approach that offers a rational means of exploiting strain hardening. A cross-section's deformation capacity is defined as the maximum allowable strain that can be carried，as limited by local buckling，normalised by the yield strain. This measure of deformation capacity，referred to as the 'strain ratio' of the cross-section，is determined from the cross-section slenderness through a single 'base curve'. Once the allowable strain is known，the corresponding stress distribution can be derived from an elastic，linear-hardening material model，and hence cross-section capacity may be calculated，assuming plane section remain plane，by means of basic mechanics. Based on this approach，simple design expressions for cross-section resistance have been proposed. Comparisons with test data on steel sections under pure compression，pure bending and combined loading reveal that the Continuous Strength Method offers a better prediction of resistance (i. e. an improved mean prediction and a reduction in scatter) than existing design approaches. Further work is underway to consider global instability and indeterminate structures.

REFERENCES

［1］Gardner，L.，"The continuous strength method"，Proceedings of the Institution of Civil Engineers-Structures and Buildings，161(3)，2008，pp. 127–133.
［2］EN 1993－1－5.，"Eurocode 3：Design of steel structures—Part 1－5：Plated structural elements"，European Standard，CEN，2006.
［3］Seif，M. and Schafer. B. W.，"Local buckling of structural steel shapes"，Journal of Constructional Steel Research，66(10)，2010，pp. 1232–1247.
［4］Gardner，L.，Wang，F. and Liew.，A. "Influence of strain hardening on the behavior and design of steel structures"，International Journal of Structural Stability and Dynamics，11(5)，2011，pp. 855–875.
［5］Akiyama，H.，Kuwamura，H.，Yamada，S.，and Chiu，J. C. "Influences of manufacturing processes on the ultimate behaviour of box-section members"，Proceedings of the Third Pacific Structural Steel Conference (PSSC)，1996，Tokyo，Japan.
［6］Gardner，L.，Saari，N. and Wang，F.，"Comparative experimental study of hot-rolled and cold-formed structural steel hollow sections"，Thin-Walled Structures，48(7)，2010，pp. 495-507.
［7］Zhao，X. L. and Hancock，G. J.，"Tests to determine plate slenderness limits for cold-formed rectangular hollow sections of grade C450"，Journal of the Australian Steel Institute，25(4)，1991，pp. 2–16.
［8］Rasmussen，K. J. R. and Hancock，G. J.，"Plate slenderness limits for high-strength steel sections"，Journal of Constructional Steel Research，23(1–3)，1992，pp. 73–96.
［9］Gao，L.，Sun，H.，Jin，F. and Fan，H.，"Load-carrying capacity of high-strength steel box sections I：Stub columns"，Journal of Constructional Steel Research，65(4)，2009，pp. 918–924.
［10］Hu，S. D.，Ye，B. and Li，L. X.，"Material properties of thick-wall cold-rolled welded tube with a rectangular or square hollow section"，Construction and Building Materials，25(5)，2011，pp. 2683–2689.
［11］Elchalakani，M.，Zhao，X. L. and Grzebieta，R.，"Tests on concrete filled double-skin (CHS outer and SHS inner) composite short columns under axial compression"，Thin-Walled Structures，40(5)，2002，pp. 415–441.
［12］EN 1993－1－1.，"Eurocode 3：Design of steel structures-Part 1－1：General rules and rules for buildings"，European Standard，CEN，2005.
［13］Wilkinson，T. and Hancock，G. J.，"Tests to examine compact web slenderness of cold-formed RHS"，Journal of Structural Engineering-ASCE，124(10)，1998，pp. 1166–1174.
［14］Byfield，M. P. and Nethercot，D. A.，"An analysis of the true bending strength of steel beams"，Proceedings of the Institution of Civil Engineers-Structures and Buildings，128(2)，1998，pp. 188–197.
［15］Little，G. H.，"Square box sections—experimental behaviour under combined bending and compression"，Journal of Strain Analysis，13(3)，1978，pp. 165–176.

BEHAVIOUR AND DESIGN OF INDETERMINATE STAINLESS STEEL STRUCTURES

* L. Gardner and N. Saliba

Department of Civil and Environmental Engineering，Imperial College London，
South Kensington Campus，London SW7 2AZ，UK
* Email：Leroy. gardner@imperial. ac. uk

KEYWORDS

Continuous beams，continuous strength method，indeterminate structures，lean duplex，plastic analysis，stainless steel，structures.

ABSTRACT

Despite the high material ductility of structural stainless steels and the existence of a Class 1 limit in the European structural stainless steel design code EN 1993 - 1 - 4，plastic design is not currently permitted for stainless steel structures，which leads to uneconomic design. The present paper investigates the applicability of inelastic design procedures to indeterminate stainless steel structures. A series of experiments on indeterminate stainless steel structures，comprising tubular and welded I-sections，are presented. Analysis of the results reveals that current design provisions are overly conservative and significant moment redistribution and hence material savings can be achieved if inelastic design procedures are followed at both cross-sectional level and system level.

INTRODUCTION

Stainless steel has a range of physical attributes such as high strength，stiffness，and ductility，together with excellent durability that makes it ideally suited to use in construction（Gardner[1]）. However，the initial cost of stainless steel is greater than that of structural carbon steel，and with initial expenditure being a decisive factor for material selection in the construction industry，efficient design is a paramount. In the context of stainless steel，this means full exploitation of the material's inelastic reserves，strain-hardening characteristics and ductility. Current European structural design codes use the process of cross-section classification to identify those structural sections that are suitable for plastic design，this being the method by which indeterminate structures attain a sequence of plastic hinges under increasing load until a collapse mechanism is formed. The European structural design codes for both carbon steel（EN 1993 - 1 - 1[2]）and stainless steel（EN 1993 - 1 - 4[3]）define four classes of cross-section based on their susceptibility to local buckling – plastic design can only be applied to indeterminate carbon steel structures comprising Class 1 sections. For stainless steel，plastic design is not currently allowed. For these reasons，an experimental and analytical research program investigating the applicability of plastic design to

indeterminate stainless steel structures was initiated. The present paper summarizes the laboratory tests performed on lean duplex stainless steel (Grade 1. 416 2 (EN 10088 – 4[4])) welded I-sections. The experiments include eight simple beam tests(Gardner and Saliba[5]), and eight continuous beam tests on lean duplex welded I-sections. The obtained experimental results, together with the results of previous tests performed on cold-formed lean duplex hollow sections by Theofanous and Gardner[6], are reported and analyzed herein. The results show that neglecting material strain-hardening and moment redistribution in the continuous beams, which is the approach of the current design provisions of EN 1993 – 1 – 4[3], results in overly conservative designs, while application of alternative approaches[7, 8] provides improved efficiency.

EXPERIMENTAL INVESTIGATION

Introduction

An experimental study of the structural response of Grade 1. 416 2 lean duplex stainless steel welded I-section beams has been carried out. The material properties are summarised in Table 1, where E is Young's modulus, $\sigma_{0.2}$ is the 0. 2% proof stress, $\sigma_{1.0}$ is the 1. 0% proof stress, σ_u is the ultimate tensile stress and n and $n'_{0.2, 1.0}$ are strain-hardening exponents for the compound Ramberg-Osgood model (Mirambell and Real[9], Rasmussen[10]) as modified by Gardner and Nethercot[11, 12].

TABLE 1   MEASURED MATERIAL PROPERTIES FROM TENSILE COUPON TESTS

Plate thickness (mm)	E (N/mm^2)	$\sigma_{0.2}$ (N/mm^2)	$\sigma_{1.0}$ (N/mm^2)	σ_u (N/mm^2)	n	$n'_{0.2, 1.0}$
6.00	192 000	512	553	723	11.5	2.1
6.02	195 000	520	562	732	9.9	2.2
8.08	196 000	505	548	727	12.3	2.2
8.07	210 000	503	543	728	12.0	2.2
10.10	215 000	505	558	765	11.5	1.9
10.08	218 000	497	556	772	12.0	2.5
12.36	197 000	466	—	734	—	—
12.42	214 000	447	506	711	10.0	2.4

Simply Supported Beam Tests

A total of eight welded I-sections were tested in bending-four in a three-point configuration and four in a four-point configuration (Gardner and Saliba[5]). The beams had a total length of 3 000 mm and were simply supported between two steel rollers placed 100 mm inwards from the each end. Lateral restraints were provided at the beam ends and the load points. Load was applied at mid-span for the three-point bending tests, while for the 4-point bending tests the load was applied at two points (900 mm from each support). The tests were displacement-controlled tested at a rate of 3. 0 mm/min. The section dimensions and key experimental results from the simple beam tests are summarised in Table 2, where M_u is the ultimate test moment, M_{el} is the elastic moment capacity, M_{pl} is the plastic moment capacity and a is the weld throat. The employed specimen designation system begins with section type, and followed by section depth $h \times$ flange width $b \times$ flange thickness$t_f \times$ web thicknesst_w.

<div align="center">TABLE 2   DIMENSIONS AND KEY RESULTS FOR SIMPLE BEAM TESTS</div>

Type of test	Cross-section	h (mm)	b (mm)	t_f (mm)	t_w (mm)	a (mm)	M_u (kN·m)	M_u/M_{el}	M_u/M_{pl}
Three-point bending	I－200×140×6×6－1	202.05	138.89	6.12	6.01	5.00	134	1.21	1.08
	I－200×140×8×6－1	200.17	139.04	8.11	6.03	5.00	195	1.42	1.29
	I－200×140×10×8－1	198.72	139.00	10.18	8.00	6.00	264	1.60	1.44
	I－200×140×12×8－1	199.00	139.29	12.54	8.05	6.00	305	1.63	1.45
Four-point bending	I－200×140×6×6－2	202.05	138.60	6.11	6.01	5.00	132	1.20	1.07
	I－200×140×8×6－2	200.60	139.30	8.11	6.06	5.00	169	1.23	1.12
	I－200×140×10×8－2	199.27	139.00	10.26	7.99	6.00	219	1.32	1.18
	I－200×140×12×8－2	198.87	139.64	12.32	8.07	6.00	259	1.39	1.25

Continuous Beam Tests

A total of eight continuous beam tests were conducted，with the nominal section dimensions being the same as those employed for the simple beam tests，to allow a direct assessment of the effect of moment redistribution on ultimate capacity. The beams had a total length of 5 000 mm and were continuous over three rollers；the end rollers allowed free axial displacements while the central roller was fixed against axial displacement. The clear span distance between the roller supports was 2 400 mm and a further 100 mm was provided at each end of the beam. The measured geometric properties for the welded I-sections are shown in Table 3.

<div align="center">TABLE 3   DIMENSIONS OF THE CONTINUOUS BEAM SPECIMENS</div>

Configuration	Cross-section	h (mm)	b (mm)	t_f (mm)	t_w (mm)	a (mm)
1/2 span	I－200×140×6×6－1	202.40	139.22	6.07	6.02	5.00
	I－200×140×8×6－1	200.40	139.49	8.07	6.00	5.00
	I－200×140×10×8－1	199.30	139.62	10.21	8.05	5.00
	I－200×140×12×8－1	199.00	139.7	12.46	8.07	6.00
1/3 span	I－200×140×6×6－2	202.6	139.20	5.99	5.98	6.00
	I－200×140×8×6－2	200.60	139.68	8.09	5.95	5.00
	I－200×140×10×8－2	199.10	139.59	10.2	8.07	6.00
	I－200×140×12×8－2	198.70	139.61	12.42	8.06	6.00

All tests were displacement-controlled tested at a rate of 3.0 mm/min. Two symmetrical loading configurations were employed to vary the required rotation capacity and moment redistribution before collapse. In the first configuration，denoted '1/2 span' in Table 3，the loads were applied at mid-span，whilst in the second configuration，'denoted 1/3 span'，the loads were applied at a distance equal to 800 mm (1/3 of the clear span length) from the central support. As before，lateral restraints were provided at the support and load points to prevent lateral torsional buckling. The key experimental results are summarised in Table 4 including the total ultimate test load F_u (i.e. the sum of the two point loads)，the theoretical total load corresponding to the formation of the first plastic hinge at the central support，F_{h1}，and the theoretical total collapse load F_{coll}. The load F_{h1} was determined based on elastic calculations，whereas F_{coll} was determined by classical plastic analysis procedures. The measured load-deflection curves are shown in Figures 1 and 2.

TABLE 4   TEST RESULTS FOR CONTINUOUS BEAMS

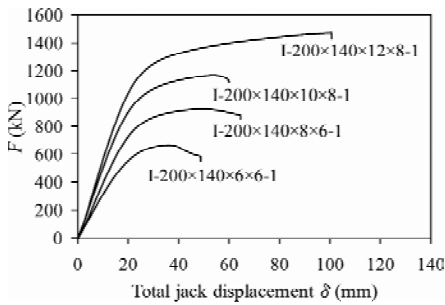| Configuration	Cross-section	Test F_u (kN)	Calculated F_{h1} (kN)	Calculated F_{coll} (kN)
1/2 span	I − 200 × 140 × 6 × 6 − 1	668	552	620
	I − 200 × 140 × 8 × 6 − 1	926	668	752
	I − 200 × 140 × 10 × 8 − 1	1 192	822	924
	I − 200 × 140 × 12 × 8 − 1	1 474	934	1 050
1/3 span	I − 200 × 140 × 6 × 6 − 2	820	552	766
	I − 200 × 140 × 8 × 6 − 2	1 062	678	942
	I − 200 × 140 × 10 × 8 − 2	1 402	832	1 154
	I − 200 × 140 × 12 × 8 − 2	1 614	938	1 302

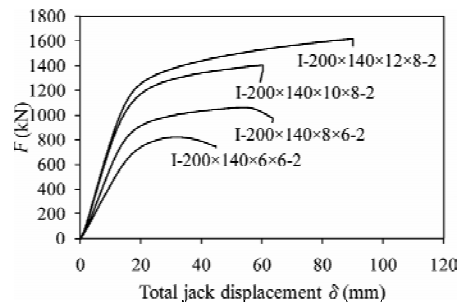**Figure 1   Total load versus jack displacement for 1/2 span configuration**

Figure 2   Total load versus jack displacement for 1/3 span configuration

ANALYSIS OF TEST RESULTS AND DESIGN RECOMMENDATIONS

Introduction

The results obtained from the tests reported in this paper on the lean duplex welded I-sections together with those performed on cold-formed hollow sections by Theofanous and Gardner[6] are analyzed and discussed in this section. Three design methods, the EN 1993 − 1 − 4[3] method using both current and proposed[7] slenderness limits, the conventional plastic design method, and the continuous strength method (CSM)[1, 7, 8, 13], are outlined and assessed based on the available test data.

European Codified Design Predictions

EN 1993 − 1 − 4[3] differentiates between Class 1 and Class 2 sections through the provision of separate slenderness limits, but, with plastic design disallowed in the code, their treatment is in fact the same. Test results and predicted moment capacities for the simple beams were compared based on the EN 1993 − 1 − 4[3] and proposed (Gardner and Theofanous[7]) slenderness limits. Results from Table 5 show that EN 1993 − 1 − 4[3] underestimates the average test capacity by 26% with a coefficient of variation (COV) of 8%, while calculations based on the proposed limits[7] showed slightly better results.

TABLE 5   COMPARISON OF TEST AND CODE PREDICTED MOMENT CAPACITIES FOR SIMPLE BEAMS

Type of test	Cross-section	EN 1993 − 1 − 4[3]		Proposed limits[7]	
		Class	M_{pred}/M_u	Class	M_{pred}/M_u
Three-point bending	I − 200 × 140 × 6 × 6 − 1	4	0.72	4	0.76
	I − 200 × 140 × 8 × 6 − 1	4	0.69	3	0.70
	I − 200 × 140 × 10 × 8 − 1	1	0.69	1	0.69
	I − 200 × 140 × 12 × 8 − 1	1	0.69	1	0.69
Four-point bending	I − 200 × 140 × 6 × 6 − 2	4	0.73	4	0.77
	I − 200 × 140 × 8 × 6 − 2	4	0.79	3	0.81
	I − 200 × 140 × 10 × 8 − 2	1	0.85	1	0.85
	I − 200 × 140 × 12 × 8 − 2	1	0.80	1	0.80
	MEAN		0.74		0.76
	COV		0.08		0.08

A comparison between the test and predicted failure loads for the continuous beams based on EN 1993 − 1 − 4[3] and the proposed[7] slenderness limits was also performed，as shown in Table 6. EN 1993 − 1 − 4[3] underestimates test failure capacity by an average of 27%，with a marginal improvement when the proposed slenderness limits are employed. This underestimation of capacity is due to the fact that EN 1993 − 1 − 4[3] assumes that continuous beams fail when the most heavily stressed cross-section reaches its codified resistance，with no allowance for moment redistribution.

TABLE 6   COMPARISON OF TEST AND CODE PREDICTED FAILURE LOADS FOR CONTINUOUS BEAMS

Configuration	Cross-section	EN 1993 − 1 − 4[3]		Proposed limits[7]	
		Class	F_{pred}/F_u	Class	F_{pred}/F_u
1/2 span	I − 200 × 140 × 6 × 6 − 1	4	0.72	4	0.76
	I − 200 × 140 × 8 × 6 − 1	4	0.70	3	0.74
	I − 200 × 140 × 10 × 8 − 1	1	0.72	1	0.72
	I − 200 × 140 × 12 × 8 − 1	1	0.66	1	0.66
1/3 span	I − 200 × 140 × 6 × 6 − 2	4	0.73	4	0.78
	I − 200 × 140 × 8 × 6 − 2	4	0.77	3	0.81
	I − 200 × 140 × 10 × 8 − 2	1	0.77	1	0.77
	I − 200 × 140 × 12 × 8 − 2	1	0.75	1	0.75
	MEAN		0.73		0.75
	COV		0.05		0.06

Conventional Plastic Analysis

As previously mentioned，plastic analysis and moment redistribution for indeterminate structures is not currently allowed for in EN 1993 − 1 − 4[3]. This is a major drawback for the design of stainless steel structures，since moment redistribution in plastic design leads to better estimations of load-carrying capacity for stocky cross-sections. In this section，plastic design is used to predict the capacities of the continuous beams with Class 1 cross-sections，while the resistances of Class 2，Class 3 and Class 4 sections are calculated using the plastic moment capacity（but with no redistribution），the elastic moment capacity and effective moment capacity respectively. The comparison between predicted and test results are shown in Table 8. An increase in capacity of between about 5% and 10% is achieved for the Class 1 sections，

while restraining safe side predictions. Plastic design therefore appears safely applicable to indeterminate stainless steel structures.

**TABLE 7   COMPARISON BETWEEN TEST AND PREDICTED FAILURE LOADS FOR
CONTINUOUS BEAMS ALLOWING FOR PLASTIC DESIGN**

Configuration	Cross-section	EN 1993 − 1 − 4[3]		Proposed limits[7]	
		Class	F_{pred}/F_u	Class	F_{pred}/F_u
1/2 span	I − 200 × 140 × 6 × 6 − 1	4	0.72	4	0.76
	I − 200 × 140 × 8 × 6 − 1	4	0.70	3	0.74
	I − 200 × 140 × 10 × 8 − 1	1	0.78	1	0.78
	I − 200 × 140 × 12 × 8 − 1	1	0.71	1	0.71
1/3 span	I − 200 × 140 × 6 × 6 − 2	4	0.73	4	0.78
	I − 200 × 140 × 8 × 6 − 2	4	0.77	3	0.81
	I − 200 × 140 × 10 × 8 − 2	1	0.82	1	0.82
	I − 200 × 140 × 12 × 8 − 2	1	0.81	1	0.81
	MEAN		0.75		0.78
	COV		0.06		0.05

The Continuous Strength Method（CSM）without Moment Redistribution

The CSM is a recently developed deformation-based design method[1, 7, 8, 13]. It replaces traditional cross-section classification with a continuous non-dimensional measure of the deformation capacity of a cross-section，and employs a strain-hardening material model. The capacities of the tested beams（with no redistribution）were found by CSM；the results are presented in Table 8. The comparisons show improved predictions for the simply supported beams. For the continuous beam tests，the CSM provides better predictions than EN 1993 − 1 − 4[3] but still fails to accurately estimate their capacity. This is mainly due to the fact that the moment redistribution is not accounted for in the applied CSM. Similar conclusions were found by Theofanous and Gardner[6]，where CSM accurately predicted the ultimate capacity of simply supported beams，but showed some conservatism for the continuous beam tests. It should be noted that for sections I − 200 × 140 × 6 × 6 − 1 and I − 200 × 140 × 6 × 6 − 2，the CSM was not applied since the element slenderness exceeds the specified limit of application of $\bar{\lambda}_p = 0.748$.

TABLE 8   ASSESSMENT OF THE CSM FOR THE SIMPLY SUPPORTED AND CONTINUOUS BEAMS

Cross-section	F_{pred}/F_u	
	Simple beams	Continuous beams
I − 200 × 140 × 6 × 6 − 1	—	—
I − 200 × 140 × 8 × 6 − 1	0.77	0.76
I − 200 × 140 × 10 × 8 − 1	0.80	0.76
I − 200 × 140 × 12 × 8 − 1	0.81	0.70
I − 200 × 140 × 6 × 6 − 2	—	—
I − 200 × 140 × 8 × 6 − 2	0.88	0.84
I − 200 × 140 × 10 × 8 − 2	0.97	0.82
I − 200 × 140 × 12 × 8 − 2	0.97	0.82
MEAN	0.87	0.78
COV	0.10	0.06

Continuous Strength Method with Moment Redistribution

Improved ultimate capacity predictions over current codified design of the tested welded I-sections by both the continuous strength method and the conventional plastic method. This is due to the fact that the continuous strength method allows for material strain-hardening，and conventional plastic analysis allows for moment redistribution. That said，conventional plastic analysis provides better results than the continuous strength method for indeterminate structures (i. e. continuous beams) owing to the allowance for moment redistribution. A hybrid approach proposed by Gardner et al.[13] is therefore considered. This method is similar to the conventional plastic analysis in terms of moment redistribution，but in addition to that，it allows for the exploitation of material strain-hardening at the location of the first plastic hinge，followed by partial strain-hardening at subsequent hinges. The method is still under development，but application to the continuous beams tested herein resulted in a 13% average under prediction of capacity，with COV of 6%，representing an approximately 10% improvement in predictions over other methods.

CONCLUSIONS

An experimental program investigating the behaviour and design of indeterminate stainless steel welded I-sections has been performed at Imperial College London. A series of tests have been carried out on both lean duplex stainless steel welded I-sections and austenitic stainless steel cold-formed hollow sections，including three-point and four-point bending tests and continuous beam tests. The obtained results were used to evaluate the current provisions for stainless steel indeterminate structures in EN 1993 − 1 − 4[3]，conventional plastic analysis，the continuous strength method[1, 7, 8, 13]，and a hybrid approach[13]. The comparison showed that the lack of allowance for inelastic reserves in EN 1993 − 1 − 4[3] leads to conservative results when estimating the capacity of the tested sections. The results obtained from both the continuous strength method (without moment redistribution) and conventional plastic method showed that material strain-hardening at cross-sectional level and moment redistribution have a significant effect on the ultimate capacity predictions of the stainless steel sections and should，therefore，be employed in design. Finally，initial results obtained from a hybrid approach for indeterminate structures[13] yields the closest prediction of observed physical behaviour.

ACKNOWLEDGMENTS

REFERENCES

［1］Gardner，L.，"The use of stainless steel in structures"，Progress in Structural Engineering and Materials，2005，7 (2)，pp. 45-55.

［2］EN 1993 − 1 − 1，"Eurocode 3：Design of steel structures - Part 1. 1：General rules-General rules and rules for buildings"，CEN，2005.

［3］EN 1993 − 1 − 4，"Eurocode 3：Design of steel structures - Part 1. 4：General rules - Supplementary rules for stainless steel"，CEN，2005.

［4］EN 10088 − 4，"Stainless steels-Part 4：Technical delivery conditions for sheet/plate and strip of corrosion resisting

steels for general purposes", CEN, 2009.

［5］Gardner, L. and Saliba, N., "Experimental study of lean duplex stainless steel", Proceedings of Eurosteel 2011 Conference, Budapest, 2011.

［6］Theofanous, M. and Gardner, L., "Plastic design of stainless steel structures", Proceedings of Stability and Ductility of Steel Structures Conference, Rio de Janeiro, Brazil, 2010, pp. 665-673.

［7］Gardner, L. and Theofanous, M., "Discrete and continuous treatment of local buckling in stainless steel elements", Journal of Constructional Steel Research, 2008, 64(11), pp. 1207-1216.

［8］Ashraf, M., Gardner, L. and Nethercot, D. A., "Structural stainless steel design: Resistance based ondeformation capacity". Journal of Structural Engineering, ASCE, 2008, 134(3), pp. 402-411.

［9］Mirambell, E. and Real, E., "On the calculation of deflections in structural stainless steel beams: an experimental and numerical investigation", JCSR, 2000, 54(1), pp. 109-133.

［10］Rasmussen, K. J. R., "Full-range stress-strain curves for stainless steel alloys", JCSR, 2003, 59(1), pp. 47-61.

［11］Gardner, L. and Nethercot, D. A., "Numerical Modeling of Stainless Steel Structural Components-A Consistent Approach", Journal of Structural Engineering, ASCE, 2004, 130(10), pp. 1586-1601.

［12］Gardner, L. and Nethercot, D. A., "Experiments on stainless steel hollow sections-Part 1: Material and cross sectional behaviour", JCSR, 2004, 60(9), pp. 1291-1318.

［13］Gardner, L., Wang, F. and Liew, A., "Influence of strain hardening on the behavior and design of steelstructures". International Journal of Structural Stability and Dynamics, 2011, 11(5), pp. 855-875.

DYNAMIC BEHAVIORS OF HOT-ROLLED STEEL BEAMS UNDER DROP WEIGHT IMPACT LOADING

* J. S. Huo[1], J. Q. Zhang[1], B. S. Chen[1] and Y. Xiao[1, 2]

[1] China Ministry of Education Key Laboratory of Building Safety and Energy Efficiency，
Hunan University，Changsha，410082，China；
[2] University of Southern California，Los Angeles，CA90089，USA
* Email：jingsihuo@gmail.com

KEYWORDS

Restrained steel beam，impact loading，dynamic behavior，catenary action

ABSTRACT

Four hot-rolled H-shaped steel beams were tested to investigate into the dynamic behaviors and catenary action mechanism of the double-span steel beams. The steel beams were horizontally axially- restrained and tested under different drop weight impact loading at the mid-span. The impact load，the mid-span displacement and strains in flange and web plates versus time history relations were recorded to analyze the dynamic behaviors of axially-restrained steel beams. The tested results showed that the impact velocity and impact energy within the tested parameters in the paper have no significant effects on the maximum impact loads of the restrained steel beams and the time history responses of impact force. However，the impact loading time was obviously prolonged and the mid-span displacements remarkably increased owing to increasing the impact energy. Additionally，the steel beams experienced obvious global buckling and local buckling of top flange and web plates close to the impact loading point. Although the restrained steel beams suffered larger rotations ranging from 0.047 rad to 0.098 rad，the steel beams still kept in good integrity. It demonstrated that hot-rolled H-shaped steel beams have an excellent impact resistance to progressive collapse.

INTRODUCTION AND BACKGROUND

The structural engineers and researchers are gradually paying much attention to the damage of structures or progressive collapse caused by extreme abnormal loading conditions such as terrorism attack，fire，impact and earthquake. Without better robustness and resistance to abnormal loading conditions，an initial local damage or local failure possibly result in propagation of local failure or progressive collapse of the overall structural system due to the failure of a key structural component. A series of studies have been conducted to investigate the dynamic behaviors of some typical structures under terrorist attacks in order to develop a performance-based anti-progressive collapse design approach. Currently，available

design specifications for anti-progressive collapse design include Eurocode 1–action on structure 1991[1], General Services Administration 2003[2] and Department of Defense 2005[3]. Although the above-mentioned design specifications perhaps can be used to prevent structures from disproportionate collapse, they are not sufficient enough to make a reasonable performance-based anti-progressive collapse design because there is little knowledge of the dynamic mechanism of progressive collapse and how to precisely improve the ductility of a structure and the chance to experience catenary action under abnormal loading conditions. Simplified analytical method was used to assess the mechanical behaviors of structures[4, 5, 6, 7].

In addition, several analytical and experimental studies on the impact behaviors of beam and catenary action have been conducted recently. Bambach[8] tested hollow and concrete filled steel hollow sections to experimentally study the dynamic behaviors under transverse impact loads and an elastic-plastic theoretical method is developed to establish the force-displacement and energy absorption relationships for hollow and concrete filled sections. Fujikake[9] studied the impact response of RC beams and a simplified nonlinear analysis was carried out to evaluate the flexural capacity of the RC beams. Kim[10] concluded that the progressive collapse-resisting capacities of steel moment frames had close relation with the plastic rotation and the axial force due to catenary action. Based on the above-mentioned literatures, the mechanical properties and the development of catenary action were rather complicated due to the complex interaction of geometric and material nonlinearity under impact force. However, only a small number of studies have investigated into the dynamic behaviors of restrained steel beams under drop-weight impact loads.

Therefore, a drop-weight impact tests on the behaviors of four double-span restrained steel beams in the paper was carried out in order to investigate the impact resistance to collapse. The effects of impact velocity and impact energy on the dynamic behaviors of the horizontally-restrained steel beams were investigated. The main purpose of this paper was to experimentally study the dynamic behaviors and the development of catenary action and an analysis method was carried out to determine the inner force of the steel beams with their respective impact response.

EXPERIMENTAL PROGRAM

Specimen Preparation

The details of the specimens and partial test results were summarized in Table 1. The steel beams were made of hot-rolled section HM250 × 125 × 6 × 9 mm. The geometrical dimensions and constructional details of the specimens are shown in Figure 1. The full consideration of plasticity in the cross-section of the hot-rolled steel beam under impact loading is expected due to the hot-rolled section with the flange
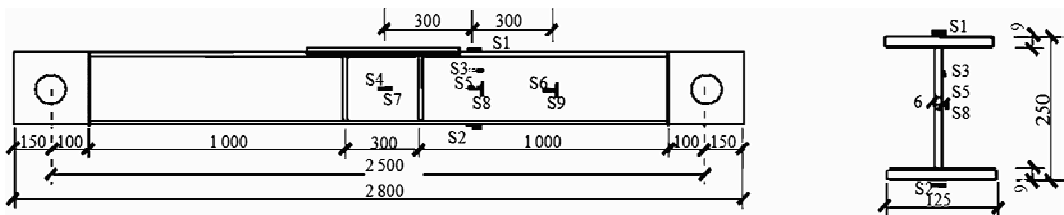

Figure 1　The details of restrained steel beam (mm)

slenderness ratio ($b_f/2t_f = 7$) and the web slenderness ratio ($h_0/t_w = 39$, h_0 is the clear height of web plate). Additionally, in order to experimentally study the formation of catenary action of the steel beams under impact loading, the steel beams were reinforced by transverse stiffeners and cover plates at the mid-span and the two ends to guarantee the fully developed plasticity of the steel beams. In addition, the hot-rolled section was made of Q235 grade steel and the average yield strengths (f_{sy}) for flange and web plates are 239.1MPa and 251.1MPa respectively.

TABLE 1   SUMMARY OF TESTED RESTRAINED STEEL BEAMS

specimen	Sectional dimension $h \times b_f \times t_w \times t_f$ mm	M(kg)	H(m)	$F_{u, max}$ (kN)	F_y (kN)	F_p (kN)	φ_{max} (rad)	φ_u (rad)	E_1 (kJ)	E_2 (kJ)	$\dot{\varepsilon}$
HR4-3	250×125×6×9	450	3.2	847	226	295	0.047	0.045	14.1	12.6	2.32
HR4-6	250×125×6×9	450	6.0	790	230	305	0.075	0.068	26.5	23.3	3.93
HR4-8	250×125×6×9	450	8.0	819	233	310	0.098	0.079	35.3	29.8	5.17
HR5-6	250×125×6×9	575	6.0	627	233	300	0.097	0.08	33.8	30.6	4.84

Note: M amd H denote the hammer weight and drop height. The ultimate impact bearing capacity ($F_{u, max}$) was defined as the maximum impact force measured in the impact tests; the plastic collapse load of the cross-section (F_y) was determined by a theoretical method, while plastic impact load in the test (F_p) was determined by the average value of the maximum and minimum of the second fluctuation on impact force. Energy application (E_1) was determined according to $E = mv^2/2$, while total energy absorption (E_2) was determined by calculating as the area between the impact load versus displacement curve. φ_{max} and φ_u denote the maximum rotation and the residual rotation of steel beams, which were calculated by the related vertical deformation divided the clear span length.

Test Setup

The impact tests on the dynamic behaviors of steel beams were conducted using a drop hammer with its up to 10 kN weight and a maximum height of 16 meters. Figure 2 shows the general view of the impact test set-up. The steel beam with a span length of 2 500 mm was simply-connected to a rigid steel support frame with two hinged immovable supports.
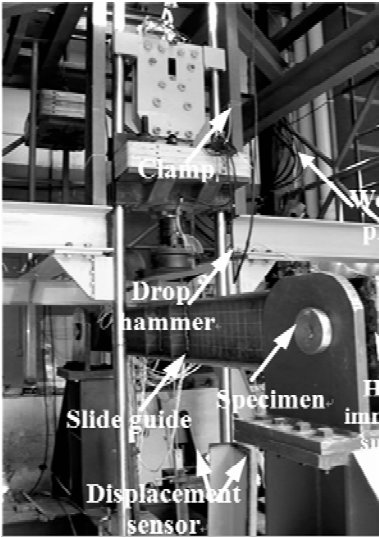

Figure 2   Drop-weight impact test setup

The impact force, vertical deflections of the steel beams and microscopic deformations in the steel beam's

flange and web plates were recorded. Strain gauges were mounted onto the flange and web plates of the Steel beams at different sections of the steel beams，as shown in Figure 1. An oscilloscopic fast data acquisition system was used to capture the electric signals of the load transducer mounted on the hammer，strain gauges and voltage type displacement transducers at a rate of 50 millions sample/s per channel.

EXPERIMENTAL RESULTS

Failure Mode

Typical failure modes of the steel beams after the impact loading test were shown in Figure 3. It can be shown that the steel beams suffered obvious global and local buckling，and the increased impact energies led to more remarkable local buckling and larger global deflections at the mid-span section. The behavior was initially dominated by a combination of local distortion and global beam bending，and subsequently when the transverse displacements became finite by axial （tension），membrane forces also （e. g. Bambach[8]）. Additionally，although suffering remarkable residual deformation with the maximum rotation of 0.098 rad，there was no cracks and rupture found in the steel beams and the cross sections were kept good integrity. Within the limited test parameters，all specimens exhibited excellent dynamic behaviors，i. e. the excellent anti-resistance to impact loading.
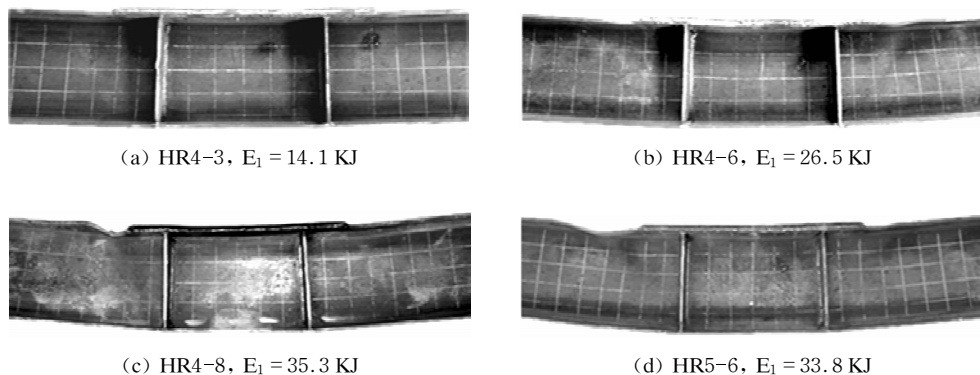

(a) HR4-3，$E_1 = 14.1$ KJ   (b) HR4-6，$E_1 = 26.5$ KJ

(c) HR4-8，$E_1 = 35.3$ KJ   (d) HR5-6，$E_1 = 33.8$ KJ

Figure 3　Local failure modes of the mid-span sections

Impact Response

Figure 4 and Figure 5 show the measured impact load （F） versus time （t） relation and mid-span deflections （δ） versus time （t） relation curves of the restrained steel beams，respectively. The measured impact load versus time responses were characterized by an initial shorter impulse wave stage with extremely high amplitudes followed by a longer smooth impulse wave stage with relatively lower amplitude. The phenomenon is similar to the tested results described in the literature （Fujikake[9]） and Lee[8]. The steel beams generally were loaded to the maximum forces within 1.0 ms and the impact forces increased and fell sharply twice at the initial stage and tended to be flatter gradually，finally decreased to zero at the unloading stage. Although the steel beams were loaded under different impact energies，they suffered almost the same maximum impact loads and exactly the same dynamic responses of impact force versus time relations. However，the duration of impact loading was obviously affected by drop height and weight，and it increased with the increase of impact energy.
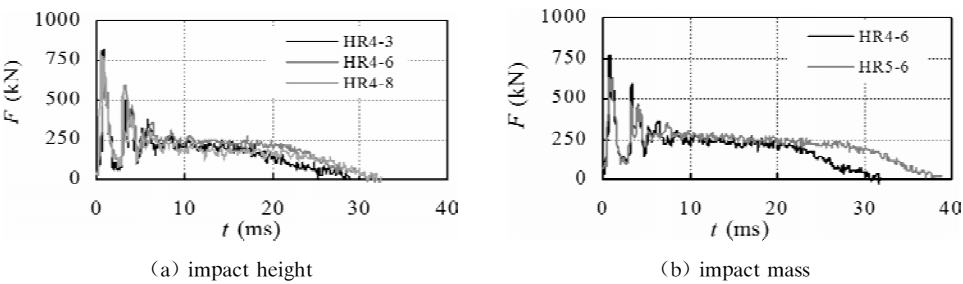
(a) impact height

(b) impact mass

Figure 4   Impact force versus time relations of restrained steel beams
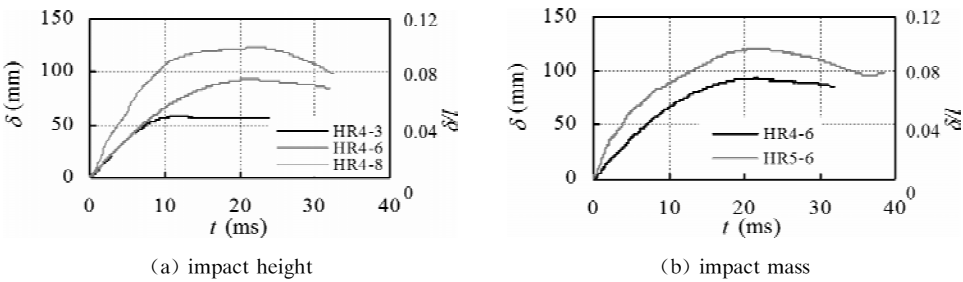

(a) impact height

(b) impact mass

Figure 5   Mid-span displacement versus time relations of restrained steel beams

It can be shown from Figure 5 that all the steel beams suffered remarkable collapse deflections are larger than the plastic deflection corresponding to the plastic moment. The restrained hot-rolled steel beams behaved well under the extreme dynamic loading and had excellent resistance to larger plastic deformations. The mid-span vertical deflection increased proportionally with time during the initial oscillating impact loading stage and developed nonlinearly during the stabilizing loading stage. The maximum mid-span deflection increased with the increase of impact energy by changing the impact height （impact velocity） and the weight of drop hammer.

ANALYSIS OF CAETENARY ACTION

Internal Force Analysis

The tested results in the paper showed that all steel beams had suffered larger deformations under impact loading，as shown in Figure 3 and Figure 5. The larger deformations would led to the fact that the restrained steel beams experienced complicated stress state transformation from in bending to under catenary action under impact loading. In order to understand the dynamic mechanism of restrained steel beams under impact loading，some strain gauges were mounted onto the flange plates and web plates，which are shown in Figure 1，to record the strain versus time history relations. Figure 6 shows the strain versus time relation curves at the mid-span section of Specimens HR4-3 and HR5-6. The longitudinal strain distributions in the mid-span section at different impact loading stages are shown in Figure 7 in which h' denotes the distance from the strain gauge to the top flange of steel beam and η denotes the relative position of strain gauge along beam depth （h），i.e., $\eta = h'/h$.
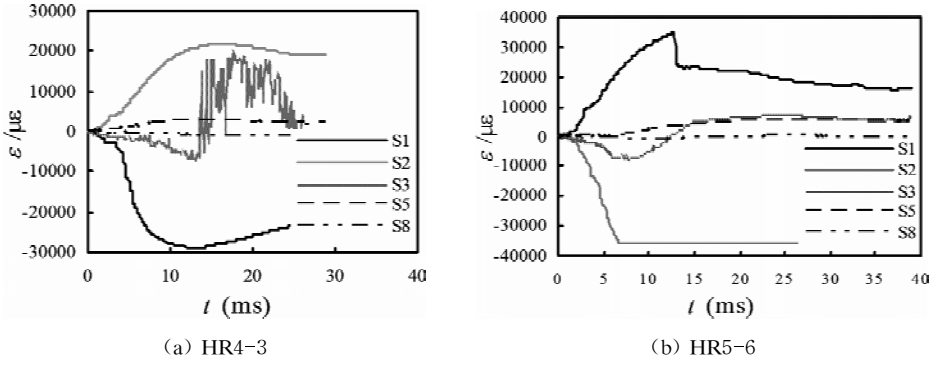
（a）HR4-3   （b）HR5-6

Figure 6   Strain versus time relations of at the mid-span section of restrained steel beams

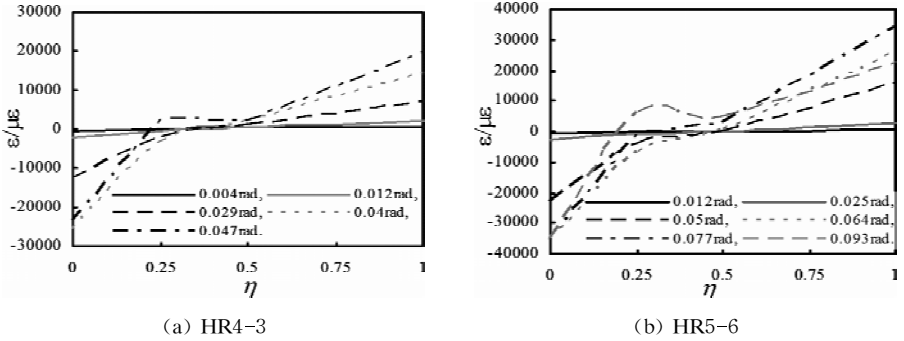（a）HR4-3   （b）HR5-6

Figure 7   Longitudinal strain distributions in the mid-span section at different impact loading stages

According to the measured longitudinal strain distributions as shown in Figure 6 and Figure 7，the steel beams were still in elastic stage as the steel beams were loaded during the initial impulse wave stage with extremely high amplitudes. The yielding moment M_y can be determined according to the elastic analysis method. Under the second impulse impact loads which were generally much smaller than the yielding loads，all the restrained steel beams entered into plastic stage with the rapid development of flange strain. The neutral axis at this stage remained in the middle of the beam section. So the bending moment at this stage can be equivalent to cross section plastic moment，also the plastic collapse loads of the cross section F_y were obtained as shown in TABLE 1. Considering the dynamic effects and ignoring the effects of inertia force and other factors，F_y was smaller than the measured load F_p. While the steel beams were loaded into the smooth impulse wave stage，the longitudinal strain in the beam web plate（S5）increased rapidly and the neutral axis moved close to the upper flange of the steel beam，and also the axial force（N）began to increase to resist the impact load. The impact force during the loading stage almost kept constant and the resistance to bending can be determined by Equation（1）based on the equilibrium condition between the internal forces and applied load.

$$M_{ui} = (F_u - 2N_i\varphi_i) \cdot L/4 \tag{1}$$

where F_u denotes the stable impact force in the smooth impulse vase stage，N_i and φ_i denote the axial force and rotation corresponding to time i，respectively.

Analysis of Catenary Action

Based on the above analytical method，the moment and axial force versus rotation relation curves can be

obtained as shown in Figure 8. The steel beams experienced four typical loading stages during the impact loading，including the elastic stage，elasto-plastic stage，catenary developing stage and the catenary action stage. In elastic stage（oa），the beam was mainly subjected to bending moment which kept growing linearly and the beam acted as a bending member. In elasto-plastic stage（ab），the lateral deflection of the steel beam increased nonlinearly and the steel beam was loaded to the maximum bending moment. Simultaneously，the axial force in the steel beam started to increase while the bending action still predominated over axial tension action. The third stage（bc）actually was a transition from bending action to catenary action during which the bending moment decreased while the axial force increased rapidly. The increasing of the axial force provided a remarkable increasing resistance to the impact loading in this stage. Subsequently，the beam was loaded into the catenary action stage finally（cd），the internal forces of the steel beam almost kept constant while the lateral deflection still increased. During this loading stage，the horizontally restrained steel beam can experience remarkable catenary action by suffering much large lateral deflection in order to absorb the impact energy.
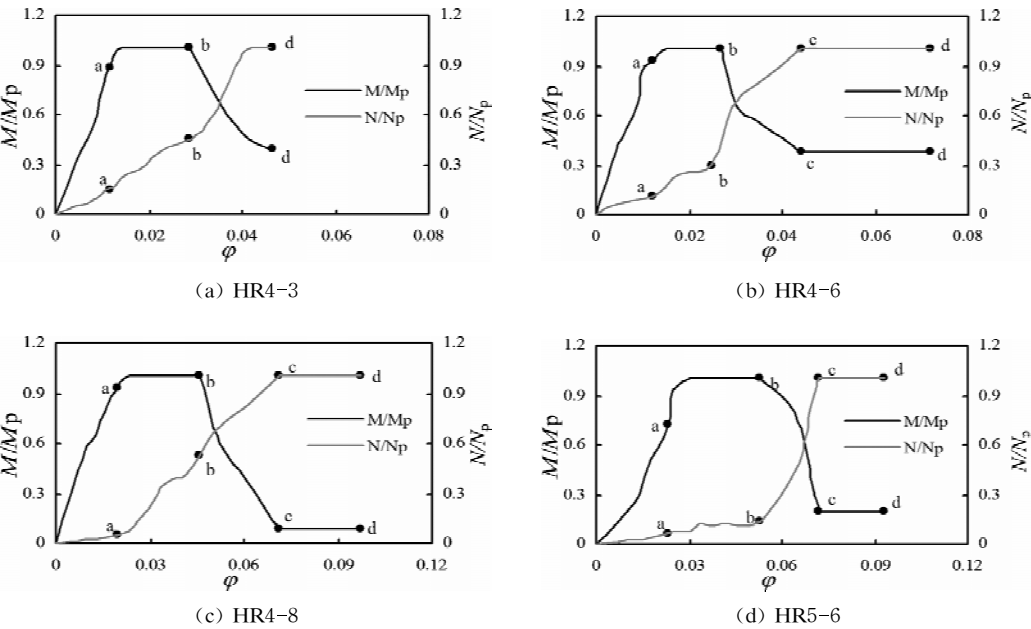

(a) HR4-3 　　　　　　　　　　　　　　　(b) HR4-6

(c) HR4-8 　　　　　　　　　　　　　　　(d) HR5-6

Figure 8　Moment versus rotation and axial load versus rotation relations of restrained steel beams

Based on the previous tested results and analysis of catenary action，the dynamic loading due to a sudden column removal would cause the horizontally restrained steel beam to suffer remarkable deformation so that the steel beam would absorb the impact energy to prevent it from collapsing. All the steel beams experienced four load bearing stages in order to form catenary action to resist the impact loading. That is，the horizontally restrained steel beams transmitted from a bending member to a tension-bending member，and finally to a member in tension. TABLE 2 shows the typical rotations of the four tested steel beams under drop-weight impact loading in the paper.

TABLE 2　ROTATIONS OF DIFFERENT LEVELS OF THE RESTRAINED STEEL BEAMS

Specimen	φ_a	φ_b	φ_c	φ_{max}
HR4-3	0.012	0.029	—	0.047
HR4-6	0.012	0.027	0.044	0.075

continued

Specimen	φ_a	φ_b	φ_c	φ_{max}
HR4-8	0.020	0.046	0.071	0.098
HR5-6	0.023	0.053	0.072	0.097

Notes: φ_a denotes the rotation at the end of the elastic stage;

φ_b denotes the rotation at the end of the plastic stage;

φ_c denotes the rotation at the beginning of the catenary action stage;

φ_{max} denotes the maximum rotation under impact load;

"—" indicates no formation of catenary action.

CONCLUSION

The paper experimentally studied the dynamic behaviors of double-span horizontally restrained steel beams under drop-weight impact loading. The mechanism of catenary action was analyzed based on the tested results. The following conclusions may be drawn based on the limited research reported.

(1) The increased impact energy led to more severe global and local buckling of the restrained steel beams under impact loading. The local buckling generally took place in the top flange plate and web plate close to the impact point.

(2) The test results showed that there was no significant effect of impact energy on the maximum impact loads and the impact load versus time history relation curves of the restrained steel beams. However, the impact loading time and the deflection of the steel beams obviously tended to increase with the increase of impact energy. The increased deflection indicated that the impact energy was dissipated by the larger deformation.

(3) The changing of the inner force in the mid-span section can be derived based on the measured stress and strains in the steel beams. The analytical results proved that the restrained steel beam under impact loading experienced four different load-bearing stages including elastic stage, plastic stage, catenary developing stage and catenary action stage. With the increase of the mid-span deflection, the restrained steel beams in bending gradually converted into suspension chains under catenary action.

REFERENCE

[1] "Draft pr EN 1991-1-7, Eurocode1-actions on structures, part 1-7: general actions-accidental actions", Brussels, European Committee for Standardization, 1991.

[2] GSA. General Services Administration, "Progressive collapse analysis and design guidelines for new federal office buildings and major modernization projects", 2003.

[3] DOD. Department of Defense, "Unified facilities criteria Design of Buildings to Resist Progressive Collapse", 2005.

[4] Kaewkulchai, G. and Williamson, E. B., "Beam element formulation and solution procedure for dynamic progressive collapse analysis", Computers and Structures, 2004, 82(7-8), pp.639-651.

[5] Tsai, M. H., "An analytical methodology for the dynamic amplification factor in progressive collapse evaluation of building structures", Mechanics Research Communications, 2010, 37(1), pp.61-66.

[6] Izzuddin, B. A., Vlassis, A. G. and Elghazouli, A. Y., et al., "Progressive collapse of multi-storey buildings due

to sudden column loss — Part I: Simplified assessment framework", Engineering Structures，2008，30(5)，pp. 1308-1318.

［7］Lee，C.，Kim，S. and Han，K.，et al.，"Simplified nonlinear progressive collapse analysis of welded steel moment frames", Journal of Constructional Steel Research，2009，65(5)，pp. 1130-1137.

［8］Bambach，M. R.，Jama，H. and Zhao，X. L.，et al.，"Hollow and concrete filled steel hollow sections under transverse impact load", Engineering Structures，2008，30(10)，pp. 2859-2870.

［9］Fujikake，K.，Li，B. and Soeun，S.，"Impact response of reinforced concrete beam and its analytical evaluation", Journal of Structure Engineer，2009，135(8)，pp. 938-950.

［10］Kim，T. and Kim，J.，"Collapse analysis of steel moment frames with various seismic connections. Journal of Constructional Steel Research"，2009，65(6)，pp. 1316-1322.